PROCEEDINGS
INTERNATIONAL SCHOOL OF PHYSICS «ENRICO FERMI»

COURSE 207

Advances in Thermoelectricity: Foundational Issues, Materials and Nanotechnology

edited by D. Narducci, G. J. Snyder and C. Fanciulli

15 - 20 July 2019

Villa Monastero
Varenna, Lake Como

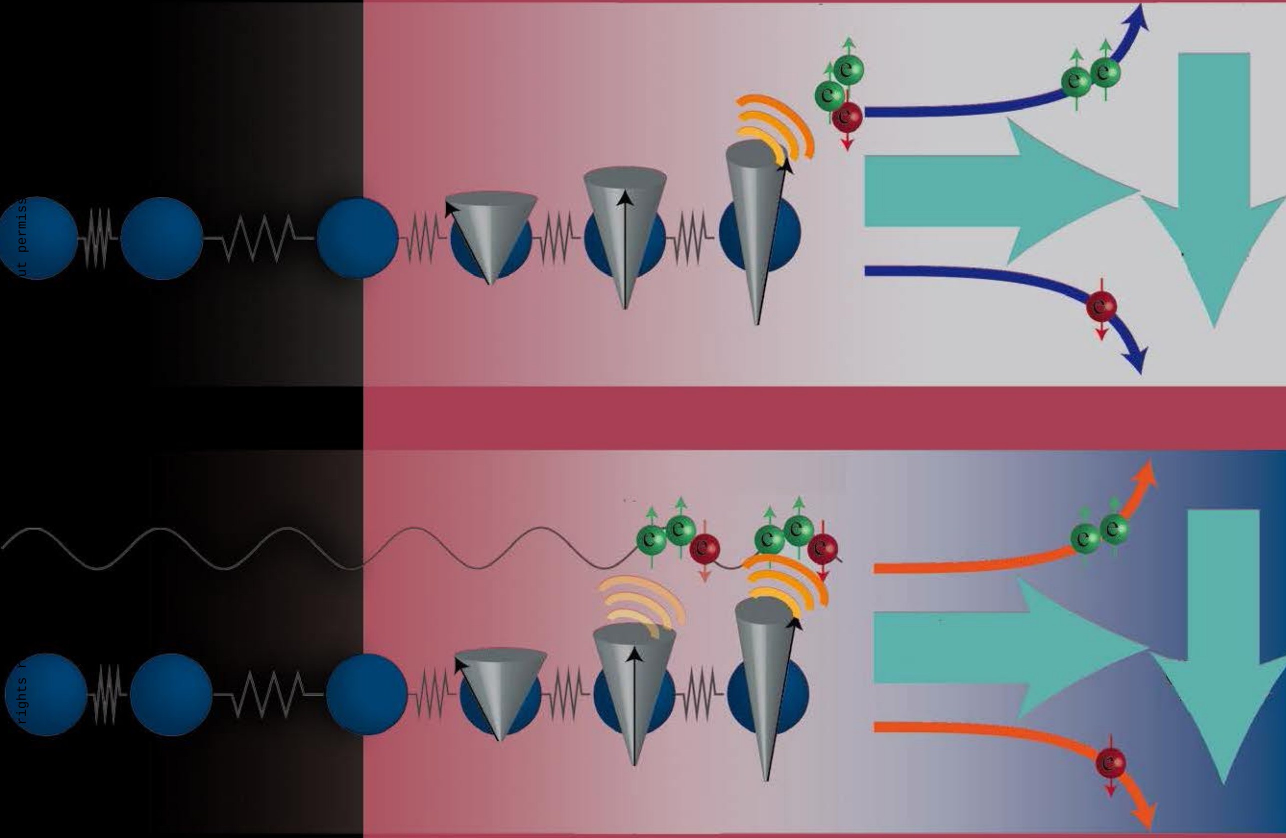

SOCIETÀ ITALIANA DI FISICA

SOCIETÀ ITALIANA DI FISICA

RENDICONTI
DELLA
SCUOLA INTERNAZIONALE DI FISICA
“ENRICO FERMI”

CCVII Corso

a cura di D. Narducci e G. J. Snyder
Direttori del Corso
e di
C. Fanciulli

VARENNA SUL LAGO DI COMO
VILLA MONASTERO
15 – 20 Luglio 2019

Recenti sviluppi della termoelettricità: aspetti fondamentali, materiali e nanotecnologie

2021

SOCIETÀ ITALIANA DI FISICA
BOLOGNA-ITALY

ITALIAN PHYSICAL SOCIETY

PROCEEDINGS
OF THE
INTERNATIONAL SCHOOL OF PHYSICS
"ENRICO FERMI"

Course 207

edited by D. Narducci and G. J. Snyder
Directors of the Course
and
C. Fanciulli

VARENNA ON LAKE COMO
VILLA MONASTERO
15 – 20 July 2019

Advances in Thermoelectricity: Foundational Issues, Materials and Nanotechnology

2021

IOS
Press

AMSTERDAM - WASHINGTON DC

ISSN 0074-784X (print)
ISSN 1879-8195 (online)

ISBN 978-1-64368-172-6 (print) (IOS Press)
ISBN 978-1-64368-173-3 (online) (IOS Press)
ISBN 978-88-7438-126-5 (SIF)

LCCN 2021935301

DOI 10.3254/ENFI207

jointly published and distributed by:

IOS PRESS
Nieuwe Hemweg 6B
1013 BG Amsterdam
The Netherlands
fax: +31 20 687 0019
`info@iospress.nl`

SOCIETÀ ITALIANA DI FISICA
Via Saragozza 12
40123 Bologna
Italy
fax: +39 051 581340
`order@sif.it`

For book sales in the USA and Canada
IOS Press, Inc.
6751 Tepper Drive
Clifton, VA 20124
USA
Tel.: +1 703 830 6300
Fax: +1 703 830 2300
`sales@iospress.com`

Supported by

Istituto Nazionale di Fisica Nucleare (INFN)

Istituto Nazionale di Geofisica e Vulcanologia (INGV)

Museo Storico della Fisica e Centro Studi e Ricerche “Enrico Fermi”

Istituto Nazionale di Ricerca Metrologica (INRiM)

Gran Sasso Science Institute (GSSI)

Università di Roma “Tor Vergata”

Univerlecco

Camera di Commercio di Lecco

Elsevier Ltd

I.S.C. Srl

BEART Engineering

Università di Milano-Bicocca

Produced by the SIF Editorial Staff

Production Editors: Marcella Missiroli, Elena Baroncini

Cover: see Joseph P. Heremans, *Thermal spin transport and spin in thermoelectrics*, p. 171.

Cover design by Renee Ripley

Graphic elaboration by Simona Oleandri

Printed in Italy by nuova MONOGRAF snc - Bologna

CONTENTS

The electronic version of volumes from 124 is available online at the IOS Press web site

`http://ebooks.iospress.nl/bookseries/proceedings-of-the-international-school-of-physics-enrico-fermi`

Figures with colour source files will appear in colour in the online version.

SIF Members are granted free access to these volumes at
`https://members.sif.it`

For a complete list of published courses see
`https://en.sif.it/books/series/proceedings_fermi`

Preface

The history of thermoelectricity is largely intertwined with the most significant advances of thermodynamics and condensed-matter physics over the last two centuries. The discovery of the thermoelectric effects (Seebeck, Peltier and Thomson) played a key role in the birth of irreversible thermodynamics, largely acting as a workbench of models and theories —including the experimental validation of the Onsager-Casimir relations. Thermoelectricity has further promoted advances in solid-state physics and chemistry, inspiring research on the relationships between thermal conductivity and crystal structure of materials over the first half of the XX century —which further extended to defect engineering in real crystals. In more recent times, research on thermoelectric materials has promoted and motivated a major research endeavor to clarify factors affecting thermal conductivity in nanostructures, in a more general effort to apply nanotechnology to enhance the performance of thermoelectric materials to be exploited in thermoelectric generators and coolers.

Thermoelectricity is today among the most exciting fields of research for a materials physicist. The challenge of devising materials with exceptional properties (low thermal conductivity, high electrical conductivity, and a large Seebeck coefficient) has triggered a global, interdisciplinary endeavor to exploit scientific creativity. The need for sustainable energy has added a technological momentum. Still, thermoelectricity remains a substantial branch of thermodynamics, and the modes of operation of a thermoelectric system still call for sophisticated theoretical analyses, which have inspired novel developments of irreversible thermodynamics, from the analysis of the efficiency at a finite rate to recent studies on phonon hydrodynamics.

The 207 Course of the International School of Physics “Enrico Fermi” dedicated to *Advances in Thermoelectricity: Foundational Issues, Materials, and Nanotechnology* encompassed the full complexity of modern thermoelectricity. Its organization aimed at exposing students to all most cogent themes relevant to current research in the field. Twelve lecturers participated in the course, and we gratefully thank both those who provided contributed written papers that are published in this volume and those who just provided their lectures.

Classes began with three series of lectures on the fundamentals of thermodynamics, solid-state physics, and statistical mechanics applied to thermoelectricity —delivered by D. Narducci ("Thermodynamics and thermoelectricity"), G. J. Snyder ("Transport property analysis method for thermoelectric materials: Materials quality factor and the effective mass model"), and R. Rurali ("A primer on phonon transport"). Applications of such concepts to materials were then the subject of the lectures given by M. Martin-Gonzalez ("Past and present of metal chalcogenides, oxides, Heusler compounds and Zintl phases as thermoelectrics: A brief summary") and K. Koumoto ("Low-dimensional inorganic/organic hybrid thermoelectrics"). Furthermore, Y. Grin and H. Sirringhaus delivered lectures on silicon and silicides and on charge and heat transport in organics. Additional insights into applications of nanoscience to thermoelectricity were provided by G. Benenti ("Theoretical approaches for nanoscale thermoelectric phenomena"), and N. Neophytou ("Electronic transport simulations in complex band structure thermoelectric materials") while J. P. Heremans contributed highlights on spin thermoelectrics and related topics ("Thermal spin transport and spin in thermoelectrics"). The driving force from advanced technology was covered by the lectures delivered by C. Fanciulli ("Thermoelectric harvesting: Basics on design optimization and applications") and B. Lorenzi ("Heat conversion in solar thermoelectric harvesters" and "Heat conversion in hybrid solar thermoelectric harvesters").

The course gathered 51 students from 24 countries and was organized to foster informal and continual interactions among students and lecturers. The lively, participative spirit of the course was one of its major successes. This was also the result of the exceptional organizational framework provided by the Varenna secretary. We wish also to gratefully acknowledge the sponsorships we received from ISC s.r.l., the Italian Thermoelectric Society, Elsevier, and the University of Milano-Bicocca, which enabled the partial or full waiving of registrations fees for students coming from less-developed countries and which concurred to support travel expenses of some of the lecturers coming from non-European countries. Last but not least, we gratefully acknowledge the Italian Physical Society that provided us with the opportunity of organizing this course in the prestigious framework of the "E. Fermi" School of Physics.

DARIO NARDUCCI, G. JEFFREY SNYDER and CARLO FANCIULLI

This page intentionally left blank

Italian Physical Society
INTERNATIONAL SCHOOL OF PHYSICS «E. FERMI»
COURSE 207
15 - 20 July 2019
VILLA MONASTERO – VARENNA, LAKE COMO

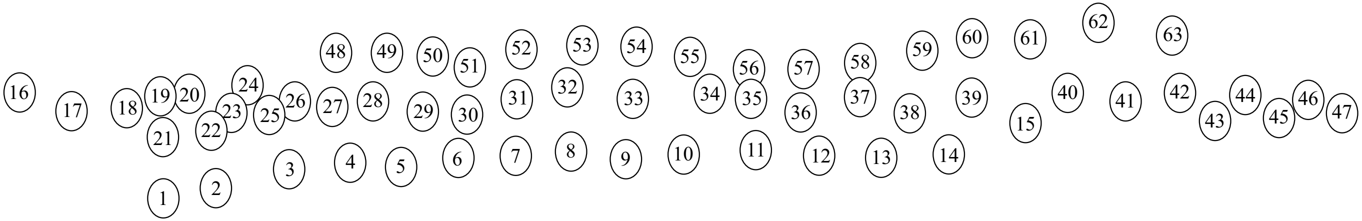

1) Francesca Cosenza
2) Ramona Brigatti
3) Barbara Alzani
4) Carlo Fanciulli
5) Neophytos Neophytou
6) Yuri Grin
7) Dario Narducci
8) Bruno Lorenzi
9) Joseph Heremans
10) Marisol Martin-Gonzalez
11) Henning Sirringhaus
12) Kunihito Koumoto
13) Riccardo Rurali
14) Giuliano Benenti
15) Hikaru Horii
16) Ketan Lohani
17) Eleonora Isotta
18) Ramya Gurunathan
19) Jaywan Chung
20) Marijn Van de Putte
21) Joana Ribeiro
22) Chiara Cignarella
23) Julia Camut
24) Filipe Correia
25) Vanira Trifiletti
26) Dionisius H. L. Tjhe
27) Anastasiia Tukmakova
28) Francesco Aversano
29) Caterina La Terra
30) Candida Pipitone
31) Felix Kaiser
32) Mohamed Atwa
33) Giovanna Latronico
34) Oliver Schmuck
35) Panagiotis Mangelis
36) Georgios Mesaritis
37) Kamil Ciesielski
38) Laura De Sousa Oliveira
39) Duarte Moço
40) Nikola Kanas
41) Shrikant Saini
42) Pengpeng Shang
43) Lu Zhang
44) Fernan Saiz
45) Stefano Magagna
46) Raimondo Cecchini
47) Arturo Klaus Marquez Guaman
48) Dhritiman Chakraborty
49) Ruben Bueno Villoro
50) Antonio Cappai
51) Federica Ursi
52) Yaron Amouyal
53) Rodrigo Rubio Govea
54) Trevor Bailey
55) Busra Mete
56) Haruno Kunioka
57) Mujde Yahyaoglu
58) Kunal Mitra
59) Shoya Kawano
60) Alberto Castellero
61) Michele Pigliapochi
62) Dennis Groeneveld
63) Matteo Mastellone

This page intentionally left blank

Proceedings of the International School of Physics "Enrico Fermi"
Course 207 "Advances in Thermoelectricity: Foundational Issues, Materials and Nanotechnology",
edited by D. Narducci, G. J. Snyder and C. Fanciulli
(IOS, Amsterdam; SIF, Bologna) 2021
DOI 10.3254/ENFI210002

Thermodynamics and thermoelectricity

D. Narducci

University of Milano Bicocca, Department of Materials Science
via R. Cozzi 55, I-20125 Milan, Italy

Summary. — The aim of this lecture was an analysis of the thermodynamics of thermoelectric phenomena and of thermoelectric generators seen as heat engines. The basic theory of classical irreversible thermodynamics is recalled, and the conversion efficiency of thermoelectric generators is computed thereof under Dirichlet boundary conditions both in the constant-property limit (namely for vanishingly small temperature differences) and by using the concept of thermoelectric compatibility (for large temperature differences).

1. – Introduction

Thermoelectricity encompasses a set of physical phenomena correlating heat or charge fluxes to temperature gradients or electric fields. Empirical evidence of the possibility of eliciting an electric voltage through the application of a temperature difference dates back to Volta (1794) although it is customary to credit the discovery of the phenomenon to Seebeck, who independently rediscovered it in 1821. The reverse effect, namely the generation of a heat flux flowing from a cold to a hot thermostat upon application of an electric current, was instead reported for the first time by Peltier in 1834.

The discovery of thermoelectric effects was soon paralleled by the discovery of many other coupled transport processes where thermodynamic affinities are capable of generating also non-entropy-conjugated thermodynamic fluxes. This class of phenomena found a proper theoretical framework within non-equilibrium thermodynamics, at one time driving its historical development and taking advantage of its achievements over the last part of the 19th century and the first half of the 20th century.

This paper summarizes the lectures given in 2019 at the *E. Fermi International School of Physics* in the frame of a course dedicated to thermoelectricity. Lectures moved from thermodynamics, recalling basic concepts of equilibrium thermodynamics (sect. **2**) and extending them to non-equilibrium processes in the frame of the so-called Classical Irreversible Thermodynamics (CIT) (sect. **3**). Then, its results are applied to the analysis of thermoelectric phenomena in sect. **4**. Finally, since, beyond metrologic applications, thermoelectricity has practical applications to convert heat into useful work, the efficiency of thermoelectric devices operating as heat engines is also discussed (sects. **5** and **6**).

2. – Gibbsian equilibrium thermodynamics

Thermodynamics is a physical theory aiming at describing the interaction among many-particle systems and, more precisely, exchanges of energy and matters that result thereof. This is achieved by introducing non-mechanical quantities, such as internal energy U, temperature θ, and entropy S; and the concept of thermodynamic state, defined as an ensemble of quantities unambiguously describing the system, namely enabling its exact replication.

In its historical development, thermodynamics has initially focused on processes (transformations) joining special classes of states, named equilibrium states. An equilibrium (thermodynamic) state may be provisionally defined as the state of a homogeneous, time-invariant system. Two systems are said to be in equilibrium with each other if their interaction cannot lead to any perturbation of their states.

Gibbsian equilibrium thermodynamics (GET) provides a complete set of axioms (laws of thermodynamics) that allow to distinguish among possible and impossible transformations between pairs of states.

2˙1. *Fundamental principles of equilibrium thermodynamics.*

– The first non-mechanical quantity defined by GET is temperature. The zeroth law of thermodynamics states that, when no mechanical, electrical or nuclear work(1) may be done by systems, if systems A and B are in equilibrium with a third system C, then they are also in equilibrium with each other. This axiom may be used to construct ensembles (classes of equivalence) of states which are all in equilibrium with each other. A temperature θ may be then defined as a suitable function of the (mechanical and geometric) quantities describing the states and such that $\theta_A = \theta_B$ for each and all states in equilibrium. This also implies that any transformation resulting from the interaction of two systems at the

---

(1) Hereafter *work* for short.

same temperature and leading to a variation of their states is impossible if the systems do not do any work on each other.

The first law of thermodynamics may be seen as an extension of the principle of energy conservation. To this aim, one needs to introduce the concept of adiabatic walls, defined as system borders such that two systems in contact through adiabatic walls cannot perturb each other if the separating walls are rigid. A process occurring within rigid adiabatic walls is said to be adiabatic.

The first law states that in an adiabatic cyclic process work may be neither generated or destroyed. Instead, in non-adiabatic cyclic processes the effect of the work done by or on the system is always the same, independently of the path. This leads to define a new potential, named internal energy (U). In an adiabatic process, $\mathrm{d}U := đW$, where W is the work done by the system; while for a generic process it is customary to introduce an extensive quantity named heat (Q) and defined as $đQ := \mathrm{d}U - đW$. The first law of thermodynamics states that $\mathrm{d}U$ is an exact differential (while $đQ$ and $đW$ are not), so that

$$\oint \mathrm{d}U = \oint đQ + \oint đW = 0 \tag{1}$$

over any cyclic process. This encompasses both work conservation for adiabatic cycles ($\oint \mathrm{d}U = \oint đW = 0$) and the invariance of the (thermal) effect of the work done by or on the system ($\oint đQ = -\oint đW$). Even more significantly, it implies that only cyclic transformations that conserve U are possible. Equation (1) is obtained for steady systems in the absence of external fields. It may be generalized by defining $E = U + K + E_{\mathrm{pot}}$, where K is the kinetic energy and E_{pot} is the potential energy associated to external fields (*e.g.*, gravitational). Then

$$\oint \mathrm{d}E = \oint đQ + \oint đW = 0. \tag{2}$$

The second law of thermodynamics deals with transformations that, although complying with the zeroth and the first laws, are anyway impossible. In an isolated system a new potential named entropy (S) is defined for a quasi-static process as $\mathrm{d}S := đQ/T$, where T is a suitable positive-defined instantiation of θ, so that $\mathrm{d}S \geq 0$ for any adiabatic process. Conversely, adiabatic processes for which $\mathrm{d}S < 0$ are impossible. Therefore, since equilibrium states are stable, one may also state that at equilibrium $\mathrm{d}S = 0$ and $\mathrm{d}^2S < 0$.

Although the Clausius' formulation of the second law in limited to isolated systems, it may be restated for closed and open system by splitting $\mathrm{d}S$ in two parts, namely the change of entropy associated to internal processes $\mathrm{d_i}S$ and the change due to matter and energy exchanges with the ambient $\mathrm{d_e}S$. Thus $\mathrm{d}S = \mathrm{d_i}S + \mathrm{d_e}S$. The second law prescribes that $\mathrm{d_i}S \geq 0$ while it sets no limitation on the sign of $\mathrm{d_e}S$ (and therefore of $\mathrm{d}S$).

The first and second law of thermodynamics may be jointly used to write, for a reversible transformation, that

$$\mathrm{d}U = T\,\mathrm{d}S - P\,\mathrm{d}V, \tag{3}$$

which is known as Gibbs' equation. Note that in this form Gibbs' equation only accounts for mechanical work. Further to the addition of terms related to non-mechanical work, for open systems Gibbs' equation needs to be completed with the work associated to matter flowing through system boundaries:

$$\text{đ}W_{\mathrm{m}} = \sum_k \mu_k \mathrm{d}m_k, \tag{4}$$

where μ_k is the chemical potential of the k-th exchanged species (per mass unit) and $\mathrm{d}m_k$ is the change of its mass. The sum runs over all exchanged species. The term $\text{đ}W_{\mathrm{m}}$ is somewhat misleadingly named "chemical work", although it clearly does not necessarily refer to chemical reactions. Gibbs' equation for open system reads then

$$\mathrm{d}U(S, V, \{m_k\}) = T\,\mathrm{d}S - P\,\mathrm{d}V + \sum_k \mu_k \mathrm{d}m_k. \tag{5}$$

Gibbs' equation allows to express all intensive variables as derivatives of U:

$$T = \left(\frac{\partial U}{\partial S}\right)_{V,\{m_k\}}, \tag{6a}$$

$$P = -\left(\frac{\partial U}{\partial V}\right)_{S,\{m_k\}}, \tag{6b}$$

$$\mu_k = \left(\frac{\partial U}{\partial m_k}\right)_{S,V,\{m_{i\neq k}\}}. \tag{6c}$$

An additional consequence of Gibbs' equation is that, since U is an extensive variable, then $U(\lambda S, \lambda V, \{\lambda m_k\}) = \lambda U(S, V, \{m_k\})$ for any λ. Hence, using eqs. (5) and (6), it is easy to obtain Euler's relation

$$U = TS + pV + \sum_k \mu_k m_k. \tag{7}$$

Differentiating it and in view once again of eq. (5), it is immediate to obtain the Gibbs-Duhem's equation

$$S\,\mathrm{d}T - V\,\mathrm{d}P + \sum_k m_k \mathrm{d}\mu_k = 0 \tag{8}$$

that counts the degrees of freedom of an arbitrary thermodynamic system.

As already noted, Gibbs' equation leads to a functional dependence of U on the extensive quantities S, V, and $\{m_k\}$. In many situations it may be more convenient to describe thermodynamic systems by using their conjugated intensive variables T, $-P$, and μ_k. To this aim, by applying partial Legendre transformations [1] to U, three so-called auxiliary thermodynamic potentials are defined. Specifically:

1) for the conjugated variables S and T, being $\mathrm{d}(ST) = S\,\mathrm{d}T + T\,\mathrm{d}S$ and replacing $T\,\mathrm{d}S$ into eq. (5), one obtains

$$\mathrm{d}(U - TS) = -S\,\mathrm{d}T - P\,\mathrm{d}V + \sum_k \mu_k \mathrm{d}m_k \tag{9}$$

that defines the Helmholtz free energy $F := U - TS$;

2) for the conjugated variables V and $-P$, being $\mathrm{d}(pV) = P\,\mathrm{d}V + V\,\mathrm{d}P$ and replacing $P\,\mathrm{d}V$ into eq. (5), one obtains

$$\mathrm{d}(U + pV) = T\,\mathrm{d}S + V\,\mathrm{d}P + \sum_k \mu_k \mathrm{d}m_k \tag{10}$$

that defines the enthalpy $H := U + pV$;

3) finally, applying the Legendre transformation both to V and $-P$ and to S and T, eq. (5) leads to

$$\mathrm{d}(U - TS + pV) = -S\,\mathrm{d}T + V\,\mathrm{d}P + \sum_k \mu_k \mathrm{d}m_k \tag{11}$$

that defines the Gibbs free energy $G := U + pV - TS$.

It may be worth to note that the application of the full Legendre transformation leads to the Gibbs-Duhem's relation. Therefore, H, F, and G are the only three new thermodynamic potentials that may be obtained.

2˙2. *Extremum principles.* – It has been already shown that, in an isolated system, entropy tends to a maximum: $\mathrm{d}S \geq 0$ for constant U and V, where the constraints on U and V are implicit in the isolation of the system. However, since U depends on S and V, also U fulfills an extremum principle as a consequence of the second law: $\mathrm{d}U \leq 0$ for constant S and V. This is proved considering that, were U not minimal at equilibrium, some energy could be withdrawn from the system as work without changing S, and then converted into heat and returned to the system. This would leave U unchanged but would increase S, therefore violating the second law.

Combining the extremum principles for U and S with the definition of enthalpy and of the two free energies, it is easy to show [2] that

$$\mathrm{d}H \leq 0 \quad \text{for constant } S, P, \tag{12a}$$

$$\mathrm{d}F \leq 0 \quad \text{for constant } T, V, \tag{12b}$$

$$\mathrm{d}G \leq 0 \quad \text{for constant } T, P. \tag{12c}$$

2˙3. *Stability.* – The second law implies that equilibrium in an isolated system is stable, *i.e.* that no perturbation may lead to permanent modifications of the thermodynamic state of the system. Therefore, fluctuations may only cause temporary departures from the equilibrium state, which is then unavoidably recovered. This sets constraints on the sign of phenomenological quantities such as the isochoric heat capacity $C_V := \mathrm{đ}Q_{\mathrm{rev}}/\mathrm{d}T$ and the isothermal compressibility $\beta_T := -V^{-1}(\partial V/\partial P)$, which have to be both positive [3]. Furthermore, being $\mathrm{d}^2U(S,V) \geq 0$, internal energy is a jointly convex function of S and V, namely

$$\frac{\partial^2 U}{\partial S^2} \geq 0, \qquad \frac{\partial^2 U}{\partial V^2} \geq 0, \qquad \frac{\partial^2 U}{\partial S^2}\frac{\partial^2 U}{\partial V^2} - \left(\frac{\partial^2 U}{\partial S \partial V}\right)^2 \geq 0. \tag{13}$$

2˙4. *Closed and open systems.* – The second law of thermodynamics provides a simple criterion of equilibrium in isolated systems. Such a criterion has been extended to closed systems exchanging energy with the ambient by considering that when a closed systems reaches equilibrium its energy exchange with the ambient vanishes, since conditions of thermal and mechanical equilibrium with the ambient are attained. This is properly described by the fact that pertinent intensive quantities (T and P) take the same value within the system and at its boundaries.

For open systems, exchanging both matter and energy with the ambient, a similar approach applies. At equilibrium, both energy and matter exchanges with the ambient vanish, and chemical equilibrium with the ambient is set (in addition to the thermal and mechanical ones) when chemical potentials of all components are the same within the system and at its boundaries.

The analysis of open systems leads to the most general writings of the laws of thermodynamics. They may be conveniently stated by introducing specific potentials and quantities (per unit mass) u, q, and s in place of U, Q, and S. The first law reads [4]

$$\frac{\mathrm{d}u}{\mathrm{d}t} = \frac{\mathrm{đ}q}{\mathrm{d}t} - P\frac{\mathrm{d}\nu}{\mathrm{d}t} - \nu\mathsf{\Pi} : \mathrm{Grad}\,\mathbf{v} + \nu\sum_k \mathbf{J}_k \cdot \mathbf{F}_k, \tag{14}$$

where ν is the specific volume and $\mathbf{v}$ is the barycentric velocity per unit mass(2). It displays how the work changes with time due to two contributions: a volume-work term $-P\,\mathrm{d}\nu/\mathrm{d}t - \nu\mathsf{\Pi} : \mathrm{Grad}\,\mathbf{v}$ (where the pressure P is split into a hydrostatic (scalar) part P and a tensorial part $\mathsf{\Pi}$ as $\mathsf{P} = P\mathsf{U} + \mathsf{\Pi}$, with U the unity tensor); and a kinetic contribution $\nu\sum_k \mathbf{J}_k \cdot \mathbf{F}_k$ due to the fluxes of the k-th component $\mathbf{J}_k$ under the action of the pertinent force (per unit mass) $\mathbf{F}_k$ applied to it. For a motionless system eq. (14) simplifies to

$$\frac{\mathrm{d}u}{\mathrm{d}t} = \frac{\mathrm{đ}q}{\mathrm{d}t} - P\frac{\mathrm{d}\nu}{\mathrm{d}t} + \nu\sum_k \mathbf{J}_k \cdot \mathbf{F}_k \tag{15}$$

---

(2) The scalar product of two tensors S and T is defined as $\mathsf{S} : \mathsf{T} = \sum_{ik} S_{ik}T_{ki}$ while the gradient of a vector is the tensor $\mathsf{V} = \mathrm{Grad}\,\mathbf{v} = \frac{\partial v_k}{\partial x_i}$.

further reducing to the more familiar form $\mathrm{d}u = \text{đ}q - P\,\mathrm{d}\nu$ for a closed system. The second law takes instead the form [4]:

$$\frac{\partial(\rho s)}{\partial t} = -\boldsymbol{\nabla}\cdot\mathbf{J}_{\mathrm{s,tot}} + \sigma_{\mathrm{s}}, \quad \sigma_{\mathrm{s}} \geq 0 \tag{16}$$

where $\rho = \nu^{-1}$ is the density per unit mass. In the previous equation the total entropy flux per unit area $\mathbf{J}_{\mathrm{s,tot}}$ and the entropy production σ_{s} account for the two components of the entropy production, namely

$$\frac{\mathrm{d_e}S}{\mathrm{d}t} = -\int_{\partial V}\mathbf{J}_{\mathrm{s,tot}}\cdot\hat{\mathbf{n}}\,\mathrm{d}\Omega, \tag{17a}$$

$$\frac{\mathrm{d_i}S}{\mathrm{d}t} = \int_{V}\sigma_{\mathrm{s}}\mathrm{d}V, \tag{17b}$$

where $\hat{\mathbf{n}}$ is the versor normal to the infinitesimal surface element of area $\mathrm{d}\Omega$.

Making use of the fact that for any analytical field function $f(\mathbf{r},t)$ the identity $\partial(\rho f)/\partial t = \rho\,\mathrm{d}f/\mathrm{d}t + \boldsymbol{\nabla}\cdot(f\rho\mathbf{v})$ holds, eq. (16) may be recast in the form of a balance equation:

$$\rho\frac{\mathrm{d}s}{\mathrm{d}t} = -\boldsymbol{\nabla}\cdot\mathbf{J}_{\mathrm{s}} + \sigma_{\mathrm{s}}, \quad \sigma_{\mathrm{s}} \geq 0, \tag{18}$$

where $\mathbf{J}_{\mathrm{s}} = \mathbf{J}_{\mathrm{s,tot}} - \rho s\mathbf{v}$ is the non-convective part of the entropy flux.

Entropy production may be further elucidated by feeding eq. (18) into Gibbs' equation (5). Using specific potentials, Gibbs' equation reads

$$\mathrm{d}s = \frac{1}{T}\mathrm{d}u + \frac{P}{T}\mathrm{d}\nu - \sum_k \frac{\mu_k}{T}\mathrm{d}c_k, \tag{19}$$

where ρ_k is the specific density per unit mass of the k-th component and $c_k \equiv \rho_k/\rho = m_k/m$. Thus, in view of eq. (15), $\mathrm{d}s/\mathrm{d}t$ simplifies as

$$\frac{\mathrm{d}s}{\mathrm{d}t} = \frac{1}{T}\frac{\text{đ}q}{\mathrm{d}t} - \frac{\rho^{-1}}{T}\Pi : \mathrm{Grad}\,\mathbf{v} + \frac{\rho^{-1}}{T}\sum_k \mathbf{J}_k\cdot\mathbf{F}_k - \frac{1}{T}\sum_k \mu_k\frac{\mathrm{d}c_k}{\mathrm{d}t}\,. \tag{20}$$

Further considering r chemical reactions to occur, the density ρ_k of the k-th chemical evolves with time as

$$\frac{\partial\rho_k}{\partial t} = -\boldsymbol{\nabla}\cdot(\rho_k\mathbf{v}_k) + \sum_{j=1}^{r}\nu_{kj}J_j, \tag{21}$$

where $\mathbf{v}_k$ is the velocity of the k-th chemical and ν_{kj} is its stoichiometric coefficient for the j-th reaction having reaction rate J_j. Since $\mathrm{d}\rho/\mathrm{d}t = -\rho\boldsymbol{\nabla}\cdot\mathbf{v}$, one obtains

$$\rho\frac{\mathrm{d}c_k}{\mathrm{d}t} = -\boldsymbol{\nabla}\cdot\mathbf{J}_k + \sum_{j=1}^{r}\nu_{kj}J_j, \tag{22}$$

where $\mathbf{J}_k \equiv \rho_k(\mathbf{v}_k - \mathbf{v})$.

Furthermore, in view of eqs. (14) and (21) and setting $\rho\,\mathrm{d}q/\mathrm{d}t = -\boldsymbol{\nabla}\cdot\mathbf{J}_q$, one obtains

$$\begin{aligned}(23)\qquad \rho T\frac{\mathrm{d}s}{\mathrm{d}t} &= -\boldsymbol{\nabla}\cdot\mathbf{J}_q - \Pi : \mathrm{Grad}\,\mathbf{v} + \sum_k \mathbf{J}_k\cdot\mathbf{F}_k - \rho\sum_k \mu_k\frac{\mathrm{d}c_k}{\mathrm{d}t}\\ &= -\boldsymbol{\nabla}\cdot\mathbf{J}_q - \Pi : \mathrm{Grad}\,\mathbf{v} + \sum_k \mathbf{J}_k\cdot\mathbf{F}_k - \sum_k \mu_k\left(-\boldsymbol{\nabla}\cdot\mathbf{J}_k + \sum_j \nu_{kj}J_j\right).\end{aligned}$$

Defining the chemical affinity of the j-th reaction as $\mathcal{A}_j := \sum_k \mu_k\nu_{kj}$ and being $\mu_k\boldsymbol{\nabla}\cdot\mathbf{J}_k = \boldsymbol{\nabla}\cdot(\mu_k\mathbf{J}_k) - \mathbf{J}_k\cdot\boldsymbol{\nabla}\mu_k$ while $T^{-1}\boldsymbol{\nabla}\mu_k = \boldsymbol{\nabla}(\mu_k/T) - (\mu_k/T^2)\boldsymbol{\nabla}T$, the previous equation reads

$$\begin{aligned}(24)\qquad \rho\frac{\mathrm{d}s}{\mathrm{d}t} = -\boldsymbol{\nabla}\cdot\left(\frac{\mathbf{J}_q - \sum_k\mu_k\mathbf{J}_k}{T}\right) - \frac{1}{T^2}\boldsymbol{\nabla}T\cdot\left(\mathbf{J}_q - \sum_k\mu_k\mathbf{J}_k\right) - \frac{1}{T}\Pi : \mathrm{Grad}\,\mathbf{v}\\ +\frac{1}{T}\sum_k \mathbf{J}_k\cdot\mathbf{F}_k - \frac{1}{T}\sum_j\mathcal{A}_jJ_j - \sum_k\mathbf{J}_k\cdot\left(\frac{\mu_k}{T^2}\boldsymbol{\nabla}T + \boldsymbol{\nabla}\frac{\mu_k}{T}\right).\end{aligned}$$

Comparing it to eq. (16), the entropy flux is found to be

$$(25)\qquad \mathbf{J}_\mathrm{s} = \frac{\mathbf{J}_q - \sum_k\mu_k\mathbf{J}_k}{T}$$

while the entropy production reads

$$\begin{aligned}(26)\qquad \sigma_\mathrm{s} = -\frac{1}{T^2}\mathbf{J}_q\cdot\boldsymbol{\nabla}T - \frac{1}{T}\Pi : \mathrm{Grad}\,\mathbf{v} - \frac{1}{T}\sum_j\mathcal{A}_jJ_j\\ +\sum_k\mathbf{J}_k\cdot\left(\frac{\boldsymbol{\nabla}T}{T^2}\mu_k + \frac{1}{T}\mathbf{F}_k - \frac{\mu_k}{T^2}\boldsymbol{\nabla}T - \boldsymbol{\nabla}\frac{\mu_k}{T}\right)\end{aligned}$$

that simplifies to

$$(27)\qquad \sigma_\mathrm{s} = -\frac{1}{T^2}\mathbf{J}_q\cdot\boldsymbol{\nabla}T - \frac{1}{T}\Pi : \mathrm{Grad}\,\mathbf{v} - \frac{1}{T}\sum_j\mathcal{A}_jJ_j + \frac{1}{T}\sum_k\mathbf{J}_k\cdot\left(\mathbf{F}_k - T\boldsymbol{\nabla}\frac{\mu_k}{T}\right).$$

3. – Classical irreversible thermodynamics

Manifestly enough, Gibbsian thermodynamics is remarkably focused on systems, and their interaction with the ambient is fully accounted for by intensive quantities such as pressure P and temperature θ [5]. This makes its extension to out-of-equilibrium contexts twice complicated, as it must encompass *open* systems and transformations joining non-equilibrium states. This difficulty was evident since Thomson and Clausius, who first attempted to reuse equilibrium thermodynamics to develop pseudo-equilibrium theories accounting for non-equilibrium processes. Two formidable issues are to be dealt with, namely

1) computing entropy variations in irreversible processes joining states that cannot be connected by quasi-static transformation because initial and final states are themselves non-equilibrium states(3);
2) defining a temperature (or an equivalent index of state) in a context where the zeroth law of thermodynamics does not apply.

Classical irreversible thermodynamics (CIT) was the first systematic attempt to extend thermodynamics to out-of-equilibrium states and to transformations between them. It mostly aimed at supplying a proper thermodynamic support to phenomenological transport laws, being advanced in the first half of the 19th century by Fourier, Fick, Ohm, and Stokes, along with the first evidence of coupled transport phenomena (Soret, Dufour, Seebeck, and Peltier effects).

In all transport processes, incoming and outgoing thermodynamic fluxes of mass, momentum, or energy are non-zero. However, when they equal each other the thermodynamic state of the system does not change with time, leading to a non-equilibrium steady state. This suggested to advance a construing heuristic hypothesis that extends to non-equilibrium steady states the same thermodynamic relations that are valid in equilibrium conditions —the so-called principle of local equilibrium or, better named, the local equilibrium hypothesis (LEH).

3˙1. *The local equilibrium hypothesis.* – The local equilibrium hypothesis states that in a system out of equilibrium thermodynamic quantities *locally* and *instantaneously* hinge on each other through the same relations holding in a uniform system in equilibrium. This implies that 1) thermodynamic field potentials per unit mass $e(\mathbf{r},t)$, $u(\mathbf{r},t)$ and $s(\mathbf{r},t)$ may be defined; and 2) that first and second laws remain *locally* and *instantaneously* valid. It also implies that a local and instantaneous absolute temperature exists, defined as

$$T(\mathbf{r},t)^{-1} = \left(\frac{\partial s(\mathbf{r},t)}{\partial u(\mathbf{r},t)}\right)_v . \tag{28}$$

It may be worth noting immediately that the LEH *does not* state that the system is locally or instantaneously at equilibrium. Instead, it more weakly assumes that 1) equilibrium-like thermodynamic (field) potentials may be defined; 2) energy conservation principle (first law) holds true locally and instantaneously; and 3) spontaneous evolution of systems is ruled by a computable quantity having the same definition as Clausius' entropy.

---

(3) They will be referred to as *essential* non-equilibrium transformations, to mark the difference with respect to paths joining two equilibrium states through non–quasi-static (*i.e.* irreversible) processes.

Within the limits of validity of the LEH, Gibbs' equation (eq. (5)) is rewritten as

$$\mathrm{d}s(\mathbf{r},t)=\frac{1}{T(\mathbf{r},t)}\mathrm{d}u(\mathbf{r},t)+\frac{P(\mathbf{r},t)}{T(\mathbf{r},t)}\mathrm{d}v(\mathbf{r},t)-\sum_k\frac{\mu_k(\mathbf{r},t)}{T(\mathbf{r},t)}\mathrm{d}c_k(\mathbf{r},t), \tag{29}$$

where $c_k(\mathbf{r},t):=m_k(\mathbf{r},t)/\sum_k m_k(\mathbf{r},t)$. It shows how $\mathrm{d}s(\mathbf{r},t)$ is a quadratic form of the field thermodynamic potentials ($u(\mathbf{r},t)$, $v(\mathbf{r},t)$, and $c_k(\mathbf{r},t)$) multiplied by the conjugated intensive field state variable ($1/T(\mathbf{r},t)$, $P(\mathbf{r},t)/T(\mathbf{r},t)$, and $\mu_k(\mathbf{r},t)/T$, respectively).

It is a remarkable point of strength of the LEH (and of CIT thereof) that of solving the problem of defining (and making computable) the entropy variation along *essential* irreversible transformations —one of the main prices to be paid when relaxing the LEH. Furthermore, as long as entropy definition is inherited from GET, also the second law of thermodynamics retains the same form used for open systems at equilibrium, save that specific potentials (per unit mass) are replaced by field potentials. Thus,

$$\rho(\mathbf{r},t)\frac{\mathrm{d}s(\mathbf{r},t)}{\mathrm{d}t}=-\boldsymbol{\nabla}\cdot\mathbf{J}_\mathrm{s}(\mathbf{r},t)+\sigma_\mathrm{s}(\mathbf{r},t),\quad \sigma_\mathrm{s}(\mathbf{r},t)\geq 0. \tag{30}$$

3·2. *Linear flux-affinity relations and the Onsager-Casimir reciprocal relations.* – Inspection of eq. (27) shows that entropy production may be seen as the sum of products of thermodynamic fluxes of energy ($\mathbf{J}_q$), momentum ($\mathrm{Grad}\,\mathbf{v}$), mass ($\mathbf{J}_k$), and reaction rates ($J_j$) multiplied by the conjugated thermodynamic affinities ($\boldsymbol{\nabla}(1/T)$, $-\Pi/T$, $\mathbf{F}_k/T-\boldsymbol{\nabla}(\mu_k/T)$ (see footnote(4))), and $-\mathcal{A}_j/T$, respectively) causing them.

Manifestly, each flux is silenced by shutting down affinities. Therefore, it is sensible to expand each flux $J_\alpha=J_\alpha(X_1,X_2,\ldots)$ around $X_\beta=0\ \forall\beta$:

$$J_\alpha=\sum_\beta L_{\alpha\beta}X_\beta,\quad L_{\alpha\beta}=\left.\frac{\partial J_\alpha}{\partial X_\beta}\right|_{\{X_\beta=0\}_\beta}. \tag{31}$$

Fourier's, Ohm's, and Fick's laws suggest that truncation of the expansion to the linear term is a fair approximation, covering a wide set of experimental contexts —albeit not all, since deviations from linearity are known, for very large values of X_α (*e.g.*, electric fields or temperature gradients) [6].

Under stipulation of linear flux-affinity, entropy production reads

$$\sigma_\mathrm{s}=\sum_{\alpha,\beta}L_{\alpha\beta}X_\alpha X_\beta\geq 0 \tag{32}$$

---

(4) Note that $\mathbf{F}_k/T$ accounts for mass drift, due to external forces, while $-\boldsymbol{\nabla}(\mu_k/T)$ describes mass diffusion due to gradients of chemical potentials.

that implies

$$L_{\alpha\alpha} \geq 0, \tag{33a}$$

$$L_{\alpha\alpha} L_{\beta\beta} \geq \frac{1}{4}(L_{\alpha\beta} + L_{\beta\alpha})^2. \tag{33b}$$

Further restrictions on the phenomenological coefficients $L_{\alpha\beta}$ are set forth by the Onsager-Casimir reciprocal relations [7-9]. Since from a strict macroscopic viewpoint the reciprocal relations are to be considered as an axiom, they will be introduced without any proof. Readers may find a modern proof based on statistical mechanics in ref. [2].

Onsager-Casimir reciprocal relations state that

$$L_{\alpha\beta} = \epsilon_\alpha \epsilon_\beta L_{\beta\alpha}, \tag{34}$$

where $\epsilon_i = \pm 1$ is the time-reversal parity of the relevant state variable.

3˙3. *System dynamics.* – Since CIT is a local and instantaneous instantiation of GET, it enables the computation of a unique evolution equation for any thermodynamic system, provided that a model is additionally supplied for the dependency of thermodynamic fluxes on the variation of intensive thermodynamic variables. The general path followed to this aim is outlined, and its implementation to the analysis of heat conduction is shown. Additional details may be found in ref. [2].

3˙3.1. Description of the thermodynamic state. As in GET, also in irreversible thermodynamics one has to ensure that the description of the initial and final state of the system is complete. Completeness implies that the thermodynamic state as described by the collection of state variables is unique. In addition, state variables must also be admissible, namely their dynamics (if any) must occur on a time scale larger than that of any variable ruling the system evolution at the microscopic level. This is required based on the LEH(5). Typical examples of suitable state variables include thermodynamic potential, pressure, volume, barycentric velocity, and compositional indices. The complete set of state variables will be referred to as the ensemble $a(\mathbf{r},t) \equiv \{a_1(\mathbf{r},t), a_2(\mathbf{r},t), \ldots, a_N(\mathbf{r},t)\}$.

For the exemplar problem of the heat conduction in a non-deformable, elemental, isotropic body, the single thermodynamic field potential u provides a complete description of the system state.

3˙3.2. Evolution equations. For each and any $a_i(\mathbf{r},t)$, a balance equation is required, linking the time evolution of a_i to the flux of a_i across system boundaries $\mathbf{J}_{a_i}$and its production σ_{a_i} within the system, if a_i is not conserved:

$$\rho \frac{\mathrm{d}a_i(\mathbf{r},t)}{\mathrm{d}t} = -\boldsymbol{\nabla} \cdot \mathbf{J}_{a_i} + \sigma_{a_i}. \tag{35}$$

---

(5) And in view of the applicability of the Onsager-Casimir relations —cf. ref. [2].

Convenient reference may be made to standard balance equations [4]:

$$\rho\frac{\mathrm{d}\nu}{\mathrm{d}t} = \nabla\cdot\mathbf{v} \qquad \text{(mass)} \tag{36a}$$

$$\rho\frac{\mathrm{d}c_k}{\mathrm{d}t} = -\nabla\cdot\mathbf{J}_k + \sum_j \nu_{kj}J_j \qquad \text{(concentration)} \tag{36b}$$

$$\rho\frac{\mathrm{d}\mathbf{v}}{\mathrm{d}t} = -\operatorname{Div}\mathsf{P} + \sum_k \rho_k\mathbf{F}_k \qquad \text{(momentum)} \tag{36c}$$

$$\rho\frac{\mathrm{d}u}{\mathrm{d}t} = -\nabla\cdot\mathbf{J}_q - P\nabla\cdot\mathbf{v} - \mathsf{\Pi} : \operatorname{Grad}\mathbf{v} + \sum_k \mathbf{J}_k\cdot\mathbf{F}_k \qquad \text{(internal energy)} \tag{36d}$$

where $(\operatorname{Div}\mathsf{P})_i \equiv \sum_j \frac{\partial P_{ji}}{\partial x_j}$. Since system evolution is ruled by the entropy production ($\sigma_\mathrm{s} > 0$), one may use balance equations along with the bilinear (flux-affinity) form of the entropy production to obtain an explicit expression for σ_s, which is always of the general form $\sum_i J_{a_i}X_{a_i}$, where the product is meant to be a product of two scalars, the scalar product of two vectors, or the double scalar product of two tensors.

In the case of heat conduction, assuming no heat source within the body and in view of eq. (36d), one immediately writes

$$\rho\frac{\mathrm{d}u}{\mathrm{d}t} = -\nabla\cdot\mathbf{J}_q. \tag{37}$$

Thus, eq. (27) for a rigid, elemental, non-reactive system simply provides

$$\sigma_\mathrm{s} = -\frac{1}{T^2}\mathbf{J}_q\cdot\nabla T \tag{38}$$

that immediately points out to the relevant flux ($\mathbf{J}_q$) and affinity ($\nabla(1/T)$).

3$\dot{}$3.3. Phenomenological relations and Onsager-Casimir theorem. The final step is that of applying the multi-linear relations connecting fluxes to affinities, bearing in mind 1) the constraints on tensorial ranks imposed by the Curie's principle [10]; 2) the restriction arising from the Onsager-Casimir theorem; and 3) the restraints originating from the second law (eq. (33)). They lead to the final form of the needed transport equation, which may be directly compared to the experiment.

For heat transport, linear relation is of the form $\mathbf{J}_q = L_{qq}(T)\nabla(1/T)$, where we stressed the fact that the phenomenological coefficient depends on the temperature. Thus, a heat transport coefficient may be defined, such that

$$\mathbf{J}_q = -\kappa(T)\nabla T, \quad \kappa \equiv L_{qq}(T)/T^2 \tag{39}$$

sometimes referred to as the first Fourier's equation. Equation (33) sets $\kappa(T) \geq 0$. The heat equation is obtained by recalling that for a rigid body (constant volume) $c_V =$

$\partial u/\partial T$. Thus,

$$\rho c_V \frac{\mathrm{d}T}{\mathrm{d}t} = -\boldsymbol{\nabla}\cdot\mathbf{J}_q \tag{40}$$

Using again eq. (39), one finally obtains

$$\frac{\mathrm{d}T}{\mathrm{d}t} = \frac{\boldsymbol{\nabla}\cdot(\kappa(T)\boldsymbol{\nabla}T)}{\rho c_V} = \boldsymbol{\nabla}\cdot(\lambda(T)\boldsymbol{\nabla}T), \quad \lambda(T)\equiv\kappa(T)/(\rho c_V). \tag{41}$$

In summary, the procedure outlined in this subsection provides a general way to formally obtain through a first-principle analysis all the linear equations ruling mass, charge, energy, and momentum transport phenomena in continuum media, setting restraints to transport coefficient values and relating them to thermodynamics. In the next section, use will be made of such a procedure to gain insights into thermoelectric processes, an archetypal instance of coupled transport phenomena jointly involving two fluxes and affinities.

4. – Application of CIT to thermoelectricity

4·1. *System dynamics.* – Let us consider an open system, and let $\mathbf{J}_q$ be the heat flux (W/m^2) flowing through the system boundaries, while let $\mathbf{J}_\mathrm{N}$ be the corresponding particle flux (m^{-2}s^{-1}). Note that the two fluxes are independent of each other. Assuming that only one type of charge carrier (electrons, holes, ions) may flow through the system, the overall energy flux reads

$$\mathbf{J}_\mathrm{E} = \mathbf{J}_q + \widetilde{\mu}_\mathrm{e}\mathbf{J}_\mathrm{N} \tag{42}$$

where $\widetilde{\mu}_\mathrm{e}$ is the electrochemical potential. As expected, the energy flux encompasses both the energy transported by particles and the heat exchange with the ambient.

In the presence of a temperature gradient and/or of an electrochemical potential gradient, two thermodynamic affinities are therefore active, namely

$$\mathbf{X}_\mathrm{N} = \boldsymbol{\nabla}\left(-\frac{\widetilde{\mu}_\mathrm{e}}{T}\right), \qquad \mathbf{X}_\mathrm{E} = \boldsymbol{\nabla}\left(\frac{1}{T}\right) \tag{43}$$

Thus, in the linear limit it follows that

$$\begin{bmatrix}\mathbf{J}_\mathrm{N}\\ \mathbf{J}_\mathrm{E}\end{bmatrix} = \mathsf{L}' \begin{bmatrix}\boldsymbol{\nabla}\left(-\dfrac{\widetilde{\mu}_\mathrm{e}}{T}\right)\\ \boldsymbol{\nabla}\left(+\dfrac{1}{T}\right)\end{bmatrix}, \tag{44}$$

that may be rewritten in view of eq. (42) as

$$\begin{bmatrix} \mathbf{J}_{\mathrm{N}} \\ \mathbf{J}_q \end{bmatrix} = \mathsf{L} \begin{bmatrix} -\dfrac{1}{T}\boldsymbol{\nabla}\widetilde{\mu}_{\mathrm{e}} \\ \boldsymbol{\nabla}\left(\dfrac{1}{T}\right) \end{bmatrix} \tag{45}$$

Both L' and L are 2×2 matrices of phenomenological coefficients, linearly correlating affinities and fluxes. Limiting to isotropic systems, each element of L' and L is a scalar. Extension to anisotropic systems is formally simple, leading to tensorial matrix elements [11].

4˙2. *Phenomenological coefficients.* – Insights in the physical meaning of L elements may be achieved by decoupling affinities and fluxes.

In an isothermal system ($\boldsymbol{\nabla}(1/T) \equiv \mathbf{0}$) eq. (45) reads

$$\mathbf{J} := e\mathbf{J}_{\mathrm{N}} = -\frac{e\mathsf{L}_{11}}{T}\boldsymbol{\nabla}\widetilde{\mu}_{\mathrm{e}}, \tag{46}$$

where $\mathbf{J}$ is the charge current density. Since $\widetilde{\mu}_{\mathrm{e}} = \mu_{\mathrm{e}} + e\mathscr{V}$ (where $\mathscr{V}$ is the electric potential), then $-(\boldsymbol{\nabla}\widetilde{\mu}_{\mathrm{e}})/e = -\boldsymbol{\nabla}\mathscr{V} = \mathscr{E}$, where $\mathscr{E}$ is the electric field. Thus, one easily obtains that

$$\mathbf{J} = \sigma_T \mathscr{E} \tag{47}$$

with the isothermal electric conductivity $\sigma_T = e^2\mathsf{L}_{11}/T$. Therefore,

$$\mathsf{L}_{11} = \frac{\sigma_T T}{e^2}\,. \tag{48}$$

Equation (45) may be alternately solved when no electric current flows, namely $\mathbf{J} = \mathbf{J}_{\mathrm{N}} = \mathbf{0}$. In such an (electric) open-circuit (oc) scenario, it is immediate to write

$$\mathbf{J}_{q\ \mathrm{oc}} = \frac{1}{T^2}\left(\frac{\mathsf{L}_{21}\mathsf{L}_{12} - \mathsf{L}_{11}\mathsf{L}_{22}}{\mathsf{L}_{11}}\right)\boldsymbol{\nabla}T \tag{49}$$

so that, in view of Fourier law, the open-circuit thermal conductivity κ_{oc} reads

$$\kappa_{\mathrm{oc}} = \frac{1}{T^2}\left(\frac{\mathsf{L}_{21}\mathsf{L}_{12} - \mathsf{L}_{11}\mathsf{L}_{22}}{\mathsf{L}_{11}}\right). \tag{50}$$

Should instead the electric circuit be closed (cc), a heat current sets up under the alternate constraint $\boldsymbol{\nabla}\widetilde{\mu} = \mathbf{0}$ (namely, no electric field may be sustained through the system). The heat flux reads then $\mathbf{J}_{q\,\mathrm{cc}} = \frac{\mathsf{L}_{22}}{T^2}\boldsymbol{\nabla}T$ that leads to the closed-circuit thermal conductivity κ_{cc}:

$$\kappa_{\mathrm{cc}} = \frac{\mathsf{L}_{22}}{T^2}\,. \tag{51}$$

Moving to coupled fluxes and forces, let us consider once again an open-circuit configuration (namely $\mathbf{J} \equiv \mathbf{0}$). Thus, eq. (45) reads

$$-\mathsf{L}_{11}\frac{\boldsymbol{\nabla}\widetilde{\mu}_{\mathrm{e}}}{T} + \mathsf{L}_{12}\boldsymbol{\nabla}\left(\frac{1}{T}\right) = \mathbf{0}. \tag{52}$$

Thus one may define the Seebeck coefficient α as

$$-\frac{1}{e}\boldsymbol{\nabla}\widetilde{\mu}_{\mathrm{e}} := \alpha\boldsymbol{\nabla}T \tag{53}$$

or, equivalently, as $\alpha\boldsymbol{\nabla}T := \mathscr{E}_{\mathrm{oc}}$. Thus $\alpha = \frac{1}{eT}\frac{\mathsf{L}_{12}}{\mathsf{L}_{11}}$ so that

$$\mathsf{L}_{12} = \frac{\alpha\sigma_T T^2}{e}\,. \tag{54}$$

Instead, closing the circuit but setting isothermal conditions one may write $\mathbf{J} = \frac{e\mathsf{L}_{11}}{T}\boldsymbol{\nabla}\widetilde{\mu}_{\mathrm{e}}$ and $\mathbf{J}_q = -\frac{\mathsf{L}_{21}}{T}\boldsymbol{\nabla}\widetilde{\mu}_{\mathrm{e}}$ so that $\mathbf{J}_q = \frac{\mathsf{L}_{12}}{e\mathsf{L}_{11}}\mathbf{J}$. This returns the Peltier coefficient Π, which is defined as $\mathbf{J}_q := \Pi\mathbf{J}$(6):

$$\Pi = \frac{\mathsf{L}_{12}}{e\mathsf{L}_{11}}\,. \tag{55}$$

Note that, as a direct consequence of Onsager's relations and in view of eq. (53), $\Pi = \alpha T$. Therefore, in summary

$$\mathbf{J} = e\mathbf{J}_{\mathrm{N}} = \sigma_T\mathscr{E} - \alpha\sigma_T\boldsymbol{\nabla}T, \tag{56a}$$

$$\mathbf{J}_q = \alpha\sigma_T T\mathscr{E} - \kappa_{\mathrm{cc}}\boldsymbol{\nabla}T. \tag{56b}$$

The Seebeck coefficient admits a remarkably strong physical interpretation. Using eq. (45) one may write the *total* entropy flux (eq. (16)) as

$$\mathbf{J}_{\mathrm{s,tot}} = \frac{\mathsf{L}_{21}}{eT\mathsf{L}_{11}}\mathbf{J} + \frac{\mathsf{L}_{22}}{T}\boldsymbol{\nabla}\left(\frac{1}{T}\right). \tag{57}$$

The equation shows once again how the entropy flux is made of two terms: while the second term is the standard thermal component of $\mathbf{J}_{\mathrm{s}}$, the first one accounts instead for the entropy flux associated to the particle flux. More explicitly, the particle-borne (convective) entropy flux $\mathsf{L}_{21}/(T\mathsf{L}_{11})\mathbf{J}_{\mathrm{N}}$ leads to compute an entropy contribution per particle of $\mathsf{L}_{21}/(T\mathsf{L}_{11}) = \alpha$. Thus,

$$\mathbf{J}_{\mathrm{s}} = \alpha\mathbf{J} - \frac{\kappa_{\mathrm{cc}}\boldsymbol{\nabla}T}{T}\,. \tag{58}$$

---

(6) Note that for anisotropic materials both α and Π are tensors.

Therefore, the Seebeck coefficient may be interpreted as the (average) contribution of carriers to the entropy flux. *i.e.* as the convective part of the entropy flux.

As an additional result of our analysis, closed- and open-circuit thermal conductivities (eqs. (50) and (51)) are correlated to each other through α and σ_T as

$$\kappa_{\mathrm{cc}} - \kappa_{\mathrm{oc}} = T\alpha^2\sigma_T. \tag{59}$$

A rigorous application of linear thermodynamics deals with phenomenological coefficients as constant quantities. Nonetheless, both the electrical conductivity, the Seebeck coefficient, and the Peltier coefficient depend on the temperature. Specifically, for the Seebeck coefficient one defines for its temperature coefficient a quantity named Thomson coefficient τ [12]:

$$\tau := T\frac{\mathrm{d}\alpha}{\mathrm{d}T}\,. \tag{60}$$

Manifestly enough, the Thomson coefficient is also temperature dependent.

The Thomson coefficient may be alternately (and equivalently) introduced considering the heat exchanged when an electric current passes through a circuit composed of a single material that has a temperature difference along its length. In addition to the Joule heat, a Peltier heat is exchanged as a result of the non-zero Seebeck coefficient of the materials itself (Thomson effect).

5. – Thermoelectric efficiency in the constant-property limit

The first evaluation of efficiency of a thermoelectric generator (TEG) under Dirichlet boundary conditions (fixed heat sink temperatures) is due to Altenkirch [13] although it was restated and rewritten in a more rigorous and general way by Ioffe in his famous book *Semiconductor Thermoelements and Thermoelectric Cooling* [14].

Under Dirichlet boundary conditions, in this Section it will be assumed that all transport coefficients are constant, namely that materials are homogeneous phases and that thermal and electric conductivities as well as the Seebeck coefficient are independent of the temperature. Manifestly enough, this makes all conclusions rigorously valid only when the temperature difference across the thermoelectric materials is vanishingly small. Therefore, appropriateness of the formula to predict the efficiency of real systems depends upon the temperature difference experienced by the active parts of the TEG. We will refer to this set of assumptions as constant-property limit (CPL).

5˙1. *Dirichlet boundary conditions.* – In general terms, a TEG is often (although not necessarily) made of pairs of p- and n-type semiconductors connected to form a series electric circuit while being set in a thermal parallel circuit with respect to the two heat sinks (fig. 1). It is commonplace to refer to this configuration as a Π-configuration. Since each element nominally senses the same temperature difference $\Delta T_{\mathrm{TEG}} \equiv T_{\mathrm{H}} - T_{\mathrm{C}}$, where T_{H} and T_{C} are the temperatures of the two heat sinks (with $T_{\mathrm{H}} \geq T_{\mathrm{C}}$), the thermovoltage

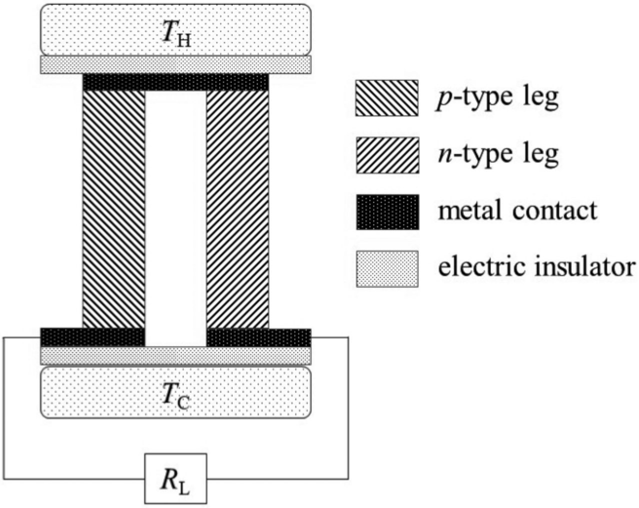

Fig. 1. – Standard Π-type layout of a thermoelectric generator, setting a series *p*-*n* electric circuit in a parallel connection with the two heat sinks.

developed by each element (often referred to as *leg*) sum to each other, leading to a total thermovoltage $\mathscr{V}_{\text{tot}} = N(|\alpha_n| + |\alpha_p|)\Delta T_{\text{TEG}}$ where N is the number of leg pairs.

The most widely used formulas to assess the thermoelectric efficiency of a TEG assume that the temperature of each sink equals the temperature of the relevant end of each leg. This implicitly stipulates that no thermal contact resistance occurs at the sink-TEG interface and that any temperature drop due to electrically insulating but thermally conductive layers interposed between the sinks and the legs may be neglected. It is rather obvious that such assumptions are a strong oversimplification of the actual thermal chain, and more realistic analyses are needed even when the Dirichlet CPL (DCPL) model is a legitimate approximation. The reader may refer to the technical literature for more realistic DCPL analyses [15].

Following Domenicali [16, 17], let us rearrange first eqs. (56a) and (56b). Replacing $\mathscr{E}$ from eq. (56a) into eq. (56b) we obtain

$$\mathbf{J}_q = \alpha T \mathbf{J} + (\alpha^2 \sigma_T T - \kappa_{\text{cc}})\boldsymbol{\nabla} T \tag{61}$$

that, in view of eq. (59), reads

$$\mathbf{J}_q = \alpha T \mathbf{J} - \kappa_{\text{oc}}\boldsymbol{\nabla} T. \tag{62}$$

Let us now consider (without loss of generality) a single leg of a thermoelectric phase. Using eqs. (16) and (62), the total energy flux $\mathbf{J}_{\text{E}}$ (eq. (42)) reads

$$\mathbf{J}_{\text{E}} = \mathbf{J}_q + \widetilde{\mu}_{\text{e}}\frac{\mathbf{J}}{e} = (\alpha T \mathbf{J} - \kappa_{\text{oc}}\boldsymbol{\nabla} T) + \widetilde{\mu}_{\text{e}}\frac{\mathbf{J}}{e}\,. \tag{63}$$

Taking the divergence, energy conservation imposes $\boldsymbol{\nabla}\cdot\mathbf{J}_{\mathrm{E}}=0$ so that

$$\mathbf{J}\cdot(\alpha\boldsymbol{\nabla}T+T\boldsymbol{\nabla}\alpha)-\boldsymbol{\nabla}(\kappa_{\mathrm{oc}}\boldsymbol{\nabla}T)+\frac{\mathbf{J}}{e}\boldsymbol{\nabla}\widetilde{\mu}_{\mathrm{e}}=0. \tag{64}$$

Thus, in view of eqs. (45), (48), and (54) one may write $\mathbf{J}_{\mathrm{N}}=-\frac{\sigma}{e^2}\boldsymbol{\nabla}\widetilde{\mu}_{\mathrm{e}}-\frac{\alpha\sigma_T}{e}\boldsymbol{\nabla}T$ that returns $\boldsymbol{\nabla}\widetilde{\mu}_{\mathrm{e}}=-\frac{e}{\sigma}\mathbf{J}-\alpha e\boldsymbol{\nabla}T$. Replacing it into eq. (64) and simplifying, one obtains

$$T\mathbf{J}\cdot\boldsymbol{\nabla}\alpha-\boldsymbol{\nabla}(\kappa_{\mathrm{oc}}\boldsymbol{\nabla}T)-\frac{\mathbf{J}\cdot\mathbf{J}}{\sigma_T}=0, \tag{65}$$

which is the stationary form of the Domenicali equation [16].

In the CPL $\boldsymbol{\nabla}\alpha=\boldsymbol{\nabla}\kappa_{\mathrm{oc}}=\mathbf{0}$ so that

$$\frac{\mathbf{J}\cdot\mathbf{J}}{\sigma_T}=-\kappa_{\mathrm{oc}}\nabla^2T. \tag{66}$$

In a one-dimensional conductor aligned along the x-axis it reduces to $T''(x)=-\frac{J^2}{\sigma_T\kappa_{\mathrm{oc}}}$.

Since all terms but T are independent of x, it is immediate to compute that

$$T(x)=-\frac{1}{2}\frac{J^2\ell^2}{\sigma_T\kappa_{\mathrm{oc}}}\left(\frac{x^2}{\ell^2}-\frac{x}{\ell}\right)-\Delta T_{\mathrm{TEG}}\frac{x}{\ell}+T_{\mathrm{H}}, \tag{67}$$

where ℓ is the length of the conductor and the hot and cold heat sinks are at $x=0$ and $x=\ell$, respectively.

The electric power flow J_w generated by the thermoelectric element computes to $J_w=-\int_0^\ell J\mathscr{E}(x)\mathrm{d}x$, where the electric field follows from eq. (56a):

$$\mathscr{E}(x)=\frac{J}{\sigma_T}+\alpha T'(x). \tag{68}$$

Thus, the electric power density reads $J_w=-\frac{J^2}{\sigma_T}\ell+J\alpha\Delta T_{\mathrm{TEG}}$. Correspondingly, eq. (62) provides the heat flux. In one dimension

$$J_q(x)=-\kappa_{\mathrm{oc}}T'(x)+\alpha JT(x) \tag{69}$$

The heat injected at the hot side is then

$$J_q(0)=\kappa_{\mathrm{oc}}\frac{\Delta T_{\mathrm{TEG}}}{\ell}-\frac{1}{2}\frac{J^2\ell}{\sigma_T}+\alpha JT_{\mathrm{H}}. \tag{70}$$

The efficiency may be then immediately written as a function of the charge current density:

$$\phi_{\mathrm{DCPL}}(J)=\frac{J_w}{J_q(J)|_{x=0}}=\frac{J\alpha\Delta T_{\mathrm{TEG}}-(J^2\ell/\sigma_T)}{(\kappa_{\mathrm{oc}}\Delta T_{\mathrm{TEG}}/\ell)-\frac{1}{2}(J^2\ell/\sigma_T)+\alpha JT_{\mathrm{H}}}\,. \tag{71}$$

It is interesting to analyze eq. (71). One recognizes that three terms show up in the expression of the adsorbed heat, namely the heat transmitted by thermal conduction ($\kappa_{\rm oc}\Delta T_{\rm TEG}/\ell$), the Peltier heat at the hot side ($\alpha J T_{\rm H}$) and half of the Joule heat generated by the circulating charge current ($J^2\ell/\sigma_T$). The electric power flux at the numerator shows instead that the non-zero circulating current leads to a reduction of the available output power density with respect to the thermoelectric power density $J(\alpha\Delta T_{\rm TEG})$ by the Joule effect $J^2\ell/\sigma_T$.

One may proceed to optimize either the efficiency $\phi_{\rm DCPL}(J)$ or the electric energy flux $J_W(J)$ with respect to J. In the latter case, setting $(\partial J_W(J)/\partial J)_\ell = 0$ (*i.e.* maximizing for fixed ℓ) the current density computes to

$$J^{\max W} = \frac{\alpha\sigma_T\Delta T_{\rm TEG}}{2\ell} \tag{72}$$

so that

$$J_W^{\max} = \frac{\alpha^2\sigma_T\Delta T_{\rm TEG}^2}{4\ell} \tag{73}$$

and

$$\eta_w^{\rm DCPL} \equiv \phi(J^{\max W}) = \frac{2z\Delta T_{\rm TEG}}{8 + z(4T_{\rm H} - \Delta T_{\rm TEG})} \tag{74}$$

(where $z := \sigma_T\alpha^2/\kappa_{\rm oc}$) that, with a little of algebra, returns

$$\eta_w^{\rm DCPL} = \frac{\eta_{\rm Carnot}}{2}\frac{1}{1 + \frac{2}{zT_{\rm H}} - \frac{\Delta T_{\rm TEG}}{4T_{\rm H}}} \tag{75}$$

Equation (72) let also compute the matching load resistance $R_{\rm L}$. Since $jA = \alpha\Delta T_{\rm TEG}/(R_{\rm s} + R_{\rm L})$ (where $R_{\rm s} = (\sigma_T\ell/A)^{-1}$ is the leg resistance and A is the cross sectional area of the leg), then it is immediate to obtain that, *for a given and fixed* $R_{\rm s}$, $R_{\rm L} = R_{\rm s}$.

Instead, optimization of the efficiency $\phi(J)$ leads to a current density

$$J^{\max \eta} = \frac{\sigma_T\alpha\Delta T_{\rm TEG}}{\ell z\overline{T}}\left(\sqrt{1 + z\overline{T}} - 1\right) \tag{76}$$

while the maximum efficiency computes to

$$\eta_{\max}^{\rm DCPL} = \frac{\Delta T_{\rm TEG}}{T_{\rm H}}\frac{\sqrt{1 + z\overline{T}} - 1}{\sqrt{1 + z\overline{T}} + T_{\rm C}/T_{\rm H}}. \tag{77}$$

Also in this case, the optimal load resistance may be computed by setting $J^{\max \eta}A = \alpha\Delta T_{\rm TEG}/(R_{\rm s} + R_{\rm L})$, obtaining $R_{\rm L}/R_{\rm s} = \sqrt{1 + z\overline{T}}$.

It should be remarked that the efficiency at maximum power and the maximum efficiency differ from each other only when the device layout (namely R_s) is set independently of R_L. Instead, the efficiency at maximum power occurs for $R_\mathrm{L}/R_\mathrm{s} = \sqrt{1+z\overline{T}}$ (therefore taking the same value as $\eta_\mathrm{max}^\mathrm{DCPL}$) when device geometry is optimised (as of its thermal and electrical resistance) with respect to its load [18, 19].

For an infinitesimal ΔT_TEG the previous equation reads

$$\delta\eta_\mathrm{max}^\mathrm{DCPL} = \frac{\delta T_\mathrm{TEG}}{T}\frac{\sqrt{1+zT}-1}{\sqrt{1+zT}+1}\,. \tag{78}$$

6. – Thermoelectric efficiency in the presence of large temperature differences

6·1. *Thermoelectric compatibility.* – Whenever the temperature difference over which a TEG operates is large or it is anyway inconvenient to neglect the temperature dependency of transport parameters, the analysis carried out in the previous Section is almost unavoidably bound to set only an upper limit to the actual TEG efficiency.

Taking full account of the temperature dependence of σ_T, α, and κ_oc may be carried out often only by numerical methods [20, 21]. Nonetheless, the concept of *thermoelectric compatibility* (hereafter more simply referred to as *compatibility*) may be of support to devise limits and possibility of real materials to be used in TEGs.

The concept of compatibility was introduced by Snyder in 2003 [22, 23] and refers to the reduced electric current flowing through a thermoelectric element that leads to the TEG maximum efficiency. In a one-dimensional system aligned along the x axis, in view of eqs. (68) and (69) one may write that

$$\begin{aligned} \mathscr{E} &= \alpha T'(x) - \rho_T J, \\ J_q &= \alpha T(x) J + \kappa_\mathrm{oc} T'(x), \end{aligned} \tag{79}$$

where $\rho_T = 1/\sigma_T$ and signs were reverted so that the energy balance is referred to the system. Therefore, the electric power consumed by the TEG (*e.g.*, by Joule effect) is hereafter negative.

Energy conservation obviously sets that the electric power flux J_W must equal the net heat flux J_q so that, if $w = \mathscr{E}J$ is the specific electric power (power per volume of thermoelectric material), then $\mathrm{d}J_q/\mathrm{d}x = w$. Thus, in view of eqs. (79) one may conclude that charge build-up is disallowed, namely $\mathrm{d}J/\mathrm{d}x = 0$. Note that such a result is different from simply stating that $\boldsymbol{\nabla}\cdot\mathbf{J} = \mathbf{0}$ since in the present case $J = J(T(x))$.

One of the key points of this analysis relies on the observation that temperature may be used as the space metrics since the temperature monotonically drops from the hot to the cold side of the thermoelectric element. Thus, $T(x)$ is invertible, namely $x = x(T)$ is a single-valued function. Therefore, under steady-state conditions

$$\frac{\mathrm{d}}{\mathrm{d}x}\left(\kappa_\mathrm{oc} T'(x)\right) = -T(x)\frac{\mathrm{d}\alpha}{\mathrm{d}T} J T'(x) - \rho_T J^2, \tag{80}$$

so that

$$\frac{\mathrm{d}(\alpha T)}{\mathrm{d}x} = T\frac{\mathrm{d}\alpha}{\mathrm{d}T}T'(x) + \alpha T'(x), \tag{81}$$

where $\alpha = \alpha(x(T), T)$ and $\mathrm{d}\alpha/\mathrm{d}T$ is the total derivative of α with respect to T.

One may now define a reduced current density u (see footnote(7))

$$u := \frac{J}{\kappa_{\mathrm{oc}} T'(x)} \tag{82}$$

Thus, replacing $\mathscr{E}$ from the first of eqs. (79) in w one obtains

$$w = \alpha J T' - \rho_T J^2 = \kappa_{\mathrm{oc}} (T')^2 u(\alpha - u\rho_T \kappa_{\mathrm{oc}}) \tag{83}$$

while the second of eqs. (79) reads

$$J_q = \kappa_{\mathrm{oc}} T'(\alpha u T + 1). \tag{84}$$

Finally, eq. (80) may be recast as

$$\frac{\mathrm{d}u}{\mathrm{d}T} = u^2 T \frac{\mathrm{d}\alpha}{\mathrm{d}T} + u^3 \rho_T \kappa_{\mathrm{oc}}\,. \tag{85}$$

An infinitesimal efficiency may be immediately written as a measure of power $w\,\mathrm{d}x$ produced over an infinitesimal distance $\mathrm{d}x$:

$$\delta\eta = \frac{w\,\mathrm{d}x}{J_q} = \frac{\mathrm{d}T}{T}\frac{u(\alpha - u\rho_T\kappa_{\mathrm{oc}})}{u\alpha + \frac{1}{T}} \tag{86}$$

that may be rearranged as $\delta\eta \equiv \delta\eta_{\mathrm{C}} \times \eta_{\mathrm{r}}$ where $\delta\eta_{\mathrm{C}}$ is the infinitesimal Carnot efficiency, while

$$\eta_{\mathrm{r}} = \frac{u(\alpha - u\rho_T\kappa_{\mathrm{oc}})}{u\alpha + \frac{1}{T}} = \frac{1 - u\frac{\alpha}{z}}{1 + \frac{1}{u\alpha T}}\,, \tag{87}$$

where the last equality holds true if both u (J) and α are non-zero.

Manifestly enough, η_{r} has a maximum over u. This maximum must depend on T as all terms in eq. (87) depend on T. One easily obtains that such a maximum occurs for $u = s$, where

$$s = \frac{\sqrt{1 + zT} - 1}{\alpha T} \approx \frac{z}{2\alpha} \tag{88}$$

---

(7) Not to be confused with the internal energy.

is named *(thermoelectric) compatibility.* The maximum relative efficiency computes to

$$\max_u \eta_{\mathrm{r}} = \frac{\sqrt{1+zT}-1}{\sqrt{1+zT}+1}\,. \tag{89}$$

It may be worth comparing eq. (89) to the infinitesimal efficiency (eq. (78)) computed in the CPL. The relative efficiency at maximum u clearly coincides with the efficiency that would be reached over an infinitesimal temperatuire difference, where trivially $u = s$ always.

It should be remarked that u may be adjusted to s (by changing the electric load, typically) only for a given temperature as u is set by eq. (84). Thus, one has to reach the conclusion that *no thermoelectric device may operate optimizing its local efficiency* $\delta\eta$ *at each point.* However, electric currents in TEGs are usually small so that actual local efficiency may be kept to within ≈ 20% of its maximum value [23]. Much more relevant is the issue in Peltier cooler, where electric currents are much larger.

6·2. *Thermoelectric potential.* – It is convenient to further recast the previous equations by introducing a *thermoelectric potential* Φ. Setting $\Phi := \alpha T + u^{-1}$ [23] it is easy to show that

$$\Phi = \alpha T + \frac{\kappa_{\mathrm{oc}} T'}{J}\,, \tag{90}$$

while $J_q = J\Phi$ and $\mathscr{E} = \Phi'(x)$. Therefore, the efficiency of a finite-length thermoelectric element may be written as

$$\int_{T_{\mathrm{C}}}^{T_{\mathrm{H}}} \eta_{\mathrm{r}} \frac{\mathrm{d}T}{T} = \int_{T_{\mathrm{C}}}^{T_{\mathrm{H}}} \frac{w\,\mathrm{d}x}{J_q} = \int_{T_{\mathrm{C}}}^{T_{\mathrm{H}}} \frac{J\Phi'(x)\mathrm{d}x}{J\Phi} = \int_{T_{\mathrm{C}}}^{T_{\mathrm{H}}} \frac{\mathrm{d}\Phi}{\Phi} = \ln\left(\frac{\Phi(T_{\mathrm{H}})}{\Phi(T_{\mathrm{C}})}\right). \tag{91}$$

In an alternate view, one may use instead eq. (87) to compute the actual efficiency considering the leg as a series of infinitesimal thermoelectric elements. Thus

$$1 - \eta_{\mathrm{series}} = \prod_i (1 - \eta_{\mathrm{r},i}). \tag{92}$$

With a little of algebra one obtains

$$\eta_{\mathrm{series}} = 1 - \exp\left(-\int \frac{\eta_{\mathrm{r}}}{T} \mathrm{d}T\right), \tag{93}$$

where the approximation $\ln(1-\eta_{\mathrm{r}}) \approx -\eta_{\mathrm{r}}$ was used.

Comparing now eqs. (91) and (93) one immediately obtains that

$$\eta_{\text{series}} = 1 - \frac{\Phi(T_{\text{C}})}{\Phi(T_{\text{H}})} \tag{94}$$

or, using the definition of Φ,

$$\eta_{\text{series}} = 1 - \frac{\alpha(T_{\text{C}})T_{\text{C}} + 1/u(T_{\text{C}})}{\alpha(T_{\text{H}})T_{\text{H}} + 1/u(T_{\text{H}})}\,. \tag{95}$$

6˙3. *Comparison to CPL efficiency.* – One expects eq. (89) to reduce to eq. (77) in the CPL. If all transport coefficients are independent of the temperature, eq. (80) may be analytically solved for u to give

$$u(T)^{-2} = u(T_{\text{C}})^{-2} - 2(T - T_{\text{C}})\kappa_{\text{oc}}\rho_T. \tag{96}$$

Setting $T = T_{\text{H}}$ in the previous equation, efficiency from eq. (95) may be maximized using T_{H} as a free parameter. One obtains

$$u(T)^{-2} = s(\overline{T})^{-2} + (\overline{T} - T)^2\kappa_{\text{oc}}\rho_T + \left(\frac{\Delta T_{\text{TEG}}}{2}\kappa_{\text{oc}}\rho_T s(\overline{T})\right)^2, \tag{97}$$

where it may be worth noting that both u and s remain dependent on the temperature even when the transport parameters are not. Thus

$$\begin{aligned} u(T_{\text{C}})^{-1} &= s(\overline{T})^{-1} + \frac{\Delta T_{\text{TEG}}}{2}\kappa_{\text{oc}}\rho_T s(\overline{T}) \\ u(T_{\text{H}})^{-1} &= s(\overline{T})^{-1} - \frac{\Delta T_{\text{TEG}}}{2}\kappa_{\text{oc}}\rho_T s(\overline{T}) \end{aligned} \tag{98}$$

so that the efficiency recovers the known CPL result (eq. (95)), namely

$$\eta_{\text{series}}^{\text{CPL}} = \frac{\Delta T_{\text{TEG}}}{T_{\text{H}}}\frac{\sqrt{1 + z\overline{T}} - 1}{\sqrt{1 + z\overline{T}} + T_{\text{C}}/T_{\text{H}}}\,. \tag{99}$$

6˙4. *Compatibility and efficiency.* – From the previous analysis it should be apparent that, since s depends upon T while u is independently set by eq. (80), it will be uncommon to have that all parts of a thermoelectric generator operating over a large temperature difference may work with its highest efficiency. Even in the CPL, could each section of the series operate at optimal efficiency (*i.e.* could a leg be made of an infinitesimally graded material fulfilling at each point the condition $u = s$, while keeping z constant

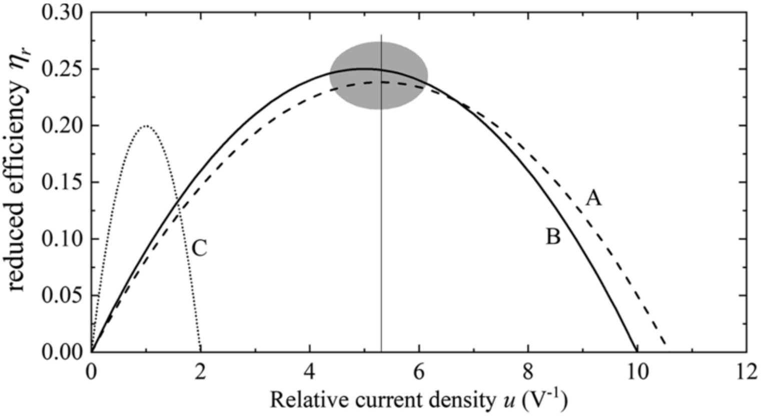

Fig. 2. – Reduced efficiencies of three hypothetical thermoelectric materials *vs.* their reduced current density. Note how A and B materials are *compatible* to each other, *i.e.* a u value may be set that keep both material efficiencies close to their maximum. Instead, no u enables A and C (or B and C) to operate in series (same u) efficiently. Therefore, the overall leg would provide conversion yields lower than those achievable in a single-segment leg.

throughout) one would obtain from eq. (93) that

$$\begin{aligned}\eta^*_{\text{series}} &= 1 - \exp\left(-\int_{T_\text{C}}^{T_\text{H}} \frac{\sqrt{1+zT}-1}{\sqrt{1+zT}+1}\frac{\mathrm{d}T}{T}\right) \\ &= 1 - \left(\frac{1+\sqrt{1+zT_\text{C}}}{1+\sqrt{1+zT_\text{H}}}\right)^2 \exp\left[\frac{2(\sqrt{1+zT_\text{H}}-\sqrt{1+zT_\text{C}})}{(1+\sqrt{1+zT_\text{C}})(1+\sqrt{1+zT_\text{H}})}\right].\end{aligned} \tag{100}$$

As a way of example, for $z = 3\times10^{-3}\ \text{K}^{-1}$, $T_\text{C} = 300$ K, and $T_\text{H} = 1000$ K one would obtain $\eta^{\text{CPL}}_{\text{series}} = 24.90\%$ *vs.* $\eta^*_{\text{series}} = 25.18\%$.

In a real situation, segmented legs may approximate such a situation. Two or more materials are used in a thermal series, where each segment is chosen so as to provide the largest efficiency in the range of temperatures it operates. However, the simple criterion of choosing the material based on its thermoelectric figure of merit may not be the best. Instead, materials should be selected so that each may work at u values as close as possible to their relevant s. Figure 2 displays η_r for three hypothetical thermoelectric materials A, B, and C. It shows that while a good compromise on u may be obtained to achieve high efficiencies from A and B, combining A and C (or B and C) would lead to largely sub-optimal η_r values for one of the two segments. Therefore, the series efficiency would be severely affected. In principle, being s temperature-dependent, also a single-material leg may run into compatibility issues, meaning that no u value may be set that is sufficiently close to $s(T)$ over the whole range of temperatures spanned by the leg. Such a *self-compatibility* problem is however uncommon in homogeneous thermoelectric materials, while it may show up in graded thermoelectrics.

7. – Summary and conclusions

Moving from equilibrium thermodynamics in its axiomatic (Gibbsian) instantiation, we have discussed how concepts of GET have been inherited by the CIT through the LEH. The limits of such an assumption have been briefly discussed. CIT remains anyway an excellent framework for the analysis of transport phenomena as long as the system size is large compared to the mean free path of the relevant carriers and steady-state conditions are considered.

CIT has been then extensively used to model thermoelectric phenomena. Onsager-Casimir reciprocal relations enabled to connect Seebeck and Peltier coefficients. Since, further to metrologic applications (measurements of temperature by thermocouples), thermoelectricity is mainly used either to convert heat into electricity or to use electricity to transfer heat from colder to hotter thermostats, a large part of this paper was devoted to critically analyze the efficiency of thermoelectric heat engines. Over small temperature difference, neglecting the temperature dependence of transport coefficients on T is a fair approximation. Simple expressions relate the thermoelectric figure of merit to the engine efficiency. Instead, when temperature differences are larger, the dependence of z (and Z) on T has to be accounted for. The concept of compatibility well encompasses the interplay of $\sigma(T)$, $\alpha(T)$, and $\kappa(T)$, also providing guidance to the making of segmented and graded thermoelectric legs [24].

By choice, all theory was kept at the macroscopic level. This notwithstanding, the thermodynamic modelling of thermoelectricity gives strong indications about the best candidate materials to be sought to enhance efficiency. In particular, the link between the Seebeck coefficient and the convective part of the entropy flux highlights constraints concerning mobile carrier density. This picture will be extended and further commented upon in the next lectures, where a systematic connection between macroscopic and microscopic views of thermoelectricity will be elaborated upon.

REFERENCES

[1] PATRA B., *An Introduction to Integral Transforms* (CRC Press) 2018.

[2] LEBON G., JOU D. and CASAS-VÁZQUEZ J., *Understanding Non-equilibrium Thermodynamics: Foundations, Applications, Frontiers*, (SpringerLink: Springer e-Books, Springer, Berlin, Heidelberg) 2008.

[3] KONDEPUDI D. and PRIGOGINE I., *Modern Thermodynamics: From Heat Engines to Dissipative Structures*, *CourseSmart Series* (Wiley) 2014.

[4] DE GROOT S. and MAZUR P., *Non-Equilibrium Thermodynamics*, *Dover Books on Physics* (Dover Publications) 2013.

[5] LAVENDA B., *Thermodynamics of Irreversible Processes*, *Dover Classics of Science and Mathematics* (Dover) 1993.

[6] JACOBONI C., CANALI C., OTTAVIANI G. and QUARANTA A. A., *Solid-State Electron.*, **20** (1977) 77.

[7] ONSAGER L., *Phys. Rev.*, **37** (1931) 405.

[8] ONSAGER L., *Phys. Rev.*, **38** (1931) 2265.

[9] CASIMIR H. B. G., *Rev. Mod. Phys.*, **17** (1945) 343.

[10] Moszynski J., Hoshiko T. and Lindley B., *Biochim. Biophys. Acta*, **75** (1963) 447.

[11] Zabrocki K., Goupil C., Ouerdane H., Apertet Y., Seifert W. and Müller E., "Continuum theory of TE elements", in *Continuum Theory and Modeling of Thermoelectric Elements*, edited by Goupil C. (Wiley, Weinheim) 2016, Chapt. 2, pp. 75–156.

[12] Domenicali C. A., *Rev. Mod. Phys.*, **26** (1954) 237.

[13] Altenkirch E., *Phys. Z.*, **10** (1909) 560.

[14] Ioffe A., *Semiconductor Thermoelements and Thermoelectric Cooling* (Infosearch Ltd., London) 1957.

[15] Rowe D., *CRC Handbook of Thermoelectrics* (CRC Press) 1995.

[16] Domenicali C. A., *Phys. Rev.*, **92** (1953) 877.

[17] Domenicali C. A., *J. Appl. Phys.*, **25** (1954) 1310.

[18] Apertet Y., Ouerdane, H., Glavatskaya, O., Goupil, C. and Lecoeur P., *EPL*, **97** (2012) 28001.

[19] Yazawa K. and Shakouri A., *J. Appl. Phys.*, **111** (2012) 024509.

[20] Sherman B., Heikes R. R. and Ure R. W. jr., *J. Appl. Phys.*, **31** (1960) 1.

[21] El-Genk M. S. and Saber H. H., *Energy Convers. Manag.*, **44** (2003) 1069.

[22] Snyder G. J. and Ursell T. S., *Phys. Rev. Lett.*, **91** (2003) 148301.

[23] Snyder G. J., "Thermoelectric Power Generation", in *Thermoelectrics Handbook: Macro to Nano*, edited by Rowe D. M. (CRC Press) 2005, pp. 9–26.

[24] Rowe D. M., *Thermoelectrics Handbook: Macro to Nano* (CRC Press) 2018.

Proceedings of the International School of Physics "Enrico Fermi"
Course 207 "Advances in Thermoelectricity: Foundational Issues, Materials and Nanotechnology",
edited by D. Narducci, G. J. Snyder and C. Fanciulli
(IOS, Amsterdam; SIF, Bologna) 2021
DOI 10.3254/ENFI210003

Transport property analysis method for thermoelectric materials: Material quality factor and the effective mass model(*)

Stephen Dongmin Kang

Department of Applied Physics and Materials Science, California Institute of Technology CA 91125, USA

Department of Materials Science and Engineering, Northwestern University - IL 60208, USA

G. Jeffrey Snyder

Department of Materials Science and Engineering, Northwestern University - IL 60208, USA

Summary. — Thermoelectric semiconducting materials are often evaluated by their figure-of-merit, zT. However, by using zT as the metric for showing improvements, it is not immediately clear whether the improvement is from an enhancement of the inherent material property or from optimization of the carrier concentration. Here, we review the quality factor approach which allows one to separate these two contributions even without Hall measurements. We introduce practical methods that can be used without numerical integration. We discuss the underlying effective mass model behind this method and show how it can be further advanced to study complex band structures using the Seebeck effective mass. We thereby dispel the common misconception that the usefulness of effective band models is limited to single parabolic band materials.

(*) Reproduced from Zevalkink A. *et al.* "A practical field guide to thermoelectrics: Fundamentals, synthesis, and characterization", *Appl. Phys. Rev.*, **5** (2018) 021303, https://doi.org/10.1063/1.5021094, with permission of AIP Publishing.

1. – The effective mass model

In semiconducting band conductors, charge transport properties of interest are typically governed by the states near the band edge. Because the dispersion relation *at the band edge* is typically parabolic ($E = \hbar^2k^2/m^*$), it is often helpful to use an effective mass (m^*) model to characterize experimentally measured transport data. The general approach is to consider the electronic structure of the majority carriers, whether holes or electrons, to be described by an effective mass m^* that is independent of temperature and doping level. This approach puts our primary interest on data where transport contribution from minority carriers is not significant.

We introduce in the next section a simple and accessible method —the quality factor approach— to analyze transport data using an effective mass model without the need for performing numerical integration of the Fermi function or even explicitly determining the effective mass. Even the simplest application of this model by using only thermopower ($|S|$), electrical conductivity (σ), and thermal conductivity (κ) measurements allows one to predict the maximum $zT = TS^2\sigma/\kappa$ that would be expected from optimizing the doping. With the further use of Hall measurements to extract a value for m^*, the effective mass model makes it easy to identify complexities in the band structure and compare to theory.

2. – Material quality factor analysis using only S, σ, and κ

Thermoelectric materials research typically aims to identify good thermoelectric materials and optimize their properties so that they can achieve the best possible zT. Since the zT of a material peaks at an optimum carrier concentration (fig. 1), measuring zT of one sample does not immediately provide an idea of the ultimate potential of a given material for thermoelectrics; a material initially measured with $zT < 0.1$ might end up with $zT > 1$ after tuning the carrier concentration.

Given the conductivity, Seebeck coefficient, and thermal conductivity of a single sample at an arbitrary doping level, what would be the best guess for its highest zT expected after optimizing its carrier concentration? Should one increase or decrease the amount of free carriers? These questions can be answered even without a Hall or mobility measurement. The quality factor analysis, [1,2] based on an effective mass model, is devised to aid in the search for good thermoelectric materials by providing a convenient means for finding these answers.

The essence of the approach is to treat zT as a function of two independent variables: the reduced Fermi level (reduced electron chemical potential) $\eta = E_\mathrm{F}/k_\mathrm{B}T$ (fig. 1(a)), and the "material quality factor B." The former is a function of doping and temperature, and can be extracted from the Seebeck coefficient. In the steps described below, it is, in fact, not necessary to directly calculate a value of η. The latter is a material property largely independent of doping (though still dependent on temperature) given by [3]:

$$B = \left(\frac{k_\mathrm{B}}{e}\right)^2 \frac{\sigma_{E_0}}{\kappa_\mathrm{L}} T. \tag{1}$$

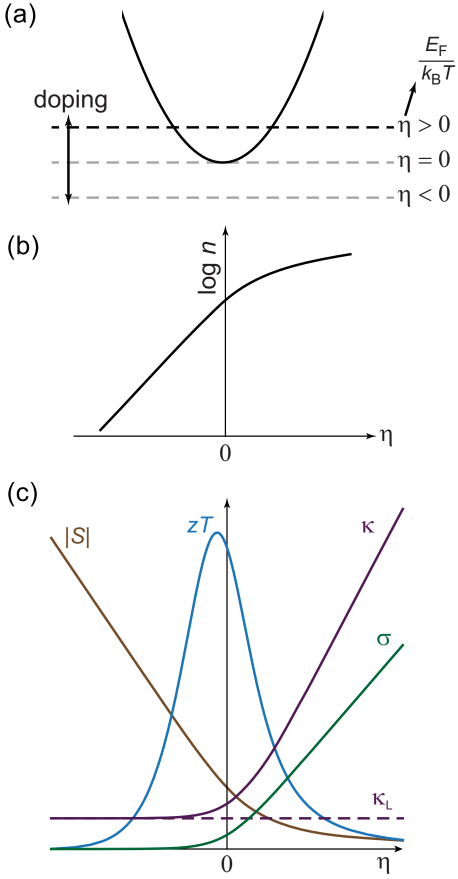

Fig. 1. – Reduced chemical potential η for transport modeling. (a) η is defined as the Fermi level E_F measured from the band edge, divided by $k_\mathrm{B}T$. Changing the carrier concentration by doping is equivalent to adjusting η. (b) Carrier concentration is a monotonically increasing function of η. (c) Thermopower ($|S|$) decreases with η while electrical and thermal conductivities increase, making zT highest at an optimum η.

Here, k_B is the Boltzmann constant, κ_L is lattice thermal conductivity and σ_{E_0} is a transport coefficient with units of conductivity that characterizes how well a material conducts electricity for a given η (*i.e.*, at a given carrier concentration). The material quality factor effectively removes all dependences on η (*i.e.*, on carrier concentration), and retains only the *inherent* material properties that determine zT. This approach is successful because both m^* (which is encompassed in σ_{E_0}) and κ_L remain relatively constant for the range of η values that is experimentally tested by changing the carrier concentration (*e.g.* doping, fig. 1(b)).

The thermopower $|S|$ at any temperature or doping concentration is best described as a function of only η [4, 5]: $|S(\eta)|$ (schematically shown in fig. 1(c)). Thermopower is

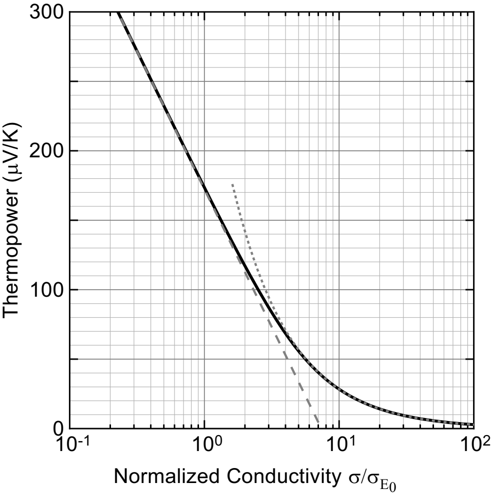

Fig. 2. – Determining σ_{E_0} from a S-σ pair. Thermopower ($|S|$) determines the σ/σ_{E_0} of a sample, which allows one to determine σ_{E_0} from a pair of measured S and σ. The analytical relations for the high S limit (eq. (3)) (dashed line) and low S limit (eq. (4)) (dotted line) are also shown together.

merely an indicator of η or E_F. High $|S|$ does *not* necessarily indicate a high quality thermoelectric material, nor does it directly determine the quality factor B. For semiconductors that can be doped, S indicates the doping level which depends on defects and impurities; making tabulated values of S for "pure" semiconductors or insulators is virtually meaningless. To optimize the zT of a material, η, and thus S, must be tuned to an optimal value via doping (fig. 1(c)). In the method presented here, we simply use S as a direct indicator of the doping level —there is no need to calculate η.

Conductivity, on the other hand, depends on σ_{E_0} as well as η:

$$\sigma = \sigma_{E_0} \cdot \ln(1 + e^{\eta}). \tag{2}$$

Here, the η term describes the increase in charge carriers as the Fermi level is increased. It is seen that σ_{E_0} describes the conductive "quality" of charge carriers in the material (magnitude of conductivity for a given η). Typically, σ_{E_0} is broken down to m^* and the mobility parameter μ_0 (determination of each requires a Hall measurement), but this decomposition is not always necessary for a basic use of the quality factor analysis. σ_{E_0} can be estimated from a pair of S and σ measurements on the same sample. As shown in fig. 2, S *vs.* σ/σ_{E_0} follows a universal curve; *i.e.* one can graphically find the σ/σ_{E_0} that corresponds to the measured S to find σ_{E_0}. Alternatively, one can use the analytical expressions in the limits when is $|S|$ is large (within 5% when $|S| > 120\,\mu\mathrm{V/K}$):

$$\sigma_{E_0} = \sigma \cdot \exp\left[\frac{|S|}{k_\mathrm{B}/e} - 2\right], \tag{3}$$

or small (within 5% when $|S| < 75\,\mu\text{V/K}$):

$$\sigma_{E_0} = \sigma \cdot \frac{3}{\pi^2} \frac{|S|}{k_\text{B}/e}\,. \tag{4}$$

The graphical method is better for intermediate $|S|$ values.

Low lattice thermal conductivity, κ_L, is also a relevant descriptor for a good thermoelectric material because κ_L is typically independent of η. κ_L is obtained by subtracting, from the measured κ, the electronic portion (κ_e) which is η dependent:

$$\kappa_\text{L} = \kappa - \kappa_\text{e} = \kappa - L\sigma T. \tag{5}$$

Here, the Lorenz number L, defined by $\kappa_\text{e} = L\sigma T$, is also a function of only η (like $S(\eta)$) [4,5]: $L(\eta)$. Keeping in mind that S is the experimental indicator of η, the value of L at a given temperature can be approximated using measurements of S using [6]

$$L\,[10^{-8}\,\text{W}\Omega/\text{K}^2] \approx 1.5 + \exp\left(-\frac{|S|}{116\,\mu\text{V/K}}\right). \tag{6}$$

To see how the definition of B in eq. (1) is justified, we can now separate the η-dependent terms from zT:

$$\begin{aligned} zT &= \frac{S^2\sigma T}{\kappa_\text{L} + \kappa_\text{e}} = \frac{S^2}{\frac{\kappa_\text{L}}{\sigma T} + L} \\ &= \frac{S^2(\eta)}{\frac{\kappa_\text{L}}{T\sigma_{E_0} \cdot \ln(1+e^{\eta})} + L(\eta)} \\ &= \frac{S^2(\eta)}{\frac{(k_\text{B}/e)^2}{B\ln(1+e^{\eta})} + L(\eta)}\,, \end{aligned} \tag{7}$$

where B combines all the η-independent material parameters, giving the definition of the *dimensionless material quality factor* in eq. (1). The natural unit of the Lorenz number $(k_\text{B}/e)^2$ was multiplied in the term containing $1/B$ to make B dimensionless for convenience (some authors [5] use $\beta = B/(k_\text{B}/e)^2$).

This quality factor B completely determines the zT *vs.* η curve (fig. 3(a)) for a given material at a given temperature. Therefore, B is a good descriptor to estimate the maximum zT achievable from a material when the carrier concentration (and, thus η) is optimized; B also determines the optimum level of doping (fig. 3(b)). Practically, tuning towards the optimum is most easily done by looking at the optimum thermopower that is expected from a given B. For example, if $B = 0.4$ and $S = 50\,\mu\text{V/K}$ was obtained from a sample at a given temperature, one can expect to reach $zT > 1$ by decreasing the carrier concentration until $S = 240\,\mu\text{V/K}$.

Given S, σ, and κ of a single sample at a given temperature, one can estimate σ_{E_0} and κ_L, which allows the estimation of B at that temperature using eq. (1). The approximate

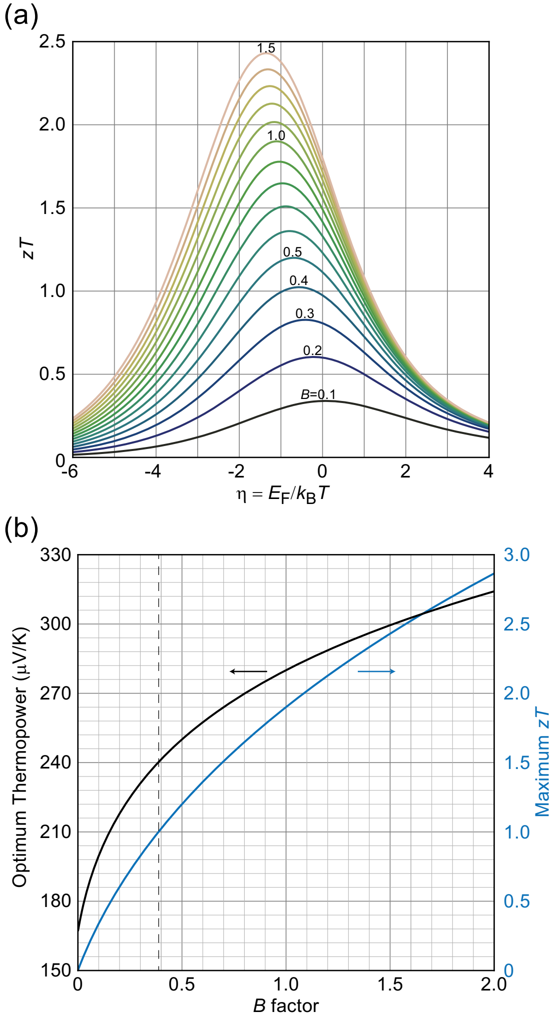

Fig. 3. – Material quality factor analysis. (a) The zT *vs.* η relation is determined by the material quality factor B, making maximum zT and optimum η a function of B. (b) Thermopower at optimum η as a function of B (black line, left axis), which can be used as a guide for optimization. Maximum zT is also plotted together (blue line, right axis). The vertical dashed line indicates when maximum $zT = 1$, corresponding to $B \approx 0.4$ which serves as a convenient reference value for a good thermoelectric material.

methods (eqs. (6) and (3), (4)) described above make this estimation quick and easy. The full calculation is also straightforward, but requires numerical integration and root finding using the expressions of $|S(\eta)|$ and $L(\eta)$ which can be found in ref. [5]. The first step is to estimate η from the measured S by numerical solving. Then, one could use η and the measured conductivity to estimate σ_{E_0} using eq. (2). Lastly, to estimate the lattice thermal conductivity κ_{L} from measured κ (eq. (5)), one can calculate $L(\eta)$ using the η estimated from S.

The application of the B-factor zT analysis is simple once σ_{E_0} and κ_{L} is determined. One can calculate B from eq. (1). Then fig. 3(b) can be used to find the maximum zT and optimum thermopower.

The approach of separating η dependence (or doping dependence) from intrinsic material parameters can be extended to atypical cases, such as conducting polymers [3], where transport behaves in a different way (different energy dependency of transport and different scale of B) than found in inorganic crystalline materials.

3. – Bipolar effects

A particular material is well described by a single B as long as the carriers in the η range of interest are well characterized by a single m^*. The most common situation in which a single m^* does *not* suffice is when there is non-negligible contribution from minority carriers. This bipolar transport happens in all semiconductors at high temperatures (*i.e.*, when $k_{\mathrm{B}}T$ becomes comparable to $\approx E_{\mathrm{g}}/4$, where E_{g} is the band gap). The onset of bipolar conduction is best identified from the thermopower showing a flattening or rollover with increasing temperature (*i.e.* diminishing slope in $|S|$ *vs.* T). It is possible to estimate B of the majority carriers in the bipolar region by extrapolating σ_{E_0} *vs.* T from the non-bipolar region. In the most common case of acoustic-phonon scattering, σ_{E_0} is nearly constant with respect to T. At a temperature where bipolar conduction dominates, one would realize that the optimum S required for maximum zT, as evaluated from the B of majority carriers, is not obtainable at that temperature due to the canceling contribution of minority carriers. The maximum thermopower obtainable ($|S_{\mathrm{max}}(T_{\mathrm{max}})|$) is related to the band gap ($E_{\mathrm{g}} \approx 2e|S_{\mathrm{max}}|T_{\mathrm{max}}$) [7], demonstrating how the maximum zT becomes band-gap limited. An example calculation can be found in ref. [8], where the effective overall B is smaller than that of the majority carriers due to bipolar contribution.

A higher peak zT value is obtainable from a larger band gap for a given σ_{E_0} of the majority carriers. The temperature at which the peak zT is found increases with a larger band gap, leading to a higher zT. This principle motivates to tune the band gap (*e.g.* by alloying) either to increase the peak zT or to shift the peak zT temperature. Because the band gap and σ_{E_0} are often not independent to each other and material stability limits the maximum temperature of a material, the optimum band gap tends to depend on the material and application.

It is worth to note that the bipolar effect from a given band gap can be suppressed if the majority carriers have a higher σ_{E_0} than minority carriers. In this sense, materials with highly contrasted conduction and valence band structures have a larger effective gap when doped with its superior type of carriers.

4. – Effective m^* for studying complex electronic structures

Evaluating σ_{E_0} (but not m^*) was sufficient for the quality factor analysis; assessment of m^* offers a further step through which one can study the band structure of materials using transport measurements.

The equations used so far (eqs. (2)–(4)) are from a model of free carriers (*i.e.* parabolic dispersion) being scattered by acoustic phonons [4] and is sometimes referred to as the single parabolic band model; however, the use of these equations does not necessarily require a single parabolic band assumption. Even for complicated band structures that are non-single or significantly non-parabolic, we can build upon the same approach to characterize the free-carrier equivalent, an effective m^* that can change with temperature and energy. Then, one can relate certain band complexities to particular trends in m^*.

For this purpose, we can break down σ_{E_0} in terms of m^*. In anticipation that, in the case of non-simple band structures, m^* will be differently determined depending on how it is assessed, we will distinguish m^*'s with a subscript. In band conductors, σ_{E_0} is [3]:

$$\sigma_{E_0} = \frac{8\pi e(2m_\mathrm{e}k_\mathrm{B}T)^{3/2}}{3h^3}\cdot\mu_0\left(\frac{m^*_\mathrm{S}}{m_\mathrm{e}}\right)^{3/2}. \tag{8}$$

Here, $\mu_0 = e\tau_0/m^*_\mathrm{I}$ is a mobility parameter, where τ_0 describes the relaxation time of carriers through $\tau = \tau_0\cdot(E/k_\mathrm{B}T)^{-1/2}$ and m^*_I is the inertial effective mass. m^*_S is the Seebeck effective mass and m_e is the mass of an electron.

The quantity $\mu_\mathrm{w} = \mu_0(m^*_\mathrm{S}/m_\mathrm{e})^{3/2}$ is called the weighted mobility and is directly proportional to σ_{E_0} for a given T. Some authors [2] use the non-degenerate limit drift mobility ($\mu_\mathrm{cl} = 4/3\sqrt{\pi}\cdot\mu_0$) to define μ_0 (and thus, μ_w)(1).

The Seebeck effective mass describes the number of states for a given reduced chemical potential η, where η is evaluated using $|S|$ and the number of states at that η is evaluated using a Hall measurement. m^*_S can be calculated within 2% by using the following equations. When $|S| > 75\,\mu\mathrm{V/K}$:

$$m^*_\mathrm{S} \approx \frac{h^2}{2k_\mathrm{B}T}\left\{\frac{3n_\mathrm{H}}{16\sqrt{\pi}}\left(\exp\left[\frac{|S|}{(k_\mathrm{B}/e)}-2\right]-0.17\right)\right\}^{2/3}. \tag{9}$$

and, when $|S| < 75\,\mu\mathrm{V/K}$:

$$m^*_\mathrm{S} \approx \frac{3h^2}{8\pi^2k_\mathrm{B}T}\frac{|S|}{(k_\mathrm{B}/e)}\left(\frac{3n_\mathrm{H}}{\pi}\right)^{2/3}. \tag{10}$$

Here, n_H is the Hall carrier concentration. A heavier m^*_S gives higher $|S|$ for a given n_H (alternatively, a higher n_H for a given $|S|$). A plot of $|S|$ with respect to n_H is called a "Pisarenko plot", by which one can determine m^*_S from a set of data points.

---

(1) Inconsistently interchanging μ_0 and μ_cl could lead to errors in B by a factor of $3\sqrt{\pi}/4 \approx 1.33$ (*e.g.*, fig. 1 in ref. [9]).

The inertial mass is not easily separable from the relaxation time, and we thus keep it in the form of $\mu_0 = e\tau_0/m_\mathrm{I}^*$. We can nevertheless understand how band structure impacts μ_0 using the deformation potential model by Bardeen and Shockley [10]:

$$\mu_0 = \frac{\pi e \hbar^4 C_\mathrm{l}}{\sqrt{2} m_\mathrm{I}^* {m_\mathrm{b}^*}^{3/2} (k_\mathrm{B}T)^{3/2} \Xi^2}. \tag{11}$$

Here, m_b^* is the effective mass that describes the density-of-states of an individual Fermi-surface pocket. Ξ is the deformation potential and C_l is the longitudinal elastic constant.

The combination of eqs. (9), (10) and (11) helps one understand what type of band is good for thermoelectrics: $\mu_\mathrm{w} \propto (m_\mathrm{S}^*/m_\mathrm{b}^*)^{3/2}/m_\mathrm{I}^*$. Suppose that symmetry provides N_V multiple bands with the same dispersion (multi-valley degeneracy). Then μ_0 of a single band is identical to the μ_0 of all the multiple bands together. On the other hand, m_S^* is larger than that of a single band by $N_\mathrm{V}^{2/3}$ because the density-of-states (and thus n_H in eqs. (9), (10)) is larger by a factor of N_V. Overall, μ_w (and, thus σ_{E_0} and B) scales with $N_\mathrm{V}/m_\mathrm{I}^*$. Therefore, multi-valleys and lighter bands (small m_I^*) are advantageous for thermoelectrics.

In general, when multiple bands contribute to transport, they are not necessarily identical or aligned; nevertheless, the trend of m_S^* and μ_w both increasing simultaneously with advantageous band complexity remains similar [11], allowing one to relate transport measurements to understandings of the electronic structure. Therefore, it is best to keep track of both m_S^* and μ_w when analyzing transport data.

An advanced example would be a case when two conduction bands have their band edges offset by a small amount on the order of a few $k_\mathrm{B}T$. When E_F is below the lower band, the upper band would not contribute significantly to transport. With doping, once E_F moves within a few $k_\mathrm{B}T$ to the edge of the upper band, both bands would start contributing. In experimental characterization, one would observe m_S^* and μ_w both increasing at a threshold of η, where the threshold indicates how much the bands are offset from each other. Such a signature would be a strong motivation to further investigate the band structure using more specific methods such as optical absorption.

The usefulness of m_S^*, or any m^* in general, comes from the fact that it is a convenient metric to characterize an electronic structure and so used to characterize diverse measurements such as the electronic specific heat, plasma frequency, as well as Seebeck coefficient. Mathematically, the procedure could be understood as a change of variables. While E, k, σ_E, τ, or density-of-states change dramatically with experimental variables such as doping or temperature, the various m^*'s as defined though different measurements (Seebeck, specific heat, plasma frequency, etc.) remain relatively constant and thus m^*'s are typically reported as results of such measurements. Just as m^*'s are reported rather than specific values of electronic specific heat (*e.g.*, heavy fermion metals) or optical absorption (plasma frequency measurements), it would be more useful to report m_S^* than specific values of S in many insulators and semiconductors. All of these effective masses are expected to change somewhat with doping, temperature and even alloying and structural modification. In fact, observing and quantitatively characterizing how

m^* changes might be the best way to identify changes in parabolicity or multiple band effects [12-14]. In this way, the effective m^* approach does not simply assume, or impose an approximation of, a single parabolic band, but rather provides a helpful means to characterize data and identify deviations from single or parabolic electronic structures.

REFERENCES

[1] Chasmar R. P. and Stratton R., "The thermoelectric figure of merit and its relation to thermoelectric generators", *J. Electron. Control*, **7** (1959) 52.

[2] Wang Heng, Pei Yanzhong, LaLonde Aaron D. and Snyder G. Jeffrey, "Material design considerations based on thermoelectric quality factor", in *Thermoelectric Nanomaterials: Materials Design and Applications*, edited by Koumoto Kunihito and Mori Takao (Springer Berlin Heidelberg) 2013, pp. 3–32.

[3] Kang Stephen Dongmin and Snyder G. Jeffrey, "Charge-transport model for conducting polymers", *Nat. Mater.*, **16** (2017) 252, Supplementary Information.

[4] Fistul Viktor I., *Heavily Doped Semiconductors* (Plenum Press) 1969, Chapt. 3.

[5] May Andrew F. and Snyder G. Jeffrey, "Introduction to modeling thermoelectric transport at high temperatures", in *Materials, Preparation, and Characterization in Thermoelectrics*, edited by Rowe D. M. (CRC Press) 2012, pp. 1–18.

[6] Kim Hyun-Sik, Gibbs Zachary M., Tang Yinglu, Wang Heng and Snyder G. Jeffrey, "Characterization of Lorenz number with Seebeck coefficient measurement", *APL Mater.*, **3** (2015) 041506.

[7] Gibbs Zachary M., Kim Hyun-Sik, Wang Heng and Snyder G. Jeffrey, "Band gap estimation from temperature dependent Seebeck measurement – deviations from the $2e|S|_{\max}T_{\max}$ relation", *Appl. Phys. Lett.*, **106** (2015) 022112.

[8] Kang Stephen Dongmin, Pöhls Jan-Hendrik, Aydemir Umut, Qiu Pengfei, Stoumpos Constantinos C., Hanus Riley, White Mary Anne, Shi Xun, Chen Lidong, Kanatzidis Mercouri G. and Snyder G. Jeffrey, "Enhanced stability and thermoelectric figure-of-merit in copper selenide by lithium doping", *Mater. Today Phys.*, **1** (2017) 7.

[9] Pei Yanzhong, Wang Heng and Snyder G. Jeffrey, "Band engineering of thermoelectric materials", *Adv. Mater.*, **24** (2012) 6215.

[10] Bardeen J. and Shockley W., "Deformation potentials and mobilities in non-polar crystals", *Phys. Rev.*, **80** (1950) 72.

[11] Gibbs Zachary M., Ricci Francesco, Li Guodong, Zhu Hong, Persson Kristin, Ceder Gerbrand, Hautier Geoffroy, Jain Anubhav and Snyder G. Jeffrey, "Effective mass and Fermi surface complexity factor from *ab initio* band structure calculations", *npj Comput. Mater.*, **3** (2017) 8.

[12] Wang Heng, Gibbs Zachary M., Takagiwa Yoshiki and Snyder G. Jeffrey, "Tuning bands of PbSe for better thermoelectric efficiency", *Energy Environ. Sci.*, **7** (2014) 804.

[13] Tang Yinglu, Gibbs Zachary M., Agapito Luis A., Li Guodong, Kim Hyun-Sik, Nardelli Marco Buongiorno, Curtarolo Stefano and Snyder G. Jeffrey, "Convergence of multi-valley bands as the electronic origin of high thermoelectric performance in $CoSb_3$ skutterudites", *Nat. Mater.*, **14** (2015) 1223.

[14] Kim Hyun-Sik, Heinz Nicholas A., Gibbs Zachary M., Tang Yinglu, Kang Stephen D. and Snyder G. Jeffrey, "High thermoelectric performance in $(Bi_{0.25}Sb_{0.75})_2Te_3$ due to band convergence and improved by carrier concentration control", *Mater. Today*, **20** (2017) 452.

Proceedings of the International School of Physics "Enrico Fermi"
Course 207 "Advances in Thermoelectricity: Foundational Issues, Materials and Nanotechnology",
edited by D. Narducci, G. J. Snyder and C. Fanciulli
(IOS, Amsterdam; SIF, Bologna) 2021
DOI 10.3254/ENFI210004

A primer on phonon transport

P. Torres and R. Rurali

Institut de Ciència de Materials de Barcelona (ICMAB–CSIC), Campus de Bellaterra
08193 Bellaterra, Barcelona, Spain

Summary. — In this paper we give a general and basic introduction to the most important concepts related with phonon transport. We first revise Fourier's equation and the diffusive transport regime, focusing on the main scattering mechanisms that yield a finite thermal conductivity in insulators: anharmonic phonon-phonon scattering, impurity scattering, and boundary scattering. Next we focus on transport regimes beyond Fourier, namely ballistic transport and phonon hydrodynamics.

1. – Introduction

The law of heat transport that relates the heat flow to the temperature is named after the French mathematician and physicist Jean-Baptiste Joseph Fourier who introduced it in his *The Analytical Theory of Heat* [1]. Fourier's law has the form

$$\mathbf{Q} = -\boldsymbol{\kappa}\boldsymbol{\nabla} T \tag{1}$$

and states that, in Fourier's own words, "the time rate of heat transfer through a material is proportional to the negative gradient in the temperature and to the area". In eq. (1) $\mathbf{Q}$ is the heat flux vector —an energy per unit time and area, with units of $\mathrm{W/m^2}$, $\boldsymbol{\kappa}$ is the thermal conductivity tensor, and ∇T is the thermal gradient. Often we will consider one-dimensional heat transport, in which case Fourier's law reduces to $Q_z = \kappa \partial T/\partial z$, taking z as the transport direction, and where for simplicity we dropped the index from κ_{zz}, the relevant element of the thermal conductivity tensor in that case. Fourier's law is a phenomenological equation that has no formal derivation, but that nevertheless can describe a wealth of experimental observations and laid the foundations of heat transport theory. It is valid under the following assumptions:

– steady-state heat conduction,

– one directional heat flow,

– the material is homogeneous,

– there is no internal heat generation or destruction,

– the transport is diffusive.

The requirement of steady-state heat conduction means that the system must have reached a stationary non-equilibrium transport regime where all thermal transients must be over and that the thermal bias conditions are not time dependent, *i.e.* the bounding surfaces are kept at constant temperatures. The condition that the material must be homogeneous, on the other hand, means that the thermal conductivity is constant; this in turn implies that the temperature gradient is constant as well and thus the temperature profile is linear for small thermal gradients.

The assumption of diffusive transport regime is central to Fourier's law. It implies that the thermal resistance results from the multiple collisions that phonons suffer when traveling from the hot to the cold side of the material. In this regime, the thermal resistance scales linearly with the length of the sample, L, and with the inverse of the cross-section, A. Therefore, the thermal resistance, R, and conductance, G, are extensive quantities that can be expressed as a function of the resistivity and conductivity, ρ and κ, intensive quantities that describe an intrinsic property of the material, and of geometric factors of the sample as

$$R = \rho \frac{L}{A}\,, \tag{2}$$

$$G = \kappa \frac{A}{L}\,, \tag{3}$$

where $\kappa = 1/\rho$. For the transport to be diffusive L has to be large enough so that phonons can collide with each other. The different scattering mechanisms that we will describe below are characterized by relaxation times, τ, which measure the average time between collisions. Accordingly, if the phonons travel at velocity v, we can define a mean free path, $l = v\tau$, which is the distance traveled between collisions. If the sample length is shorter than any relevant mean free path (remind that each scattering mechanism has its own) the phonons propagate without collisions: this is the ballistic regime, where the thermal resistance is length-independent and thus intensive quantities such as the resistivity and the conductivity are ill-defined. In the ballistic regime the conductance is not infinite, however, and is limited by the quantum nature of phonons. This transport regime will be discussed in sect. **7**.

In the diffusive transport regime we can distinguish at least three classes of scattering mechanisms: i) phonon-phonon scattering, three- or higher-order phonon processes that are possible because of the anharmonicity of the lattice; ii) impurity scattering or, more in general, scattering from crystal imperfections, hence including extended defects such as grain boundaries, dislocations and stacking faults, besides point defects; iii) boundary scattering, which specifically acquires a great importance in low-dimensional nanostructures. In this paper we will review the microscopic origin of these scattering mechanisms and discuss their relevance in the different, prototypical transport conditions. We will keep the algebraic formalism to a minimum level to convey the most important physical concepts, and, as a general rule, we will avoid full derivations or demonstrations that the interested reader can normally find in Ziman's *Electrons and Phonons* [2], in Srivastava's *The Physics of Phonons* [3] or in the papers specifically cited.

2. – Phonon-phonon scattering

The harmonic approximation settles the foundations of lattice dynamics. Therein, the dynamics of the crystal lattice is described in terms of a quadratic potential, where we keep only the first non-zero term of a Taylor expansion of the energy as a function of the atomic displacements. This approximation is extremely useful to introduce several important concepts and to calculate many quantities that account for the behavior of a material in thermodynamic equilibrium, such as the phonon dispersion or the specific heat.

When it comes to transport, however, one must depart by definition from equilibrium and many important physical effects cannot be described at the harmonic level. In particular, within the harmonic approximation lattice waves travel without interactions, obeying the superposition principle. In such a transport regime, each phonon propagates with its own velocity and, in absence of crystal imperfections or boundaries, the thermal conductivity would be infinite, which is in clear contradiction with the experimental observations. Therefore, anharmonic effects must be invoked to account for the finite thermal conductivity of pure, perfect crystals. Formally, this means considering higher-order terms in the expansion of the energy, though for many practical purposes it is enough to consider anharmonicities up to the third order and thus introduce only one more term. That is why from now on we will often use anharmonic scattering and three-phonon scattering as synonyms, although this is not rigorous. As firstly recognized by Peierls [4], we must distinguish between two possible three-phonon processes:

- *Class 1 processes*, where two phonons are annihilated and one phonon is created;
- *Class 2 processes*, where one phonon is annihilated and two phonons are created.

The Feynman diagrams of these two types of three-phonon scattering events are illustrated in fig. 1. The conservation laws of energy and momentum that *Class 1* processes

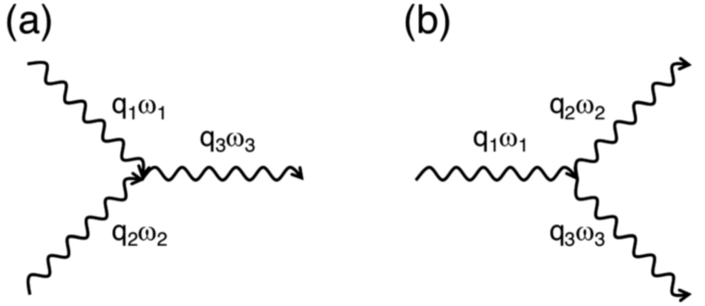

Fig. 1. – Feynman diagrams for (a) *Class 1* and (b) *Class 2* three-phonon scattering.

must fulfill are

$$\omega_1 + \omega_2 = \omega_3, \tag{4}$$

$$\mathbf{q}_1 + \mathbf{q}_2 = \mathbf{q}_3 + \mathbf{G}, \tag{5}$$

while those of *Class 2* are

$$\omega_1 = \omega_2 + \omega_3, \tag{6}$$

$$\mathbf{q}_1 = \mathbf{q}_2 + \mathbf{q}_3 + \mathbf{G}. \tag{7}$$

In these expressions $\mathbf{G}$ is a vector of the reciprocal lattice. Then we have to further distinguish between normal scattering (N-processes), where the momentum of the phonons is conserved ($\mathbf{G} = 0$), and Umklapp scattering (U-processes), where part of the momentum is transferred to the crystal lattice ($\mathbf{G} \neq 0$). Making this difference is crucial when it comes to calculate the thermal conductivity of a system: U-processes are momentum-destroying processes that lead to the finite value of the thermal conductivity observed experimentally when the heat transport regime is diffusive; N-processes, on the other hand, are non resistive processes that redistribute, but conserve momentum among the phonons that scatter each other. U-processes tend to return the phonon system to an equilibrium distribution, whereas N-processes lead to a displaced non-equilibrium distribution. The sketch in fig. 2 helps understanding pictorially the different nature of N- and U-processes, taking a *Class 1* process where a phonon of momentum and energy $\mathbf{q}_1$, $\hbar\omega_1$ and a phonon of momentum and energy $\mathbf{q}_2$, $\hbar\omega_2$ are annihilated and a third phonon of energy and momentum $\mathbf{q}_3$, $\hbar\omega_3$ is created. If $\mathbf{q}_1 + \mathbf{q}_2$ lies outside the first Brillouin zone, the resulting vector $\mathbf{q}_3$ is backscattered with the help of a reciprocal lattice vector. When a thermal bias is established phonons travel on average against the thermal gradient, from the hot to the cold end of the system. The direction of the scattered phonon $\mathbf{q}_3$ of one of these *Class 1* U-processes is opposite to that of $\mathbf{q}_1$ and $\mathbf{q}_2$, thus these momentum non-conserving collisions produce a resistance to heat flow. (Note that from now on to simplify the notation we will use $\mathbf{q}_i$ to refer to a phonon with momentum $\mathbf{q}_i$ and energy $\hbar\omega_i$.)

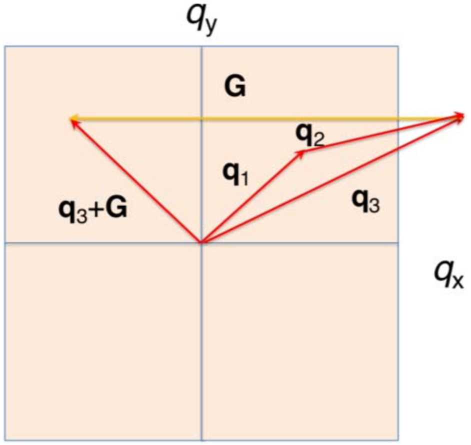

Fig. 2. – Sketch of a three-phonon process $\mathbf{q}_1 + \mathbf{q}_2 = \mathbf{q}_3 + \mathbf{G}$. The shaded square represents the first Brillouin zone. In the case of U-process $\mathbf{q}_3$ falls outside the Brillouin zone and, to bring it inside, it is necessary adding or subtracting a reciprocal lattice vector $\mathbf{G}$. The N-process is the particular case when $\mathbf{G} = 0$ because $\mathbf{q}_1 + \mathbf{q}_2 = \mathbf{q}_3$ falls inside the Brillouin zone.

The perturbation Hamiltonian due to three-phonon scattering is written as

$$H' = \frac{1}{3!} \sum_{\mathbf{q}_1,\mathbf{q}_2,\mathbf{q}_3} \delta_{\mathbf{q}_3+\mathbf{G},\mathbf{q}_1+\mathbf{q}_2} \mathcal{F}_{\mathbf{q}_1,\mathbf{q}_2,\mathbf{q}_3} \left(a^\dagger_{\mathbf{q}_1} - a_{\mathbf{q}_1}\right) \left(a^\dagger_{\mathbf{q}_1} - a_{\mathbf{q}_2}\right) \left(a^\dagger_{\mathbf{q}_1} - a_{\mathbf{q}_3}\right), \tag{8}$$

where $\delta_{\mathbf{q}_3+\mathbf{G},\mathbf{q}_1+\mathbf{q}_2}$ guarantees that only terms satisfying the conservation laws of eq. (5) are included in the sum and the factor $\mathcal{F}_{\mathbf{q}_1,\mathbf{q}_2,\mathbf{q}_3}$ is proportional to the average of the Fourier transformed anharmonic tensor projected over the directions of the polarization vectors. We now have to evaluate the probability of transition from the initial state

$$|i\rangle \equiv |n_{\mathbf{q}_1}, n_{\mathbf{q}_2}, n_{\mathbf{q}_3}\rangle \tag{9}$$

to the final state, which, for *Class 1* processes is

$$|f\rangle \equiv |n_{\mathbf{q}_1} - 1, n_{\mathbf{q}_2} - 1, n_{\mathbf{q}_3} + 1\rangle \tag{10}$$

and for *Class 2* processes is

$$|f\rangle \equiv |n_{\mathbf{q}_1} - 1, n_{\mathbf{q}_2} + 1, n_{\mathbf{q}_3} + 1\rangle\,. \tag{11}$$

We do that by means of Fermi golden rule. In the case of *Class 1* processes we have

$$P^{\mathbf{q}_3}_{\mathbf{q}_1,\mathbf{q}_2} = \frac{2\pi}{\hbar} \left|\langle n_{\mathbf{q}_1} - 1, n_{\mathbf{q}_2} - 1, n_{\mathbf{q}_3} + 1|\, H' \,|n_{\mathbf{q}_1}, n_{\mathbf{q}_2}, n_{\mathbf{q}_3}\rangle\right|^2 \mathcal{O}(\hbar\omega_3 - \hbar\omega_2 - \hbar\omega_1). \tag{12}$$

Substituting eq. (8) and after some algebra we obtain

$$P^{\mathbf{q}_3}_{\mathbf{q}_1,\mathbf{q}_2} = \frac{2\pi}{\hbar} n_{\mathbf{q}_1} n_{\mathbf{q}_2} (n_{\mathbf{q}_2} + 1) |\mathcal{F}_{\mathbf{q}_1,\mathbf{q}_2,\mathbf{q}_3}|^2 \delta_{\mathbf{q}_3+\mathbf{G},\mathbf{q}_1+\mathbf{q}_2} \mathcal{O}(\hbar\omega_3 - \hbar\omega_2 - \hbar\omega_1), \tag{13}$$

where the factors $\mathcal{O}(\hbar\omega_3 - \hbar\omega_2 - \hbar\omega_1)$ and $\delta_{\mathbf{q}_3+\mathbf{G},\mathbf{q}_1+\mathbf{q}_2}$ ensure that the transition probability vanishes for those processes that do obey the conservation laws of energy and momentum.

We can then define an intrinsic transition probability, independent of the phonon distribution, as

$$Q^{\mathbf{q}_3}_{\mathbf{q}_1,\mathbf{q}_2} = \frac{2\pi}{\hbar} |\mathcal{F}_{\mathbf{q}_1,\mathbf{q}_2,\mathbf{q}_3}|^2 \delta_{\mathbf{q}_3+\mathbf{G},\mathbf{q}_1+\mathbf{q}_2} \mathcal{O}(\hbar\omega_3 - \hbar\omega_2 - \hbar\omega_1) \tag{14}$$

which allows obtaining a simplified form of eq. (13)

$$P^{\mathbf{q}_3}_{\mathbf{q}_1,\mathbf{q}_2} = n_{\mathbf{q}_1} n_{\mathbf{q}_2} (n_{\mathbf{q}_2} + 1) Q^{\mathbf{q}_3}_{\mathbf{q}_1,\mathbf{q}_2} \tag{15}$$

and analogously for *Class 2* processes

$$P^{\mathbf{q}_3,\mathbf{q}_2}_{\mathbf{q}_1} = (n_{\mathbf{q}_1} + 1) n_{\mathbf{q}_2} n_{\mathbf{q}_2} Q^{\mathbf{q}_3,\mathbf{q}_2}_{\mathbf{q}_1}. \tag{16}$$

The total probability that mode $\mathbf{q}_1$ suffers a *Class 1* scattering process is obtained by integrating over all the possible $\mathbf{q}_2$ and $\mathbf{q}_3$:

$$P^{\mathbf{q}_1} = \iint P^{\mathbf{q}_3}_{\mathbf{q}_1,\mathbf{q}_2} \mathrm{d}\mathbf{q}_2 \mathrm{d}\mathbf{q}_3 = \iint n_{\mathbf{q}_1} n_{\mathbf{q}_2} (n_{\mathbf{q}_2} + 1) Q^{\mathbf{q}_3}_{\mathbf{q}_1,\mathbf{q}_2} \mathrm{d}\mathbf{q}_2 \mathrm{d}\mathbf{q}_3. \tag{17}$$

The integral of eq. (17) has six degrees of freedom (each of $\mathbf{q}_2$ and $\mathbf{q}_3$ has three), which are reduced to two because of the four constraints imposed by the conservation laws of eqs. (4), (5). Yet, its solution is rather complicated and it is instructive considering some of the limiting cases of low energy phonons addressed in detail by Herring [5]. In this regime, where phonons have long wavelengths and low frequencies, the intrinsic probability for *Class 1* processes is now proportional to the wave numbers of the interacting modes, because in the low frequency limit $\omega(\mathbf{q}) \propto \mathbf{q}$, and the transition probability is

$$P^{\mathbf{q}_3}_{\mathbf{q}_2,\mathbf{q}_1} \propto \mathbf{q}_1 \mathbf{q}_2 \mathbf{q}_3 n_{\mathbf{q}_1} n_{\mathbf{q}_2} (n_{\mathbf{q}_2} + 1). \tag{18}$$

Notice that even if modes $\mathbf{q}_2$ and $\mathbf{q}_3$ are high frequency modes for which the acoustic approximation $\omega(\mathbf{q}) \propto \mathbf{q}$ is not valid, the proportionality of $P^{\mathbf{q}_3}_{\mathbf{q}_2,\mathbf{q}_1}$ with $\mathbf{q}_1 n_{\mathbf{q}_1}$ still holds, provided that the mode is in the acoustic range. *Class 2* processes, on the other hand, can be neglected, because they normally involve the decay of a high frequency mode into two lower frequency modes.

We now consider the relaxation time of mode $\mathbf{q}_1$ and write it as

$$\frac{1}{\tau_{\mathbf{q}_1}} = - \lim_{n_{\mathbf{q}_1} \to n^0_{\mathbf{q}_1}} \frac{(\mathrm{d}n_{\mathbf{q}_1}/\mathrm{d}t)_{scatt}}{n_{\mathbf{q}_1} - n^0_{\mathbf{q}_1}}, \tag{19}$$

where $n^0_{\mathbf{q}_1}$ is the occupation number in equilibrium. This expression, firstly proposed by Klemens, is what later became known as relaxation time approximation (RTA) and consists in assuming that a phonon mode relaxes to equilibrium with its own relaxation time, regardless of what the other phonons do. In other words, if a system is in equilibrium and we selectively excite one single mode, this excitation will decay to equilibrium with the relaxation time of eq. (19). Clearly, this is a situation that can be reproduced in specifically designed experiments, but that does not represent the typical non-equilibrium condition that lead to phonon transport in a material where many phonons modes are dragged out of equilibrium. The rate of change of $n_{\mathbf{q}_1}$ in eq. (19) depends on the phonon-phonon collisions and can be written by summing the transition probabilities:

$$\left(\frac{\mathrm{d}n_{\mathbf{q}_1}}{\mathrm{d}t}\right)_{scatt} = \sum_{\omega_2,\omega_3} \int \left(P^{\mathbf{q}_3}_{\mathbf{q}_2,\mathbf{q}_1} - P^{\mathbf{q}_1,\mathbf{q}_2}_{\mathbf{q}_3}\right) \mathrm{d}\mathbf{q}_2 \mathrm{d}\mathbf{q}_3, \tag{20}$$

where $P^{\mathbf{q}_1,\mathbf{q}_2}_{\mathbf{q}_3}$ is the reverse process. It is worth noting that $P^{\mathbf{q}_1,\mathbf{q}_2}_{\mathbf{q}_3}$ is formally a *Class 2* process, where a phonon is destroyed and two phonons are created. Here, however, we look at this process from the viewpoint of phonon $\mathbf{q}_1$, which is one of the two phonons created. Explicitly, the transition probabilities are integrated over $\mathbf{q}_2$ and $\mathbf{q}_3$ and summed over all the branches ω_2 and ω_3. Herring showed that the integral above, together with eq. (15) and to the analogous relation for the reverse process, leads to the following expression for the relaxation time:

$$\frac{1}{\tau_{\mathbf{q}_1}} \propto \sum_{\omega_2,\omega_3} \int \mathbf{q}_1 \mathbf{q}_2 \mathbf{q}_3 \left(n^0_{\mathbf{q}_2} - n^0_{\mathbf{q}_3}\right) \frac{\partial \Delta\omega}{\partial q_{2\perp}} \mathrm{d}S_2, \tag{21}$$

where $\Delta\omega = \omega(\mathbf{q}_1 + \mathbf{q}_2) - \omega(\mathbf{q}_1) - \omega(\mathbf{q}_2)$ accounts for the departure from energy conservation and $q_{2\perp}$ is the component of $\mathbf{q}_2$ perpendicular to the surface S_2. Even without knowing the exact value of the normal derivative of $\Delta\omega$ or the form of the energy conservation surface S_2, it is now possible to derive two scaling laws for $\tau^{-1}_{\mathbf{q}_1}$ in the low and high temperature regime.

Low temperature. At low temperature the scaling of the inverse of the relaxation time is given by the celebrated Herring's fifth power law [5]

$$\tau^{-1}_{\mathbf{q}_1} \propto \mathbf{q}^a_1 T^{5-a}, \tag{22}$$

which is sometimes written as $\tau^{-1}_{\mathbf{q}_1} \propto \omega^a T^b$, with $a + b = 5$. The exponent a depends on the lattice symmetry and has the form

$$a = -\lim_{q\to 0} \frac{\mathrm{d}\ln \tau(\mathbf{q},T)}{\mathrm{d}\ln \mathbf{q}}\,. \tag{23}$$

Its value has been calculated by Herring for different crystal geometries [5].

High temperature. At high temperature all modes are highly excited and transition probabilities such as the one of eq. (16) depend on the temperature only though a linear term in the n^0 terms. Therefore one obtains

$$\tau_{\mathbf{q}_1}^{-1} \propto T^{-1}. \tag{24}$$

2˙1. *Optical phonons.* – The role of optical modes in anharmonic three-phonon scattering processes has been thus far neglected. The reason is twofold: 1) acoustic phonons have much larger velocities and they alone can often account for the thermal conductivity of a material and for much of the underlying physics; 2) the foundations of the theory of heat transport, because of the mathematical complexity deriving from including optical phonons and because of the importance of acoustic phonons, often relied exclusively on the latter. The prototypical example of this situation is the Debye model, which completely neglects the existence of optical phonons (and gives an approximate description of acoustic phonons). In other contexts, approximations are invoked to simplify complicated mathematical formulations. Above, for instance, we have developed a comprehensive theory of anharmonic scattering that, up to eq. (17), included all phonons modes. Then, however, to make sense of that complicated integral and to gain some physical insight, we considered the limiting case of low energy phonons where the probability of a scattering process was proportional to wave numbers.

The modern theory of heat transport, however, cannot be understood without optical phonons. On the one hand, the scope of research in thermal transport and phononics [6-8] has considerably broadened and many materials whose thermal properties cannot be accounted for without optical phonons are routinely studied; let alone the fact that phononic devices only seldom operate at those low temperatures were the approximation of restricting to acoustic phonons is justified and lead to reasonable results. On the other hand, the powerful machinery of numerical simulations makes it possible to treat all the modes on equal footing and there is no longer any practical reason to exclude optical phonons. Finally, optical phonons are central for many experimental techniques, such as Raman spectroscopy and infrared spectroscopy.

To evaluate the effect of optical phonons on the anharmonic scattering one has to consider that normally optical branches lie higher in energy than acoustic branches and, as a general rule $a + o \rightleftarrows a$ processes (where a is an acoustic mode and o is an optical mode) are forbidden because they cannot conserve the energy. Similarly, as optical modes occupy a rather narrow frequency band, $o + o \rightleftarrows o$ processes too cannot conserve the energy and three-phonon scattering event that involve optical phonons must include at least one acoustic phonon. However, for optical modes that have not too high frequencies, processes of the kind of $a + a \rightleftarrows o$ are permitted and can contribute to the destruction of heat carrying acoustic modes.

Therefore, while it is true that due to their low group velocities optical phonons usually do not carry much heat, they can impact indirectly the thermal conductivity by expanding the phase space of possible three-phonon processes that involve acoustic phonons, beyond $a + a \rightleftarrows a$ processes.

These considerations can be exploited to design materials with a tailor-made thermal conductivity, which is in the end the ultimate goal of phononics. Jain and McGaughey [9], for instance, showed how the mass ratio in binary compound semiconductors determined the feasibility of certain three-phonon processes that involve optical phonons and that, in turn, affects the thermal conductivity. The main control parameters are i) the *a*-*o* gap, which is the difference between the maximum acoustic frequency and the minimum optical frequency, ii) the acoustic (optical) width, which is the difference between the maximum and minimum acoustic (optical) frequencies, and iii) the acoustic *bunching*, defined as the maximum difference between the maximum frequencies of the three acoustic phonon polarizations. In particular they showed that the mass difference of the two species affects the thermal conductivity by modifying the *a*-*o* gap, the acoustic-width and their ratio. As the *a*-*o* gap widens, at first fewer $a + a \rightleftarrows o$ processes are permitted. Then, when the *a*-*o* gap becomes greater than the acoustic width these processes cannot satisfy anymore the energy conservation selection rule and become forbidden. When this happens, optical phonons can only scatter through $a + o \rightleftarrows o$ processes, while acoustic phonons can still scatter through $a + a \rightleftarrows a$ and $a + o \rightleftarrows o$ processes. At this point, widening further the *a*-*o* gap has minimal effect on the thermal conductivity, which is then mainly affected by acoustic bunching, acoustic width, and optical width.

Similar arguments have been used to explain the reduction of the thermal conductivity in hexagonal polymorphs of various semiconductors with respect to the cubic polytype [10, 11]. In cubic Si, for instance, $a + a \rightleftarrows o$ scattering and $a + o \rightleftarrows a$ processes involving only transverse acoustic modes are largely suppressed because at most of the $\mathbf{q}$-points the *a*-*o* gap is larger than the acoustic bandwidth and energy cannot be conserved. The situation changes in lonsdaleite Si —a hexagonal polytype of Si— where low and medium-frequency optical modes arising from the reduced symmetry of the unit cell shrink the *a*-*o* gap and dominate the scattering rate.

3. – Impurity scattering

Crystals —according to Cambridge professor Colin Humphreys— *are like people: it is the defects in them which tend to make them interesting* [12]. Certainly defects play an important role in heat transport and in some temperature and frequency range they can give rise to the dominant phonon scattering mechanism. At variance with electrons, phonons are sensitive to a widespread class of defects, namely mass fluctuations of the crystal lattice. Although isotope purification techniques exist, in practice every material features a distribution of different isotopes, which have different masses. *Natural* Si, for instance, is a mixture of three stable isotopes: ^{28}Si (the most abundant, at 92.23%), ^{29}Si

(4.67%), and ^{30}Si (3.1%) and the mass of 28.0855 that one finds when looking it up in a periodic table is nothing else than the weighted average of those three masses. The situation is even more complex in Ge, which has five naturally occurring isotopes, with a much more distributed relative population and no dominating isotope: ^{70}Ge (20.52%), ^{72}Ge (27.45%), ^{73}Ge (7.76%), ^{74}Ge (36.52%), and ^{76}Ge (7.75%). Mass defects have a great importance and, as they occur naturally, they can even, up to some extent, be considered as contributing to the intrinsic thermal conductivity of a material. Due to their ubiquitous nature they are often, though erroneously, considered as the only lattice defects that are relevant to phonon scattering, while this is not of course the case. We can distinguish at least three classes of lattice imperfections:

- Mass defects;
- Intrinsic defects, such as vacancies, interstitials and antisites, and extrinsic defects, where also the chemical identity changes;
- Extended defects: dislocations, stacking faults and grain boundaries.

We now briefly review the pioneering work of Klemens [13] on defect scattering, which, under many aspects, is still a reference work nowadays. The energy of a harmonic crystal is

$$E = \sum_{\mathbf{q}} \hbar\omega_{\mathbf{q}} \left(N + \frac{1}{2} \right). \tag{25}$$

The normal modes are orthogonal and travel unperturbed. Real materials, however, are not harmonic crystals and lattice waves are not true normal modes and can exchange energy. Anharmonicities, as discussed in sect. **2**, are one possible mechanism for such an interaction, but not the only one. Static imperfections of the lattice also scatter phonons elastically, fulfilling the following energy and momentum conservation laws:

$$\omega_1 = \omega_2, \tag{26}$$

$$\mathbf{q}_1 = \mathbf{q}_2 + \mathbf{G}. \tag{27}$$

The situation is schematically depicted in the Feynman diagram of fig. 3, where a phonon $\mathbf{q}_1$ is annihilated and a phonon $\mathbf{q}_2$ is created. Notice that defect-mediated scattering makes two-phonon processes possible, while anharmonic scattering required at least three-phonon processes. In general, a crystal imperfection has a threefold contribution to the perturbation energy. It alters a) the kinetic energy due to a mass difference, b) the potential energy due to a change in the elastic constant of the bonds surrounding the defect, and c) the potential energy due to an elastic strain field. Klemens tackled separately each of these mechanisms [13] and worked out an expression of the matrix elements that in the Fermi golden rule give the probability of converting a phonon $\mathbf{q}_1$ into a phonon $\mathbf{q}_2$, with $\omega_1 = \omega_2$ because of the conservation law of eq. (26).

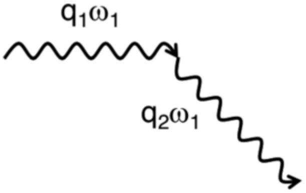

Fig. 3. – Feynman diagram for phonon-impurity interactions. Notice that the frequency of the incoming and scattered phonons is the same, as a result of the conservation law of eq. (26).

In the following, because of their importance, we focus on the case of mass defects. A mass defect is a substitutional impurity atom with mass $M + \Delta M$, which is otherwise identical to the rest of the atoms of the lattice that have mass M. Because of their importance and of the conceptually simpler formalism, much of the theory of defect scattering has been developed for this kind of static imperfections. Mass defects deserve a special place in the review of scattering centers that we are conducting and their importance can hardly be overestimated. Although isotopically purified materials can be obtained by different isotope separation techniques, materials naturally feature a distribution of various isotopes such that the phonon relaxation time of this scattering process contributes to the intrinsic thermal conductivity, just like anharmonic scattering. The study of mass fluctuations on phonon scattering was first tackled by Klemens [13]. That theory was later generalized by Tamura [14], who came up with expressions for the relaxation time, which represent the state-of-the-art of our current understanding of isotope scattering. The Hamiltonian of a system consisting of atoms arranged in a perfect crystal lattice, where the only defects are substitutional isotopic atoms, has the form

$$H = \frac{1}{2}\sum_{\alpha l \sigma} m(l\sigma)\dot{u}_\alpha^2(l\sigma) + V_2, \tag{28}$$

where the index l specifies the position of a unit cell and σ the atom inside the unit cell; α runs over the three Cartesian directions. V_2 is the harmonic potential which is quadratic in the lattice displacement vector u. If the mass fluctuations introduced by the presence of different isotopes are considered as a perturbation, we can write the Hamiltonian as

$$H = H_0 + H_I \tag{29}$$

the sum of H_0, the unperturbed Hamiltonian of the perfect crystal

$$H_0 = \frac{1}{2}\sum_{\alpha l \sigma} \bar{m}(\sigma)\dot{u}_\alpha^2(l\sigma) + V_2 \tag{30}$$

and H_I, which accounts for the presence of the mass defects

$$H_I = \frac{1}{2}\sum_{\alpha l \sigma}[m(l\sigma) - \bar{m}(\sigma)]\dot{u}_\alpha^2(l\sigma) = \frac{1}{2}\sum_{\alpha l \sigma}\Delta m(l\sigma)\dot{u}_\alpha^2(l\sigma). \tag{31}$$

In these equations we have introduced the average mass of σ atoms

$$\bar{m}(\sigma) = \frac{1}{N}\sum_{l} m(l\sigma) = \sum_{\alpha l\sigma} f_i(\sigma) m_i(\sigma). \tag{32}$$

Notice that we are assuming that interatomic forces do not change as a result of substituting an atom with an isotope of different mass and thus the harmonic potential V_2 only appears in the unperturbed Hamiltonian.

The theory of mass defects that we are reviewing here was initially developed for the case of Ge where, because of the large isotopic variability mentioned above, the most interesting experimental results were obtained. Making thus use of the cubic symmetry of the Ge lattice and assuming that isotopes are distributed randomly on the host lattice sites, after some algebra, whose details can be found in ref. [14], one arrives at the following expression for the relaxation time:

$$\tau^{-1} = \frac{\pi}{6} V_0 \gamma \omega^2 D(\omega), \tag{33}$$

where

$$\gamma = \sum_{l} f_i(\sigma)\left(1 - \frac{m_i(\sigma)}{\bar{m}(\sigma)}\right)^2 \tag{34}$$

and $D(\omega)$ is the phonon density of states.

Notice that if we use the Debye density of states in eq. (33) we recover the formulation given previously by Klemens [13]:

$$\tau^{-1} = \frac{1}{4\pi v^3} V_0 \gamma \omega^4, \tag{35}$$

where the scattering of mass defects is described as a Rayleigh scattering, the process that in optics describes the scattering originated by particles much smaller than the wavelength of the radiation and that it is notoriously responsible of the blue color of the sky.

In the low frequency regime the density of states can indeed be satisfactorily described within the Debye approximation and thus the relaxation time has a ω^{-4} dependence. On the other hand, at high frequency the dispersion relation flattens as the wave vector approaches the zone boundary —a feature not captured by the Debye approximation— and the density of states increases more rapidly than ω^2, which results in a stronger frequency dependence of the relaxation time, which is shortened much faster than ω^{-4}. The formalism of Tamura that we have here reviewed represents the most exhaustive description of our current understanding of mass defect scattering. However, the simplified model of Klemens is still a very good approximation, because in the low temperature range where defect scattering plays an important role with respect to the other scattering mechanisms, high frequency modes are not populated and the errors associated to assuming a Debye density of states up to the zone boundary are small.

4. – Boundary scattering

When a phonon hits the surface of a material it is scattered. This process is known as boundary scattering and its lifetime depends on the size and dimensionality of the material and on the atomic scale nature of the surface. Samples are finite and thus there is always a boundary to scatter phonons, but of course in low-dimensional materials, such as nanowires or nanoscale membranes, which are important in many phononic applications, it plays a central role in determining the thermal conductivity. Whenever the mean free path associated to anharmonic scattering is shorter than the characteristic size of the material, boundary scattering becomes the dominant scattering mechanism. Simply put, it is more likely that a phonon hits the surface of the sample rather than it is scattered by other phonons. This happens at low temperature, where anharmonic scattering is less efficient, and in low-dimensional, nanoscale materials, where surface-to-volume ratios are higher and the probability of being scattered by a boundary is enhanced. Accordingly, below a certain temperature the dominant scattering process is related to the boundaries and this temperature increases as the characteristic size of the sample shrinks down. This heat transport regime, where the thermal conductivity is entirely determined by fully diffuse boundary scattering is known as the *Casimir limit*. A beautiful example of this behavior is the dependence of the thermal conductivity on the temperature of thin Si nanowires [15] of different diameters experimentally measured by Li *et al.* [16]. These results show that not only the thinner are the wires, the larger the temperature range where boundary scattering determines the thermal conductivity, but also that the functional dependence of $\kappa(T)$ changes. In bulk, millimetric samples the thermal conductivity has a T^3 dependence, which is roughly followed by the thicker nanowires. However, as the diameter decreases the slope of the $\kappa(T)$ curve is smoothed and it becomes linear with the temperature for the thinner nanowires. The importance of boundary scattering was recognized in the early work of Casimir [17], who showed that it is possible to account for it with the following remarkably simple expression for the associated relaxation time

$$\tau_B^{-1} = \frac{v}{L_{eff}}\,, \tag{36}$$

where L_{eff} is an effective dimension of the sample and v, although taken to be constant and equal to the sound velocity of the material in the original paper by Casimir, is the (frequency dependent) phonon group velocity. L_{eff} accounts for the size and dimensionality and has been calculated to be

$$L_{eff} = 1.12\sqrt{A} \tag{37}$$

for a sample with square cross-section A,

$$L_{eff} = D \tag{38}$$

for a nanowire of diameter D, and

$$L_{eff} = 2.25h \tag{39}$$

for a thin film of thickness h.

The atomic structure of the surface where boundary scattering takes place has a great importance. Clearly, it is not the same to be scattered by a perfectly flat surface or by a rough one. This fact is usually accounted for by correcting the effective length with a specularity factor $0 < p < 1$, which takes the value 0 for maximally rough surface that results in a fully diffusive scattering and the value 1 for specular scattering. A comprehensive theory of phonon scattering by a randomly rough surface is still lacking and the specularity factor is often a phenomenological quantity that qualitatively describes the surface polish and in numerical modeling is typically taken as an adjustable parameter. An expression for p can be derived in some limiting case. If the correlation length of the surface roughness, $\mathcal{L}$, is much larger than the phonon wavelength, $\mathbf{q}\mathcal{L} \gg 1$, the specularity reduction amounts to $4\eta^2\mathbf{q}^2$, where η is the rms of the surface roughness and $\mathbf{q}$ is the phonon wave vector, in agreement with the Kirchoff approximation [2,18,19]. In the opposite limiting case of deeply subwavelength scatterers, $\mathbf{q}\mathcal{L} \ll 1$, on the other hand, the probability of diffuse scattering scales as $\mathbf{q}^4$, similarly to Rayleigh scattering, and the specularity reduction is proportional to $\eta^2\mathbf{q}^4\mathcal{L}$. In a recent paper Maznev has gone beyond these limiting cases and discussed the dependence of the specularity factor on whether the medium is solid or liquid, and in the former case on whether the incident wave is longitudinal or transverse [20].

5. – Thermal transport beyond Fourier

It is well known that the diffusive thermal transport described by Fourier reproduces in general the steady-state experimental data in bulk samples [21] and alloys [22], where the mean free path (MFP) is significantly shorter than the characteristic length of the sample.

The advances in technology and development of new experimental techniques to both prepare and measure experimental samples have highlighted that Fourier's law is not always valid to describe the thermal transport [23-29]. This can happen when the samples or devices are very small (sub micrometer scales) or when the operation conditions vary quickly ($\sim$ THz). In these situations different transport regimes can emerge, like ballistic, hydrodynamic, superdiffusive transport, or a combination of all of them (see the sketch in fig. 4).

The phonon ballistic transport appears when the intrinsic phonon MFP is larger than the sample size. Here the phonons travel through the sample without suffering any scattering event. In such circumstances the measured thermal conductivity is smaller than the bulk one due to the fact that the MFP $\Lambda_{\mathbf{q}}$ has been reduced due to the finite size, in contrast of what would be expected from electronic ballistic transport theory. As $\boldsymbol{\kappa}_{\mathbf{q}} \propto \Lambda_{\mathbf{q}}$, the smaller the $\Lambda_{\mathbf{q}}$ the smaller the $\boldsymbol{\kappa}_{\mathbf{q}}$.

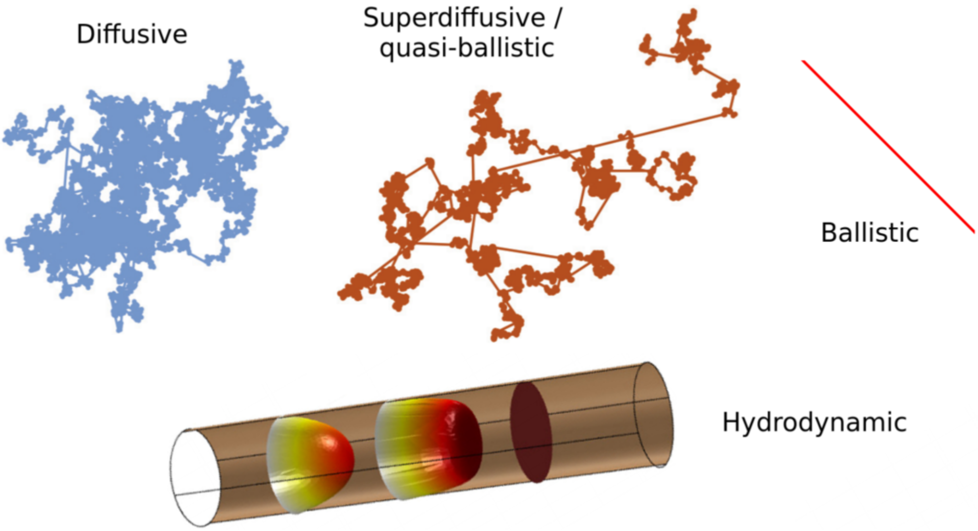

Fig. 4. – Sketch of diffusive (Brownian motion), superdiffusive (Lévy flight), ballistic and hydrodynamic transport [30, 31].

From first principles calculations, we know that the phonon spectra spans a large range of time and space scales, and therefore the distinctions from diffusive, ballistic or other transport regimes need to be treated carefully, as all of them can coexist in the same sample. For instance, in samples with complex geometries hydrodynamic effects can be observed close to the edges while in homogeneous parts the transport remains diffusive.

In order to understand the thermal transport beyond Fourier, conservation laws and thermodynamic constraints should be revised, modifying then the relaxation processes of individual phonons. Doing so, memory and non-local effects will appear naturally in the transport equations, as it has been shown in recent works through the Truncated Lévy Flights (TLF) model [32] based on superdiffusivity or in the Extended Irreversible Thermodynamics (EIT) [33] and the Kinetic Collective Model (KCM) [21], whose framework is phonon hydrodynamics. In addition, analogously to electronic transport, Landauer equation can be used to describe pure ballistic thermal conductance [34].

5˙1. *Memory and non-local effects.* – Spatial and temporal memory effects appear when thermal transport is evaluated at times or sizes of the order of the mean free time (MFT) or MFP of the heat carriers. In such situations the heat flux in one point at a certain time depends on the heat flux of its surroundings and at earlier times. These are the so-called memory and non-local effects.

As we have seen in sect. **1**, in Fourier diffusive transport the heat transport and the thermal energy are related by

$$\mathbf{Q}(\mathbf{r},t) = -\boldsymbol{\kappa}\nabla T, \tag{40}$$

where $\mathbf{Q}$ is the heat flux, $\boldsymbol{\kappa}$ the thermal conductivity and ∇T the temperature gradient.

In situations where memory and non-local effects appear, eq. (40) is no longer valid. From the EIT [33], by including more orders of the momentum conservation, a more general transport equation taking into account these effects can be obtained:

$$\dot{e} = -\nabla \mathbf{Q}^{(1)}, \tag{41}$$

$$\tau \dot{\mathbf{Q}}^{(1)} + \mathbf{Q}^{(1)} = -\kappa \boldsymbol{\nabla} T + \nabla \cdot \mathbf{Q}^{(2)}, \tag{42}$$

$$\tau_{(2)} \dot{\mathbf{Q}}^{(2)} + \mathbf{Q}^{(2)} = -\ell^2_{(2)} \nabla \mathbf{Q}^{(1)} + \nabla \cdot \mathbf{Q}^{(3)}, \tag{43}$$

$$\tau_{(3)} \dot{\mathbf{Q}}^{(3)} + \mathbf{Q}^{(3)} = -\ell^2_{(3)} \nabla \mathbf{Q}^{(2)}, \tag{44}$$

where e is the internal energy, $\mathbf{Q}^{(1)} = \mathbf{Q}$ is heat flux, $\mathbf{Q}^{(2)}$ the flux of the heat flux, and $\mathbf{Q}^{(3)}$ represents a higher-order flux. The parameters $\ell_{(i)}$ and $\tau_{(i)}$ correspond to different order characteristic lengths and relaxation times. These set of equations represent the evolution of the heat transport at different moment orders, and define a full framework to deal with thermal transport in presence of memory and non-local effects [35, 33, 36].

With a little algebra, combining the second moment equation, eq. (42), with the first moment equation, eq. (43), we obtain

$$\tau \dot{\mathbf{Q}}^{(1)} + \mathbf{Q}^{(1)} = -\kappa \boldsymbol{\nabla} T + \ell^2_{(2)} \left(\nabla^2 \mathbf{Q}^{(1)} + 2 \boldsymbol{\nabla} \nabla \cdot \mathbf{Q}^{(1)} \right), \tag{45}$$

where we have considered $\dot{\mathbf{Q}}^{(2)} = 0$ and $\mathbf{Q}^{(3)} = 0$ as a first-order approximation. Equation (45) is a general hydrodynamic heat flux equation that includes memory (time derivative term) and non-local effects (Laplacian term).

In the second half of the last century, Guyer and Krumhansl [37, 38] solved the Boltzmann Transport Equation (BTE) in a suitable basis in the normal (N) process collision vector space for each moment representation of the distribution function. This formalism allows to obtain expressions for energy and momentum conservation. Those equations can be evaluated in the limits where resistive (R) or N scattering processes dominate. The first limit is the so-called kinetic limit, and the latter the collective one. This formalism was forgotten for several years until at the beginning of this century De Tomás *et al.* recovered it [21, 39, 40] to express their equations in a simpler formalism, and more recently dealing with first principles calculations [41, 42], in the so-called Kinetic Collective Model (KCM), named like that after the two limits defined by Guyer and Krumhansl. According to their expressions, in the kinetic limit when R processes dominate ($R \gg N$) Fourier's law for heat transport is recovered. On the contrary, in the collective limit when N processes dominate ($N \gg R$) a more complex equation is obtained:

$$\tau_C \frac{\mathrm{d}\mathbf{Q}}{\mathrm{d}t} + \mathbf{Q} = -\hat{\kappa}_C \boldsymbol{\nabla} T + \ell^2_C (\nabla^2 + 2 \boldsymbol{\nabla} \nabla \cdot) \mathbf{Q}, \tag{46}$$

where τ_C is the phonon relaxation time, κ the thermal conductivity and ℓ a non-local spatial scale defined as $\ell^2_C = \langle c^2 \tau_N \rangle \langle \tau_C \rangle$ in the isotropic case. This defines a hydrodynamic heat flux equation in the collective regime. Indeed, in more recent works it has been demonstrated that considering higher orders in the kinetic regime for the momentum conservation an equivalent expression to eq. (46) is obtained, just replacing the subindex $_C \Longleftrightarrow {}_K$. For more details about how all the terms are calculated the interested reader is referred to refs. [41, 43, 44].

This hydrodynamic equation in the kinetic regime can be obtained as well through gray medium models. In this case the crystal is idealized by a single-phonon relaxation time and MFP. Vermeersch *et al.* demonstrated that by a simple 1D analysis of a two-phonon channel of the BTE, a heat transport solution including memory and non-local effects can be obtained. Their analysis consists in studying the response of a single pulse $P(\xi, s)$ in the Fourier-Laplace domain of $P(x, t)$, considering that the low frequency channel (1) governs the thermal transport, and the other, corresponding to high frequency, governs the heat capacity:

$$P(\xi, s) \simeq \left[s + \frac{D_0 \xi^2}{1 + \xi^2 \Lambda_{(1)}^2} \right]^{-1}, \tag{47}$$

where $\Lambda_{(1)}$ corresponds to the MFP of the low frequency phonon, and D_0 is the thermal diffusivity. By doing the inverse Fourier transform of the pulse and using the energy conservation relation

$$\partial Q(x, t) \partial x + \partial P(x, t) \partial t = \delta(x) \delta(t) \tag{48}$$

together with the initial conditions, the temporal and spatial evolution of this pulse can be expressed as

$$\frac{\partial Q(x, t)}{\partial t} + Q(x, t) - \Lambda_{(1)}^2 \frac{\partial^2 Q(x, t)}{\partial x^2} = -\kappa_0 \frac{\partial \Delta T(x, t)}{\partial x}, \quad \text{for } t \gg \tau. \tag{49}$$

One can observe that three different derivations lead to the same type of hydrodynamic heat equation, eqs. (45), (46), (49), which is a strong indication of the presence of this phenomena in actual heat transport.

6. – Phonon hydrodynamics

A generalization of the Fourier's law including memory and non-local effects has been obtained from both thermodynamic and BTE frameworks [37, 38, 33, 43]. Using the previous heat transport equations, considering steady state $\dot{\mathbf{Q}} = 0$, strong geometric effects (spatial variations of $\mathbf{Q}$ are higher than $\mathbf{Q}$ itself) $\mathbf{Q} \ll \ell^2 \nabla^2 \mathbf{Q}$, and neglecting the term $2\boldsymbol{\nabla}\nabla \cdot \mathbf{Q}^{(1)}$, eq. (45) reduces to

$$\nabla^2 \mathbf{Q} = \kappa_0 / \ell^2 \boldsymbol{\nabla} T. \tag{50}$$

The latter expression is analogous to Navier-Stokes equation of a fluid doing the analogy $\mathbf{Q} \Leftrightarrow \mathbf{v}$, $T \Leftrightarrow p$ and $\eta \Leftrightarrow \ell^2/\kappa_0$, where $\mathbf{v}$ is the velocity, p the pressure and η the shear viscosity. For simplicity $\ell_{(2)} = \ell$. This analogy is the responsible of the emergence of the name *phonon hydrodynamics*.

The hydrodynamic equation can be solved analytically for simple geometries like cylinders, slabs or thin films [36,45,46]. For instance, for a cylindrical geometry, the heat flux in the cross-section can be expressed as

$$Q(r) = \frac{\kappa_0 \Delta T}{4\ell^2 L}(R^2 - r^2), \tag{51}$$

which is equivalent to a Poiseuille-like equation for the heat flow, where non-slip conditions ($\mathbf{v} = 0$, *i.e.* zero tangential flux on the wall) have been considered. This allows defining an effective thermal conductivity as

$$\kappa_{eff} = \frac{\kappa_0 R^2}{8\ell^2} = \frac{\kappa_0}{8\mathrm{Kn}^2}\,, \tag{52}$$

where $\mathrm{Kn} = \ell/R$ is the Knudsen number and R and L are the radius and length of the sample. Equation (52) is derived for a cylindrical geometry in analogy to the flow in a pipe. This expression shows a dependence $\kappa_{eff} \propto R^2$ as a result of imposing non-slip condition at the walls. Thanks to experimental results it has been demonstrated that $\kappa_{eff} \propto R$ for small samples, where $R \ll \ell$. In order to obtain this trend it is enough to include a slip boundary condition, also known as Maxwell boundary condition, like:

$$Q_B = C\ell \left(\frac{\partial Q}{\partial r}\right)_{r=R}, \tag{53}$$

where C is a parameter that might depend on the geometry and the roughness of the sample, and it is related to the reflectivity and the diffusivity of the surface. By solving eq. (51) with slip boundary conditions for cylindrical geometry, the effective thermal conductivity takes the form [47]:

$$\kappa_{eff} = \frac{\kappa_0}{8\mathrm{Kn}^2}\left[1 + 4C\mathrm{Kn}\right], \tag{54}$$

where now we obtain a non-zero flux on the walls in a certain X-Y region, defining a curve heat flux profile, as shown in fig. 5.

Now eq. (54) agrees with the experimental observations. For small samples where $R \ll \ell$, $\mathrm{Kn} \ll 1$, eq. (54) leads to a linear dependence of R on the thermal conductivity. The region where the heat flux can feel the effect of the boundary is the so-called Knudsen layer, which has a penetration of the order of ℓ.

From this derivation we can conclude that hydrodynamic effects will be visible when the boundaries play an important role in heat transport. This will be observed specially in sub-micrometer samples and in any sample with sub-micrometer features, like metallic heaters or holes.

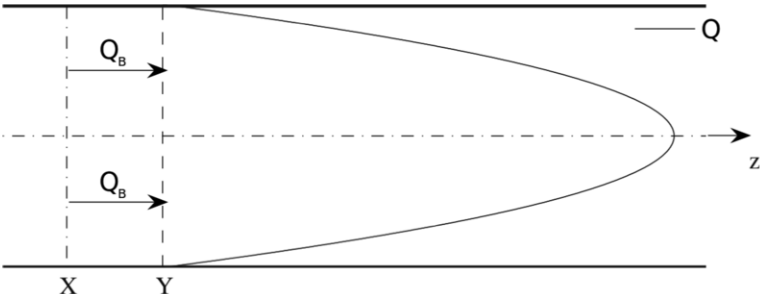

Fig. 5. – Heat flux profile with slip boundary condition [36].

The boundary conditions for simple geometries are rather easy to control, but in more complex geometries are still far to be fully understood. In this sense a combination of first principles calculations and thermodynamics through finite elements modeling can shed new light on the topic [48-50, 43].

7. – Ballistic transport

As a general idea, the opposite limit of the classic diffusive thermal transport, is the ballistic transport. In this case it is assumed that phonons can move inside the material without suffering any scattering process. In order to evaluate how this phonons contribute to the thermal conductance one can refer to the Landauer framework for which, in analogy to electrons, the total thermal conductance can be expressed as [51]:

$$C = \left(\frac{k_b^2 T \pi^2}{3h}\right) \int W_{ph} \mathrm{d}(\hbar\omega), \tag{55}$$

where $k_b^2 T\pi^2/3h$ defines the quantum of conductance. W_{ph} is the window function defined as

$$W_{ph} = \frac{3}{\pi^2}\left(\frac{\hbar\omega}{k_b T}\right)^2 \left(-\frac{\partial n_0}{\partial(\hbar\omega)}\right), \tag{56}$$

where, in the case of phonons, n_0 is the Bose-Einstein distribution function. The terms can be rearranged and the thermal conductance can be expressed as

$$C = \frac{1}{2\pi k_b T^2} \int (\hbar\omega)^2 \frac{e^x}{e^x - 1} \mathrm{d}\omega, \tag{57}$$

where $x = \hbar\omega/k_b T$.

In the framework of the BTE the contribution to thermal conductivity of each ballistic phonon will be limited for the sample size. Therefore a phonon that in an ideal infinite sample has a contribution $\boldsymbol{\kappa}_{\mathbf{q}}(\Lambda_{\mathbf{q}}) = C_{v,\mathbf{q}}\Lambda_{\mathbf{q}} v_{\mathbf{q}}$, for a real finite sample of size L the

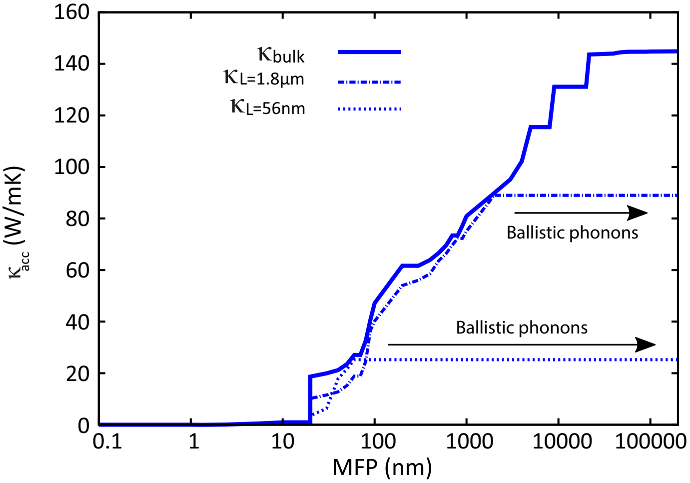

Fig. 6. – Accumulated thermal conductivity as a function of mean free path (MFP) for silicon samples with different size L [44].

contribution will be $\boldsymbol{\kappa}_{\mathbf{q}}(L) = C_{v,\mathbf{q}} L v_{\mathbf{q}}$. As by definition in ballistic transport $L < \Lambda_{\mathbf{q}}$, the thermal conductivity will be smaller ($\boldsymbol{\kappa}_{\mathbf{q}}(L) < \boldsymbol{\kappa}_{\mathbf{q}}(\Lambda_{\mathbf{q}})$).

In fig. 6 the accumulated thermal conductivity for bulk silicon ($L = \infty$), $L = 830\,\text{nm}$ and $L = 56\,\text{nm}$ is represented. It can be observed that the phonons with a MFP larger than L travel ballistically through the sample and do not contribute to thermal conductivity beyond the sample size L. In the case of bulk samples, the maximum value of MFP is limited by the intrinsic phonon MFP.

8. – Superdiffusive transport

As we know from recent first principles calculations, the phonon MFP and MFT can span several orders of magnitude [52, 53, 41, 22], and therefore we can find systems where some phonons can be ballistic and other diffusive, or even in a transition regime between them. This transient regime is known as superdiffusive or quasi-ballistic regime. New experimental techniques using alternate current sources with a modulated frequency are able to excite different energy phonons at different time scales and then phonons with certain MFT can be studied [30, 54]. The starting point to study such phenomena is usually the Maxwell-Cattaneo equation:

$$\tau \frac{\partial^2 T}{\partial t^2} + \frac{\partial T}{\partial t} = \chi \nabla^2 T, \tag{58}$$

which gives temperature T in terms of time t, where τ is the MFT of phonons and χ is the thermal diffusivity of the sample. This expression provides more insight on the ballistic to diffusive transition. In the diffusive regime $\tau \frac{\partial^2 T}{\partial t^2} \ll \frac{\partial T}{\partial t}$ and the diffusion

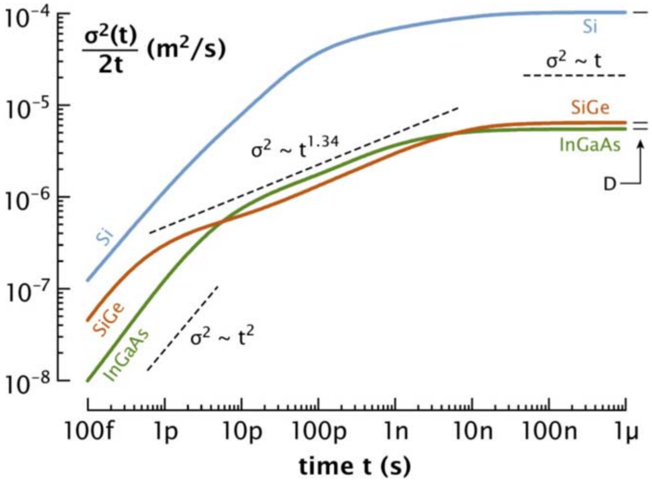

Fig. 7. – Renormalized MSD obtained from the BTE for Si, SiGe and InGaAs [32].

equation is recovered. When the inertial terms are important, $\tau \frac{\partial^2 T}{\partial t^2} \gg \frac{\partial T}{\partial t}$ and the wave equation is obtained.

In the simple picture described by the Maxwell-Cattaneo equation the transition from diffusive to ballistic transport occurs at the same time for all the phonons. Now we know that this is not true, as each phonon has its own MFP and MFT [52, 53, 41, 22], and therefore ideally it would be necessary to solve eq. (58) for each phonon mode in order to reproduce the real effects. As this procedure would generate an extremely large number of equations the TLF model has been proposed as a framework to deal with this diffusive to ballistic transition.

8˙1. *The truncated Lévy flight (TLF) model.* – In the TLF framework the effect of the different phonon time scales is captured by quantifying the deviation from the diffusive behavior at short time scales using fractal exponents, which are calculated from the scaling law of the accumulated thermal conductivity in terms of MFP [32]. The key point of this model is to take into account that energy carriers are not independent, but are related by the energy conservation. The 1D transport equation for a single pulse with thermal energy density $P(x,t)$ with fractional exponents is expressed as

$$\frac{\partial^\beta P(x,t)}{\partial t^\beta} = D_{\alpha\beta} \frac{\partial^\alpha P(x,t)}{\partial |x|^\alpha}\,, \tag{59}$$

where α and β are the fractal space and time dimensions of the superdiffusion transport regime, respectively. In a pure diffusive regime $P_0(x,t) = C_{v,0}T$, being $C_{v,0}$ the specific heat and T the temperature.

Figure 7 represents the temporal evolution of the heat transport through the normalized mean-square displacement (MSD) of the thermal energy with time [55]. A superdiffusive regime governed by a fractal exponent can be appreciated in the time space between 1 ps and 10 ns for SiGe and between 10 ps and 1 ns for InGaAs. It can be appreciated that there is a transition from a ballistic regime at very small times ($t < 10^{-12}$ s), where $\sigma^2 \sim t^2$, to a diffusive regime $\sigma^2 \sim t$ for $t > 10^{-8}$ s. In InGaAs and SiGe, this transition can be expressed by $\sigma^2 \sim t^\beta$, while in Si there is a smooth transition without any clear exponent. A full discussion of the relation of the fractal exponents to the dominant scattering mechanism can be found in ref. [22]. From this, it can be concluded that in the diffusive limit $\alpha \to 2$ and $\beta \to 1$, in the ballistic limit $\alpha \to 1$ and $\beta \to 2$, while in the superdiffusive transition the exponents will be fractal.

By using the TLF model it is possible to characterize the diffusive, ballistic and the quasi-ballistic regime, but geometry (non-local) effects from phonon hydrodynamics are neglected. A model including all these transport regimes will be necessary in order to fully understand the heat transport to further improve in the development of electronic and thermal devices.

9. – Conclusions

In this paper we have provided a general introduction to phonon transport in crystalline solids, focusing on the most important scattering processed and discussing the different transport regimes. Understanding how phonons propagate is essential to allow controlling and manipulating them and have important implications in renewable energy applications —such as vibrational energy harvesting [56] and thermoelectricity [57]— and for the implementation of a phonon-based logic, where information is transmitted and processed by heat carriers [6-8].

* * *

We acknowledge financial support by the Ministerio de Economía, Industria y Competitividad (MINECO) under grant FEDER-MAT2017-90024-P and the Severo Ochoa Centres of Excellence Program under Grant SEV-2015-0496 and by the Generalitat de Catalunya under Grant no. 2017 SGR 1506.

REFERENCES

[1] Fourier J., *The Analytical Theory of Heat* (Dover Publication, New York) 1955.

[2] Ziman J. M., *Electrons and Phonons* (Clarendon Press, Oxford) 1960.

[3] Srivastava G. P., *The Physics of Phonons* (Adam Hilger, Bristol, now Taylor and Francis Group) 1990.

[4] Peierls R., *Ann. Phys.*, **395** (1929) 1055.

[5] Herring C., *Phys. Rev.*, **95** (1954) 954.

[6] Li N., Ren J., Wang L., Zhang G., Hänggi P. and Li B., *Rev. Mod. Phys.*, **84** (2012) 1045.

[7] Volz S., Ordonez-Miranda J., Shchepetov A., Prunnila M., Ahopelto J. Pezeril Th., Vaudel G., Gusev V., Ruello P., Weig E. M., Schubert M., Hettich M., Grossman M., Dekorsy Th., Alzina F., Graczykowski B., Chavez-Angel E., Reparaz J. S., Wagner M. R., Sotomayor-Torres C. M., Xiong S., Neogi S. and Donadio D., *Eur. Phys. J. B*, **89** (2016) 15.

[8] Zardo I. and Rurali R., *Curr. Opin. Green Sustain. Chem.*, **17** (2019) 1.

[9] Jain A. and McGaughey A. J. H., *J. Appl. Phys.*, **116** (2014) 073503.

[10] Raya-Moreno M., Aramberri H., Seijas-Bellido J. A. Cartoixà X., and Rurali R., *Appl. Phys. Lett.*, **111** (2017) 032107.

[11] Raya-Moreno M., Rurali R., and Cartoixà X., *Phys. Rev. Mater.*, **3** (2019) 084607.

[12] Humphreys C. J., *Stem Imaging of Crystals and Defects*, edited by Hren J. J., Goldstein J. I. and Joy D. C. in *Introduction to Analytical Electron Microscopy* (Springer, Boston, MA) 1979.

[13] Klemens P. G., *Proc. Phys. Soc. A*, **68** (1955) 1113.

[14] Tamura S., *Phys. Rev. B*, **27** (1983) 858.

[15] Rurali R., *Rev. Mod. Phys.*, **82** (2010) 427.

[16] Li D., Wu Y., Kim P., Shi L., Yang P. and Majumdar A., *Appl. Phys. Lett.*, **83** (2003) 2934.

[17] Casimir H. B. G., *Physica*, **5** (1938) 495.

[18] Soffer S. B., *J. Appl. Phys.*, **38** (1967) 1710.

[19] Rice S. O., *Commun. Pure Appl. Math.*, **4** (1951) 351.

[20] Maznev A. A., *Phys. Rev. B*, **91** (2015) 134306.

[21] De Tomas C., Cantarero A., Lopeandia A. F. and Alvarez F. X., *Proc. R. Soc. A*, **470** (2014) 20140371.

[22] Torres P., Mohammed A., Torello A., Bafaluy J., Camacho J., Cartoixà X., Shakouri A. and Alvarez F. X., *Phys. Chem. Chem. Phys.*, **20** (2018) 6805.

[23] Johnson J. A., Maznev A. A., Cuffe J., Eliason J. K., Minnich A. J., Kehoe T., Sotomayor Torres C. M., Chen G. and Nelson K. A., *Phys. Rev. Lett.*, **110** (2013) 025901.

[24] Siemens M. E., Li Q., Yang R., Nelson, K. A., Anderson E. H., Murnane M. M. and Kapteyn H. C., *Nat. Mater.*, **9** (2010) 26.

[25] Minnich A. J., Johnson J. A., Schmidt A. J., Esfarjani K., Dresselhaus M. S., Nelson K. A. and Chen G., *Phys. Rev. Lett.*, **107** (2011) 095901.

[26] Regner K. T., Sellan D. P., Su Z., Amon C. H., McGaughey A. J. H. and Malen J., *Nat. Commun.*, **4** (2013) 1640.

[27] Wilson R. B. and Cahill D. G., *Nat. Commun.*, **5** (2014) 5075.

[28] Hu Y., Zeng L., Minnich A. J., Dresselhaus M. S. and Chen G., *Nat. Nanotechnol.*, **10** (2015) 701.

[29] Hoogeboom-Pot K. M., Hernandez-Charpak J. N., Gu X., Frazer T. D., Anderson E. H., Chao W., Falcone R. W., Yang R., Murnane M. M., Kapteyn H. C. and Nardi D., *Proc. Natl. Acad. Sci. U.S.A.*, **112** (2015) 4846.

[30] Vermeersch B., Mohammed A. M. S., Pernot G., Koh Y. R. and Shakouri A., *Phys. Rev. B*, **91** (2015) 085203.

[31] Melis C., Rurali R., Cartoixà X. and Alvarez F. X., *Phys. Rev. Appl.*, **11** (2019) 054059.

[32] Vermeersch B., Carrete J., Mingo N. and Shakouri A., *Phys. Rev. B*, **91** (2015) 085202.

[33] Jou D., Casas J. and Lebon G., *Extended Irreversible Thermodynamics* (Springer, Fourth Edition, Berlin) 2010.

[34] Saito K., Nakamura J. and Natori A., *Phys. Rev. B*, **76** (2007) 115409.

[35] Jou D., Lebon G. and Criado-Sancho M., *Phys. Rev. E*, **82** (2010) 031128.

[36] Sellitto A., Alvarez F. X. and Jou D., *J. Appl. Phys.*, **107** (2010) 064302.

[37] Guyer R. A. and Krumhansl J. A., *Phys. Rev.*, **148** (1966) 766.

[38] Guyer R. A. and Krumhansl J. A., *Phys. Rev.*, **148** (1966) 778.

[39] De Tomas C., Cantarero A., Lopeandia A. F. and Alvarez F. X., *J. Appl. Phys.*, **115** (2014) 164314.

[40] De Tomas C., Cantarero A., Lopeandia A. F. and Alvarez F. X., *J. Appl. Phys.*, **118** (2014) 134305.

[41] Torres P., Torello A., Bafaluy J., Camacho J., Cartoixà X. and Alvarez F. X., *Phys. Rev. B*, **95** (2016) 165407.

[42] Torres P., *Kinetic Collective Model: BTE-based hydrodynamic model for thermal transport*, `https://physta.github.io/`.

[43] Torres P., Ziabari A., Torello A., Bafaluy J., Camacho J., Cartoixà X., Shakouri A. and Alvarez F. X., *Phys. Rev. Mater.*, **2** (2018) 076001.

[44] Torres P., *Thermal Transport in Semiconductors: First Principles and Phonon Hydrodynamic* (Springer Nature, Switzerland) 2018.

[45] Calvo M., Hennessy M., Torres P., Myers T. and Alvarez F. X., *Int. Commun. Heat Mass Transfer*, **91** (2018) 57.

[46] Calvo M., Hennessy M., Torres P., Myers T. and Alvarez F. X., *Int. J. Heat Mass Transfer*, **126** (2018) 1120.

[47] Alvarez F. X., Jou D. and Sellitto A., *J. Appl. Phys.*, **105** (2009) 014317.

[48] Cepellotti A. and Marzari N., *Nano Lett.*, **17** (2017) 4675.

[49] Lee S., Broido D., Esfarjani K. and Chen G., *Nat. Commun.*, **6** (2015) 6290.

[50] Beardo A., Calvo M., Camacho J., Myers T., Torres P., Sendra L., Alvarez F. X. and Bafaluy J., *Phys. Rev. Appl.*, **11** (2019) 034003.

[51] Jeong C., Datta S. and Lundstrom M., *J. Appl. Phys.*, **111** (2012) 093708.

[52] Esfarjani K., Chen G. and Stokes H. T., *Phys. Rev. B*, **84** (2011) 085204.

[53] Zhang H., Hua C., Ding D. and Minnich A. J., *Sci. Rep.*, **5** (2015) 9121.

[54] Ziabari A., Torres P., Vermeersch B., Cartoixà X., Torello A., Xuan Y., Bahk J.-H., Koh Y., Ye P., Alvarez F. X. and Shakouri A., *Nat. Commun.*, **9** (2018) 255.

[55] Vermeersch B., Mohammed A. M. S., Pernot G., Koh Y. R. and Shakouri A., *Phys. Rev. B*, **90** (2014) 014306.

[56] Pop E., *Nano Res.*, **3** (2010) 147.

[57] Benenti G., Casati G., Saito K. and Whitney R. S., *Phys. Rep.*, **694** (2017) 1.

Proceedings of the International School of Physics "Enrico Fermi"
Course 207 "Advances in Thermoelectricity: Foundational Issues, Materials and Nanotechnology",
edited by D. Narducci, G. J. Snyder and C. Fanciulli
(IOS, Amsterdam; SIF, Bologna) 2021
DOI 10.3254/ENFI210005

Past and present of metal chalcogenides, oxides, Heusler compounds and Zintl phases as thermoelectrics: A brief summary

Marisol Martin-Gonzalez

Instituto de Micro y Nanotecnología, IMN-CNM, CSIC (CEI UAM+CSIC)
Isaac Newton, 8, E-28760, Tres Cantos, Madrid, Spain

Summary. — The development of high–figure-of-merit (zT) thermoelectric materials has become a need to fight environmental problems such as global warming, climate change and to save scarce non-renewable energy, such as oil. In the XXI century, the improvement in the knowledge of how nanostructuration alters and improves the properties, improvements in the band structure calculations, etc. are helping to obtain materials with much higher zTs. This review tries to give a short overview of the state of the art of metal chalcogenides, oxides, Heusler compounds and Zintl phases.

1. – Metal chalcogenides

These compounds take the name from their composing elements which are one or more chalcogen, that is, S, Se or Te and a metal. They have a less ionic character than the metal oxides and, in particular, those formed with metals of the p-block of the periodic table (Bi, Pb, Sn, etc.) are the most studied semiconductor materials for thermoelectric applications. This is due to the fact that they have electronic properties that can be tuned for different applications at different temperature ranges and, moreover, they have an intrinsically low thermal conductivity [1-4]. We will review the different kinds of metal chalcogenides in detail next.

1˙1. *Bismuth chalcogenides.* – The most relevant member of this family, bismuth telluride (Bi_2Te_3), is one of the best materials for applications around room temperature, and it has been commercialized to this end since the ‘50s [5-7]. It was discovered in 1815 in Norway, with its mineral form: tellurobismuthite [8]. This material, along with its alloys, some of which are p-type, as $Bi_{2-x}Sb_xTe_3$ or n-type, such as $Bi_2Te_{3-x}Se_x$, have been used for thermoelectric applications for years [7,9,10]. All of them have in common a layered structure of different elements, in which some of those layers are kept together due to Van der Waals forces, and this peculiarity gives them their high anisotropy and their good performance for thermoelectricity. One of the main drawbacks of this family of materials is that both tellurium and bismuth are not abundant on Earth, which should be taken into account when designing devices based on them [11].

They can be synthesized in various ways. Given their low melting point, they can be obtained as single crystals via the Bridgman method, although other techniques such as zone melting can be used [7]. In order to obtain polycrystalline samples, dense pellets can be sintered from the powder of the constituent elements, which produce samples with improved mechanical properties [12]. Although the first studies by Goldsmid of Bi_2Te_3 date from 1954 [5], and there followed a quick research on the ternaries as best materials for low-temperature applications, with zT around 1 at RT for both p-type $Bi_{2-x}Sb_xTe_3$ and n-type $Bi_2Te_{3-x}Se_x$ [13-15], there was no significant progress for a long time, until quite recently, when new approaches to obtain nanostructured materials with low thermal conductivity appeared in the field, such as Poudel in 2008 where the phonon scattering was increased thanks to the increased number of grain boundaries and a zT of 1.4 at 373 K was reached [16]. Another interesting approach was the incorporation of grain boundary dislocations proposed by Kim *et al.*, reaching a value of 1.9 in zT at 323 K [17], although this value has not been reproduced by any other group.

1˙2. *Lead chalcogenides.* – Another metal chalcogenide that has been used for decades in RTGs with applications in mid-range temperatures (600–800 K) is heavily doped PbTe [18, 19]. It was discovered in 1845 in the altaite mineral [20], which is quite rare compared with galena (PbS). The main drawback with these compounds (PbTe, PbSe and PbS) is that lead is more toxic, and several countries, such as those belonging to the European Union, are trying to minimize or even avoid its use.

Lead chalcogenides are usually synthesized by melting in sealed quartz tubes and then sintered. In order to improve their mechanical stability, which is quite poor in the case of PbTe [21, 22], they are usually altered using eutectic mixtures such as PbTe-Si [23] or PbTe-Ge [24], to prevent crack propagation. This is important to achieve good performances in the thermoelectric modules, which are exposed to thermal gradients when in use. The first studies of these materials for thermoelectricity was performed by Seebeck in PbS, and then, a century afterwards, Ioffe described their properties in a whole [19,25-27]. Nowadays it is considered that the zT for optimized lead chalcogenides is around 1.4 and 1.2 for PbSe n- and p-type, respectively [28-31]. As in the case of bismuth chalcogenides, the most recent progress in the field of lead chalcogenides was achieved through the nanostructuration of the materials and the reduction in the lattice thermal conductivity, such as the results from Hsu in 2004, where a solution of PbTe and $AgSbTe_2$ exhibited a zT of 1.7 at 700 K [32]. In these materials there have been also improvements in their thermoelectric performance due to band-structure engineering, modifying the bands by alloying, as it has been shown for PbTe alloyed with Se [33] or Na-doped $PbTe_{0.85}Se_{0.15}$ [34-36]. A surprisingly high zT obtained in this materials has been 2.2 at 915 K, reported by Biswas *et al.* in a Na-doped $Pb_{1-x}Sr_xTe$ which incorporated all-scale hierarchical architectures [37]. Following this work, but modifying the amount of Sr in the final material, a record value as high as 2.5 at 923 K of zT has been reported [38].

1˙3. *Copper selenide and tin selenide.* – Copper chalcogenides were studied first by Becquerel, who realized their high thermopower [39], followed by more studies in the ‘60s by 3M, where they concluded that the high mobility of the Cu ions, when exposed to an electric field, produced the decomposition of the material and rendering it not suitable for thermoelectric applications [40, 41]. Nevertheless, its low cost made it interesting and further studies were carried out, mainly focused on the phase transition at around 400 K that this material undergoes, where it changes to a superionic conductor of ultralow thermal conductivity and zT of 1.5 at around 1000 K [42]. In the case of SnSe, it has attracted much attention only five years ago (in 2014), when it was shown a zT as high as 2.6 at 923 K for single crystals, which arises from a particular structural anisotropy and an ultralow thermal lattice conductivity [43]. The main advantage of these materials is that they are cheaper and less toxic than lead-based systems [44, 45]. SnSe has a reversible second-order phase transition at around 750–800 K, which makes it difficult to synthesize. Usually single crystals are obtained with the Bridgman method. SnS has also been studied, but its thermoelectric performance is lower than SnSe.

In 2014 a zT value of 2.6 at 973 K was reported by Zhao *et al.*, which was caused by an ultralow thermal conductivity of the material due to a highly anisotropic bonding along the measured direction [43]. Other studies have shown that at the phase transition temperature, a dramatic enhancement in the PF is obtained, while the performance at low temperatures can be improved if the material is heavily doped, for example with Na (for p-type) [46], reaching values of zT of 1.34 in the range of 300–773 K. Other record values obtained are zT of 2.2 at 733 K in Bi-doped SnSe and 2.7 at 773 for Br-doped SnSe [47, 48].

1˙4. *Rare-earth and complex ternary chalcogenides.* – For applications over 1000 K, the best thermoelectric materials are rare-earth chalcogenides, such as $La_{3-x}Te_4$, which offer high thermal stability at those temperatures [49,50]. Finally, the latest results in the study of metal chalcogenides have been the study of binary and ternary chalcogenides, which thanks to their complex structures, offer an ultralow thermal conductivity. Since then, with the aid of solid-state chemistry to design and select the compounds to be studied, different ternary chalcogenide systems which show zT values over 1 due to their ultralow thermal conductivity and complex structures have been reported, such as $AgBi_3S_5$ [51] or $CsAg_5Te_3$ [52].

2. – Metal oxides

In the case of metal oxides, their main advantage for being used as thermoelectric materials is not their performance, which is in general quite modest, but their suitability for high-temperature applications, where other materials may suffer melting, or decomposition, or oxidization. Another advantage that they present is that in general, metals are abundant in the earth crust and cheap, and the fabrication of the metal oxides can be made in large amounts by solid-state reactions or direct synthesis followed by compaction, which is also a low manufacturing cost. Among their properties, they usually have large carrier mobilities which are an advantage, but they also have high values of thermal conductivity due to the strong bonding in the metal oxides and the small atomic mass of oxygen. Different families of metal oxides, such as layered cobaltites and oxyselenides are the best materials for p-type thermoelectric oxides, allowing decoupling of the transport properties. The n-type materials are mostly Ruddlesden-Popper phases and zinc oxides, which for the moment are promising but do not show the same high performances.

2˙1. *Layered cobaltites.* – The best compounds of this family are $\mathrm{NaCo_2O_4}$ and $\mathrm{Ca_3Co_4O_9}$. In fact, $\mathrm{NaCo_2O_4}$ crystals were the first metal oxides proposed for thermoelectric applications, when Terasaki discovered their high power factor in 1997 at 1323 K [53]. The structure of this metal oxide is layered, with the electrical transport occurred in the $\mathrm{CoO_2}$ layers and the $\mathrm{Na^+}$ cations behaving as phonon-scattering centers between the layers, producing a reduced thermal conductivity [54]. All of this combined gives it an overall zT of 1. Different ways of modifying the thermoelectric properties are the variation of the valence cation, as in the so-called misfit-layered alkaline earth cobaltite $\mathrm{Ca_3Co_4O_9}$ [55, 56], or by doping with Bi, Ba, Fe, etc. [57]. For instance, a record zT of 0.74 at 800 K was presented by substituting Ca partially with Tb [58].

2˙2. *Layered oxyselenides.* – These compounds contain oxide and selenide anions, and by varying the cation composition the thermoelectric properties can be relatively tuned. They have been studied in the past as potential semiconductors [59], optoelectronics [60], and since 2010, as potential thermoelectric materials [61]. They usually have low Seebeck coefficient and low carrier concentration, although higher values such as $-130\,\mu\mathrm{V/K}$ have been found in materials as LaFeAsO at 100 K [62], which can be due to a certain 2D electron confinement in the FeAs layers or even to electron correlation. Another material of this family, BiCuSeO, also presents a Seebeck coefficient of $350\,\mu\mathrm{V/K}$ at room temperature and of $425\,\mu\mathrm{V/K}$ at 923 K, which has led to a record zT of 1.4 at 923 K [63].

2˙3. *Ruddlesden-Popper phases.* – Those phases can be described as layered perovskites with interlayer cations, with the form $A_{n+1}B_nX_{3n+1}$, being n the number of layers in each octahedral, A and B cations and X an anion. $\mathrm{SrTiO_3}$ shows large Seebeck coefficient, and its insulating nature can be tuned by substitution with $\mathrm{La^{3+}}$ or $\mathrm{Nb^{5+}}$ to semiconducting or metallic [64]. Although the zT of perovskites is not very high due to their high thermal conductivity, there are different strategies that can be followed to increase it, such as structural deformations. But the record zT value obtained in these materials corresponds to a superlattice structure in which the electrons suffer a 2D confinement, obtaining a zT of 2.4 at room temperature [65].

2˙4. *Zinc oxides.* – Zn and O are both abundant and cheap, and ZnO presents a high power factor at room temperature. Nevertheless, as it is the general case with metal oxides, it also presents a high thermal conductivity, which decreases at high temperatures, going from $40\,\mathrm{W \cdot m^{-1} \cdot K^{-1}}$ to around $5\,\mathrm{W \cdot m^{-1} \cdot K^{-1}}$ at 1000 K, thanks to an anisotropic thermal expansion that occurs when increasing the temperature. In order to reduce the thermal conductivity without affecting the Seebeck coefficient or electrical conductivity, several routes have been explored. One such example is the introduction of a secondary phase as a nano-precipitate. For instance, the introduction of Al-nanocomposites reduces the thermal conductivity to $2\,\mathrm{W \cdot m^{-1} \cdot K^{-1}}$ at 1000 K producing a zT of 0.44 at this temperature [66]. Another route is the combination of nanostructuration with selective doping or co-doping, which has resulted in values of zT as high as 0.65 for temperatures of 1247 K [67].

3. – Heusler compounds

These compounds, which present an elemental formula X_2YZ, were discovered in 1903 by Fritz Heusler [68]. There is also a variant, called Half-Heusler (HH), which adopts an XYZ formula (with vacancies on the X site) and consists of three face-centred cubic sublattices which are interlaced. To date, only a handful of HH compounds have been characterized from the thermoelectric point of view, which suggests that there can be many other possible candidates among them. HH compounds contain elements of high melting points, such as Hf, Ti, Ni, or Co (all above 1500 K) combined with others of lower melting points as Sn or Sb, both below 100 K. Therefore, in order to synthesize these HH compounds, high temperatures of alloying are necessary. Arc melting, induced heating, melt spinning or spark plasma sintering are also used [69-73], as well as microwave oven processes [74]. All these methods have to be followed by additional heat treatments at temperatures over 100 K for several days with subsequent quenching into ice water to eliminate secondary phases [75]. The resulting materials have high thermal and mechanical stability [76]. In the HH compounds, one has the possibility of substituting the different elements of each of the three sublattices individually, which gives them a high tunability. The only drawback that they present is their high thermal conductivity, which can reach values of $10\,\mathrm{W \cdot m^{-1} \cdot K^{-1}}$ [77-81].

3˙1. *N-type MNiSn and p-type MCoSb* $(\mathrm{M} = \mathrm{Ti}, \mathrm{Zr}, \mathrm{Hf})$. – Firstly, it was established by Aliev *et al.* that their bandgaps, in the case of MNiSn, were narrow, of 0.12, 0.18 and 0.22 eV for M = Ti, Zr, and Hf, respectively [82], and then it was shown that they exhibited large Seebeck coefficient values [83]. Given that the main concern for their use as thermoelectric material was then their high thermal conductivity, different alloys were studied to reduce it. For instance, $\mathrm{Zr}_{1-x}\mathrm{Hf}_x\mathrm{NiSn}$ showed a reduction in thermal conductivity while preserving the power factor [77]. It was also shown that the thermal conductivity depends on the annealing treatments performed in the samples. Another path to reduce the thermal conductivity was to increase the phonon scattering by introducing disorder in the X-sites. Following this route, a zT of 0.7 at 800 K [84] or 0.8 at 1073 K [85] was obtained. The highest obtained value was 1.5 at 700 K [86], but this value has not been successfully reproduced to date. Finally, the thermal conductivity can also be reduced if, like in the work of Shutoh in 2005, a phase decomposition between a Zr/Hf-rich and a Ti-rich phase takes place, obtaining a zT of 1.2 [87]. In the case of p-type compounds, the thermal conductivity is twice or three times larger, and thus its reduction is under study nowadays, such as through nanostructuration of these HH (see for instance reviews on the subject) [75, 88, 89] or increasing the phonon scattering by increasing the differences in mass and size of the composing elements, as done by Yan *et al.* in p-type HH $Hf_{1-x}Ti_xCoSb_{0.8}Sn_{0.2}$, where a zT of 0.9 at 973 K was obtained [90]. Currently, the highest zT obtained in HH was 1.2 at 983 for p-type Co-based HH compounds [91], by tuning the elements for obtaining the highest phonon scattering and at the same time, the best electronic properties.

3˙2. *RFeSb* (R = V *and* Nb). – These are HH compounds with abundant constituent elements and thermoelectric properties promising for high-temperature applications. For instance, n-type VeFeSb has a high PF, but as in the case of the previously commented materials, it also has a large thermal lattice conductivity [92,93]. Different improvements through alloying [93] or nanostructuring [94, 95] have been pursued, but the final zT obtained has only been of 0.33 at 650 K. In the last years, p-type RFeSb solid solutions have been studied as p-type TE materials, obtaining a much higher zT of 0.8 at 900 K when Ti is used as dopant [96] or even 1.1 at 1100 K Ti-doped NbFeSb [97]. These results were obtained by combining band engineering to reduce the effective mass along with a reduction of the thermal lattice conductivity. The highest zT obtained in these kinds of HH has been 1.6 at 1200 K reported by Yu *et al.* in a Ta alloyed $(Nb_{1-x}Ta_x)_{0.8}Ti_{0.2}FeSb$ solid solution.

3˙3. *L2₁ Heusler compounds.* – There are several promising families of half-metallic Heusler compounds which present the $L2_1$ structure. For instance, the family $TiCo_2Z$, where Z can be Al, Si, Ge or Sn, presents a Seebeck coefficient that is constant for a wide range of temperatures, being also high for a metallic system [98-100]. This also makes it a promising material for the combination of thermoelectric effect and half-metallic ferromagnetism for the novel research field of spincalorics [101, 102]. Another family with this structure is Fe_2Val, which has a DOS shape that abruptly changes in both the valence and conduction band, being the Seebeck coefficient highly increased when the Fermi level is shifted through doping [103-105]. Moreover, the sign of the Seebeck depends on the content of V, being good n-type materials those which are V-rich and p-type those V-deficient [103]. Nevertheless, the high values of their thermal conductivity have not permitted, to date, to obtain high-zT materials based on this family of compounds, although concepts such as combining their high power factors with the phase separation concept could enhance their performances and are current subjects of research.

4. – Zintl phases

These materials can be described as covalent-bonded polyanions which are surrounded by cations that give their valence electrons in order to obtain overall charge balance [106-108], being composed by cations such as Na, Ca and Yb. They have been studied for over one century since in 1928 Eduard Zintl synthesized and characterized a set of intermetallic phases with the shine finish of metals but the structure of a salt crystal [108]. The different Zintl phases have different polyanion dimensionalities, having from isolated 0D polyanions in $Yb_{14}MnSb_{11}$ [109], to 2D anionic Zn_2Sb_2 layers in $YbZn_2Sb_2$ [110] and 3D cation structures for Ga and Sb in $BaGa_2Sb_2$ [111]. Their appearance in the thermoelectric field is quite recent, and most of the interesting materials for this field are actually those in the boundaries of the chemistry of Zintl phases, such as those containing intrinsic defects ($Ca_9Zn_{4+x}Sb_9$, with interstitial defects [112] or $Yb_{1-x}Zn_2Sb_2$ with vacancies [113]) or covalently bonded polyanions with a marked ionic character, such as Mb_3Sb_2 [114]. Actually, the first studies of these materials for thermoelectricity are from 2005, when Gascoin *et al.* reported a zT of 0.55 at 750 K for $Ca_xYb_{1-x}Zn_2Sb_2$ [115].

The Zintl phases cannot be synthesized by melting and annealing, given that those ternary pnictides have sometimes very high melting points which are incongruent or the cations are reactive in the sealed ampoules. Therefore, the most convenient and widely used method for obtaining polycrystalline samples is a totally solid state one, that is, ball milling of the constituent elements and sintering by spark plasma or hot pressing [116]. For fabricating single crystals, the growth from a molten metal flux is used [117-119].

The salt-like nature of the Zintl compounds gives them excellent chemical stability at high temperatures, with examples such as $Yb_{14}MnSb_{11}$ with a maximum zT at 1273 K and for long times, as lifetime tests have shown when working at the maximum temperature [120]. Since 2005, new compounds and structure types have been developed, with tuneable carrier concentration and low lattice thermal conductivities [121-128]. The main drawback of these compounds is their electronic behaviour when p-type can be optimized by aliovalent doping or defects, but usually, they have low mobility. Moreover, at low temperatures they are very sensitive to air and tend to form resistive phases at ground boundaries [129-131]. Taking all these into account, the highest zT found to date is 1.6 for Te-doped $Mg_3Sb_{1.5}Bi_{0.5}$. Nevertheless, studies about their mechanical properties and thermal expansion are still needed.

REFERENCES

[1] Snyder G. J. and Toberer E. S., *Nature*, **7** (2011) 101.

[2] Lee S., Esfarjani K., Luo T., Zhou J., Tian Z. and Chen G., *Nat. Commun.*, **5** (2014) 3525.

[3] Sootsman J. R., Chung D. Y. and Kanatzidis M. G., *Angew. Chem. Int. Ed.*, **48** (2009) 8616.

[4] Nielsen M. D., Ozolins V. and Heremans J. P., *Energy Environ. Sci.*, **6** (2013) 570.

[5] Goldsmid H. J. and Douglas R. W., *Br. J. Appl. Phys.*, **5** (1954) 386.

[6] DiSalvo F. J., *Science*, **285** (1999) 703.

[7] Goldsmid H. J., *Introduction to Thermoelectricity* (Springer, Berlin, Heidelberg) 2016.

[8] Esmark,, *Trans. Geol. Soc. London*, **S1-3** (1816) 413.

[9] Goldsmid H. J., Sheard A. R. and Wright D. A., *Br. J. Appl. Phys.*, **9** (1958) 365.

[10] Goldsmid H. J., *J. Appl. Phys.*, **32** (1961) 2198.

[11] Hoffmann J. E. E. A., *Kirk-Othmer Encycl. Chem. Technol.*, **16** (2011) 1.

[12] Jiang J., Chen L., Bai S., Yao Q. and Wang Q., *Scr. Mater.*, **52** (2005) 347.

[13] Han C., Sun Q., Li Z. and Dou S. X., *Adv. Energy Mater.*, **6** (2016) 1600498.

[14] Goldsmid H. J., *Materials*, **7** (2014) 2577.

[15] Kim H.-S., Heinz N. A., Gibbs Z. M., Tang Y., Kang S. D. and Snyder G. J., *Mater. Today*, **20** (2017) 452.

[16] Poudel B., Hao Q., Ma Y., Lan Y., Minnich A., Yu B., Yan X., Wang D., Muto A., Vashaee D., Chen X., Liu J., Dresselhaus M. S., Chen G. and Ren Z., *Science*, **320** (2008) 634.

[17] Kim S. Il, Lee K. H., Mun H. A., Kim H. S., Hwang S. W., Roh J. W., Yang D. J., Shin W. H., Li X. S., Lee Y. H., Snyder G. J. and Kim S. W., *Science*, **348** (2015) 109.

[18] LaLonde A. D., Pei Y., Wang H. and Snyder G. Jeffrey, *Mater. Today*, **14** (2011) 526.

[19] Wood C., *Rep. Prog. Phys.*, **51** (1988) 459.

[20] *The Americal Journal of Science* (J.D. & E.S. Dana, New-Haven) 1880.

[21] Li G., Aydemir U., Duan B., Agne M. T., Wang H., Wood M., Zhang Q., Zhai P., Goddard W. A. and Snyder G. J., *ACS Appl. Mater. Interfaces*, **9** (2017) 40488.

[22] Petersen J. E., Scolfaro L. M. and Myers T. H., *Mater. Chem. Phys.*, **146** (2014) 472.

[23] Sootsman J. R., He J., Dravid V. P., Ballikaya S., Vermeulen D., Uher C. and Kanatzidis M. G., *Chem. Mater.*, **22** (2010) 869.

[24] Sootsman J. R., He J., Dravid V. P., Li C.-P., Uher C. and Kanatzidis M. G., *J. Appl. Phys.*, **105** (2009) 083718.

[25] Vedernikov M. V. and Iordanishvili E. K., *Seventeenth International Conference on Thermoelectrics, Proceedings ICT98* (IEEE) 1998, pp. 37–42.

[26] Ravich Y. I., Efimova B. A. and Smirnov I. A., *Semiconducting Lead Chalcogenides* (Springer, Boston) 1970.

[27] Ioffe A. F., Stil'bans L. S., Iordanishvili E. K., Stavitskaya T. S., Gelbtuch A. and Vineyard G., *Phys. Today*, **12** (1959) 42.

[28] Pei Y., LaLonde A., Iwanaga S. and Snyder G. J., *Energy Environ. Sci.*, **4** (2011) 2085.

[29] LaLonde A. D., Pei Y. and Snyder G. J., *Energy Environ. Sci.*, **4** (2011) 2090.

[30] Wang H., Pei Y., LaLonde A. D. and Snyder G. J., *Proc. Natl. Acad. Sci. U.S.A.*, **109** (2012) 9705.

[31] Wang H., Pei Y., LaLonde A. D. and Snyder G. J., *Adv. Mater.*, **23** (2011) 1366.

[32] Hsu K. F., Loo S., Guo F., Chen W., Dyck J. S., Uher C., Hogan T., Polychroniadis E. K. and Kanatzidis M. G., *Science*, **303** (2004) 818.

[33] Pei Y., Shi X., LaLonde A., Wang H., Chen L. and Snyder G. J., *Nature*, **473** (2011) 66.

[34] Chen Z., Jian Z., Li W., Chang Y., Ge B., Hanus R., Yang J., Chen Y., Huang M., Snyder G. J. and Pei Y., *Adv. Mater.*, **29** (2017) 1606768.

[35] Zheng L., Li W., Lin S., Li J., Chen Z. and Pei Y., *ACS Energy Lett.*, **2** (2017) 563.

[36] Wang H., Gibbs Z. M., Takagiwa Y. and Snyder G. J., *Energy Environ. Sci.*, **7** (2014) 804.

[37] Biswas K., He J., Blum I. D., Wu C.-I., Hogan T. P., Seidman D. N., Dravid V. P. and Kanatzidis M. G., *Nature*, **489** (2012) 414.

[38] Tan G., Shi F., Hao S., Zhao L.-D., Chi H., Zhang X., Uher C., Wolverton C., Dravid V. P. and Kanatzidis M. G., *Nat. Commun.*, **7** (2016) 12167.

[39] Tan G., Zhao L.-D. and Kanatzidis M. G., *Chem. Rev.*, **116** (2016) 12123.

[40] Brown D. R., Day T., Caillat T. and Snyder G. J., *J. Electron. Mater.*, **42** (2013) 2014.

[41] Dennler G., Chmielowski R., Jacob S., Capet F., Roussel P., Zastrow S., Nielsch K., Opahle I. and Madsen G. K. H., *Adv. Energy Mater.*, **4** (2014) 1301581.

[42] Liu H., Shi X., Xu F., Zhang L., Zhang W., Chen L., Li Q., Uher C., Day T. and Snyder G. J., *Nat. Mater.*, **11** (2012) 422.

[43] Zhao L.-D., Lo S.-H., Zhang Y., Sun H., Tan G., Uher C., Wolverton C., Dravid V. P. and Kanatzidis M. G., *Nature*, **508** (2014) 373.

[44] Zhao L.-D., Chang C., Tan G. and Kanatzidis M. G., *Energy Environ. Sci.*, **9** (2016) 3044.

[45] Zhou M., Snyder G. J., Li L. and Zhao L.-D., *Inorg. Chem. Front.*, **3** (2016) 1449.

[46] Zhao L.-D., Tan G., Hao S., He J., Pei Y., Chi H., Wang H., Gong S., Xu H., Dravid V. P., Uher C., Snyder G. J., Wolverton C. and Kanatzidis M. G., *Science*, **351** (2016) 141.

[47] Duong A. T., Nguyen V. Q., Duvjir G., Duong V. T., Kwon S., Song J. Y., Lee J. K., Lee J. E., Park S., Min T., Lee J., Kim J. and Cho S., *Nat. Commun.*, **7** (2016) 1.

[48] Chang C., Wu M., He D., Pei Y., Wu C.-F., Wu X., Yu H., Zhu F., Wang K., Chen Y., Huang L., Li J.-F., He J. and Zhao L.-D., *Science*, **360** (2018) 778.

[49] Delaire O., May A. F., McGuire M. A., Porter W. D., Lucas M. S., Stone M. B., Abernathy D. L., Ravi V. A., Firdosy S. A. and Snyder G. J., *Phys. Rev. B*, **80** (2009) 184302.

[50] May A. F., Singh D. J. and Snyder G. J., *Phys. Rev. B*, **79** (2009) 153101.

[51] Tan G., Hao S., Zhao J., Wolverton C. and Kanatzidis M. G., *J. Am. Chem. Soc.*, **139** (2017) 6467.

[52] Lin H., Tan G., Shen J.-N., Hao S., Wu L.-M., Calta N., Malliakas C., Wang S., Uher C., Wolverton C. and Kanatzidis M. G., *Angew. Chem. Int. Ed.*, **55** (2016) 11431.

[53] Terasaki I., Sasago Y. and Uchinokura K., *Phys. Rev. B*, **56** (1997) R12685.

[54] Huang Q., Foo M. L., Pascal R. A., Lynn J. W., Toby B. H., He T., Zandbergen H. W. and Cava R. J., *Phys. Rev. B*, **70** (2004) 184110.

[55] Karppinen M., Fjellvåg H., Konno T., Morita Y., Motohashi T. and Yamauchi H., *Chem. Mater.*, **16** (2004) 2790.

[56] Tian R., Zhang T., Chu D., Donelson R., Tao L. and Li S., *J. Alloys. Compd.*, **615** (2014) 311.

[57] Tian R., Donelson R., Ling C. D., Blanchard P. E. R., Zhang T., Chu D., Tan T. T. and Li S., *J. Phys. Chem. C*, **117** (2013) 13382.

[58] Saini S., Yaddanapudi H. S., Tian K., Yin Y., Magginetti D. and Tiwari A., *Sci. Rep.*, **7** (2017) 44621.

[59] Takano Y., Ogawa C., Miyahara Y., Ozaki H. and Sekizawa K., *J. Alloys. Compd.*, **249** (1997) 221.

[60] Kusainova A. M., Berdonosov P. S., Akselrud L. G., Kholodkovskaya L. N., Dolgikh V. A. and Popovkin B. A., *J. Solid State Chem.*, **112** (1994) 189.

[61] Zhao L. D., Berardan D., Pei Y. L., Byl C., Pinsard-Gaudart L. and Dragoe N., *Appl. Phys. Lett.*, **97** (2010) 092118.

[62] Pinsard-Gaudart L., Bérardan D., Bobroff J. and Dragoe N., *Phys. Status Solidi - Rapid Res. Lett.*, **2** (2008) 185.

[63] Pei Y. L., Wu H., Wu D., Zheng F. and He J., *J. Am. Chem. Soc.*, **136** (2014) 13902.

[64] Okuda T., Nakanishi K., Miyasaka S. and Tokura Y., *Phys. Rev. B*, **63** (2001) 113104.

[65] Ohta H., Kim S., Mune Y., Mizoguchi T., Nomura K., Ohta S., Nomura T., Nakanishi Y., Ikuhara Y., Hirano M., Hosono H. and Koumoto K., *Nat. Mater.*, **6** (2007) 129.

[66] Jood P., Mehta R. J., Zhang Y., Peleckis G., Wang X., Siegel R. W., Borca-Tasciuc T., Dou S. X. and Ramanath G., *Nano Lett.*, **11** (2011) 4337.

[67] Ohtaki M., Araki K. and Yamamoto K., *J. Electron. Mater.*, **38** (2009) 1234.

[68] Heusler F., *Verh. DPG*, **5** (1903) 219.

[69] Bartholomé K., Balke B., Zuckermann D., Köhne M., Müller M., Tarantik K. and König J., *J. Electron. Mater.*, **43** (2014) 1775.

[70] Makongo J. P. A., Misra D. K., Zhou X., Pant A., Shabetai M. R., Su X., Uher C., Stokes K. L. and Poudeu P. F. P., *J. Am. Chem. Soc.*, **133** (2011) 18843.

[71] Yu C. U. I., Zhu T., Xiao K. A. I., Shen J. and Zhao X., *Funct. Mater. Lett.*, **3** (2010) 227.

[72] Yan X., Joshi G., Liu W., Lan Y., Wang H., Lee S., Simonson J. W., Poon S. J., Tritt T. M., Chen G. and Ren Z. F., *Nano Lett.*, **11** (2011) 556.

[73] Garay J. E., *Annu. Rev. Mater. Res.*, **40** (2010) 445.

[74] Birkel C. S., Zeier W. G., Douglas J. E., Lettiere B. R., Mills C. E., Seward G., Birkel A., Snedaker M. L., Zhang Y., Snyder G. J., Pollock T. M., Seshadri R. and Stucky G. D., *Chem. Mater.*, **24** (2012) 2558.

[75] Chen S. and Ren Z. L. B.-Cr., *Mater. Today*, **16** (2013) 387.

[76] Verges M. A., Schilling P. J., Upadhyay P., Miller W. K., Yaqub R., Stokes K. L. and Poudeu P. F. P., *Sci. Adv. Mater.*, **3** (2011) 659.

[77] Uher C., Yang J., Hu S., Morelli D. T. and Meisner G. P., *Phys. Rev. B*, **59** (1999) 8615.

[78] Kimura Y., Ueno H. and Mishima Y., *J. Electron. Mater.*, **38** (2009) 934.

[79] Xie W., Jin Q. and Tang X., *J. Appl. Phys.*, **103** (2008) 43711.

[80] Zhou M., Chen L., Feng C., Wang D. and Li J.-F., *J. Appl. Phys.*, **101** (2007) 113714.

[81] Schwall M. and Balke B., *Appl. Phys. Lett.*, **98** (2011) 42106.

[82] Aliev F. G., Brandt N. B., Moshchalkov V. V., Kozyrkov V. V., Skolozdra R. V. and Belogorokhov A. I., *Z. Phys. B: Condens. Matter*, **75** (1989) 167.

[83] Aliev F. G., Kozyrkov V. V., Moshchalkov V. V., Scolozdra R. V. and Durczewski K., *Z. Phys. B: Condens. Matter*, **80** (1990) 353.

[84] Shen Q., Chen L., Goto T., Hirai T., Yang J., Meisner G. P. and Uher C., *Appl. Phys. Lett.*, **79** (2001) 4165.

[85] Culp S. R., Poon S. J., Hickman N., Tritt T. M. and Blumm J., *Appl. Phys. Lett.*, **88** (2006) 42106.

[86] Sakurada S. and Shutoh N., *Appl. Phys. Lett.*, **86** (2005) 2105.

[87] Schwall M. and Balke B., *Phys. Chem. Chem. Phys.*, **15** (2013) 1868.

[88] Liu W., Yan X., Chen G. and Ren Z., *Nano Energy*, **1** (2012) 42.

[89] Poon S. J., Wu D., Zhu S., Xie W., Tritt T. M., Thomas P. and Venkatasubramanian R., *J. Mater. Res.*, **26** (2011) 2795.

[90] Yan X., Liu W., Wang H., Chen S., Shiomi J., Esfarjani K., Wang H., Wang D., Chen G. and Ren Z. L. B.-Y., *Energy Environ. Sci.*, **5** (2012) 7543.

[91] Rausch E., Balke B., Stahlhofen J. M., Ouardi S., Burkhardt U. and Felser C., *J. Mater. Chem. C*, **3** (2015) 10409.

[92] Fu C. G., Xie H. H., Liu Y. T., Zhu T. J., Xie J. and Zhao X. B., *Intermetallics*, **32** (2013) 39.

[93] Fu C. G., Xie H. H., Zhu T. J., Xie J. and Zhao X. B., *J. Appl. Phys.*, **112** (2012) 124915.

[94] Zou M. M. and Li J. F., *J. Phys. D: Appl. Phys.*, **43** (2010) 415403.

[95] Fu C. G., Zhu T. J., Xie H. H. and Zhao X. B., *EPL*, **104** (2013) 46003.

[96] Fu C., Zhu T., Pei Y., Xie H., Wang H., Snyder G. J., Liu Y., Liu Y. and Zhao X., *Adv. Energy Mater.*, **4** (2014) 1400600.

[97] Fu C., Zhu T., Liu Y., Xie H. and Zhao X., *Energy Environ. Sci.*, **8** (2015) 216.

[98] Graf T., Fecher G. H., Barth J., Winterlik J. and Felser C., *J. Phys. D: Appl. Phys.*, **42** (2009) 084003.

[99] Barth J., Fecher G. H., Balke B., Ouardi S., Graf T., Felser C., Shkabko A., Weidenkaff A., Klaer P., Elmers H. J., Yoshikawa H., Ueda S. and Kobayashi K., *Phys. Rev. B*, **81** (2010) 064404.

[100] Graf T., Barth J., Balke B., Populoh S., Weidenkaff A. and Felser C., *Scr. Mater.*, **63** (2011) 925.

[101] Balke B., Ouardi S., Graf T., Barth J., Blum C. G. F., Fecher G. H., Shkabko A., Weidenkaff A. and Felser C., *Solid State Commun.*, **150** (2010) 529.

[102] Schwall M., Schoop L. M., Ouardi S., Balke B., Felser C., Klaer P. and Elmers H.-J., *Adv. Funct. Mater.*, **22** (2012) 1822.

[103] Nishino Y. and Tamada Y., *J. Appl. Phys.*, **115** (2014) 123707.

[104] Nishino Y., *J. Jpn. Inst. Met. Mater.*, **79** (2015) 548.

[105] Nishino Y., *Mater. Sci. Forum*, **449–452** (2004) 909.

[106] Kauzlarich S. M., Brown S. R. and Snyder G. J., *Dalton Trans.*, **21** (2007) 2099.

[107] Kauzlarich S., Zevalkink A., Toberer E. S., Snyder G. J., Nandhakumar I., White N. M. and Beeby S. (Editors), *Thermoelectric Materials and Devices* (Royal Society of Chemistry) 2016.

[108] Schaefer H., *Annu. Rev. Mater. Sci.*, **15** (1985) 1.

[109] Chan J. Y., Olmstead M. M. and Kauzlarich S. M., *Chem. Mater.*, **10** (1998) 3583.

[110] Zelinska O. Y., Tkachuk A. V., Grosvenor A. P. and Mar A., *Chem. Met. Alloys.*, **1** (2008) 204.

[111] Kim S.-J. and Kanatzidis M. G., *Inorg. Chem.*, **40** (2001) 3781.

[112] Xia S. and Bobev S., *J. Am. Chem. Soc.*, **129** (2007) 10011.

[113] Zevalkink A., Zeier W. G., Cheng E., Snyder G. J., Fleurial J.-P. and Bux S., *Chem. Mater.*, **26** (2014) 5710.

[114] Peng W., Chanakian S. and Zevalkink A., *Inorg. Chem. Front.*, **5** (2018) 1744.

[115] Gascoin F., Ottensmann S., Stark D., Haile S. M. and Snyder G. J., *Adv. Funct. Mater.*, **15** (2005) 1860.

[116] Zevalkink A., Smiadak D. M., Blackburn J. L., Ferguson A. J., Chabinyc M. L., Delaire O., Wang J., Kovnir K., Martin J., Schelhas L. T., Sparks T. D., Kang S. D., Dylla M. T., Snyder G. J., Ortiz B. and Toberer E., *Appl. Phys. Rev.*, **5** (2018) 021303.

[117] Canfield P. C. and Fisk Z., *Philos. Mag.*, **6** (1992) 1117.

[118] Kanatzidis M. G., Ttgen R. P. and Jeitschko W., *Angew. Chem. Int. Ed. Engl.*, **44** (2005) 6996.

[119] Ribeiro R. A. and Avila M. A., *Philos. Mag.*, **92** (2012) 2492.

[120] Paik J.-A., Brandon E., Caillat T., Ewell R. and Fleurial J.-P., "Life testing of Yb14MnSb11 for high performance thermoelectric couples", in *Nuclear and Emerging Technologies for Space (NETS) 2011, Albuquerque, NM, February 7-10, 2011*

(Jet Propulsion Laboratory, National Aeronautics and Space Administration) 2011, `http://hdl.handle.net/2014/41871`.

[121] Zevalkink A., Aydemir U., Snyder G. J. and Uher C. (Editors), *CRC Handbook of Thermoelectrics* (2016).

[122] Bux S., Zevalkink A., Janka O., Uhl D., Kauzlarich S., Snyder G. J. and Fleurial J. P., *J. Mater. Chem. A*, **2** (2013) 215.

[123] Ohno S., Aydemir U., Amsler M., Pöhls J.-H., Chanakian S., Zevalkink A., White M. A., Bux S. K., Wolverton C. and Snyder G. J., *Adv. Funct. Mater.*, **27** (2017) 1606361.

[124] Shuai J., Geng H., Lan Y., Zhu Z., Wang C., Liu Z., Bao J., Chu C. W., Sui J. and Ren Z., *Proc. Natl. Acad. Sci. U.S.A.*, **113** (2016) E4125.

[125] May A. F., Toberer E. S. and Snyder G. J., *J. Appl. Phys.*, **106** (2009) 13706.

[126] Aydemir U., Zevalkink A., Ormeci A., Bux S. and Snyder G. J., *J. Mater. Chem.*, **4** (2016) 1867.

[127] Ortiz B. R., Gorai P., Stevanović V. and Toberer E. S., *Chem. Mater.*, **29** (2017) 4523.

[128] Yi T., Cox C. A., Toberer E. S., Snyder G. J. and Kauzlarich S. M., *Chem. Mater.*, **22** (2010) 935.

[129] Zevalkink A., Toberer E. S., Zeier W. G., Flage-Larsen E. and Snyder G. J., *Energy Environ. Sci.*, **4** (2011) 510.

[130] Zevalkink A., Zeier W. G., Pomrehn G., Schechtel E., Tremel W. and Snyder G. J., *Energy Environ. Sci.*, **5** (2012) 9121.

[131] Zeier W. G., Zevalkink A., Schechtel E., Tremel W. and Snyder G. J., *J. Mater. Chem.*, **22** (2012) 9826.

Proceedings of the International School of Physics "Enrico Fermi"
Course 207 "Advances in Thermoelectricity: Foundational Issues, Materials and Nanotechnology",
edited by D. Narducci, G. J. Snyder and C. Fanciulli
(IOS, Amsterdam; SIF, Bologna) 2021
DOI 10.3254/ENFI210006

Thermoelectric harvesting: Basics on design optimization and applications

CARLO FANCIULLI(*)

CNR – ICMATE, Lecco unit - Via Previati 1/E, 23900, Lecco, Italy

Summary. — Energy harvesting is one of the ways explored nowadays to face the problem associated to electrical power needs. Typical powers involved are limited but the main advantage offered by the harvesting approach is the capability to achieve a localized power generation enabling a reduction in losses due to power distribution. Thermoelectric technology represents one of the solution for energy harvesting allowing the direct conversion of a collected or wasted heat into electrical power. This short lecture wants to provide the basic concepts associated to the thermoelectric harvesting. The work discusses the ideas associated to the optimization of a thermoelectric device and the design of a thermoelectric system for electrical power production. The discussion focuses the attention on the different critical aspects a researcher has to face in order to produce an operating system able to match the constrains of a target application. To conclude, a description of some reference cases is reported introducing the reader to the technological impact, actual and possible, of an old technology living a renewed interest promoted by a new environment based on new paradigms for power generation and distribution, and widespread diffusion of low-power electronic devices.

1. – Introduction

The development of renewable, sustainable, green energy sources to replace fossil fuels is one of the most challenging issues in energy research. In this perspective, energy harvesting, representing the energy derived from ambient sources directly converted into

---

(*) E-mail: `carlo.fanciulli@cnr.it`

electrical energy, represents an opportunity for the growth of a distributed power generation network. This way to provide energy is mainly valuable when no other energy source is available (*i.e.*, off-grid condition) to supply small- and medium-sized electronic devices, as well as electrical systems [1,2]. Energy harvesting usually refers to an environment with regular and well-assessed ambient energy sources. In particular, renewable forms of energy such as sunlight, wind, rain, tides/waves, and geothermal heat have been extensively studied as alternative energy sources [3-7]. Next to the direct sources conversion an approach based on waste power recovery can provide a route for energy saving and improve systems efficiency. Energy harvesting is generally applied when there is a match between the available energy and the energy required. Eventually, these forms of energy must be integrated with the major power grids to meet the requirements of larger power scales.

In recent years, smart electronics have become widespread everywhere in our daily lives. Such devices are designed for high energy efficiency running on battery for a long time period. This characteristic closes the gap between the accessible power generated by a harvesting system and the power needs of the electronic device. At the same time, the large number of devices and the widespread distribution promote the development of power supplying systems similarly spread out. In these circumstances, sustainable power sources are valuable for the independent, maintenance-free, and continuous operation of such low-energy-consumption devices.

Over the past decades, energy harvesters based on different phenomena, such as the piezoelectric [8-10] effects for harvesting mechanical energy, the photovoltaic (PV) [11-13] effect for harvesting solar energy and thermoelectric [14-16] effects for harvesting thermal energy, have been extensively studied for practical applications. These energy technologies are simply classified by their different energy conversion mechanisms, but the aim of all the energy harvesters is the conversion of wasted environmental energy to electricity. Nevertheless, all of the energy harvesters utilize only one type of energy, with the other types wasted. Any energy harvester consists of

- an energy source
- one or more transducers that convert environmental energy into electrical energy;
- an energy storage device (*e.g.*, a rechargeable battery or a capacitor that stores the harvested energy);
- process control electronics.

Where the input energy is thermal energy, the most common transformation system is the thermoelectric generator (TEG). A TEG converts heat directly into electrical energy according to the Seebeck effect. The basic principles of TEG operation are described in the following section. Pure thermoelectric harvesting systems, collecting heat from natural sources, can generate powers from hundreds of μW to mW, but considering systems based on waste heat recovery (form industrial processes, engines or other human activities) the power scale can reach the order of KW. A thermoelectric harvester produces green energy for energy harvesting with a multitude of advantages: maintenance-free, because of the use of highly reliable and compact solid-state device; silent and quiet; highly efficient in environmental terms because the heat is harvested from waste heat sources and converted into electricity; useful scalable applications configured to harvest wide amounts of energy when necessary; possibility to harvest power from both hot surface or cold surface; green energy behavior, being eco-friendly [17]. A TEG device produces energy without using fossil fuel, leading to a reduction of greenhouse gas emissions. It is desirable to obtain the maximum electric output power and efficiency when a TEG system operates [18]. In case of waste heat recovery applications [19], only electric output power is significant and the heat not recovered is lost [20]. Considering that thermal energy harvesting has a reduced efficiency (5–6%), this could represent a major barrier for its extensive use.

2. – Thermoelectric phenomena

The thermoelectric harvesting is based on the capability of some materials to produce electrical power when a thermal gradient is applied. The physical principle is the Seebeck effect, and it is described by the Seebeck coefficient, α, defined as the ratio between the open circuit voltage produced at the ends of the material investigated, and the temperature difference applied to it

$$\alpha = \frac{\Delta V}{\Delta T}\,. \tag{1}$$

It is important to report the dependence of Seebeck by the character of the carriers in the material. In fact, in the presence of electronic conduction, the Seebeck coefficient results to be negative, while if the majority carriers are holes, the Seebeck coefficient is positive. This characteristic allows identifying two classes of thermoelectric materials, p and n, which correspond to the ones of semiconductors [21].

The thermal counterpart of the Seebeck effect is the Peltier effect. The principle states that when an electric current circulate through a thermoelectric material, a temperature difference is created between the two ends. Such a difference is proportional to the current applied and is related to the heat pumped through the material by the moving carriers. The principle is described by the relationship

$$\dot{Q} = \Pi I, \tag{2}$$

where $\dot{Q}$ is the heat flow and Π is the Peltier coefficient. The two effects described has the same origin, so the Seebeck and Peltier coefficients are related by the equation

$$\Pi = \alpha T. \tag{3}$$

Seebeck and Peltier coefficients depend on temperature, so their values, being measured in the presence of a temperature difference, are typically associated to the mean temperature between the hot and the cold one. A third thermoelectric effect is the Thomson effect which describes the heat transfer in a material when a current flows in the presence of a thermal gradient. The heat flow in a conductive material results in

$$\dot{Q} = \frac{1}{\sigma} j^2 - \mu j \nabla T, \tag{4}$$

where j is the current density, σ the electrical conductivity and μ the Thomson coefficient. The $\nabla T = \mathrm{d}T/\mathrm{d}x$ is the temperature gradient along the conducting material. The first term represents the Joule heating while the second one the Thomson effect. Again μ and α are related by the temperature as

$$\mu = T \frac{\mathrm{d}\alpha}{\mathrm{d}T}\,. \tag{5}$$

In the following calculations it will be neglected in most of the cases due to the lower effect on the device performances in standard operating conditions. Naturally, whenever a large ΔT is applied or a major current flows into the system, the contribution due to Thomson effect has to be applied to the equations in order to achieve the correct result. A deeper description of the principles can be found in [21-23].

3. – Thermoelectric module

A harvester is a system able to collect the available source energy and transform it into electric energy useful for supplying a device or for storage. The core of the harvester is the device capable of the conversion: for the solar source, it is a photovoltaic material or panel, for mechanical energy a piezoelectric system. In case of thermal energy, the thermoelectric materials are at the basis of the conversion system. The system is based on a collector able to transfer the heat at one side of the thermoelectric device, a thermoelectric module, based on materials displaying suitable performances, and a heat sink, necessary to keep the thermal gradient on the materials preventing their uncontrolled warming up. A thermoelectric module (TEM) is a device made of a series of thermocouples connected electrically in series and thermally in parallel. A schematic of the system is reported in fig. 1.

The thermocouple is the basic brick of any thermoelectric device and is made of two semiconducting materials, one with p character and the other n, electrically connected at one end and submitted to the same thermal gradient. Depending on the end use and on the shape of the thermoelements, different architectures can be considered for the modules: the most common one follows the shape of a π (fig. 1), where the two thermoelements are the vertical legs, while the third line is the electrical joint. The thermocouple is characterized by different parameters useful to define the final TEM performance. The first one is the electrical resistance of the couple given by the sum of the resistivity of the two materials, p and n, scaled with the corresponding aspect ratios. Next to the contribution due to the legs, a contact resistance is always present due to

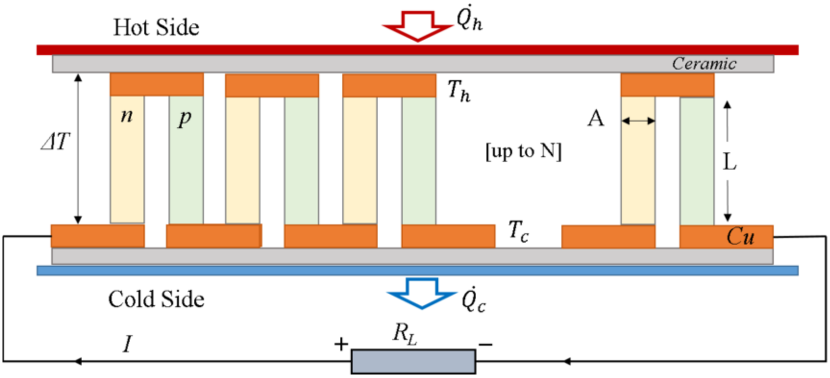

Fig. 1. – The schematic of a thermoelectric module. The system is made of N thermocouples connected electrically in series and thermally in parallel. The Seebeck voltage generated by the external ΔT applied corresponds to the one measured in open circuit. It results in the sum of the single thermocouple voltages. Connecting an external load, a current circulates through the system: it is equal for all the system depending on the electrical resistance. So, in a TEM, the voltage output can be controlled modifying the number of thermocouples while the current playing with the cross section of the legs.

the multiple joints in the electrical chain of thermoelements. In a similar way, a thermal conductance related to the conductivities of the thermoelements can be considered. The Seebeck of a thermocouple is the one obtained by the difference between the ones of p and n materials. As a consequence of the architecture of the module, the electrical voltage output produced when a ΔT is applied results in the sum of the Seebeck contributions from the n thermocouples:

$$V_{TEM} = nRI - n\alpha_{pn}\Delta T. \tag{6}$$

The current produced by the TEM can be evaluated considering an external load, R_L, connected to the outputs of the devices. So,

$$I = \frac{n\alpha_{pn}\Delta T}{nR + R_L}\,. \tag{7}$$

So, the electric power output delivered by the TEG to the load can be written as

$$P = I^2 R_L = \left(\frac{n\alpha_{pn}\Delta T}{nR + R_L}\right)^2 R_L. \tag{8}$$

This expression, as a function of the electric current, can be maximized when $R_L = nR$, as to say the external load matches the internal resistance of the module. In such a condition the power values [24]:

$$P_{max} = \frac{(\alpha_{pn}\Delta T)^2}{4R}\,. \tag{9}$$

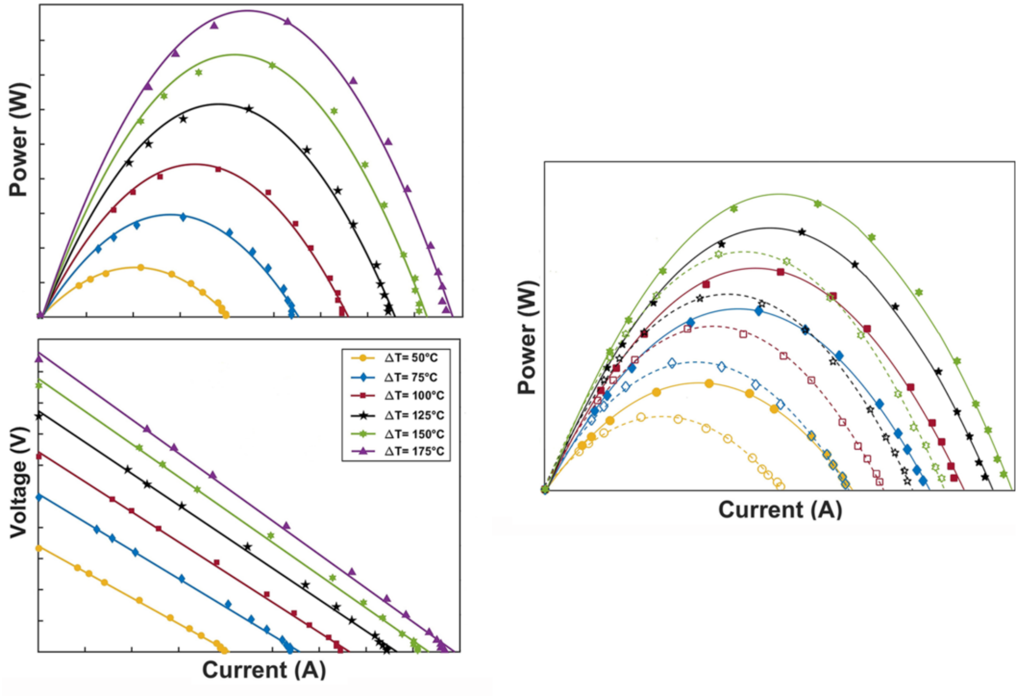

Fig. 2. – Power and voltage characteristics for a thermoelectric module operating at different ΔTs. In the second part, the output corresponding to constant ΔT and constant power input are reported in solid and dashed lines, respectively. All the data are collected in a regime state where the heat flow reached the equilibrium.

And the corresponding current circulating is

$$I_{max} = \frac{\alpha_{pn}\Delta T}{2R}\,. \tag{10}$$

These equations describe the voltage and power outputs of a TEM exposed to a constant ΔT. The typical output of a TEM characterization is reported in fig. 2: here, the V and P outputs are plotted as a function of the current. The characteristic curves for the TEM performances are reported for different ΔT applied. The data points are obtained applying different loads between open and short circuit. It has to be noticed how, during the measurement time, the outputs decrease down to a regime condition. This is due to the Peltier effect operating in a way to reduce the applied ΔT. In the figure the data collected at constant ΔT (solid lines), obtained restoring the starting condition increasing the input power at the hot side, are compared to the ones collected at constant input power (dashed lines), where the ΔT scales down with increasing current. The performances at constant ΔT correspond to the maximum outputs achievable from the device; however, the constant power curves are usually useful to design an operating system where no feedback on input power is available, stating the real outputs achievable with the device in regime conditions.

4. – Efficiency assessment of a thermoelectric device

The electrical efficiency of a thermoelectric module is defined by the ratio between the electrical power output, P, the one applied to an external load, and the heat flow absorbed at the hot side of the module, $\dot{Q}_h$. The heat flow at the hot junction is related to the thermal gradient, the conductance of the thermocouples, the heat produced by the current flowing into the system due to Joule effect and the heat moved by the current into the thermoelements associated to the Peltier effect. As a result, $\dot{Q}_h$ can be written as

$$\dot{Q}_h = n\left(\alpha_{pn} T_h I - \frac{1}{2} R I^2 + K\Delta T\right), \tag{11}$$

where R and K are the resistance and the thermal conductance of the thermocouple, respectively. Therefore, the efficiency can be expressed as

$$\eta = \frac{P}{\dot{Q}_h} = \frac{n R_L \Delta T \alpha_{pn}^2}{K(nR+R_L)^2 + n\alpha_{pn}^2 (R_L T_h + nR\overline{T})}, \tag{12}$$

where $\overline{T}$ is the temperature mean value between T_h and T_c ($= \frac{(T_h+T_c)}{2}$). It is possible to calculate the thermoelectric efficiency corresponding to the maximum power, as previously defined ($R_L/nR = 1$):

$$\eta_{P\,max} = \frac{\Delta T}{4/Z + T_h + \overline{T}}. \tag{13}$$

Here, the module parameter Z is defined as [23, 25, 26]:

$$Z = \frac{\alpha_{pn}^2}{RK} = \frac{(|\alpha_p| + |\alpha_n|)^2}{(\sqrt{\rho_p \kappa_p} + \sqrt{\rho_n \kappa_n})^2}. \tag{14}$$

Such parameter is named the figure of merit of the module and relates the performance of the device to the characteristics of the thermoelements (shape, size, joints) and the properties of the materials involved. The external load can be used as a parameter to maximize the efficiency of the thermoelectric device. The resulting condition is [27]

$$\frac{R_L}{nR} = \sqrt{1 + Z\overline{T}} \tag{15}$$

leading to the expression for η_{max} [23, 25]:

$$\eta_{max} = \frac{\Delta T}{T_h} \frac{\sqrt{1+Z\overline{T}} - 1}{\sqrt{1+Z\overline{T}} + T_c/T_h}. \tag{16}$$

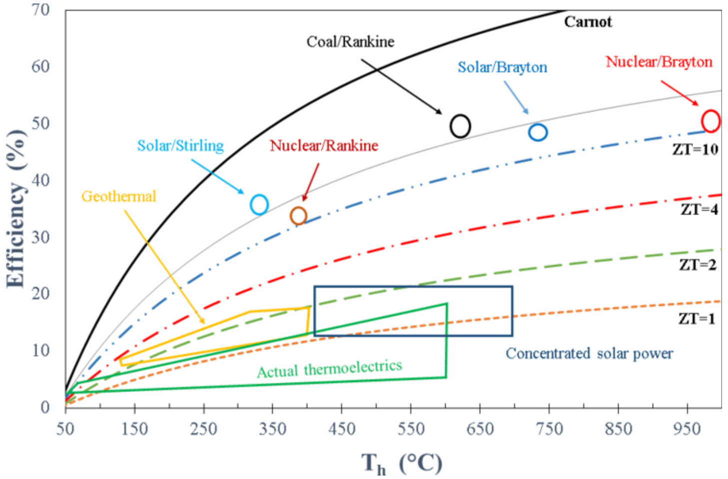

Fig. 3. – Efficiency calculated for different ZT as a function of hot side temperature compared to the efficiencies reported for other thermal conversion solutions applied to different sources [28].

The first term of the expression represents the Carnot efficiency for a thermal engine operating between T_h and T_c. The relation reported shows how the Carnot efficiency is the upper limit for the thermoelectric conversion. At the same time, from the equation it is possible to observe that increasing the figure of merit of the module the overall efficiency of the TEM increases.

In fig. 3 the efficiency of a thermoelectric module is reported as a function of the T_h for different ZT [28]. In the same plot the efficiency for other power generating technologies is reported: the thermoelectric solution can be considered advantageous for low T_h, where other thermal engines do not operate or display poor efficiencies. When the temperature scales up, improving the available thermal power input, ZT has to be in the order of 4 to make thermoelectric conversion a valuable opportunity. Actual devices operate with a ZT average approximatively equal to 1, and with a hot temperature close to 280 °C–300 °C, leading to a thermoelectric module efficiency in the range of 10%.

Designing a thermoelectric generator (TEG), made of all the elements required by the system to achieve the electrical power production by the coupling to the heat source, requires the definition of the operating performance needs in order to set the device parameters optimal for the target use. This can be easily understood by observing how the maximum efficiency do not correspond to the maximum power production for the thermoelectric device. The matching load condition is common to all the electrical power generation systems. It is important to remember that the maximum power condition for a thermoelectric module is the one in which the internal resistance is zero: this allows no losses due to the current circulating enabling a perfect TEG. On the other hand, in the real case, having a finite resistance of the system, it becomes critical to set the load applied to the TEG in a way to take advantage of the best operating conditions available. So, the matching load defines the optimal configuration for the power output while eq. (15) optimizes the device in terms of conversion efficiency. A further correction has to be considered in the optimization design: the contact resistance related to the joints between the legs has been neglected in the previous relations. The maximum efficiency condition as a function of the external load can be written as [29]:

$$\frac{R_L}{nR} = \sqrt{(1+\delta)^2 + (1+\delta)Z\overline{T}}, \tag{17}$$

where $\delta = R_{contact}/R$ keeps into account the effect associated to the contact resistance in each thermocouple. This equation reduces to eq. (15) whenever $R_{contact}$ goes to zero. One last consideration has to be reported about the efficiency and power optimization and is related to the effect of a varying ΔT on the device performance. In fact, as reported by Hendricks *et al.*, the thermal gradient is not constant on a power-efficiency curve, a direct consequence of the power expression (8). Determining the external load that defines the maximum power point when ΔT changes leads to the relationship described in Hendricks *et al.* [30]:

$$R_{L,opt} = NR + \frac{2R_{L,opt}(NR + R_{L,opt})}{\Delta T}\frac{\partial \Delta T}{\partial R_L}\,. \tag{18}$$

This relation shows how the Load applied maximizing the power output is greater than the internal resistance. The value can be obtained solving the quadratic relationship in $R_{L,opt}$ allowing the performance analysis for any given device design. The resulting assessment gives a relationship on the maximum performances scaling with the external loads as

$$\left(\frac{R_{L,}}{nR}\right)_{\max\, efficiency} > \left(\frac{R_{L,}}{nR}\right)_{\max\, power} > 1, \tag{19}$$

stating a ratio always greater than 1. As a consequence, despite the optimal loads corresponding to maximum efficiency and maximum power for the module can be quite close, in energy harvesting applications, where ΔT is not constant, it is necessary not to assume the matching load applies [29].

5. – System optimization

The optimization process for a thermoelectric harvester is related to the definition of the conditions for optimal components as well as to the design of a thermal chain effective in collecting the heat flow for the thermoelectric conversion. The target of the design is to satisfy three major requirements:

- The optimization of the module performance in terms of power and efficiency.
- The maximization of the temperature gradient useful for the conversion.

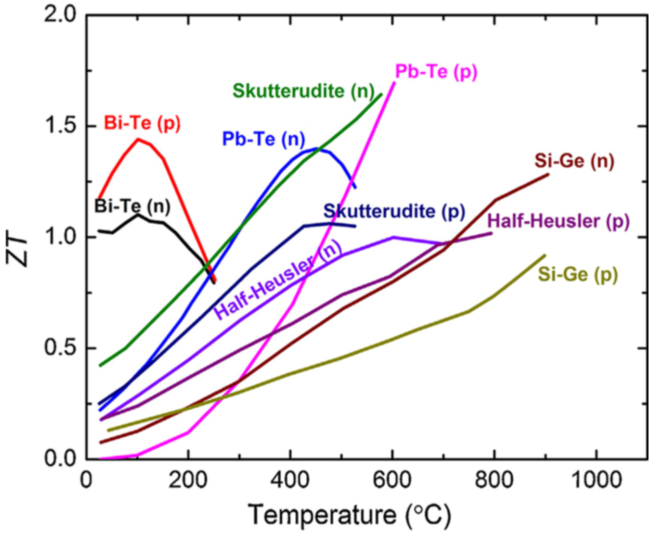

Fig. 4. – Adimensional figure of merit for different materials classes [31]. A number of materials reported show promising performance in the intermediate temperature range (200–500 °C): this comes from the interest for automotive applications promoting the focus of research on materials enabling exhausts heat recovery.

- The selection of materials and components for the TEG able to minimize the costs of the device.

The first strategy of device optimization is related to the choice of the materials used for the thermoelements. The parameter used to select the materials is the adimensional figure of merit, ZT. It is defined as

$$ZT = \frac{\alpha^2}{\rho\kappa}T \tag{20}$$

and describes the characteristics necessary to a material to be a good thermoelectric. In fact, a high Seebeck allows an effective voltage production in the presence of the thermal gradient. At the same time, a good electrical conductivity enables an effective reduction of Joule losses associated to the current into the material. To complete the picture, due to the need of a thermal gradient, the most efficient way to keep it stable with the lower loss of energy is to prevent a fast heat transfer from the hot to the cold side through the material. Such a condition requires a low thermal conductivity of the materials involved. The ZT parameter depends on temperature, so, in order to choose the materials for the module, the range of temperature involved in the harvesting process has to be correctly identified. In fig. 4 an example of ZT curves for different materials is reported [31]. The actual technology for thermoelectric devices is based on chalcogenides materials: based on $(Bi,Sb)_2(Te,Se)_3$ family of compounds, they offer the best ZT in the temperature range between 0 °C and 200 °C [24]. Increasing the temperature range no commercial devices, available for the market distribution, can be found. In the intermediate range, 200–500 °C, skutterudites [32], tellurides [33] and half Heusler compounds [31, 32] represent new promising materials capable of good performances but still suffering in terms of technology readiness in particular in terms of joint solutions and long-term thermal stability. In the high-temperature range, the best solution is offered by silicon-based alloys (Si-Ge alloys) [34]. It is to stress the need, as already reported discussing the efficiency, to select the materials with the best ZT's.

An important aspect to consider for the materials choice is related to the behavior under a temperature gradient. In the efficiency relationship the ZT considered at the mean temperature between T_h and T_c is considered. However, from the application point of view, the effective Z for each material is the one averaged among the temperature interval considered. As a consequence, a peaked behavior with temperature of ZT for a material, despite the high absolute value reached, results low efficient in terms of operating performance. A good material is the one having a broad dependence on temperature in the range of interest. The thermoelectric performances are not the only properties to be kept into account for the material selection. In fact, a major role is played by both chemical and mechanical stabilities. The thermal cycling next to the high temperatures play a critical role for the legs of the module, experiencing a mechanical pressure due to thermal expansion and an aging effect associated to the temperature [29]. Moreover, the presence of different materials in the module plays a role introducing internal mechanical stresses both between legs and at the joints. So, a critical aspect is the one associated to the mechanical compatibility of the materials used. This means to have materials with similar thermo-mechanical properties, allowing their coupling into the system without introducing mechanical stresses. These effects play a critical role in the designing of a segmented leg. The segmentation consists in coupling different materials along the leg in order to take advantage of the best performing material in a specific temperature range when a large ΔT is applied. In order to optimize the design in this specific case the compatibility between the materials involved has to be considered. In fact, not only the thermo-physical properties have to match, but the ZT curves of the materials have to be similar. Composing materials too different leads to a loss of efficiency due to an unbalance in the supported flows (can be heat or current) between the materials. More details are described and reported in the literature [35, 36].

A second step of device optimization is correlated to the impact of geometry of the elements on the device performance: it has been proved that a relevant improvement of electrical power output from the TEG can be obtained by optimizing the legs geometry. In fact, the number of thermocouples and the shape (length, section) of the legs, affecting the internal resistance, define the electrical output of the module. In particular, a low number of couples produce a low energy conversion, with a not sufficient voltage available. On the other side a large number of elements generates a high resistance into the module responsible for relevant Joule losses in operating conditions. Similarly, long, narrow legs promote high-voltage production, but the high electrical resistance limits the current. Short, large legs, instead, allow high currents but also promote the thermal exchange, reducing the temperature difference applied. The resulting strategy to optimize the design of the module is based on the balancing of the internal resistance in order to face the requirements of the final use of the TEG, following the guidelines already discussed for maximum power end efficiency of the module. At the same time, having two different materials involved in the thermocouple, a mutual equilibrium related to the heat and current flowing through the system has to be set in order to promote homogeneity in performance. The resulting condition relates the geometry of the elements to the properties of the materials used. The optimal design condition for promoting the best Z parameter for the module is

$$\frac{L_n A_p}{L_p A_n} = \sqrt{\frac{\rho_p \kappa_n}{\rho_n \kappa_p}}, \tag{21}$$

where L_i and A_i are the legs length and cross area, respectively [23, 25, 26, 37].

A further step in the optimization of the TEG is related to the maximization of the thermal coupling at hot and cold sides in order to take advantage of all the gradient available avoiding losses along the thermal chain. This problem is strongly related to the technology available for the heat exchangers. These components are often considered as a minor focus in thermoelectric technology development, however, due to the relevant effect played by the efficiency of the thermal exchange on the final TEG performance and costs, it is important to analyze this stage of the TEG design. Considering the final net efficiency of a TEG, the preferred solution for the heat exchangers should be the one based on passive systems, able to save electrical power. The metallic finned structure promotes the surface heat transfer: the parameters involved are the number of the fins and their height [38]. Increasing the two parameters favors a larger heat transfer affecting the final electrical output of the system. Here a critical aspect to be considered is the interface between the thermoelectric device and the heat exchanger. In fact, each interface acts as a thermal barrier to the heat transfer reducing the efficiency in ΔT achieving. In order to minimize the temperature loss, the coupling between the elements of the thermal change is usually promoted by filling layers able to reduce the thermal resistance of the interface. Filler materials can be in the form of paste or solid pads: typically, pastes promote a more effective thermal coupling between the components but their performances at temperatures above 250 °C are usually poor. Moreover, their efficiency is strongly affected by the homogeneity of the distribution, a factor not easy to reproduce and evaluate for a large-scale production. Thermal pads display a reproducible thermal contact, homogeneous on the whole surface, and the availability of different materials allow to select the effective solution for each temperature range. Unfortunately, thermal pads performances are usually dependent on the pressure applied to the system and the thermal resistances achievable are usually higher than the one allowed by pastes.

Considering the heat sink design, in order to maximize the electrical power output of a TEG, a condition on the thermal resistances of the different components can be written [39]. The thermal resistance for the heat sink, Θ_{HS}, at the hot side of the TEG can be written as

$$\Theta_{HS} = \frac{T_{Heat\,Sink} - T_{amb}}{\dot{Q}_h} . \tag{22}$$

And the same can be calculated at the cold side. Approximating with $\dot{Q}_h$ the total heat flow through the TEG, the thermal chain can be described by the relationship

$$\dot{Q}_h = \frac{T_{Heat\,Source} - T_{amb}}{\Theta_{tot}} = \frac{T_{Heat\,Source} - T_{amb}}{\Theta_{HS\,h} + \Theta_{HS\,c} + \Theta_{TEM}} , \tag{23}$$

considering the TEG operating between a heat source at $T_{Heat\,Source}$ and ambient temperature. The heat flow can be related by eq. (8) to the electrical power produced by the system resulting in an optimal power output when the condition

$$\frac{\Theta_{TEM}}{\Theta_{HS\,h} + \Theta_{HS\,c}} = 1 \tag{24}$$

is satisfied [39]. These results allow designing the thermal chain looking for the optimization of the overall TEG performance. Many experiments based on models are reported in the literature discussing the effective role of the heat exchangers in the maximization of the performances of a thermoelectric device. A basic analysis for the design of a heat dissipater can be found in [23, 29]. Here no specific discussion on other kind of heat exchangers is reported but, in order to manage the high heat flows proper of harvesting applications based on high-temperature sources, it is typically necessary to move from passive to active systems, in particular for the cold-side dissipation. The use of intermediate means with proper heat capacity and promoting a more efficient convection, allows more compact design and higher power densities. Moreover, the convective nature of the heat transfer leads to a relevant improvement both in power dissipated and in regime delay time. However, these systems introduce an operating power requirement affecting the net power production of the TEG.

To conclude the design optimization discussion, a short comment on costs optimization has to be done. The actual thermoelectric technology is suffering in the competition for the electrical power generation not only due to the low-efficiency characteristic of the actual state of the art, but also due to the high costs involved in the development of a novel device. In fact, the limited use of thermoelectric solutions does not promote a cost reduction coming from a large-scale market distribution. But this is not the only limitation for thermoelectrics: the commercial modules are actually based on tellurium compounds, expensive, not eco-friendly and, most of all, not earth-abundant materials. In addition to these critical characteristics of the material, the limited range of operating temperatures does not allow the access to more valuable heat, where the starting Carnot limit is higher. These considerations pushed the research in the development of new materials able to face the challenge of the high-temperature waste heat recovery. However, moving to this more profitable area, also provides a larger number of competing solutions for heat to electricity conversion. As a consequence, the need for higher ZT's becomes mandatory in order to make thermoelectricity a profitable option. Despite the wide availability of literature related to materials development, from the cost point of view a fast analysis of the state of the art underlines how almost 30% of the costs associated to the thermoelectric systems come from the heat exchangers. These are metallic components typically made of aluminum or copper alloys which can be customized in size and shape depending on the target use. The technologies involved in the components preparation are usually updated leading to a relevant cost growth when special design is proposed. A further development of a new generation of heat exchangers, based on novel technological solutions both for thermal transport and production processes could improve the opportunities for thermoelectricity as well as an improvement in active materials performance.

Out of the optimization focus, but still in the stream related to the potential solutions able to provide a future to thermoelectric technology, it is the development of new modules architectures. The flat configuration, extremely effective for the coupling to standard heat sinks, shows some limitations whenever the thermoelectric device has to face curved surfaces. The capability to provide a flexible device able to be coupled to surfaces like pipes or body parts can promote the application to energy harvesting from small to industrial scales. In the recent years, flexible modules have been developed by different research groups worldwide and prototypes coupling human body are already under study [40].

6. – Thermoelectric for power generation

To conclude the discussion on the thermoelectric technology used in the field of energy harvesting few examples are reported in the following. The cases reported have been chosen in order to display the state of art of the common applications for thermoelectrics and, at the same time, offer a discussion on the future perspective for this technological solution in everyday life [41]. The thermoelectric systems can be classified depending on the power scales involved: in fig. 5 the power scales are reported and compared to the power needs of actual devices.

The key element to improve the conversion efficiency is the effect of waste heat recovery. Waste heat is the heat produced by machines, industrial processes, electrical equipment down to human body. For many thermoelectric applications, despite the limited ΔT accessible, the heat useful for the conversion overcomes the capacity of the TEG itself. In many of these cases, a constant heat flow is delivered by the source at constant ΔT, creating an ideal condition for TEG operating. In this case, the low efficiency achievable by TEG does not mean to have a low performing system. Two are the main target application ranges: 1) High-power application: basically focused on wasted heat recovery at intermediate/high range of temperature. It is the harvesting based on exhausts of cars or industrial heats (electrical transformers, heat collected by cooling facilities, heat recovery from stoves and so on) [42-44]. Most of modern development in materials and design solutions comes from this branch of research trying to achieve the capability to operate with more valuable heats. 2) Low-power applications: based on

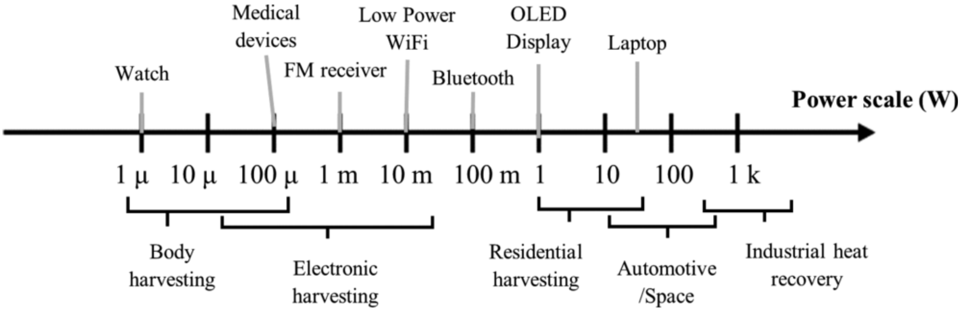

Fig. 5. – The power scales of thermoelectric generators. Next to the power generated by the TEGs, the typical supply needs for different common devices are reported. Increasing the available heat at the source (higher temperature, larger temperature drop) enables the access to an electrical power output more profitable in terms of supported devices. Actually, the most promising applications for harvesting stay in the range below 100 W.

the basic recovery from small electronic system as a stage of a heat dissipater mounted on chip. Here the heat available is at low temperature and in a limited quantity. As a consequence, the thermoelectric technology represents the only opportunity to value such a heat and the research target are the integration improvement and the production cost reduction. In this class human-body harvesting can be enlisted too.

6˙1. *High-power generation.* – Actual successful fields of application for thermoelectrics are really limited and particularly focused in the space exploration. As usually reported in the literature and conference communications speaking of thermoelectric generators, the main characteristic of these devices is the high reliability, a property making the TEGs the only effective solution for power production in the far from Earth space exploration [45]. When the photovoltaic option is no more efficient due to the low sun power availability or due to the environmental characteristics, a TEG offers, with its compact, robust and simple design, a unique solution for power generation. Here the heat source is typically a radioactive material, based on plutonium, heated by the decay up to 1000 °C, operating in the nucleus of the thermoelectric system assembled surrounding it. The design is usually made of long segmented legs able to operate at high temperature. It is to stress, the cold side of the RTEG for space exploration is kept cool mainly by radiating effects, so the materials involved are the one designed for high-temperature applications being the cold temperature in the range of 300–400 °C. Thermoelectric technology is the main source enabling outer planets missions and deep space exploration. Due to the radioactive materials involved, the RTEGs are a technological solution mainly developed by American space agencies. European Space Agency, up to now successfully supporting Sun and inner planets study, only in the last decade started a plan of funding for Am-241 based RTG development [46]. Despite the importance of the development of such complex systems, the peculiarity of the operating environments is such that the resulting contributions to standard technology development are limited. One of the main elements affecting the device, for example, is the material stability in temperature when operating in air, absent in space applications: this critical aspect strongly reduces the reliability of the device for high-temperature applications, hitting one of the main advantages of the thermoelectric solution.

The reference market for intermediate temperature applications is the automotive one. As already reported, a lot of development in thermoelectric technology has been promoted by the basic idea to integrate a thermoelectric generator on the exhausts line of a car [24, 47]. The interest in automotive comes from the large wasted heat available coming from the engine together with the presence of a cooling system already active in the car. Calculations suggest how with a TEG operating on the exhaust gases an improvement up to 16% of the car efficiency could be achieved. The temperature range proper of automotive pushed the research for new materials able to safely operate at the temperature of the exhaust. At the same time, the definition of novel design for the conversion device enables the study of more efficient and reliable assembly solutions. The target of the system development is to produce power enough to allow the removal of the alternator from the engine. This would result in a gasoline saving in the order of 3–5%. There are, for this applications, a lot of critical steps to be optimized ranging from the material to the coupling system. The materials used up to now are in the class of chalcogenides, having a ZT average close to 1 but an operating temperature range not centered to the one available in the system. As a consequence, a direct coupling of the device to the hot gas flow is not allowed. So, an appropriate design is required to collect only the heat fraction useful to achieve the suitable temperature. Moreover, the exhausts temperature depends on the engine regime, producing an unstable operating condition for the TEG. The solution to this specific problem has been explored trying to place the TEG in different positions along the exhausts line. The resulting systems developed up to now are capable of powers in the range of 500 W in duty cycle tests [24, 48]. The solutions designed are favorable for trucks, running most of the time in constant regime, and for heavy vehicles. In fact, the problem of using chalcogenide materials is not only related to the low-temperature needs, but also to the high weight of the resulting device. The weight makes it not useful for small vehicles, where the small engine suffers the fact that the increase of consumptions associated to the TEG is no more compensated by the saving due to the removal of the alternator. At the same time, the city cars driving regime is far from being constant deeply affecting the TEG performance. In recent years, the focus on electrical cars development is responsible for a loss of interest in the automotive application for thermoelectric power generation: the perspective of a removal of the thermal engine should make TEGs useless devices.

Spacecraft and automotive applications are designed for high-power generation, converting high temperature and massive heat recovered by a major source. Similar applications are the one related to industrial waste heat recovery where thermoelectrics can be used to improve the overall system efficiency or to reduce the maintenance costs thanks to the long life and high reliability of the TEGs [41]. In case of industrial applications, a further advantage for the operating system is offered by the long time operation: a continuous operation reduces the thermal cycling of the materials preventing degradations related to thermomechanical stresses associated to the heating-cooling phases.

6˙2. *Low-power generation.* – Thermoelectric harvesting is getting interesting for the low-power generation thanks to the increasing development of distributed network of electronic and portable devices. The applications associated to the microelectronic represent a growing field in which the electrical power requirements are daily increasing. Despite the large power required, the single components needs are often limited to few mW, a power scale matching the electrical power output of a small TEG. For these applications a strong constrain is usually represented by the limited volume available for the device. The compact design offered by the thermoelectric devices allows the integration of the harvester on-board enabling a localized power production useful for the self-powering of sensors or ancillary functions. The limit of such a development happens to be related to the heat dissipation capacity at the cold side of the device due to the reduced coupling surfaces and the closed volumes. As a consequence, such a solution operates on narrower ΔT as respect to the potential achievable. The optimization of the design of a thermoelectric harvesting device for microelectronic application is mainly related to the definition of the best solution for heat removal at the cold side in a close volume with the goal to make the thermal gradient across the TEM the highest possible. The target application of these harvesters is the heat recovery from chip or hot electronic components and the power produced stored in battery or charging capacitor designed to cyclically supply communication systems or active sensors. On-chip harvesting offers the potential to reduce overall energy consumption by using thermal energy to power some of the functional units on the chip [49]. The gradient available is generally low and the temperature stays below $100\,^{\circ}\mathrm{C}$ at the hot side. The best materials for this range are commercial chalcogenides allowing a conversion efficiency in the order of 5–6%. Due to the low temperature, the efficiency of the dissipaters associated both to conductive and convective mechanisms is limited. As a consequence, solutions for the thermal coupling of the cold side to larger thermal sinks are studied: a promising strategy is offered by heat pipes exchangers [50], able to enhance the heat transfer. Heat pipes do not dissipate the heat for free but allow to move the heat from the concentrated space of the TEG to a larger volume where more efficient exchange mechanisms can be adopted. The efficiency of heat pipes can be set by using appropriate phase change materials, able to improve the thermal transfer in the specific operating temperature of the device [51, 52]. A critical aspect to make the TEG profitable is the design of the output control unit: the power produced by these small devices stays between μW and mW, often too low to be used by a system. However, a suitable power output conditioning and management stage can be used to make the output useful [53, 54]. The main target for this development is the power supply of data transmission units based on WiFi or Bluetooth communication protocols [55]. Achieving the result means to be able to create an interconnected network of speaking device with a communication system self-powered: this can promote a relevant step forward in the internet of things. A comment on the development of the thermoelectric device can be added to this discussion. The search for the thermoelectric system integration into the small-scale chips suggested the development of a thermoelectric device based on silicon. This solution still represents a perspective from the technological point of view, but should offer a deep revolution in the integration process for micro-harvesters [56, 57].

Another interesting application of thermoelectric harvesting in the low power range is the one associated to the human-body heat harvesting. The human body can be seen as a heat source at constant temperature moving into an environment generally cooler than itself [58]. Following this approach, the target of body harvesting is to convert the heat released by humans into electrical power. The electrical power output achievable by a human body can be estimated considering the thermal power produced and the surface available for the heat collection. A resting male releases heat through the body in the range of 100–120 W: this heat is dissipated by the skin, so the surface power density can be roughly evaluated by dividing the power by the average surface of the body. Considering a value between $1.7\,\mathrm{m}^2$ and $1.9\,\mathrm{m}^2$, the resulting power density released is approximately $5\,\mathrm{mW/cm}^2$. As expected, the input power available is limited and, in addition, the temperature gradient is in the range of few degrees (4–10 °C). In order to determine the potential electrical power produced by a thermoelectric harvester, the ZT associated to the device has to be considered. Due to the temperature range considered, the optimal materials for the TEG are chalcogenides, allowing a ZT close to 1. The maximum efficiency corresponding to a $\Delta T = 10\,^\circ\mathrm{C}$ for the device with $ZT = 1$ stays between 1% and 3%, so the expected power output is in the order of $0.1\,\mathrm{mW/cm}^2$. The data reported are not really promising if compared to the power needs of electronic devices. However, body harvesting has the advantage to use a heat source largely available. The design of a TEG has to face challenges peculiar to body harvesting: most of them are related to the thermal coupling of the module to the body and to the heat removal through the thermal chain. The target is to take advantage of the maximum ΔT achievable. This requires, due to the low-temperature difference available, to perfectly thermally couple the module both to skin and to the environment. The standard modules, due to shape and rigidity, hardly match the body. So, the thermal resistance prevents the T_h reaching the skin value. To overcome this problem, flexible devices have been developed offering the opportunity to fit in an efficient way the irregular profile of the human skin [59-61]. Despite the advantages offered for the thermal coupling to the body by the flexible structure, the structure itself displays a number of challenges associated to the mechanical stability and the electrical integrity. Different strategies are reported in the literature to overcome this critical aspects: the two main approaches are based on thin-film modules deposited on flexible substrates and on a composite made of a polymeric matrix keeping the active thermoelectric components together. In both cases, the transfer of the ΔT to the active material stays critical. Actually, body harvesting based on thermoelectrics is used into same low-power smart devices like smart watches and medical sensors/devices: the power delivered is usually not able to fully supply the needs of the device, but it enables a enhanced period time operating.

7. – Closing remarks

In this short report the basics on the thermoelectric harvesting have been discussed: starting from the thermoelectric phenomena, the analysis moved to the description of the thermoelectric module as the starting point for a system design. Next to a theoretical approach, a description of the practical characteristics of the module has been introduced focusing on some technical aspects useful for the application development. In the following, a short analysis on the system design optimization has been done: different aspects related to materials selection, thermoelements shaping and system components dimensioning have been introduced and commented with the aim to give a general idea on the critical aspect hidden at each stage of development of a thermoelectric generator. The discussion showed how the efficiency of the TEG is strongly affected by each component of the system. Starting from a conversion efficiency of the materials potentially in the order of 10–12%, the costs associated to the assembly of the legs into a module move this value down to 4–7%. Going forward and designing the final TEG, complete of the components of the thermal chain, the final efficiency can scale down to 2–4%. The discussion here proposed tries to describe the mechanisms producing the losses observed providing possible alternatives or solutions. As closing remarks, some examples of thermoelectric applications have been reported representing the past, present and probably future challenges for thermoelectrics from the technological point of view.

REFERENCES

[1] Roundy S., Steingart D., Frechette L., Wright P. and Rabaey J., "Power sources for wireless sensor networks", in *1st European Workshop on Wireless Sensor Networks Berlin, 2004* (Springer, Berlin, Heidelberg) 2004.

[2] Vullers R. J. M., Van Schaijk R., Doms I., Van Hoof C. and Mertens R., *Solid-State Electron.*, **53** (2009) 684.

[3] Oh J., Yuan H. C. and Branz H. M., *Nat. Nanotechnol.*, **7** (2012) 743.

[4] Qin Y., Wang X. and Wang Z. L., *Nature*, **451** (2007) 809.

[5] Lingampalli S. R., Gautam U. K. and Rao C. N. R., *Energy Environ. Sci.*, **6** (2013) 3589.

[6] Dilion A. C., Jones K. M., Bekkedahl T. A., Kiang C. H., Bethune D. S. and Heben M. J., *Nature*, **386** (1997) 377.

[7] Gratzel M., *Nature*, **414** (2001) 338.

[8] Wang Z. L. and Song J., *Science*, **312** (2006) 242.

[9] Wu W., Wang L., Li Y., Zhang F., Lin L., Niu S., Chenet D., Zhang X., Hao Y., Heinz T. F., Hone J. and Wang Z. L., *Nature*, **514** (2014) 470.

[10] Xu S., Qin Y., Xu C., Wei Y., Yang R. and Wang Z. L., *Nat. Nanotechnol.*, **5** (2010) 366.

[11] Oregan B. and Gratzel M., *Nature*, **353** (1991) 737.

[12] Wang P., Zakeeruddin S. M., Moser J. E., Nazeeruddin M. K., Sekiguchi T. and Gratzel M., *Nat. Mater.*, **2** (2003) 402.

[13] You J., Dou L., Yoshimura K., Kato T., Ohya K., Moriarty T., Emery K., Chen C. C., Gao J., Li G. and Yang Y., *Nat. Commun.*, **4** (2013) 1446.

[14] Poudel B., Hao Q., Ma Y., Lan Y., Minnich A., Yu B., Yan X., Wang D., Muto A., Vashaee D., Chen X., Liu J., Dresselhaus M. S., Chen G. and Ren Z., *Science*, **320** (2008) 634.

[15] Kim S. I., Lee K. H., Mun H. A., Kim H. S., Hwang S. W., Roh J. W., Yang D. J., Shin W. H., Li X. S., Lee Y. H., Snyder G. J. and Kim S. W., *Science*, **348** (2015) 109.

[16] DRESSELHAUS M. S., CHEN G., TANG M. Y., YANG R. G., LEE H., WANG D. Z., REN Z. F., FLEURIAL J. P. and GOGNA P., *Adv. Mater.*, **19** (2007) 1043.

[17] Snyder G. J., "Thermoelectric energy harvesting", in *Energy Harvesting Technologies*, edited by PRIYA S. and INMAN D. J. (Springer, Boston, MA, USA) 2009, pp. 325–336.

[18] WANG C. C., HUNG C. I. and CHEN W. H., *Energy*, **39** (2012) 236.

[19] CAMACHO-MEDINA P., OLIVARES-ROBLES P. A., VARGAS-ALMEIDA A. and SOLORIO-ORDAZ A., *Entropy*, **16** (2014) 2890.

[20] BROWNELL E. and HODES M., *IEEE Trans. Compon. Packag. Manufact. Technol.*, **4** (2014) 612.

[21] MARCIA-BARBER E., *Thermoelectric Materials. Advances and Applications* (Taylor & Francis Group, New York, NY, USA) 2015.

[22] GOLDSMID H. J., *Introduction to Thermoelectricity* (Springer, Boston, MA, USA) 2010.

[23] ROWE D. M., *CRC Handbook of Thermoelectrics* (CRC Press, Boca Raton, FL, USA) 1995.

[24] ORR B., AKBARZADEH A., MOCHIZUKI M. and SINGH R., *Appl. Therm. Eng.*, **101** (2016) 490.

[25] ANGRIST S. W., *Direct Energy Conversion*, 4th edition (Allyn and Bacon, Boston, MA, USA) 1982.

[26] COBBLE M. H., "Calculation of Generator Performance", in *CRC Handbook of Thermoelectrics* (CRC Press, Boca Raton, FL, USA) 1995.

[27] HODES M., *IEEE Trans. Compon. Packag.*, **33** (2010) 307.

[28] HE J. and TRITT T. M., *Science*, **357** (2017) eaak9997.

[29] HENDRICKS T. J. and CRANE D. T., "Thermoelectric Energy Recovery Systems: Thermal Thermoelectric and Structural Considerations", in *Modules, Systems and Applications in Thermoelectrics*, edited by ROWE D. M. (CRC Press, Boca Raton, FL, USA) 2012.

[30] HENDRICKS T. J., KARRI N. K., HOGAN T. P. and CAUCHY C. J., *Proceedings of 44th Power Sources Conference, IEEE Power Sources Publication* (IEEE) 2010, pp. 609–612.

[31] CHEN S. and REN Z., *Mater. Today*, **16** (2013) 387.

[32] SCHIERNING G., CHAVEZ R., SCHMECHEL R., BALKE B., ROGL G. and ROGL P., *Trans. Mater. Res.*, **2** (2015) 025001.

[33] KANATZIDIS M. G., *Chem. Mater.*, **22** (2010) 648.

[34] NOZARIASBMARZ A., AGARWAL A., COUTANT Z. A., HALL M. J, LIU J., LIU R., MALHOTRA A., NOROUZZADEH P., ÖZTÜRK M. C., RAMESH V. P., SARGOLZAEIAVAL Y., SUAREZ F. and VASHAEE D., *Jpn. J. Appl. Phys.*, **56** (2017) 05DA04.

[35] SNYDER G. J., *Appl. Phys. Lett.*, **84** (2004) 2436.

[36] SNYDER G. J. and URSELL T. S., *Phys. Rev. Lett.*, **91** (2003) 148301.

[37] ALI H., SAHIN A. Z. and YILBAS B. S., *Energy Convers. Manag.*, **78** (2014) 634.

[38] ELGHOOL A., BASRAWI F., IBRAHIM T. K., HABIB K., IBRAHIM H. and IDRIS D. M. N. D., *Energy Convers. Manag.*, **134** (2017) 260.

[39] BRANOVSKI L. L., SNYDER G. J. and TOBERER E. S., *J. Appl. Phys.*, **113** (2013) 24904.

[40] BAHK J. H., FANG H., YAZAWA K. and SHAKOURI A., *J. Mater. Chem. C*, **3** (2015) 10362.

[41] JAZIRI N., BOUGHAMOURA A. and MÜLLERETAL J., *Energy Rep.* (2019) in press, available online at `https://doi.org/10.1016/j.egyr.2019.12.011`.

[42] CHAMPIER D., BEDECARRATS J. P., RIVALETTO M., STRUB F. and PIGNOLET P., *Energy*, **36** (2011) 1518.

[43] CHAMPIER D., BEDECARRATS J. P., RIVALETTO M. and STRUB F., *Energy*, **35** (2010) 935.

[44] FANCIULLI C., ABEDI H., MEROTTO O., DONDÈ R., DE IULIIS S. and PASSARETTI F., *Appl. Energy*, **215** (2018) 300.

[45] VON LUKOWICZ M., ABBE E., SCHMIEL T. and TAJMAR M., *Energies*, **9** (2016) 1.

[46] Ambrosi R. M., Williams H., Watkinson E. J., Barco A., Mesalam R., Crawford T., Bicknell C., Samara-Ratna P., Vernon D., Bannister N., Ross D., Sykes J., Perkinson M. C., Burgess C., Stroud C., Gibson S., Godfrey A., Slater R. G., Reece M. J., Chen K., Simpson K., Tuley R., Sarsfield M., Tinsley T. P., Stephenson K., Freis D., Vigier J. F., Konings R. J. M., Fongarland C., Libessart M., Merrifield J., Kramer D. P., Byrne J. and Foxcroft B., *Space Sci. Rev.*, **215** (2019) 55.

[47] Kuo Huang, Yuying Yan, Bo Li, Yong Li, Kai Li and Jun Li, *Automot. Innov.*, **1** (2018) 54.

[48] Risseh A., Nee H. P., Erlandsson O., Brinkfeldt K., Contet A., Frobenius F., Gaiser G., Saramat A., Skåre T., Nee S. and Dellrud J., "Design of a Thermoelectric Generator for Waste Heat Recovery Application on a Drivable Heavy Duty Vehicle", *SAE Int. J. Commer. Veh.*, **10** (2017) 26.

[49] Li D., Ogrenci-Memik S. and Henschen L., "On-Chip Integration of Thermoelectric Energy Harvesting in 3D ICs", in *2015 IEEE International Symposium on Circuits and Systems* (IEEE) 2015, pp. 1078–1081.

[50] Ochterbeck J. M., "Heat Pipes", in *Heat Transfer Handbook*, edited by Bejan A. and Kraus A. D. (Wyley & Sons, Hoboken, NJ, USA) 2003, pp. 1181–1230.

[51] Rashidi S., Shamsabadi H., Esfahani J. A. and Harmand S., *J. Therm. Anal. Calorim.*, **140** (2020) 1655.

[52] Ying-Che Weng, Hung-Pin Cho, Chih-Chung Chang and Sih-Li Chen, *Appl. Energy*, **88** (2011) 1825.

[53] Park H., Lee D., Park G., Park S., Khan S., Kim J. and Kim W., *J. Phys. Energy*, **1** (2019) 042001.

[54] Mamur H. and Ahiska R., *Energy Convers. Manag.*, **97** (2015) 265.

[55] Shaikh F. K. and Zeadally S., *Renew. Sustain. Energy Rev.*, **55** (2017) 1041.

[56] Calaza C., Salleras M., Dávila D., Tarancón A., Morata A., Santos J. D., Gadea G. and Fonseca L., *Mater. Today: Proc.*, **2** (2015) 675.

[57] Noyan I. D., Dolcet M., Salleras M., Stranz A., Calaza C., Gadea G., Pacios M., Morata A., Tarancon A. and Fonseca L., *J. Power Sources*, **413** (2019) 125.

[58] Zhou M., Al-Furjan M. S. H., Zou J. and Liu W., *Renew. Sustain. Energy Rev.*, **82** (2018) 3582.

[59] Kim S. J., Lee H. E., Choi H., Kim Y., We J. H., Shin J. S., Lee K. J. and Cho B. J., *ACS Nano*, **10** (2016) 10851.

[60] Sugahara T., Ekubaru Y., Van Nong N., Kagami N., Ohata K., Hung L. T., Okajima M., Nambu S. and Suganuma K., *Adv. Mater. Technol.*, **4** (2019) 1800556.

[61] Shinohara Y., *Mater. Today: Proc.*, **2** (2015) 877.

This page intentionally left blank

Proceedings of the International School of Physics "Enrico Fermi"
Course 207 "Advances in Thermoelectricity: Foundational Issues, Materials and Nanotechnology",
edited by D. Narducci, G. J. Snyder and C. Fanciulli
(IOS, Amsterdam; SIF, Bologna) 2021
DOI 10.3254/ENFI210007

Low-dimensional inorganic/organic hybrid thermoelectrics

K. Koumoto

Nagoya Industrial Science Research Institute - Chikusa-ku, Nagoya 464-0819, Japan

Summary. — Flexible thermoelectric (TE) devices for maintenance-free and long-lasting power source that makes use of the body heat, industrial waste heat and even solar heat have been of growing interest. Low-dimensional nanomaterials, such as 2D TMDCs (transition metal dichalcogenides) and 1D CNTs (carbon nanotubes), are the best-known candidate materials for high-performance flexible TE devices. TiS_2/organics hybrid superlattice materials and CNTs-based nanocomposites will be focused and their interesting structures, TE properties, and manufacturing processes are demonstrated and discussed. Some examples of device applications of the low-D nanomaterials are also presented.

1. – Introduction

Thermoelectric materials have been mostly inorganics based on metals, alloys, and inorganic compounds for a long time, but recently we have witnessed a rapid growth of organics for near room-temperature applications [1-5]. High thermoelectric performance of organic materials appear to be mainly due to their low thermal conductivity, and the guiding principle to get high ZT ($= S^2\sigma T/\kappa$, S: Seebeck coefficient, σ: electrical conductivity, κ: thermal conductivity, T: absolute temperature) is to enhance the power factor, $S^2\sigma$, of low thermal conductivity organics. This is completely opposite to that for exploiting inorganic thermoelectric materials, which usually possess high power factor but also high thermal conductivity.

Flexible thermoelectric (TE) devices for maintenance-free and long-lasting power source that makes use of the body heat, industrial waste heat and even solar heat have been of growing interest. Despite their high TE performance, conventional inorganic TE semiconductors, such as Bi_2Te_3 and skutterudites, are restricted for such applications due to their non-flexible nature and non-scalable manufacturing techniques.

Low-dimensional nanomaterials, such as TMDCs (transition metal dichalcogenides) and CNTs (carbon nanotubes), are the best-known candidate materials for flexible TE devices. Inorganic/organic hybridization based on 1D or 2D nanomaterials is a promising strategy for constructing high-performance flexible thermoelectric materials that can be applied to energy harvesting in the future IoT society.

TiS_2/organics hybrid superlattice materials [6, 7] and CNTs-based nanocomposites will be focused and their interesting structures, TE properties, and manufacturing processes will be demonstrated and discussed.

2. – 2D nanomaterials: transition metal dichalcogenides (TMDCs)

Transition metal dichalcogenides (TMDCs) with 2D layer structures are well known to show various electromagnetic and optical properties derived from their specific band structures. Applications of these compounds to nanomaterials and devices have been widely researched recently [8] because a material that is just a few atoms thick can have very different fundamental properties from a material made of the same molecules in solid form [9]. Among these TMDCs, MoS_2 is the most popular material and its thermoelectric performance has been surveyed both theoretically and experimentally [10-12]. TiS_2 is another interesting compound for a thermoelectric material due to its unique band structure, and we have investigated this compound for more than 5 years from the point of view of reducing its high thermal conductivity while maintaining its high power factor [13-17].

TiS_2 crystallizes into a CdI_2-type layer structure (trigonal system, space group) with TiS_2 slabs stacking alternately in the c-axis direction. The band structure of TiS_2 with a stoichiometric composition, *i.e.* $Ti/S = 1/2$, possesses an indirect band gap indicating it is a semimetal [18]. However, a crystal synthesized by a conventional method has a non-stoichiometric composition, $Ti_{1+x}S_2$, in which excess Ti atoms are self-intercalated into the van der Waals gap between TiS_2 layers. Excess Ti atoms become ionized and the released electrons become excited to the conduction band together with the elevation of the Fermi level, and hence it becomes an n-type degenerate semiconductor showing metallic conduction. The bottom of the conduction band is composed of triply degenerate Ti3d (t_{2g}) orbitals with high density of states, so that electrons excited to the conduction band would become heavy (effective mass $\sim 4\ m_0$) and give rise to a large Seebeck coefficient. Accordingly, TiS_2 is a good candidate TE material with high power factor even at room temperature. However, its ZT is rather low, ~ 0.16 at 300 K [19], as its thermal conductivity (4–$5\,\mathrm{Wm^{-1}\,K^{-1}}$ at room temperature) is too high compared with the conventional TE materials whose thermal conductivity is below 1–$2\,\mathrm{Wm^{-1}\,K^{-1}}$.

As the TiS_2 layers are weakly bonded by van der Waals forces, a crystal can be cleaved easily to nanosheets, just like a graphite crystal is easily cleaved to form graphene. The

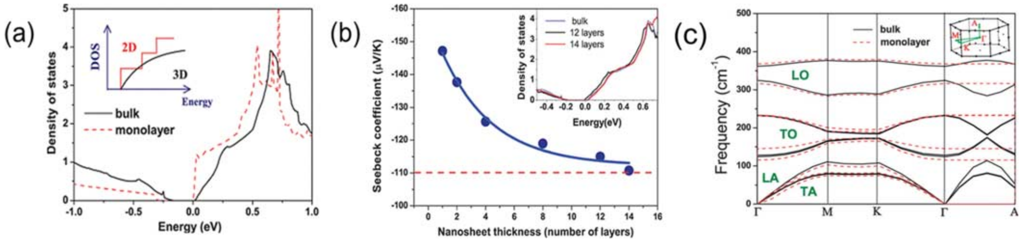

Fig. 1. – (a) DOS near the Fermi level, (b) Seebeck coefficient as a function of the number of Ti sulphene layers, (c) the phonon dispersions of bulk TiS_2 and its monolayer nanosheet [20].

resulting monolayer is called Ti sulphene [20]. When the crystal is reduced to a single layer of TiS_2, the density of states near the conduction band minimum sharply increases, two-dimensionality is very much enhanced (fig. 1(a)) and the Seebeck coefficient increases dramatically with a decreasing number of Ti sulphene layers (fig. 1(b)). So, on one hand, the two-dimensional confinement of electrons in very thin nanosheets gives rise to a large in-plane Seebeck coefficient and, on the other hand, the two-dimensional confinement of phonons reduces the thermal conductivity as the phonon dispersion is suppressed in thin nanosheets (fig. 1(c)).

Accordingly, titanium sulphene nanosheets can be regarded as very nice functional nanoblocks, and integrating them with other different nanoblocks in a periodic manner would lead to the construction of superlattice structures. For example, metal atoms or metal sulfide nanoblocks can be intercalated into the van der Waals gap between the sulphene layers to form a natural superlattice. This has been proven efficient in enhancing the thermoelectric performance of TiS_2 [13-17]. Another variation is inorganic/organic hybrid superlattices. This is exactly what we have proposed as a new strategy for the next-generation TE materials design.

3. – TiS_2/organic hybrid superlattices (intercalation complex)

3$^{\cdot}$1. *Synthesis and characterization.* – We synthesized an inorganic/organic superlattice with facile two-step chemical processes, including electrochemical intercalation and solvent exchange (fig. 2). TiS_2 single crystals, 3–5 mm in size and 0.1–0.2 mm thick, were synthesized in a silica ampoule using the chemical vapor transport method [21] and were used as the host material. The TiS_2 crystals were used as the cathode in electrochemical reaction cells with the organic salt dissolved in a solvent acting as the electrolyte. When an electrical potential was applied, part of the Ti^{4+} in TiS_2 was reduced to Ti^{3+} and the TiS_2 layers were negatively charged with additional carriers. The organic cations in the electrolyte were intercalated into the van der Waals gap, driven by the Coulomb force, and an inorganic/organic superlattice was formed. Owing to the cation-dipole effect, the solvent molecules are co-intercalated with the organic cations, which can be changed into other polar solvent molecules as desired by a solvent exchange reaction [22].

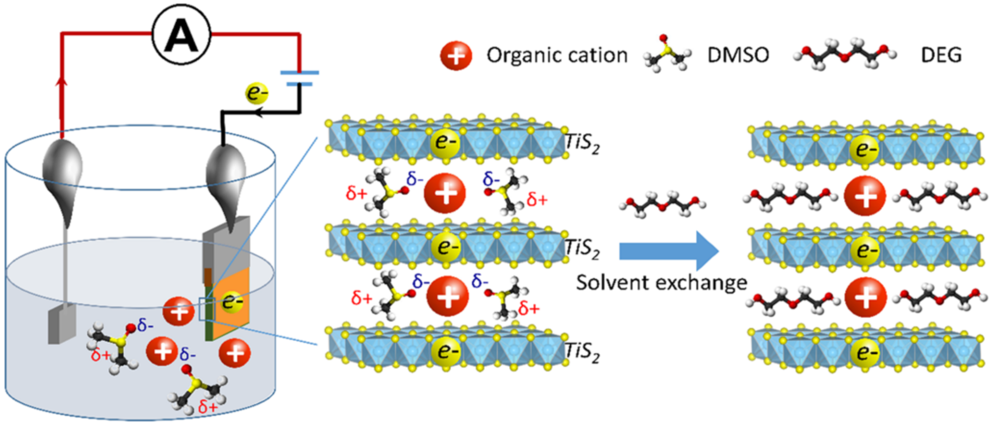

Fig. 2. – Electrochemical intercalation of solvated organic cations and hybrid superlattice formation by solvent exchange [6].

Hexylammonium (HA) chloride dissolved in dimethylsulphoxide (DMSO) was chosen here as the electrolyte. The electrochemical intercalation process was performed under a constant voltage of 1.8 V for 20 min, which resulted in a hybrid superlattice of $TiS_2(HA)_x(DMSO)_w$. The hybrid superlattice was then immersed in a solution of polar molecules to form $TiS_2(HA)_x(PM)_y(DMSO)_z$ (PM = polar molecules) after most of the DMSO molecules were exchanged with polar molecules. Thermogravimetric differential thermal analysis was performed on the samples to study their thermal stability. $TiS_2(HA)_x(DMSO)_w$ was found to have low thermal stability and continuously lost weight when it was heated above room temperature. In contrast, $TiS_2(HA)_x(PM)_y(DMSO)_z$ maintained its weight and was stable up to over 100 °C, which is suitable for thermoelectric applications around room temperature.

The nuclear magnetic resonance (NMR) analysis confirmed that the organic molecules, including HA and DMSO, had been incorporated into the TiS_2 crystal with a composition of $TiS_2(HA)_{0.09}(DMSO)_{0.15}$ after the electrochemical intercalation process. The interlayer distance between TiS_2 expanded from 5.69 Å to 13.9 Å. The as-prepared $TiS_2(HA)_{0.09}(DMSO)_{0.15}$ was then used as a precursor by being immersed in the solutions of other polar molecules and heated to 50 °C for 24 h to prepare a series of hybrid inorganic/organic superlattices through solvent exchange reactions. The NMR results showed that the target molecules had been successfully incorporated and there was no DMSO residue. There were some deviations in HA ion content, which might have been caused by the differences in the sizes and shapes of the original TiS_2 single crystals. The XRD result showed that the interlayer distance for all the hybrid materials were almost identical, around 13.9–14.2 Å. The similar XRD patterns indicated that all hybrid inorganic/organic materials have similar structures (fig. 3(a)). High angle annular dark field scanning transmission electron microscopy (HAADF-STEM) observation of $TiS_2(HA)_{0.097}(PEG1000)_{0.028}$, for example, showed the layered structure with

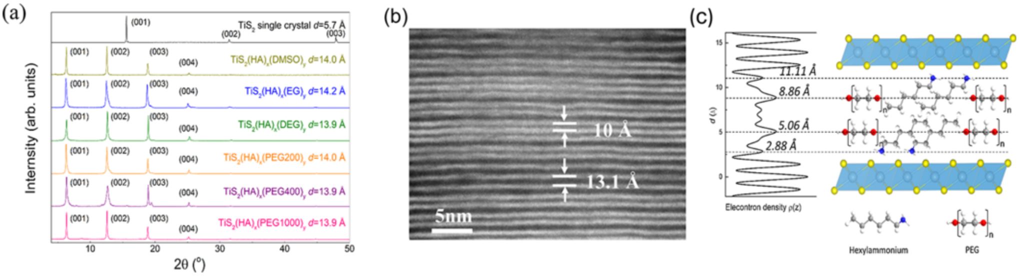

Fig. 3. – (a) XRD patterns and interlayer distances of inorganic/organic hybrid superlattices, (b) The HAADF-STEM of image of TiS_2[(HA)(PEG1000)], and (c) one-dimensional electron density map along the *c*-axis showing molecular arrangement [7].

alternating bright and dark areas, where the bright areas represent the inorganic TiS_2 layers and the dark areas are the organic layers (fig. 3(b)). The image clearly indicated that every TiS_2 layer is sandwiched between two organic layers, forming a stage-1 structure [7].

To determine the geometric structures (the size and the steric arrangement) of the intercalated organic molecules, the hybrid material was ultrasonically pulverized and a thin film was prepared by dropping the dispersion solution onto the surface of a CaF_2 substrate which was then analyzed by polarized Fourier transform infrared (FTIR) spectroscopy [7]. It was found that the HA ions and the TiS_2 layers formed an angle of 64° with respect to the normal of the TiS_2 basal plane. Long HA molecules were always well aligned and formed paraffin-like bilayer structures in the intercalation layered compounds due to the hydrophobic interactions [23]. The one-dimensional electron density map along the *c*-axis of the hybrid inorganic/organic material (derived from the Fourier transform of the XRD pattern) showed three sharp peaks appearing at -1.43, 0, and 1.43 Å (fig. 3(c)). These peaks correspond to the triple atomic planes in TiS_2, including a layer of Ti atoms (at 0 Å) sandwiched by two S atom planes (at ∓1.43 Å). The small peaks located between the neighboring strong triple peaks for TiS_2 should be due to the ordered organic molecules. The shape of the electron density map clearly suggested that the layered structure was centrosymmetric, which is consistent with the bilayer model for the HA cations. The small peaks at 2.88 and 11.11 Å corresponded to the ammonium head groups. There were also two relatively strong symmetric peaks at 5.06 and 8.86 Å, which were assigned to the PEG molecules. The PEG molecules that were confined with an interlayer distance of 8.2 Å between two TiS_2 layers could have double layers with planar zigzag conformation or could have adopted a coil conformation. However, if the latter case was true, the electron density map would have had a broadened peak, dispersed halfway between the TiS_2 peaks. The appearance of the two strong symmetric peaks (3.8 Å apart at 5.06 and 8.86 Å) instead clearly indicated that the PEG molecules had a double-layer planar zigzag conformation and the molecular planes were parallel to the TiS_2 layers, as shown in fig. 3(c).

3˙2. *Advantages of inorganic/organic hybrid superlattices.* – Construction of inorganic/organic hybrid superlattices would provide us with a lot of advantages in enhancing thermoelectric performance through interlayer as well as intralayer interactions:

- Quantum confinement effect: Electronic carriers confined in an inorganic layer sandwiched by two insulating organic layers would become heavy and generate a large Seebeck coefficient. Phonons are also confined within an inorganic layer and their two-dimensionally restricted movement would lead to lower thermal conductivity.

- Chemical interactions: Inorganic layers and organic layers in a hybrid superlattice would form certain chemical bonds that are different from weak van der Waals bond existing in a pristine inorganic layer compound. This bond formation would affect both electron and phonon transport.

- Physical interactions: Electrostatic interactions between carrier electrons (holes) in an inorganic layer and cations (anions) in organic layers would affect the electron transport. Long-range interactions between phonons in an inorganic layer and the dipole moment of polar molecules in organic layers would affect the phonon transport.

It would be possible to enhance ZT by deliberately controlling these effects and/or interactions, though they are correlated in a complicated manner. In the following sections thermoelectric properties of TiS_2-based hybrid superlattices will be described.

3˙3. *Tuning of carrier mobility.* – Charge carriers, electrons in this case, move around in the inorganic TiS_2 layers and organic cations (HA) are situated between the inorganic layers, so that the movement of negatively charged electrons is always limited by Coulomb attractive force (eq. (1)) exerted by positively charged organic cations

$$F = \frac{1}{4\pi r^2}\frac{1}{\varepsilon_0} q_1 q_2, \tag{1}$$

where F is the Coulomb attractive force, ε_0 the static dielectric constant of the medium, r the distance between two charges q_1 and q_2. However, if the polar molecules are present between the inorganic layers, they would affect the electrostatic interactions between organic cations and carrier electrons. According to eq. (1), a larger static dielectric constant of polar molecules would weaken the Coulomb attractive force and hence enhance carrier mobility.

To systematically vary the dielectric constants, a series of organic molecules with polar hydroxyl groups, including ethylene glycol (EG), diethylene glycol (DEG) and poly(ethylene glycol) of average molecular weight with 200, 400 and $1000\,\mathrm{g \cdot mol^{-1}}$ (denoted as PEG 200, PEG 400 and PEG 1000, respectively) were chosen. The static dielectric constant decreases with an increasing degree of polymerization (molecular

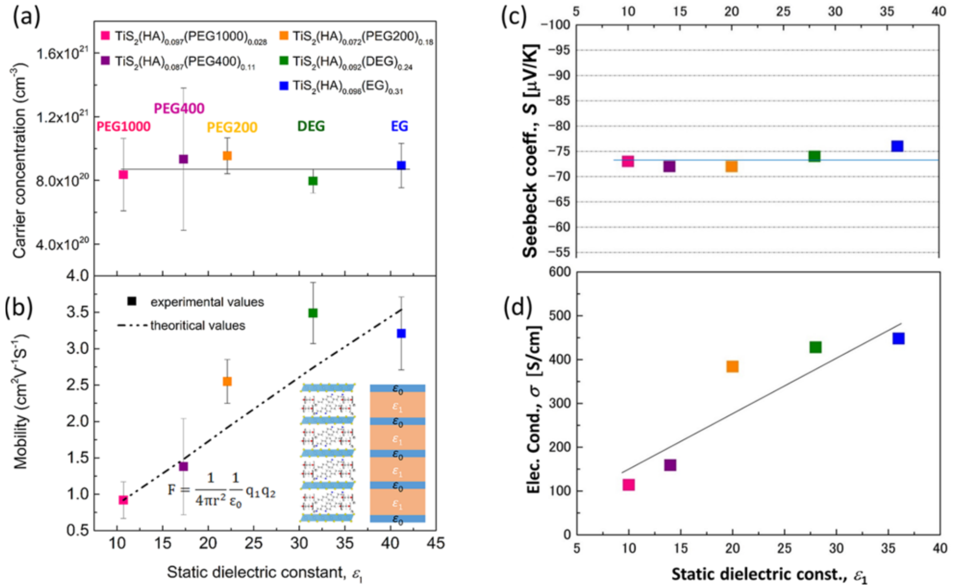

Fig. 4. – In-plane transport properties of $\mathrm{TiS_2(HA)}_x\mathrm{(PM)}_y$ hybrid superlattices as a function of static dielectric constant of polar molecule (PM = ethylene glycol series) at 300 K [7]; (a) Carrier concentration, (b) Hall mobility, (c) Seebeck coefficient, and (d) Electrical conductivity.

weight) [23]. The chemical resemblance of these molecules could result in similar structures in terms of the interlayer distance of the inorganic/organic hybrid superlattices (fig. 3(a)), enabling a systematic comparison of their transport properties.

Figures 4(a) and (b) show the carrier concentration and the in-plane Hall mobility, respectively, as a function of the static dielectric constant of the intercalated polar molecule. The Hall mobility was systematically enhanced due to the increase of the dielectric constants of the polar molecules, while the carrier concentration almost remained constant. The change of the carrier mobility is likely dominated by the relaxation time (τ) of the quasi-2D electrons inside the inorganic $\mathrm{TiS_2}$ layers. Pristine $\mathrm{TiS_2}$ singe crystals have a carrier mobility of $7.5\,\mathrm{cm^2\,V^{-1}\,s^{-1}}$, where the electrons are mainly scattered by acoustic phonons [24]. Ionic impurity scattering was introduced after incorporating organic cations (HA ions), due to the Coulomb force between the cations and the electrons, which would decrease the electron mobility. However, the overall electrical conductivity of hybrid materials could be increased due to the significant increase in carrier concentration satisfying the electrical neutrality.

Using Mathiessen's rule, the effective mobility can be expressed as

$$\mu = \left(\frac{1}{\mu_l} + \frac{1}{\mu_i}\right)^{-1} = \left(\frac{1}{\mu_l} + \frac{1}{f\varepsilon^2}\right)^{-1}, \tag{2}$$

where μ_l and μ_i denote the mobility by acoustic phonon scattering and impurity

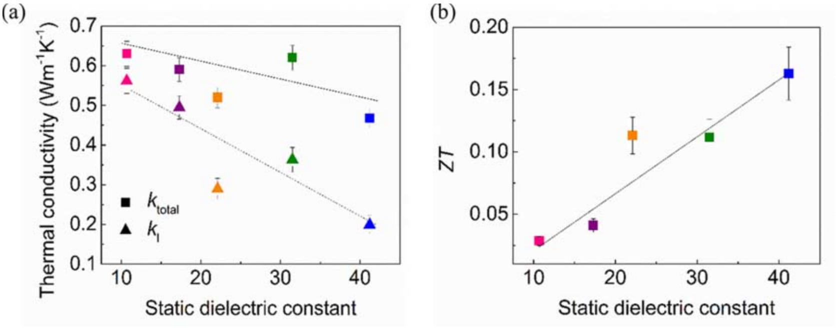

Fig. 5. – (a) Thermal conductivity as a function of static dielectric constant of the polar molecule and (b) ZT *vs.* static dielectric constant at 300 K [7].

scattering, respectively. ε is the average dielectric constant of our hybrid material, and the coefficient f is a functional parameter which relates to effective mass, effective charge of impurities and concentration of impurities. In our hybrid materials, it can be treated as a constant value [7]. To calculate the effective mobility μ, μ_l was defined as the mobility of pristine TiS_2 single crystal ($\mu_l = 7.5\,\text{cm}^2\,\text{V}^{-1}\,\text{s}^{-1}$) [24], and the coefficient f was derived from the mobility of intercalated $TiS_2(HA)_{0.096}(PEG1000)_{0.028}$ crystal, ($f = 0.00737\,\text{cm}^2\,\text{V}^{-1}\,\text{s}^{-1}$). The calculated curve of effective mobility (theoretical) is close to a straight line for $10 < \varepsilon_l < 42$ and agrees well with the experimental values of all hybrid inorganic/organic materials, as shown in fig. 4(b). Such agreement of the mobility from the simple theoretical model and experimental results, indeed, proved that the electronic band structures of these hybrid materials might have only been slightly modified by the intercalation of organic molecules, as articulated above, and the dielectric mismatch is the key to tune the electron mobility in these hybrid materials by screening the Coulomb potentials.

Accordingly, the Seebeck coefficient stayed almost constant but the electrical conductivity increased with increasing static dielectric constant of polar molecules (figs. 4(c), (d)). This is a very important finding, we believe, because it suggests that we can enhance the power factor of a hybrid superlattice by incorporating polar molecules with high static dielectric constant. It is also interesting to see that the lattice thermal conductivity was very low and decreased with increasing static dielectric constant (fig. 5(a)). This ultra-low lattice thermal conductivity would indicate that long-range interactions between the dipole moment in polar molecules and the phonons in TiS_2 layers should affect the phonon scattering process. Consequently, ZT increased with increasing static dielectric constant of polar molecules, and 0.17 at room temperature was obtained for the case of ethylene glycol, which has the largest static dielectric constant (fig. 5(b)). So, we can conclude that the intercalation of polar molecules with high static dielectric constant enhances carrier mobility and electrical conductivity, and greatly reduces lattice thermal conductivity, leading to high ZT.

3·4. *Reduction of thermal conductivity.* – It is very interesting that such a low lattice thermal conductivity can be realized in a hybrid superlattice. Both phonons and electrons contribute to the thermal conductivity, and the electronic contribution can be comparable to the phonon contribution in high-efficiency thermoelectric materials. After subtracting the electronic thermal conductivity, which was estimated according to the Wiedemann-Franz law using a calibrated Lorenz constant ($2.40 \times 10^{-8}\,\mathrm{V}^2\,\mathrm{K}^{-2}$), the in-plane lattice thermal conductivity was estimated to be $4.2\,\mathrm{Wm}^{-1}\,\mathrm{K}^{-1}$ for the TiS_2 single crystal and an ultralow value of $0.12\,\mathrm{Wm}^{-1}\,\mathrm{K}^{-1}$ was obtained for $TiS_2(HA)_{0.08}(H_2O)_{0.22}(DMSO)_{0.03}$ at 300 K. The ultralow thermal conductivities across inorganic/organic interfaces have been studied for planar self-assembled monolayers [25] and nanocrystal arrays [26]. Low cross-plane thermal conductivity has also been reported for inorganic/organic superlattices [27, 28]. However, the in-plane thermal conductivity of inorganic/organic superlattices has not been reported. Assuming that the TiS_2 layers and the organic molecules formed a parallel thermal circuit along the in-plane direction of the hybrid superlattice, the thermal conductivity was estimated to be $2.59\,\mathrm{Wm}^{-1}\,\mathrm{K}^{-1}$, almost half of the thermal conductivity of bulk TiS_2, which is much higher than the measured value.

To explain such ultra-low thermal conductivity of $TiS_2(HA)_{0.08}(H_2O)_{0.22}(DMSO)_{0.03}$, we conducted equilibrium molecular dynamics simulations with the Green-Kubo method to understand the fundamental phonon transport mechanisms in both bulk TiS_2 and the hybrid superlattice material with hexylammonium molecules. In our simulations, we observed an eightfold reduction of the lattice thermal conductivity when the TiS_2 bulk is intercalated by organic components. This reduction is significantly higher than the simple volumetric averaging, indicating that the coupling between the inorganic and organic parts plays an important role in phonon transport in the in-plane direction. As the thermal conduction in the inorganic part is much better than the organic part, the low thermal conductivity of the hybrid material could be attributed to the reduction in the thermal conductivity of the inorganic layer after the intercalation. To qualitatively explain the difference in the phonon dynamics between bulk TiS_2 and the hybrid superlattice, we calculated the spectral energy density [29], $\phi(\mathbf{k}, \omega)$, with phonon wavevector $\mathbf{k}$ and frequency ω of the bulk TiS_2 and the TiS_2 layer from the hybrid superlattice, as shown in fig. 6. The positions of peaks, ω_0, in the spectral energy density distribution for a given wavevector, $\mathbf{k}_0$, correspond to the phonon dispersion that the material supports, and the broadening of the peak in the frequency domain is related to the phonon relaxation time. The smaller the broadening is, the longer the relaxation time is. In both materials, the three acoustic branches are clearly distinguishable. For all acoustic dispersions, larger broadening can be observed for the hybrid case, indicating stronger scattering in the hybrid superlattice, which can be understood as a result of the inorganic TiS_2 layers being ionically combined with the dangling hexylammonium ions. The electrostatic interaction is much stronger than weak van der Waals interaction, which is dominant in the bulk TiS_2.

It is noted that other scattering mechanisms, besides the interfacial coupling, can potentially further reduce the thermal conductivity, which is worthy of further investigation. One possibility is the wavy structure of the layers observed for $TiS_2(HA)_{0.08}(H_2O)_{0.22}(DMSO)_{0.03}$ (fig. 7(a)). As a reference, we measured

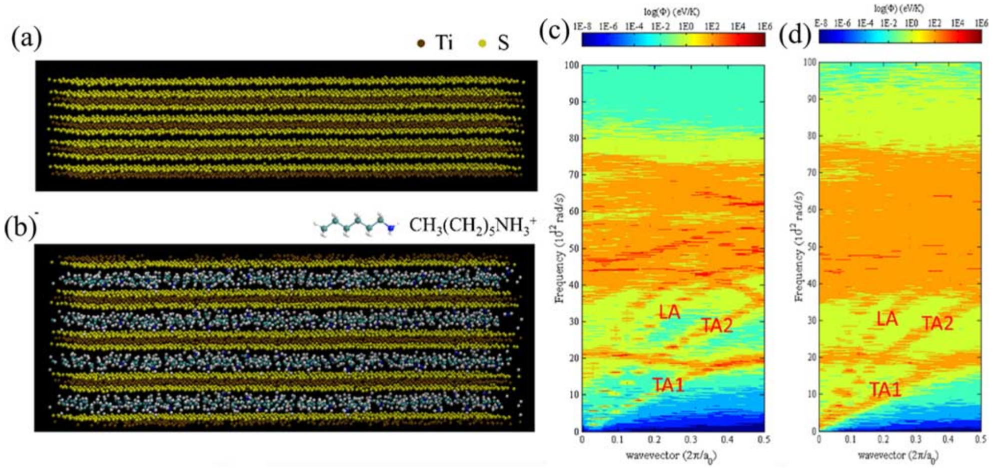

Fig. 6. – Molecular dynamics simulations of the thermal conductivities [6]; structural models of (a) TiS_2 and (b) $TiS_2(HA)_x(H_2O)_y(DMSO)_z$. Spectral energy densities of (c) TiS_2 and (d) $TiS_2(HA)_x(H_2O)_y(DMSO)_z$).

the thermal conductivity of $TiS_2(HA)_{0.097}(PEG1000)_{0.028}$, where the layers were aligned straight owing to the long chain structure of polyethylene glycol (PEG) (fig. 7(b)). The lattice thermal conductivity of the flat hybrid superlattice $TiS_2(HA)_{0.097}(PEG1000)_{0.028}$ was measured to be $0.56\,\mathrm{Wm^{-1}\,K^{-1}}$, 4–5 times higher than the wavy $TiS_2(HA)_{0.08}(H_2O)_{0.22}(DMSO)_{0.03}$. This can be further explained using the thermal conductivity accumulation as a function of the mean-free path. The phonons with a mean-free path above 10 nm (the half-wavelength of the wavy structure) that contribute to 82% of the total thermal conductivity would be strongly scattered by the wavy structure. In addition, local atomic disordering of the TiS_2 layers in the hybrid superlattice in the wavy structure could be another additional phonon scattering mechanism. Compared with the sharp peaks of XRD for TiS_2 single crystals, the peaks of $TiS_2(HA)_{0.08}(H_2O)_{0.22}(DMSO)_{0.03}$ become broader, which is a sign of structural disordering, as further confirmed by HAADF-STEM (fig. 7(a)).

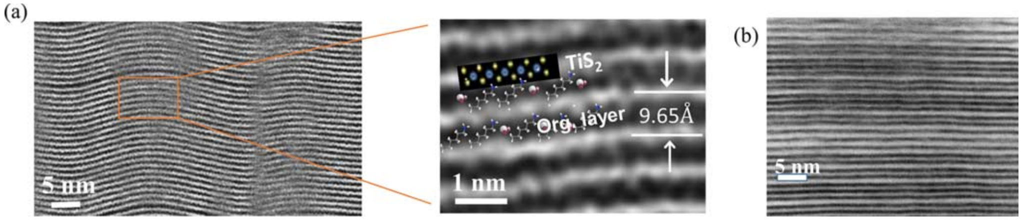

Fig. 7. – HAADF-STEM images of (a) $TiS_2(HA)_{0.08}(H_2O)_{0.22}(DMSO)_{0.03}$ and $TiS_2(HA)_{0.097}(PEG1000)_{0.028}$ [6].

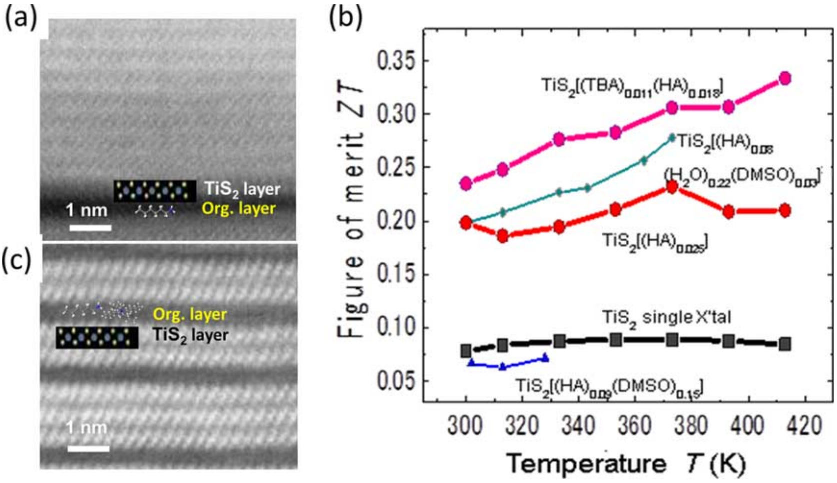

Fig. 8. – (a) HAADF-STEM image of the cross section of $TiS_2(HA)_{0.025}$ hybrid superlattice. (b) Temperature dependence of ZT for hybrid superlattices with various compositions. (c) HAADF-STEM image of the cross section of $TiS_2(TBA)_{0.011}(HA)_{0.018}$ hybrid superlattice [30].

3˙5. *Enhancement of ZT by optimizing carrier density.* – The ZT values so far obtained for the hybrid superlattices are lower than the estimated maximum value, and there are several issues to overcome in order to further enhance ZT. The most important issue to overcome is to gain control over the carrier density. It is always too high when the organic cations are fully intercalated together with the electron injection into TiS_2 layers, and hence the Seebeck coefficient is greatly suppressed. It is desirable to reduce somehow the carrier density so as to achieve higher Seebeck coefficients and higher power factors.

There are at least two ways to reduce the carrier concentration during processing. One way is to remove the organic cations by heating in vacuum. This seems to work well. The carrier concentration does decrease and the Seebeck coefficient increases. Even though the thermal conductivity greatly increases, possibly due to destruction of the superlattice structure (fig. 8(a)), ZT increases from 0.07 (for $TiS_2(HA)_{0.08}(DMSO)_{0.15}$) to 0.2 (for $TiS_2(HA)_{0.025}$) at room temperature (fig. 8(b)).

The other way is to intercalate two kinds of organic cations that possess different thermal stability. TBA (tetrabutyl ammonium) and HA (hexylammonium) are first co-intercalated into the van der Waals gap of TiS_2, and then HA, which is more thermally unstable, is removed preferentially by heating in vacuum while maintaining a slightly modified superlattice structure (fig. 8(c)). Carrier concentration decreases, the Seebeck coefficient increases, and the electrical conductivity increases as a result. Even though the thermal conductivity appears to be rather high due to certain structural modifications, the ZT is greatly enhanced and reaches about 0.33 (for TiS_2 $(TBA)_{0.011}(HA)_{0.018}$) at 413 K in an ambient atmosphere, as shown in fig. 8(b) [30].

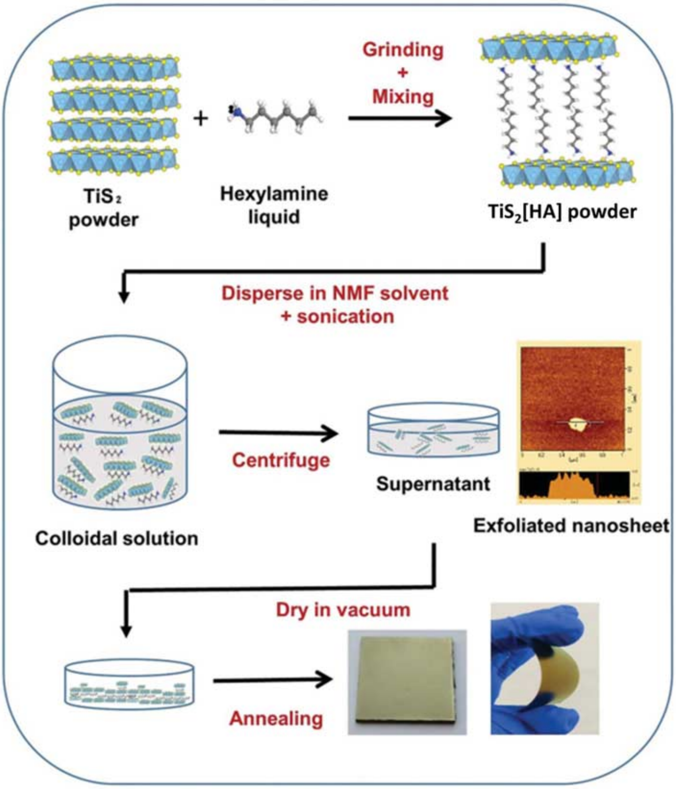

Fig. 9. – Solution-processed TiS_2/organic superlattice materials. The flow chart of synthesis procedure of TiS_2/organics superlattice films by a liquid-exfoliation and self-assembly method [31].

4. – Flexible thermoelectrics and their applications

4·1. *Solution-processable fabrication.* – Figure 9 depicts the synthesis procedures of TiS_2/organics superlattice materials [31]. Firstly, TiS_2 powders were synthesised by the chemical vapour transport method [32]. The obtained TiS_2 powders were thoroughly pulverised and mixed with hexylamine (HA) with an initial molar ratio of 1 : 4. We conducted XRD measurement on the resulting mixed powder, and the result (fig. 10(a)) indicated that HA was intercalated into TiS_2 through manual grinding, and the intercalated compound, *i.e.*, TiS_2(HA) had an interlayer spacing d as large as 22.3 Å. Considering that the HA had an alkyl chain length of 16.6 Å, it is expected that the HA molecules situated between the TiS_2 layers in a paraffin-like bilayer structure.

The pre-intercalated powders were further exfoliated into nanosheets by dispersing them into a polar solvent with large dielectric constant, *i.e.*, n-methyl formamide (NMF), followed by mild sonication. The obtained colloidal solution was then centrifugated to remove thick flakes as well as unintercalated TiS_2. AFM study indicated that the

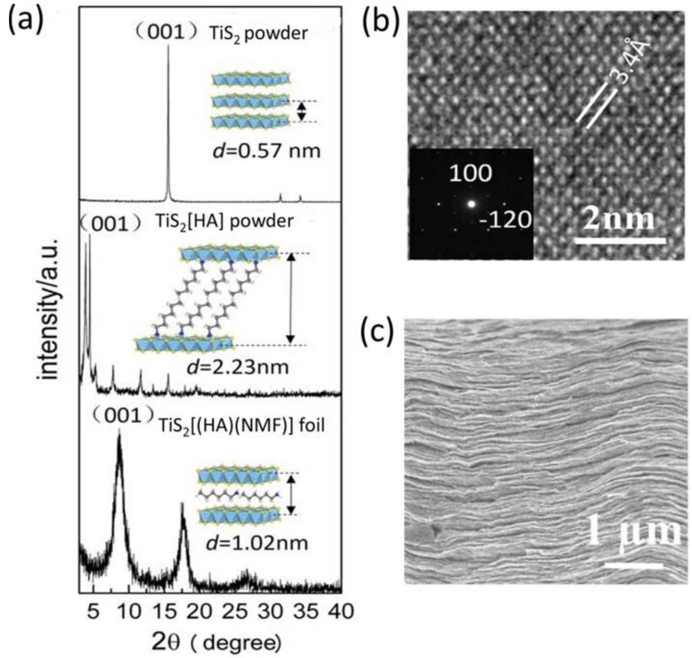

Fig. 10. – The crystal structure evolution during solution processing [32]. (a) The XRD patterns of TiS_2 powder, TiS_2[HA] powder (grinding TiS_2 with hexylamine) and the TiS_2[(HA)(NMF)] foil. (b) HR-TEM of exfoliated TiS_2[(HA)(NMF)] nanosheet, and (c) the cross-sectional SEM image of TiS_2[(HA)(NMF)] free-standing film.

exfoliated nanosheets had an average thickness of 2–3 nm and length of 200–400 nm. The TEM image (fig. 10(b)) of the nanosheet surface demonstrated an identical structure as the pure TiS_2, and organic molecules were not able to be observed through this projection due to the low scattering coefficient of electrons. These nanosheets were self-assembled into TiS_2[(HA)(NMF)] superlattice film (fig. 10(c)) when the supernatant was dried at 60 °C under low-vacuum condition. It was further annealed at 130 °C to remove the residual organic solvents. The as-synthesised film could be either free standing or deposited onto various substrates, such as glass, Si or soft polymer substrate.

4˙2. *Thermoelectric and mechanical properties of superlattice films.* – Figure 11 shows the thermoelectric properties of TiS_2[(HA)(NMF)] free-standing foil, where the properties of the pristine TiS_2 single crystal are also included for comparison. It demonstrates that the in-plane electrical conductivity of TiS_2[(HA)(NMF)] foil was increased by more than 50% after organic intercalation, whereas the Seebeck coefficient value was reduced from 180 to 70 μV/K at room temperature. This was attributed to the increased carrier concentration. The Hall measurement indicated that the carrier concentration was remarkably enhanced from $1.76 \times 10^{20}\,\mathrm{cm}^{-3}$ to $1.35 \times 10^{21}\,\mathrm{cm}^{-3}$. The largely doped electrons

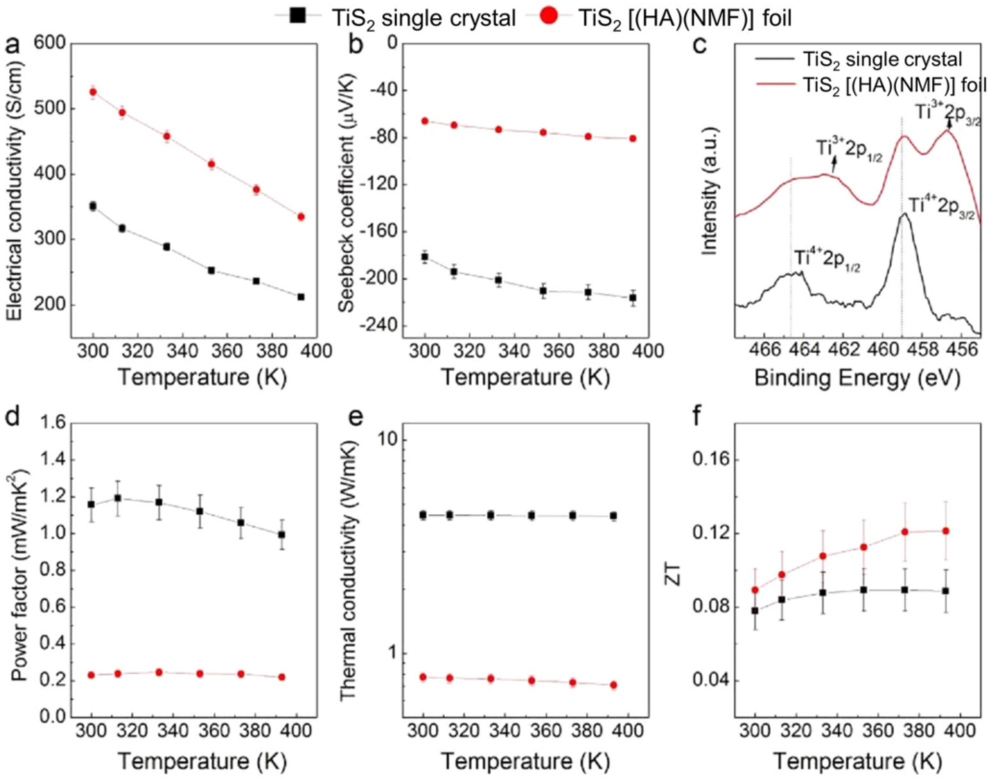

Fig. 11. – In-plane thermoelectric properties and XPS spectra of TiS_2 single crystal and TiS_2[(HA)(NMF)] foil [32]. (a) Electrical conductivity, (b) Seebeck coefficient, (c) XPS spectra, (d) power factor, (e) thermal conductivity and (f) figure of merit ZT.

resulted in the reduction of Ti^{4+} to Ti^{3+}, which was verified by the XPS measurement (fig. 11(c)). On the other hand, the electron mobility of the TiS_2 superlattice foil was decreased by a factor of three, compared to the TiS_2 single crystal. This could stem from the enhanced electron concentration and strong electron scattering at the nanosheet edges.

Despite the enhanced electrical conductivity, the power factor of TiS_2[(HA)(NMF)] foil (230 μW/mK^2) was much lower than that of its parent material (1150 μW/mK^2), due to the large reduction of Seebeck coefficient. The in-plane thermal conductivity of TiS_2[(HA)(NMF)] foil was 0.77 W/mK, which was 6–7 times lower than that of the pristine TiS_2 single crystal. Owing to the remarkable suppression of thermal conductivity, the ZT of TiS_2[(HA)(NMF)] foil reached 0.12 at 393 K, which was 50% higher than that of the bulk TiS_2 crystal. Although its ZT value was still lower than the benchmarked thermoelectric material (*i.e.*, Bi_2Te_3), it is expected that the overall thermoelectric performance could be further enhanced by optimising the carrier concentration.

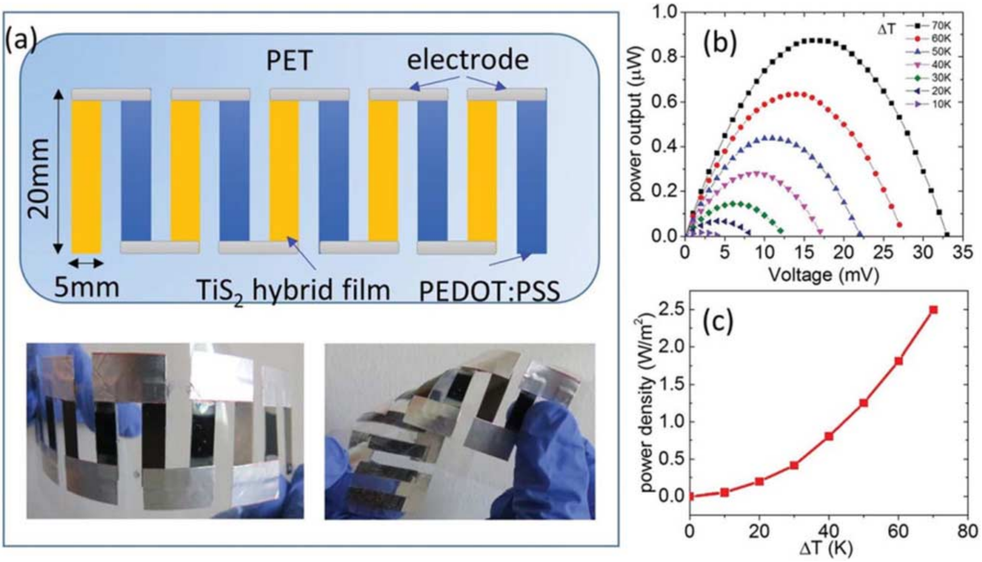

Fig. 12. – Prototype thermoelectric device and its thermoelectric performance [31]. (a) Schematic illustration and photos of thermoelectric device, where p-type PEDOT:PSS and n-type TiS_2[(HA)(NMF)] superlattice film were deposited onto flexible polymer substrate. (b) The generated power output and voltage output at a temperature gradient of 10–70 K, and (c) the power density as a function of temperature gradient.

4˙3. *Thermoelectric performance of prototype flexible thermoelectric device.* – To further evaluate the superlattice material performance, we fabricated a prototype thermoelectric device using p-type ethylene glycol treated PEDOT:PSS and n-type solution-processed TiS_2[(HA)(NMF)] thin film. The device consisted of 5 p-n pairs of thermoelectric legs, where both p- and n-type materials were deposited onto soft PET substrate to ensure device flexibility (fig. 12(a)). Silver paint was used as the metal electrodes, which had a similar work function (4.26–4.74 eV) to both PEDOT:PSS (4.8–5.3 eV) and TiS_2 (4.44 eV).

Figure 12(b) presents the measured voltage and power output of the fabricated device. At the temperature gradient of 70 K, the 5 p-n paired thermoelectric device generated a voltage output of 33 mV and a power output of 0.9 μW. The calculated power density reached 0.05 and 2.5 $\mathrm{W\,m^{-2}}$ at the temperature gradient of 10 K and 70 K, respectively (fig. 12(c)). This suggests that such a device holds great promise for powering the micro- to milli-watt wearable electronics.

Taking advantage of the flexibility of the thermoelectric materials, it would be possible to design new types of devices and modules outside of the domain of conventional solid metal or hard inorganic materials. Such new flexible devices would enable us to explore novel applications. High-power flexible solar cells, for example, will be realized hopefully by combining new thin-film solar cells and flexible thermoelectric modules [33]. Flexible thin film TE generator could power an electronic skin for health-monitoring and remote diagnosis (fig. 13) [34].

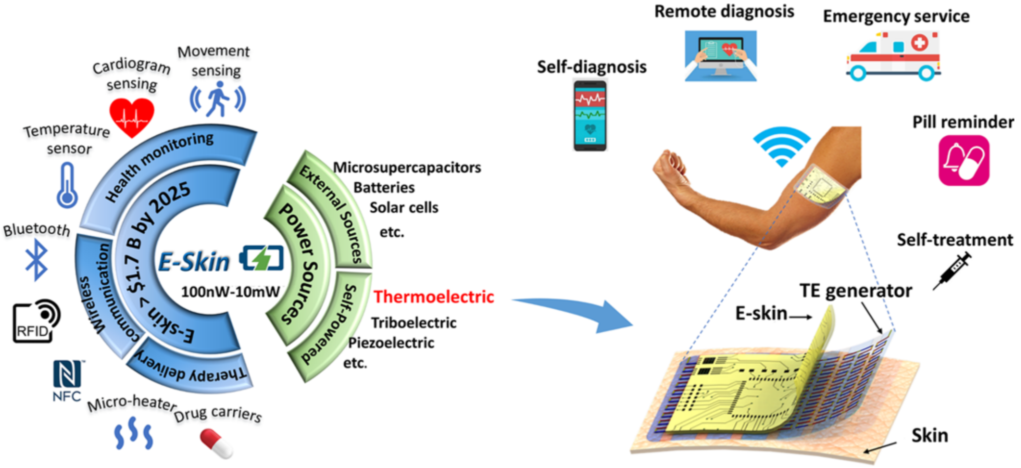

Fig. 13. – The prospects of future E-skins powered by body heat functional E-skins and power sources (left) and the schematic illustration of E-skins powered by body heat using an integrated thermoelectric (TE) generator for potential wireless health monitoring and diagnosis (right) [34].

5. – 1D nanomaterials: carbon nanotubes (CNTs)

CNTs have been extensively used to enhance the electrical conductivity of conducting polymers, due to their superior electrical conductivity. For instance, the electrical conductivity of individual CNT can reach as high as 2×10^5 S/cm and even random CNTs can have the electrical conductivity above 10^3 S/cm [35, 36]. For the composites, the type, concentration, and distribution of CNTs in the polymer matrix play important role in determining the thermoelectric performance of the composites. Previous studies reveal that the integration of high-quality single-wall CNTs generally achieves a higher power factor compared with a mixture of multi-walled CNTs, due to less structural defects [37], however, it will inevitably increase the material cost. In addition, pristine CNTs are likely to become aggregated in water due to their hydrophobic nature and thus it requires the assistance of stabilizers to achieve uniform dispersion in the polymer matrix. Conductive stabilizer is preferred, as the insulating one may deteriorate the overall electrical conduction.

In 2008, Choongho and Grunlan *et al.* first demonstrated that a loading of 20 wt% CNT into PEDOT:PSS could remarkably enhance the electrical conductivity while keeping the Seebeck coefficient and thermal conductivity relatively constant due to the segregated CNT network [38]. In 2011, they successfully enhanced the electrical conductivity to 1000 S/cm by adding 60 wt% SWCNT, leading to a power factor of $\sim 160\,\mu\text{W/mK}^2$ [39]. In 2013, they found that in contrast to insulating stabilizers such as gum arabic (GA) and polyvinyl acetate (PVAc), the addition of semi-conductive stabilizer, *i.e.* meso-tetra (4-carboxyphenyl) porphine (TCPP) to the dispersion of PEDOT:PSS/DWCNTs could promote the π-π stacking and bridge the CNTs networks, resulting in a large power factor of $500\,\mu\text{W/mK}^2$ when the concentration of

DWCNT was 40% [40]. Very recently, they demonstrated that the majority carrier type of PEDOT/CNTs hybrids can be altered from p to n type by the treatment of tetrakis(dimethylamino)ethylene (TDAE) (fig. 1). It showed unusually large Seebeck coefficient up to $-4.3\,\mathrm{mV/K}$, resulting in a very high power factor of $\sim 1050\,\mu\mathrm{W/mK^2}$ [41]. This is also the highest power factor reported so far for n-type organic-based thermoelectric materials. Although considerable effort has been made to improve the thermoelectric performance of PANI by the integration of CNTs, the power factor values are generally below $20\,\mu\mathrm{W/mK^2}$, due to the relatively low electrical conductivity (*i.e.*, below $100\,\mathrm{S/cm}$ in most cases) [42-46].

In addition to PEDOT:PSS and PANI, Guo *et al.* reported that polypyrrole (PPy)/SWCNT multi-layered nanosheets could reach a maximum power factor of $21.7\,\mu\mathrm{W/mK^2}$ [47], which was the highest value among PPy and its composites reported so far. Poly(3-hexythiophene)/CNTs composites also demonstrated competitive thermoelectric properties, yielding $25\,\mu\mathrm{W/mK^2}$ for a low filling content of 8% SWCNTs and a maximum of $95\,\mu\mathrm{W/mK^2}$ for 42–81% of SWCNTs [48].

Furthermore, Toshima and his co-workers [49, 50] developed a new hybrid thermoelectric composite made from polyvinyl chloride (PVC), SWCNTs and nano-dispersed poly(metal 1,1,2,2-ethenetetrathiolate) (n-metal-PETT). They found that such additives could promote the carrier transfer between SWCNT networks and stabilize CNTs dispersion. In addition, the n-Cu-PETT/SWCNTs composite shows a positive Seebeck coefficient of $18\,\mu\mathrm{V/K}$ and the n-Ni-PETT/SWCNTs composite exhibits a negative Seebeck coefficient of $-40\,\mu\mathrm{V/K}$. The power factor can be further enhanced by the addition of PVC stabilizer and methanol treatment due to the removal of insulating PVC, and the maximum power factor reaches to $58.6\,\mu\mathrm{W/mK^2}$ by the n-Ni-PETT/SWCNTs/PVC composite with a mass ratio of $10:8:3$.

6. – Perspective remarks on low-dimensional nanomaterials-based thermoelectrics

Figure 14 shows the room temperature power factor values of flexible thermoelectrics reported recently in the literature. In the last three years, several materials were found to show the power factor larger than $500\,\mu\mathrm{W/mK^2}$, and the yellow points correspond to the $\mathrm{TiS_2}$/organics hybrid superlattice materials whose carrier density was optimized as mentioned in sect. **3**˙5. Very recently the power factor far exceeding $1000\,\mu\mathrm{W/mK^2}$ was reported for both p and n-type CNT/polymer nanocomposites [51]. It was a real great advance in getting flexible materials with high power factors. However, the ZT values are still very low, as low as of the order of 0.01, so that these new materials cannot be used right now for actual applications.

Here I must mention about the new result recently reported by Chinese researchers [52]. Nanocomposites with layer-structured bismuth telluride deposited on carbon nanotube scaffold gave rise to a very high power factor ($\sim 1600\,\mu\mathrm{W/mK^2}$) and ZT (~ 0.89) at room temperature. It would be a good candidate material if the cost-effective manufacturing technology could be developed.

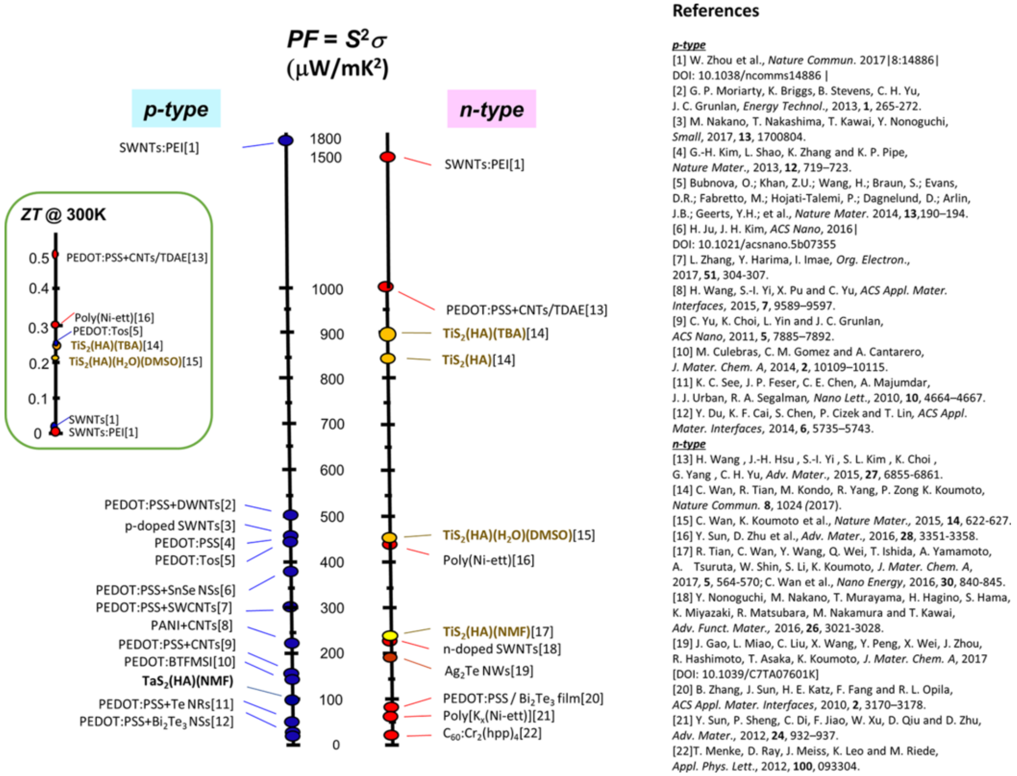

References

p-type
[1] W. Zhou et al., *Nature Commun.* 2017|8:14886| DOI: 10.1038/ncomms14886 |
[2] G. P. Moriarty, K. Briggs, B. Stevens, C. H. Yu, J. C. Grunlan, *Energy Technol.*, 2013, **1**, 265-272.
[3] M. Nakano, T. Nakashima, T. Kawai, Y. Nonoguchi, *Small*, 2017, **13**, 1700804.
[4] G.-H. Kim, L. Shao, K. Zhang and K. P. Pipe, *Nature Mater.*, 2013, **12**, 719–723.
[5] Bubnova, O.; Khan, Z.U.; Wang, H.; Braun, S.; Evans, D.R.; Fabretto, M.; Hojati-Talemi, P.; Dagnelund, D.; Arlin, J.B.; Geerts, Y.H.; et al., *Nature Mater.* 2014, **13**,190–194.
[6] H. Ju, J. H. Kim, *ACS Nano*, 2016| DOI: 10.1021/acsnano.5b07355
[7] L. Zhang, Y. Harima, I. Imae, *Org. Electron.*, 2017, **51**, 304-307.
[8] H. Wang, S.-I. Yi, X. Pu and C. Yu, *ACS Appl. Mater. Interfaces*, 2015, **7**, 9589–9597.
[9] C. Yu, K. Choi, L. Yin and J. C. Grunlan, *ACS Nano*, 2011, **5**, 7885–7892.
[10] M. Culebras, C. M. Gomez and A. Cantarero, *J. Mater. Chem. A*, 2014, **2**, 10109–10115.
[11] K. C. See, J. P. Feser, C. E. Chen, A. Majumdar, J. J. Urban, R. A. Segalman, *Nano Lett.*, 2010, **10**, 4664–4667.
[12] Y. Du, K. F. Cai, S. Chen, P. Cizek and T. Lin, *ACS Appl. Mater. Interfaces*, 2014, **6**, 5735–5743.
n-type
[13] H. Wang , J.-H. Hsu , S.-I. Yi , S. L. Kim , K. Choi , G. Yang , C. H. Yu, *Adv. Mater.*, 2015, **27**, 6855-6861.
[14] C. Wan, R. Tian, M. Kondo, R. Yang, P. Zong K. Koumoto, *Nature Commun.* **8**, 1024 (2017).
[15] C. Wan, K. Koumoto et al., *Nature Mater.*, 2015, **14**, 622-627.
[16] Y. Sun, D. Zhu et al., *Adv. Mater.*, 2016, **28**, 3351-3358.
[17] R. Tian, C. Wan, Y. Wang, Q. Wei, T. Ishida, A. Yamamoto, A. Tsuruta, W. Shin, S. Li, K. Koumoto, *J. Mater. Chem. A*, 2017, **5**, 564-570; C. Wan et al., *Nano Energy*, 2016, **30**, 840-845.
[18] Y. Nonoguchi, M. Nakano, T. Murayama, H. Hagino, S. Hama, K. Miyazaki, R. Matsubara, M. Nakamura and T. Kawai, *Adv. Funct. Mater.*, 2016, **26**, 3021-3028.
[19] J. Gao, L. Miao, C. Liu, X. Wang, Y. Peng, X. Wei, J. Zhou, R. Hashimoto, T. Asaka, K. Koumoto, *J. Mater. Chem. A*, 2017 [DOI: 10.1039/C7TA07601K]
[20] B. Zhang, J. Sun, H. E. Katz, F. Fang and R. L. Opila, *ACS Appl. Mater. Interfaces*, 2010, **2**, 3170–3178.
[21] Y. Sun, P. Sheng, C. Di, F. Jiao, W. Xu, D. Qiu and D. Zhu, *Adv. Mater.*, 2012, **24**, 932–937.
[22]T. Menke, D. Ray, J. Meiss, K. Leo and M. Riede, *Appl. Phys. Lett.*, 2012, **100**, 093304.

Fig. 14. – Power factor (PF) values at 300 K of flexible thermoelectrics.

The hybridization of low-dimensional inorganic nanomaterials with other soft nanomaterials would be a promising strategy to produce flexible thermoelectrics for the future energy harvesting. In this sense, a variety of novel 2D inorganic nanomaterials are expected to have high potential as building blocks to make flexible nanohybrid thermoelectrics. Layer-structure compounds such as SnSe [53,54] and metal nitride halide MNX (M: Ti, Zr, Hf; X: Cl, Br, I) [55, 56], and 2D pnictogens (VA elements: N, P, As, Sb, Bi) [57] are possible candidate materials.

* * *

Prof. Chunlei Wan of Tsinghua University, Prof. Yifeng Wang of Nanjing Tech University, Dr. Ruoming Tian of University of New South Wales, and my colleagues and former students are deeply acknowledged for their contributions to the thermoelectric materials research.

REFERENCES

[1] Leclerc M. and Najari A., *Nat. Mater.*, **10** (2011) 409.
[2] Bubnova O., Khan Z. U., Wang H. *et al.*, *Nat. Mater.*, **13** (2014) 190.
[3] Nonoguchi K., Ohashi K., Kanazawa R. *et al.*, *Sci. Rep.*, **3** (2013) 3344.
[4] Wei Q. S., Mukaida M., Kirihara K. *et al.*, *Appl. Phys. Express*, **7** (2014) 031601.
[5] Yan H. and Toshima N., *Chem. Lett.*, **28** (1999) 1217.
[6] Wan C., Dang F., Koumoto K. *et al.*, *Nat. Mater.*, **14** (2015) 622.
[7] Wan C., Kodama Y., Kondo M., Koumoto K. *et al.*, *Nano Lett.*, **15** (2015) 6302.
[8] Chhowalla M., Shin H. S., Eda G. *et al.*, *Nat. Chem.*, **5** (2013) 263.
[9] Gibney E., *Nature*, **522** (2015) 274.
[10] Wickramaratne D. *et al.*, *J. Chem. Phys.*, **140** (2014) 124710.
[11] Fan D. D. *et al.*, *Appl. Phys. Lett.*, **105** (2014) 133113.
[12] Wang T. *et al.*, *Nanotechnology*, **27** (2016) 28573.
[13] Guilmeau E., Maignan A., Wan C. *et al.*, *Phys. Chem. Chem. Phys.*, **17** (2015) 24541.
[14] Putri Y. E., Wan C., Wang Y. *et al.*, *Scr. Mater.*, **66** (2012) 895.
[15] Wan C., Wang Y., Koumoto K. *et al.*, *Appl. Phys. Lett.*, **100** (2012) 101913.
[16] Wan C., Wang Y., Wang N., Koumoto K. *et al.*, *Materials*, **3** (2010) 2606.
[17] Wan C., Wang Y., Wang N., Koumoto K. *et al.*, *Sci. Technol. Adv. Mater.*, **11** (2010) 044306.
[18] Samanta A., Pandey T. and Singh A. K., *Phys. Rev. B*, **90** (2014) 174301.
[19] Imai H., Shimakawa Y. and Kubo Y., *Phys. Rev. B*, **64** (2001) 241104.
[20] Zhang R., Wan C., Wang Y. *et al.*, *Phys. Chem. Chem. Phys.*, **14** (2012) 15641.
[21] Barry J. J., Hughes H. P., Klipstein P. C. *et al.*, *J. Phys. C: Solid State Phys.*, **16** (1983) 393.
[22] Schöllhorn R. and Weiss A., *J. Less Common Met.*, **36** (1974) 229.
[23] Sengwa R. J., Kaur K. and Chaudhary R., *Polym. Int.*, **49** (2000) 599.
[24] Wan C., Wang Y., Wang N. *et al.*, *J. Electron. Mater.*, **40** (2011) 1271.
[25] Losego M. D., Grady M. E., Sottos N. R. *et al.*, *Nat. Mater.*, **11** (2012) 502.
[26] Ong W.-L., Rupich S. M., Talapin D. V. *et al.*, *Nat. Mater.*, **12** (2013) 410.
[27] Liu J., Yoon B., Kuhlmann E. *et al.*, *Nano Lett.*, **13** (2013) 5594.
[28] Losego M. D., Blitz I. P., Vaia R. A. *et al.*, *Nano Lett.*, **13** (2013) 2215.
[29] Thomas J. A., Turney J. E., Iutzi R. M. *et al.*, *Phys. Rev. B*, **81** (2010) 081411.
[30] Wan C., Tian R., Koumoto K. *et al.*, *Nat. Commun.*, **8** (2017) 1024.
[31] Tian R., Wan C., Koumoto K. *et al.*, *J. Mater. Chem. A*, **5** (2017) 564.
[32] Wan C., Tian R., Koumoto K. *et al.*, *Nano Energy*, **30** (2016) 840.
[33] Zhou Y., Koumoto K., Lin H. *et al.*, *Mater. Today Energy*, **12** (2019) 363.
[34] Tian R., Koumoto K. *et al.*, *Joule*, **3** (2019) 1394.
[35] Ebbesen T., Lezec H., Hiura H., Bennett J., Ghaemi H. and Thio T., *Nature*, **382** (1996) 54.
[36] Ryu Y., Yin L. and Yu C., *J. Mater. Chem.*, **22** (2012) 6959.
[37] Kim D., Kim Y., Choi K., Grunlan J. C. and Yu C., *ACS Nano*, **4** (2010) 513.
[38] Yu C., Kim Y. S., Kim D. and Grunlan J. C., *Nano Lett.*, **8** (2008) 4428.
[39] Yu C., Choi K., Yin L. and Grunlan J. C., *ACS Nano*, **5** (2011) 7885.
[40] Moriarty G. P., Briggs K., Stevens B. *et al.*, *Energy Technol.*, **1** (2013) 265.
[41] Wang H., Hsu J. H., Yi S. I. *et al.*, *Adv. Mater.*, **27** (2015) 6855.
[42] Yao Q., Chen L., Zhang W., Liufu S. and Chen X., *ACS Nano*, **4** (2010) 2445.
[43] Meng C., Liu C. and Fan S., *Adv. Mater.*, **22** (2010) 535.
[44] Wang Q., Yao Q., Chang J. and Chen L., *J. Mater. Chem.*, **22** (2012) 17612.
[45] Zhang K., Davis M., Qiu J. *et al.*, *Nanotechnology*, **23** (2012) 385701.

[46] Chen J., Gui X., Wang Z. *et al.*, *ACS Appl. Mater. Interfaces*, **4** (2011) 81.
[47] Liang L., Chen G. and Guo C.-Y., *Compos. Sci. Technol.*, **129** (2016) 130.
[48] Bounioux C., Díaz-Chao P., Campoy-Quiles M. *et al.*, *Energy Environ. Sci.*, **6** (2013) 918.
[49] Toshima N., Oshima K., Anno H. *et al.*, *Adv. Mater.*, **27** (2015) 2246.
[50] Oshima K., Asano H., Shiraishi Y. and Toshima N., *J. Appl. Phys.*, **55** (2016) 02BB07.
[51] Zhou W., Xie S. *et al.*, *Nat. Commun.*, **8** (2017) 14886.
[52] Jin Q. *et al.*, *Nat. Mater.*, **18** (2019) 62.
[53] Wang F. Q., Zhang S., Yu J. and Wang Q., *Nanoscale*, **7** (2015) 15962.
[54] Ju H. and Kim J. H., *ACS Nano*, **10** (2016) 5730.
[55] Yamanaka S. *et al.*, *J. Mater. Chem.*, **22** (2012) 10752.
[56] Yun W. S. and Lee J. D., *Sci. Rep.*, **7** (2017) 17330.
[57] Ersan F. *et al.*, *Appl. Phys. Rev.*, **6** (2019) 021308.

Proceedings of the International School of Physics “Enrico Fermi”
Course 207 “Advances in Thermoelectricity: Foundational Issues, Materials and Nanotechnology”,
edited by D. Narducci, G. J. Snyder and C. Fanciulli
(IOS, Amsterdam; SIF, Bologna) 2021
DOI 10.3254/ENFI210008

Theoretical approaches for nanoscale thermoelectric phenomena

Carmine Antonio Perroni

*CNR-SPIN and Dipartimento di Fisica “E. Pancini”, Università degli Studi di Napoli
“Federico II”, Complesso Monte S. Angelo, via Cinthia, I-80126 Napoli, Italy*

Giuliano Benenti

*Center for Nonlinear and Complex Systems, Dipartimento di Scienza e Alta Tecnologia
Università degli Studi dell’Insubria - via Valleggio 11, 22100 Como, Italy*

Istituto Nazionale di Fisica Nucleare, Sezione di Milano - via Celoria 16, 20133 Milano, Italy

NEST, Istituto Nanoscienze-CNR - I-56126 Pisa, Italy

Summary. — We focus on the theoretical approaches aimed to analyze thermoelectric properties at the nanoscale. We discuss several relevant theoretical approaches for different set-ups of nano-devices providing estimations of the thermoelectric parameters in the linear and non-linear regime, in particular the thermoelectric figure of merit and the power-efficiency trade-off. Moreover, we analyze the role of not only electronic, but also of vibrational degrees of freedom. First, nanoscale thermoelectric phenomena are considered in the quantum coherent regime using the Landauer-Büttiker method and focusing on effects of energy filtering. Then, we analyze the effects of many-body couplings between nanostructure degrees of freedom, such as electron-electron and electron-vibration interactions, which can strongly affect the thermoelectric conversion. In particular, we discuss the enhancement of the thermoelectric figure of merit in the Coulomb blockade regime for a quantum dot model starting from the master equation for charge state probabilities and the tunneling rates through the electrodes. Finally, within the non-equilibrium Green function formalism, we quantify the reduction of the thermoelectric performance in simple models of molecular junctions due to the effects of the electron-vibration coupling and phonon transport at room temperature.

1. – Introduction

A direct conversion between temperature differences and electric voltages can be achieved through thermoelectric phenomena in solid state systems. In the linear-response regime, in addition to a small electric voltage ΔV, a small temperature difference ΔT is applied generating an electric current J_e and a heat current J_h. The main transport quantities of the linear regime [1] are the electrical conductance $G = J_e/\Delta V$ (at $\Delta T = 0$), the thermopower $S = -\Delta V/\Delta T$ (at $J_e = 0$, with ΔV thermoelectric voltage), and the thermal conductance $K = J_h/\Delta T$ (at $J_e = 0$). The figure of merit Z for the thermoelectric conversion is defined as

$$Z = \frac{GS^2}{K}\,, \tag{1}$$

with the dimension of the inverse of a temperature. In the linear regime, one temperature T typically characterizes the stationary state of the system, therefore one usually considers the dimensionless figure of merit ZT. A very efficient thermoelectric conversion is obtained when ZT is much larger than unity [1].

Actual thermoelectric devices work under a finite electric voltage ΔV and temperature difference $\Delta T = T_1 - T_2$, with T_1 temperature of the hot reservoir and T_2 of the cold one. Very important quantities are the power P_{gen} delivered to the load and the efficiency η, which is the ratio between the output power to the load and the heat flow from the hot reservoir. Both quantities P_{gen} and η can be optimized with varying the parameters of the device [2,3], and the efficiency η can never exceed the Carnot efficiency η_C defined as

$$\eta_C = \frac{\Delta T}{T_1} = 1 - \frac{T_2}{T_1}\,. \tag{2}$$

Within the linear-response regime, the maximum achievable efficiency $\eta_{\max}$ (for a given temperature difference and optimizing over the voltage) is a monotonous growing function of ZT, with $\eta_{\max} = 0$ when $ZT = 0$ and $\eta_{\max} \to \infty$ when $ZT \to \infty$ (the positivity of entropy production imposes $ZT \geq 0$).

Bulk solid state systems are usually characterized by a small value of the figure of merit ZT [4]. Even if the charge conductance of metals is high, their thermopower is low. Moreover, in metals, the Wiedemann-Franz law correlates the values of electron thermal and electric conductances limiting the values of ZT [4]. Actually, the solid state systems used in bulk thermoelectric devices are doped semiconductors which show intermediate values for both conductance and thermopower [4]. Moreover, in these semiconductors, phonons, not electrons, typically provide the most important contribution to the thermal conductance.

The use of systems with reduced dimensionality, such as nanostructures, turns out to be effective to increase the thermoelectric performances [5]. Indeed, nanoscale engineering of electronic and vibrational degrees of freedom allows not only to violate the Wiedemann-Franz law, but also to reduce the phonon thermal conductance [6]. High values of ZT have been measured in superlattice thermoelectric devices [7], in quantum dot superlattices [8], and in semiconductor nanowires [9]. Moreover, thermopower S gets enhanced in molecular junctions [10]. At the nanoscale, thermoelectric devices can be analyzed in new linear and non-linear transport regimes, for example the Coulomb blockade with multi-terminal set-ups [2], where effects of electron-electron interactions between charge carriers are relevant [6]. Finally, molecular junctions [11] offer the possibility to study thermoelectric effects in cases where both electronic and vibrational degrees of freedom cooperate to energy transport [3].

This paper will focus on several relevant theoretical approaches used to interpret the thermoelectric properties of nanoscopic systems. We expose theoretical results in different regimes for electronic and vibrational degrees of freedom, analyzing in particular the absence/presence of many-body interactions onto the nanostructure. For the sake of brevity, only the main equations for transport properties will be quoted in this paper. For illustrative purposes, a simple nanostructure model with one electronic level and, in molecular junctions, also one vibrational mode will be frequently used in this paper.

First, we shall consider thermoelectric phenomena in the quantum coherent regime, investigating the possibility of energy filtering effects. The devices can have more than two leads which represent the thermoelectric reservoirs fixing both the electrochemical potentials and temperatures. Linear and non-linear response regimes are determined through the Landauer-Büttiker method [1], hence the transport properties are derived in terms of the transmission function of the nanostructure. Already at this stage, the Wiedemann-Franz law can be violated opening the possibility to tune the nanoscopic resonances and to enhance the thermoelectric performances [2, 3].

Then, we will analyze the role played by electron-electron interactions in enhancing the thermoelectric figure of merit. In particular, we will focus on the Coulomb blockade regime for a quantum dot model. In this regime, the charging energy of the nanostructure represents the most important energy barrier for the transport which, actually, is blockaded at zero bias between source and drain in the limit of small temperature. Tunneling rates through the electrodes are introduced in order to derive the kinetic equations, whose solution provides the charge state probabilities of the Coulomb island.

Finally, we shall consider the effects of room temperature on the thermoelectric performances of nano-devices within the non-equilibrium Green function formalism. Room temperature is the reference for applications, and it favors large values of thermopower. However, it can activate the vibrational degrees of the leads and the nanostructure influencing the energy transport. We point out that both phonon transport and electron-vibration interactions onto the molecule tend to reduce the thermoelectric efficiency in simple models of molecular junctions at finite temperature.

The paper is organized as follows. In sect. **2**, theoretical results about thermoelectric properties are discussed in the coherent regime. The presence of electron-electron and electron-vibration interactions between nanostructure degrees of freedom is analyzed in sects. **3** and **4**, respectively, evaluating their effects on thermoelectric conversion. We finish with concluding remarks in sect. **5**.

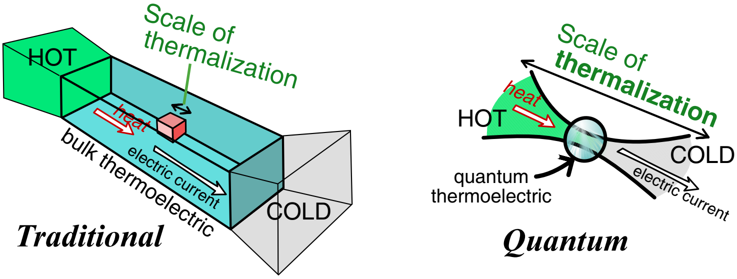

Fig. 1. – A sketch of the qualitative difference between traditional and quantum thermoelectrics. Reprinted with permission from [2].

2. – Thermoelectricity in the quantum coherent regime

In traditional bulk thermoelectrics (see fig. 1, left) the distance on which the electrons relax to a local equilibrum is much smaller than the system size. At room temperature, this relaxation length (typically some tens of nanometres) is usually of the order of the mean free path, since electron scattering is typically dominated by inelastic electron-phonon scattering, which thermalizes the electrons at the same time as causing electrical resistance by relaxing the electrons' momentum. Thus, one can treat the electrons inside the thermoelectric structure as being in local thermal equilibrium, with a local temperature which varies smoothly across the thermoelectric. The system can then be described by Boltzmann transport equations. In contrast, in nanoscale thermoelectric devices (see fig. 1, right), the thermoelectric structure is of size similar or smaller than the lengthscale on which electrons relax to a local equilibrium. Indeed, at low temperatures (typically less than a Kelvin), electron-electron and electron-phonon interactions are rather weak; as a result the relaxation length can be many microns (or in some cases even a significant fraction of a millimetre). Many systems have structures smaller than this, and one cannot make the approximations necessary to use the standard Boltzmann transport theory. Consequently the physics becomes much richer, due to quantum interference effects, strong correlations, (quantum) fluctuations and non-equilibrium events that are ubiquitous in all nanoscale devices. Moreover, transport should be described in terms of conductances rather than conductivities and therefore the figure of merit ZT is not just an intrinsic material property, but depends on system size, geometry and properties of the contacts with reservoirs.

2˙1. *Scattering theory for thermoelectricity.* – Landauer-Büttiker scattering theory is capable of describing the electrical, thermal and thermoelectric properties of non-interacting electrons in an arbitrary potential (including arbitrary disorder) in terms of the probability that the electrons go from one reservoir to another (of course, it may be challenging to calculate these probabilities in realistic, complicated nanostructures). The scattering theory is based on the idea that one can split the situation under consideration into a (small) scattering region coupled to macroscopic reservoirs of free electrons. The scattering region should then be such that each electron traverses that region from one reservoir to another without exchanging energy with other particles (electrons, phonons, etc.). Thus, an electron that enters the scattering region with energy E from a given reservoir will be represented by a wave with energy E that bounces around elastically until it escapes into a reservoir. All inelastic processes that could cause dissipation or decoherence are limited to the reservoirs. Scattering theory can be a good model even though electrons interact (repel) each other. This is the case when an electron feels the average electrostatic effect of the other electrons in a way which is captured by the mean-field Hartree approximation. However, it cannot describe 1) the physics of an electron scattering off another one, imparting part of its energy to that electron or 2) the physics of an electron scattering off the lattice (*i.e.*, electron-phonon scattering) and imparting part of its energy to the lattice. Within scattering theory, electrons leave the scatter with the same energy that they entered with, each electron only undergoes elastic scattering from the electrostatic potential due to the lattice and the flow of electrons. For instance, it does not capture the physics of single-electron interaction effects, such as Coulomb blockade (thermoelectricity in the Coulomb blockade regime will be described later in sect. **3**). In this section, we closely follow [2]. For more details and thorough discussions on the scattering theory approach, see the textbooks [12, 13].

The coupling of the scatterer to each reservoir is written in terms of a set of orthogonal modes in the contact between the scatterer and the reservoir (typically, the transverse modes of a waveguide connecting the system to the reservoirs). The probability for an electron with energy E to go from mode m of reservoir β to mode n of reservoir α is

$$P_{\alpha n;\beta m}(E) = \left|\mathcal{S}_{\alpha n;\beta m}(E)\right|^2, \tag{3}$$

where $\mathcal{S}$ is the scattering matrix. If we sum this over all modes coupled to reservoirs α and β, we get the transmission matrix elements

$$\mathcal{T}_{\alpha\beta}(E) = \sum_{nm} P_{\alpha n;\beta m}(E); \tag{4}$$

this can be interpreted as the probability to go from a given mode of reservoir β to any mode of reservoir α, summed over all modes of reservoir β. One has $\mathcal{T}_{\alpha\beta}(E) \geq 0$ for all α, β, and E. Moreover, $\sum_\alpha \mathcal{T}_{\alpha\beta}(E) = N_\beta(E)$ and $\sum_\beta \mathcal{T}_{\alpha\beta}(E) = N_\alpha(E)$, where the α and β sums are over all reservoirs and $N_\beta(E)$ is the number of modes in the coupling to reservoir β at energy E.

The Landauer-Büttiker approach tells us that one can write the charge and heat currents out of reservoir α in terms of the transmission matrix elements $\mathcal{T}_{\alpha\beta}(E)$. The charge current $J_{e,\alpha}$ out of reservoir α and into the scatterer is given by counting each electron that crosses the boundary between the scatterer and reservoir α. The number of electrons flowing out of reservoir α and into the scatterer at energy E is proportional to the number of modes $N_\alpha(E)$ multiplied by the reservoir's occupation at energy E, which is given by the Fermi function

$$f_\alpha(E) = \left(1 + \exp\left[(E-\mu_\alpha)/(k_B T_\alpha)\right]\right)^{-1}, \tag{5}$$

where μ_α and T_α are the electrochemical potential and temperature of reservoir α, and k_B is Boltzmann's constant. We must also take into account the flow of electrons from the scatterer into reservoir α. The number of electrons that flow into reservoir α at energy E from reservoir β is proportional to $\mathcal{T}_{\alpha\beta}(E)$ multiplied by reservoir β's occupation $f_\beta(E)$. The total flow of electrons into reservoir α is given by the sum of this over all β (including $\beta = \alpha$). The electrical current into the scatterer from reservoir α is then given by the flow of electrons out of the reservoir minus the total flow into it

$$J_{e,\alpha} = \sum_\beta \int_{-\infty}^{\infty} \frac{\mathrm{d}E}{h}\, e\, \left[N_\alpha(E)\,\delta_{\alpha\beta} - \mathcal{T}_{\alpha\beta}(E)\right]\, f_\beta(E), \tag{6}$$

where e is the electron charge and h the Planck constant. We can make the same argument to define the energy current out of reservoir α into the scatterer, except now each electron carries an amount of energy E instead of the charge e. Hence

$$J_{u,\alpha} = \sum_\beta \int_{-\infty}^{\infty} \frac{\mathrm{d}E}{h}\, E\, \left[N_\alpha(E)\,\delta_{\alpha\beta} - \mathcal{T}_{\alpha\beta}(E)\right]\, f_\beta(E). \tag{7}$$

To construct the equivalent formula for the heat current out of a reservoir, we must consider the definition of heat in that reservoir. We take the heat energy in a reservoir's electron gas to be the total energy of the gas minus the energy which that gas would have in its ground state at the same electrochemical potential. As such, the heat energy can be written as a sum over the energy of all electrons, measured from the reservoir's electrochemical potential. This means electrons above the electrochemical potential contribute positively to the heat, while those below the electrochemical potential contribute negatively to the heat. The latter can be understood as saying that if one removes an electron below the electrochemical potential, it increases the heat in the reservoir, because one is pushing the system further from the zero temperature Fermi distribution (in which all states below the electrochemical potential are filled). Thus, an electron with energy E leaving reservoir α carries an amount of heat, $\Delta Q_\alpha = E - \mu_\alpha$, out of the reservoir. The formula for heat current is the same as that for energy current, eq. (7), but with $(E-\mu_\alpha)$ in place of E. Hence the heat current into the scatterer from reservoir α is $J_{h,\alpha} = J_{u,\alpha} - (\mu_\alpha/e)J_{e,\alpha}$.

Given the above constraints on $\mathcal{T}_{\alpha\beta}(E)$, we can see that $\sum_\alpha J_{e,\alpha} = \sum_\alpha J_{u,\alpha} = 0$. This is nothing but Kirchoff's law of current conservation for electrical or energy currents. However, heat currents into the scatterer obey $\sum_\alpha J_{h,\alpha} = -\sum_\alpha(\mu_\alpha/e)J_{e,\alpha}$. This means that heat currents are not conserved, since the scatterer can be a source or sink for heat.

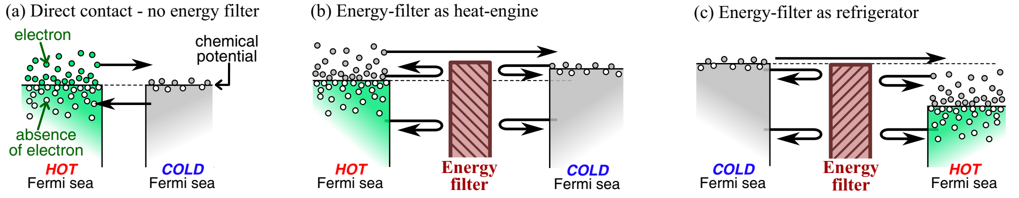

Fig. 2. – Schematic drawing of thermoelectric effects induced by an energy filter. Reprinted with permission from [2].

2·2. *Energy filtering.* – Thermoelectric effects are present whenever the dynamics of the electrons above the Fermi surface are different from the dynamics of electrons below the Fermi surface. The simplest example of a thermoelectric effect (captured by scattering theory) is that of an energy filter, schematically illustrated in fig. 2. In panel (a) we show direct connection between two reservoirs of electrons at different temperatures but the same electrochemical potential in the absence of any energy filter. Electrons in occupied (shaded) states want to flow into empty (white) states, crossing from one reservoir to the other to do so. The resulting flows are marked by the thick black arrows. In the absence of an energy-filter there is an heat current but no electrical current (the opposite flows of electrons above and below electrochemical potential cancel each other out). In panels (b) and (c) we sketch an energy-filter between the hot and cold Fermi seas which blocks all particle flow below a certain energy. In (b) we show how to use it as a heat-engine, it generates power because the temperature difference means that electrons flows from a region of lower electrochemical potential (left) to a region of higher electrochemical potential (right). In (c) we show how to use it as a refrigerator, using a potential bias to ensure that electrons above the Fermi sea can flow out of the cold reservoir, cooling it further.

It turns out that delta-energy filtering (*i.e.*, transport is possible only in a tiny energy window of width $\delta E \to 0$) is, for systems described by the scattering theory, the only mechanism leading to the Carnot efficiency [14-16]. Let us consider two terminals, assuming $T_1 > T_2$, $\mu_1 < \mu_2$, $J_{e,1} > 0$ and $J_{h,1} > 0$. The efficiency for power generation is then given by

$$\eta = \frac{[(\mu_2 - \mu_1)/e] J_{e,1}}{J_{h,1}} = \frac{(\mu_2 - \mu_1) \int_{-\infty}^{\infty} \mathrm{d}E\, \mathcal{T}(E)\, [f_1(E) - f_2(E)]}{\int_{-\infty}^{\infty} \mathrm{d}E\, (E - \mu_1)\, \mathcal{T}(E)\, [f_1(E) - f_2(E)]}\,, \tag{8}$$

where we used the shorthand notation $\mathcal{T}(E) = \mathcal{T}_{12}(E)$. When the transmission is possible only within a tiny energy window around $E = E_\star$, the efficiency reads

$$\eta = \frac{\mu_2 - \mu_1}{E_\star - \mu_1}\,. \tag{9}$$

We have $f_1(E_\star) = f_2(E_\star)$, namely the occupation of states is the same in the two reservoirs at different temperatures and electrochemical potentials, when

$$\frac{E_\star - \mu_1}{T_1} = \frac{E_\star - \mu_2}{T_2} \Rightarrow E_\star = \frac{\mu_2 T_1 - \mu_1 T_2}{T_1 - T_2}\,. \tag{10}$$

Substituting such $E_\star$ into eq. (9), we obtain the Carnot efficiency $\eta = \eta_C = 1 - T_2/T_1$. Note that Carnot efficiency is obtained in the limit $J_{e,1} \to 0$, corresponding to *reversible transport* (zero entropy production) and *zero output power*.

It is interesting to note that the abstract concept of delta-energy filtering is illustrated by a single-level quantum dot, or a single-level molecule. The model is still oversimplified, in that we make the assumption that the electrons do not interact with each other, so Coulomb blockade effects (which cannot be treated in the scattering theory) are neglected. However, it is instructive to understand the scattering theory for a quantum dot, before going on to more sophisticated models. If the dot only has one state at energy $E_\star$, and two reservoirs (each with one mode), which couple to the dot with strength w_1 and w_2, then the transmission function has a Lorentzian energy dependence:

$$\mathcal{T}(E) = \frac{\Gamma_1 \Gamma_2}{(E - E_\star)^2 + \frac{1}{4}(\Gamma_1 + \Gamma_2)^2}\,, \tag{11}$$

where we define $\Gamma_\alpha = 2\pi |w_\alpha|^2$ for $\alpha \in 1, 2$. Delta-energy filtering is obtained in the limit $(\Gamma_1 + \Gamma_2)/k_B T \to 0$.

2˙3. *Power-efficiency trade-off*. – The Carnot limit can be achieved for dissipationless heat engines. Such ideal machines operate reversibly and infinitely slowly, and therefore the extracted power vanishes. For any practical purpose it is therefore crucial to consider the power-efficiency trade-off, in order to design devices that work at the maximum possible efficiency for a given output power. This problem was solved, within scattering theory, in [17, 18]. The first ingredient to derive such bound is the Bekenstein-Pendry bound [19-21], which comes from the quantization of thermal conductance and sets an upper bound on the heat current through a single transverse mode. The heat flow out of reservoir α is maximal when that reservoir is coupled to another reservoir at zero temperature (and at the same electrochemical potential) via a constriction which lets particles flow at all energies:

$$J_{h,\alpha}^{\max} = \frac{\pi^2}{6h}\, N\, k_B^2 T_\alpha^2, \tag{12}$$

with N number of transverse modes.

The Bekenstein-Pendry upper bound on heat flow places an upper bound on the power generated by a heat-engine (since the efficiency is always finite). A rigourous two-terminal analysis [17, 18] shows that the maximum generated power is

$$P_{\text{gen}}^{\max} = A_0\, \frac{\pi^2}{h}\, N\, k_B^2 \big(T_1 - T_2\big)^2, \tag{13}$$

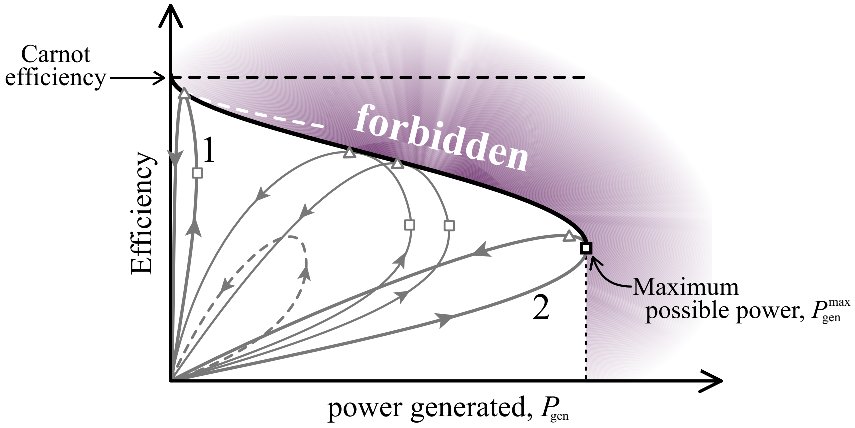

Fig. 3. – Schematic drawing of the power-efficiency curves (the grey loops) for systems with different transmission functions, at given reservoirs' temperatures T_1 and T_2. The thick black curve separates the region accessible by systems with suitably chosen transmission functions, from the region of efficiencies and powers that no system can achieve. For small power generation, such curve is approximated by the dashed white curve given by eq. (14). Each loop is formed (in the manner indicated by the arrows) by increasing the electrochemical potential bias $\Delta\mu$ from zero up to the stopping value, for which the temperature difference is no longer sufficient to push charges against the bias. The triangle marks that system's highest efficiency, while the square marks its highest power generation. Loop 1 is for a system with a narrow transmission function, which has a low power output, but is capable of achieving a high efficiency (close to Carnot efficiency). Loop 2 is for a system with a transmission in the form of a step function, its maximum efficiency is lower, but its maximum power is much higher. Reprinted with permission from [2].

where $A_0 \approx 0.0321$. This bound is strict in the sense that it is never exceeded, but is achieved by a system with a transmission function in the form of a step function (*i.e.*, a high-pass filter) which lets through all particles with $E \geq E_\star$, when one takes $\Delta\mu \approx 1.146\, k_B\, \Delta T$, with $\Delta\mu = \mu_2 - \mu_1 > 0$ and $\Delta T = T_1 - T_2 > 0$.

In general, scattering theory implies a bound on the efficiency at a given output power $P_{\rm gen}$, which equals the Carnot efficiency at $P_{\rm gen} = 0$, and decays with increasing $P_{\rm gen}$. A two-terminal calculation find the transmission function $\mathcal{T}(E)$ that maximizes the efficiency of the heat engine for a given output power (and such bound cannot be overcome for three-terminal devices [22]). It turns out that the optimal $\mathcal{T}$ is a boxcar function, $\mathcal{T}(E) = 1$ for $E_\star < E < E_{\star\star}$ and $\mathcal{T}(E) = 0$ otherwise. Here $E_{\star\star}$ is determined numerically by solving the equation $E_{\star\star} = \Delta\mu J'_{h,1}/P'_{\rm gen}$, where the prime indicates the derivative over $\Delta\mu$ for fixed $\mathcal{T}$ (this equation is transcendental since $J_{h,1}$ and $P_{\rm gen}$ depend on $E_{\star\star}$). Note that $\Delta\mu$, and consequently $E_\star$, are determined from the above optimization procedure. The bound on heat-engine efficiency for a given power output is sketched in fig. 3. At small output power, $P_{\rm gen}/P_{\rm gen}^{\rm max} \ll 1$,

$$\eta(P_{\rm gen}) \approx \eta_C \left(1 - 0.478\sqrt{\frac{T_2}{T_1}\frac{P_{\rm gen}}{P_{\rm gen}^{\rm max}}}\right). \tag{14}$$

In the limit $E_{\star\star} \to E_\star$, $P \to 0$ and $\eta \to \eta_C$. In this case, we recover the well-known delta-energy filtering mechanism to achieve the Carnot efficiency [14-16]. Note that a similar upper bound can be obtained also for the efficiency of refrigeration for a given cooling power [17, 18]. Finally, it is interesting to note that the bound from scattering theory can be overcome for classical interacting systems [23]. This result is rooted in the possibility for interacting systems to achieve the Carnot efficiency at the thermodynamic limit without delta-energy filtering [24-27], so that large efficiencies can be obtained without greatly reducing power.

3. – Thermoelectricity in the Coulomb blockade regime

3˙1. *Quantum dot model.* – A quantum dot (QD) is a paradigmatic model in the investigation of thermoelectric properties of small devices, since it is characterized by a spectrum of discrete energy levels. On one side, such system is ideal to filter the electrons participating in the charge transport to a narrow energy filter, with (see sect. **2**) a consequent increase of the thermoelectric efficiency. On the other side, for a QD one can also study the effects due to Coulomb interactions among electrons. Note that in this section we will remain within the Coulomb blockade regime and we will only consider electron transport, neglecting any contribution due to phonons. The discussed results therefore set an upper bound to the thermoelectric efficiency of the QD, approachable only in the limit in which suitable strategies to strongly reduce phonon transport are implemented. In this section, we shall follow [28], which generalizes to multi-terminal set-ups and to the calculation of the thermoelectric efficiency (both in the linear-response regime and beyond) the method put forward by [29, 30] (see also [31-33]).

The QD is tunnel-coupled to $\mathcal{N}$ electron reservoirs, each characterized by a given temperature T_α and electrochemical potential μ_α, so that the occupation of the electrons within reservoir α follows the Fermi distribution $f_\alpha(E)$. In fig. 4, E_p (with $p = 1, 2, \ldots$) are the QD single-electron energy levels (these levels can be shifted by means of an applied gate voltage). Electron-electron (Coulomb) interaction is accounted for by a capacitance C, whose associated energy scale is its charging energy $(Ne)^2/2C$, where N is the number of electrons in the QD. We assume that the QD is weakly coupled to the reservoirs through large tunneling barriers. More precisely, we assume that thermal energy k_BT, level spacing and charging energy are much larger than the coupling energy between reservoirs and QD ($\hbar \sum_\alpha \Gamma_\alpha(p)$, where $\Gamma_\alpha(p)$ is the tunneling rate from level p to reservoir α, which we assume independent of the number N of electrons inside the dot). As a consequence, the charge on the QD is quantized, *i.e.* each energy level E_p can have either zero or one electron, $n_p = 0$ or $n_p = 1$ (any degeneracy, like electron spin, can be taken into account counting each level multiple times), and transport occurs due to single-electron tunneling processes (*sequential tunneling regime*). The electrostatic energy associated with the electrons within the QD is given by $U(N) = E_C N^2$, where $E_C = e^2/2C$, $N = \sum_i n_i$.

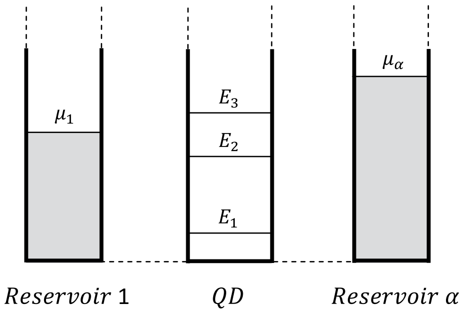

Fig. 4. – Schematic energy representation of a multilevel QD. E_1, E_2, etc. are the single-electron energy levels of the QD, while μ_1 and μ_α are the electrochemical potentials relative to reservoir 1 and α, respectively. Reprinted with permission from [28].

3·2. *Kinetic equations.* – The QD is described by states characterized by a set of occupation numbers $\{n_i\}$ relative to the energy levels. The QD changes state whenever a single-electron tunneling process takes place. Let $P(\{n_i\})$ denote the non-equilibrium probability for a given state $\{n_i\}$ to occur. The single-electron tunneling processes that contribute to changing over time $P(\{n_i\})$ are due to electrons that tunnel from the QD to the reservoirs and vice-versa. For an electron exiting the QD, initially with N electrons, from energy level E_p and going into reservoir α at energy E^{fin}, energy conservation imposes that

$$E_p + U(N) = E^{\text{fin}}(N) + U(N-1). \tag{15}$$

On the contrary, for an electron that tunnels from an initial state in reservoir α at energy E^{in} to the level E_p in the QD that initially had N electrons

$$E^{\text{in}}(N) + U(N) = E_p + U(N+1). \tag{16}$$

$P(\{n_i\})$ can then be determined by the following set of kinetic equations, one for each configuration $\{n_i\}$:

$$\begin{aligned}\frac{\partial}{\partial t}P\left(\{n_i\}\right) = &-\sum_{p\alpha}\delta_{n_p,0}P\left(\{n_i\}\right)\Gamma_\alpha(p)f_\alpha\left(E^{\text{in}}(N)\right)\\ &-\sum_{p\alpha}\delta_{n_p,1}P\left(\{n_i\}\right)\Gamma_\alpha(p)\left[1-f_\alpha\left(E^{\text{fin}}(N)\right)\right]\\ &+\sum_{p\alpha}\delta_{n_p,0}P\left(\{n_i\},n_p=1\right)\Gamma_\alpha(p)\left[1-f_\alpha\left(E^{\text{fin}}(N+1)\right)\right]\\ &+\sum_{p\alpha}\delta_{n_p,1}P\left(\{n_i\},n_p=0\right)\Gamma_\alpha(p)f_\alpha\left(E^{\text{in}}(N-1)\right),\end{aligned} \tag{17}$$

where we have introduced the notation

$$P\left(\{n_i\}, n_p = 1\right) = P\left(\{n_1, \dots, n_{p-1}, 1, n_{p+1}, \dots\}\right) \tag{18}$$

and

$$P\left(\{n_i\}, n_p = 0\right) = P\left(\{n_1, \dots, n_{p-1}, 0, n_{p+1}, \dots\}\right) \tag{19}$$

for the QD states. The first term in the right-hand side of eq. (17) accounts for the decrease of the probability $P(\{n_i\})$, with the QD initially in the state $\{n_i\}$, due to an electron coming from a reservoir and occupying an empty level in the QD. The rate of electrons coming from reservoir α will be given by a sum over all empty levels p (such that $n_p = 0$) of the tunnel rate $\Gamma_\alpha(p)$, multiplied by the probability of finding the QD in this state, $P(\{n_i\})$, and multiplied by the reservoir's occupation $f_\alpha(E^{\mathrm{in}}(N))$ at the correct energy $E^{\mathrm{in}}(N)$ to tunnel to level p. The second term accounts for the decrease of the probability $P(\{n_i\})$, with the QD initially in the state $\{n_i\}$, due an electron leaving the QD from an occupied level to tunnel into a reservoir. The third term accounts for the increase of the probability $P(\{n_i\})$ if the QD is in a state with an extra electron in level p with respect to $\{n_i\}$, and if this electron leaves the QD, tunneling to the reservoirs. The forth term accounts for the increase of the probability $P(\{n_i\})$ if the QD is in a state with a missing electron in level p with respect to $\{n_i\}$, and if this electron enters the QD in level p, tunneling from the reservoirs. The *stationary solution* of the kinetic equations, obtained imposing $\partial P/\partial t = 0$, together with the normalization request $\sum_{\{n_i\}} P(\{n_i\}) = 1$ provides a complete set of equations that uniquely defines $P(\{n_i\})$. The sum over $\{n_i\}$ means the sum over $n_i = 0, 1$, with $i = 1, 2, \dots$

Charge $J_{e,\alpha}$ and energy $J_{u,\alpha}$ currents flowing from reservoir α to the QD can be calculated as the sum of all possible tunneling processes, since the QD can be in any state $\{n_i\}$ with probability $P(\{n_i\})$ and an electron can tunnel into or out of any energy level E_p. For the charge current we have

$$J_{e,\alpha} = e \sum_{p=1}^{\infty} \sum_{\{n_i\}} P(\{n_i\}) \Gamma_\alpha(p) \left\{ \delta_{n_p,0} f_\alpha(E^{\mathrm{in}}(N)) - \delta_{n_p,1}[1 - f_\alpha(E^{\mathrm{fin}}(N))] \right\}, \tag{20}$$

while for the energy current we have

$$\begin{aligned} J_{u,\alpha} = \sum_{p=1}^{\infty} \sum_{\{n_i\}} & P(\{n_i\}) \Gamma_\alpha(p) \big\{ \delta_{n_p,0} f_\alpha(E^{\mathrm{in}}(N)) E^{\mathrm{in}}(N) \\ & - \delta_{n_p,1}[1 - f_\alpha(E^{\mathrm{fin}}(N))] E^{\mathrm{fin}}(N) \big\}, \end{aligned} \tag{21}$$

$E^{\mathrm{in}}(N)$ $[E^{\mathrm{fin}}(N)]$ being the energy carried by an electron entering (exiting) the QD. The heat currents exiting the reservoirs can then be calculated as $J_{h,\alpha} = J_{u,\alpha} - (\mu_\alpha/e) J_{e,\alpha}$.

3˙3. *Thermoelectric performance in the quantum limit.* – Starting from the above expressions for charge and heat currents, one can obtain in the so-called *quantum limit* and for equidistant levels, $E_p - E_{p-1} = \Delta E$, linear-response analytical expressions for the multi-terminal transport coefficients [28]. The quantum limit is characterized by having the energy spacing between levels of the QD and the charging energy much bigger than k_BT (while $k_BT \gg \hbar\Gamma_\alpha(p)$). At low temperatures, the lowest energy levels of the QD are occupied, so that, if there are initially $N-1$ electrons in the QD, electrons can flow mainly through level $p = N$. Such process gives the dominant contribution to transport.

In the two-terminal case and within linear response, one can in particular show [28] that peaks of both the thermoelectric figure of merit ZT and the power factor Q (which determines the maximum output power $P_{\max} = \frac{1}{4}Q(T_2 - T_1)^2$) are obtained for values of the electrochemical potential given by $\mu \approx \mu_N \pm 2.40 k_BT$, where $\mu_N \equiv (N-1)\Delta E + (2N-1)E_C$. The value Q^* of Q in these points is $Q^* \approx 0.44\gamma k_B/T$ $[\gamma \equiv \Gamma_1\Gamma_2/(\Gamma_1+\Gamma_2)]$, while the value of ZT in the same points is $ZT^* \approx 0.44\frac{e^{\Delta E/k_BT}}{(\Delta E/k_BT)^2}$. This equation shows that in the limit $\Delta E/k_BT \to \infty$, we have that $ZT^\star \to \infty$. For example, for $\Delta E = 6\,k_BT$, we reach $ZT^* \approx 5$; for $\Delta E = 10\,k_BT$, we reach $ZT^* \approx 97$, and so on. This is consistent with the energy filtering mechanism discussed in sect. **2**: a narrow transmission function yields $ZT \to \infty$. Furthermore, these peaks in ZT correspond to peaks in Q, so in these points we can optimize the maximum power $P_{\max}$ and the corresponding efficiency $\eta(P_{\max})$ (which is a monotonous growing function of ZT) simultaneously.

An important question is whether Coulomb interactions may enhance the thermoelectric performance of a QD. A positive answer (in the Coulomb blockade regime discussed in this section) can be given and explained [28] by comparing an interacting QD (with $2E_C > \Delta E \gg k_BT$) with a non-interacting QD ($E_C = 0$) that has the same energy spacing ΔE. Within the linear-response quantum limit and for a two-terminal set-up, the electric conductance and the thermopower are not affected by interactions (neglecting the fine structure in their dependence on μ, see [28]). On the other hand, Coulomb interactions dramatically suppress the thermal conductance. A comparison between the interacting and non-interacting thermal conductances is plotted in fig. 5. This figure shows a large interaction-induced reduction of the thermal conductance. Intuitively, the striking difference between the two models can be explained as follows. If we consider a single energy level QD the thermal conductance vanishes ($K = 0$) since K is computed at zero charge current and charge and heat currents are proportional in this case. However, K can be finite when at least two energy levels are available, and gets bigger by increasing the flux of electrons tunneling at different energies. Now, Coulomb interaction produces a correlation between electrons tunneling at different energies. Namely, if one electron enters the QD the electrostatic energy increases by $2E_C$, preventing other electrons from entering the QD at any other energy level. Therefore, until that electron tunnels out of the QD, all other processes are blocked: this is a manifestation of Coulomb blockade. On the contrary, in the non-interacting case all tunneling events are independent. This correlation is thus responsible for suppressing simultaneous tunneling through different energy levels in the interacting case, which results in a suppression of K. As a result of

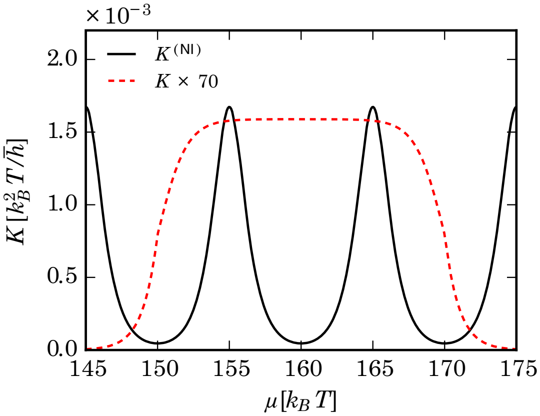

Fig. 5. – Comparison between the thermal conductances $K^{(\mathrm{NI})}$ and K, for the non-interacting and the interacting case, plotted as a function of the electrochemical potntial μ. In both cases $\Delta E = 10\,k_B T$, and $\hbar\Gamma_1(p) = \hbar\Gamma_2(p) = (1/100)\,k_B T$, while $E_C = 50\,k_B T$ in the interacting case and $E_C = 0$ in the non-interacting case. To facilitate comparison, the interacting thermal conductance has been multiplied by a factor 70. Reprinted with permission from [28].

the suppression of K (at constant G and S), Coulomb interactions dramatically enhance ZT (at constant power factor). For further results on thermoelectric transport in the Coulomb blockade regime, also beyond linear response, see [28].

4. – Effects of electron-vibration interactions on thermoelectricity

While so far we focused on low temperatures, room temperature is the reference for thermoelectric applications. On one hand an increase of temperature favors large values of thermopower, on the other hand it can activate phonon transport in the leads and electron-vibration interactions onto the nanostructure, which can strongly affect thermoelectric efficiency. Temperature effects can become very important in nanoscale systems such as molecular junctions where vibrations represent relevant degrees of freedom for energy exchanges with electrons.

Within the same approximations valid in the Coulomb blockade regime discussed in the previous section, one can include also the effects of electron-vibration interactions. In particular, together with the charging electrostatic energy U, there is the additional energy scale E_P, the electron-vibration coupling energy, which takes into account the energy barrier due to the interaction of the electrons with the vibrational degrees of freedom. If E_P is the most relevant energy, hence larger than the energy $\hbar\Gamma$ associated to the tunneling onto the nanostructure (thus Γ controls the hybridization width of the nanostructure energy levels), one enters the Franck-Condon blockade regime [34]. Therefore, one can combine electron-electron and electron-vibration effects into a master equation for electron and phonon number probabilities [35, 36] in the presence of both electronic and bosonic (such as phononic) reservoirs.

The rate equations for probabilities take into account only the incoherent charge dynamics in the presence of many-body interactions. One can improve this approach adding co-tunneling effects, that is higher orders of the perturbative expansion in the tunneling matrix elements [37]. Otherwise, one should evaluate the density matrix taking into account both diagonal (populations) and off-diagonals (coherences) elements calculating the probability amplitudes between different quantum states of the nanostructure. One way to circumvent some difficulties related to the perturbative expansion in the tunneling processes is to use another method, the non-equilibrium Green's function (NEGF) approach [38]. Within this approach, one simply recovers the coherent results in the case where many-body interactions are absent or neglected onto the nanostructure. Indeed, even if interactions are present, the coherent part of the quantum dynamics is preserved. Moreover, NEGF method is able to describe also the blockade transport phenomena induced by many-body interactions.

In the first subsection, we will provide some clues to NEGF approach, in the second one we shall apply this formalism to study electron-vibration effects in simple models of molecular junctions at room temperature.

4·1. *Non-equilibrium Green's Function.* – Within NEGF formalism [38], the electrical current $J_{e,\alpha}$ related to the lead α can be expressed in terms of the electron Green functions of the nanostructure and the electron self-energies due to the nanostructure-lead coupling:

$$J_{e,\alpha} = \frac{e}{\hbar} \int \frac{\mathrm{d}E}{2\pi}\, tr_{el}\big\{G^{>}(E)\Sigma_{\alpha}^{<}(E) - G^{<}(E)\Sigma_{\alpha}^{>}(E)\big\}, \tag{22}$$

where tr_{el} is the trace over the electronic degrees of freedom. In eq. (22), the greater electron Green function $G^{>}$ provides the number of available states in the molecule, $\Sigma_{\alpha}^{<}$ the out-tunneling rate of the occupied electronic states in the α lead. Therefore, the first term in eq. (22) provides the current flowing out of the α lead to the nanostructure. Analogously, the lesser electron Green function $G^{<}$ provides the number of occupied states in the nanostrucutre, $\Sigma_{\alpha}^{>}$ the in-tunneling rate of the available electron states in the α lead. Hence, the second term in eq. (22) with the minus sign gives the current flowing from the molecule to the α lead.

The electronic energy current $J_{u,\alpha}$ related to the lead α has an expression similar to the charge current:

$$J_{u,\alpha} = \frac{1}{\hbar} \int \frac{\mathrm{d}E}{2\pi}\, E\, tr_{el}\big\{G^{>}(E)\Sigma_{\alpha}^{<}(E) - G^{<}(E)\Sigma_{\alpha}^{>}(E)\big\}. \tag{23}$$

The greater $G^{>}$ and the lesser $G^{<}$ electron Green functions are related to the retarded G^{r} and advanced G^{a} electron Green functions through the Keldysh equation [38]:

$$G^{>,<} = G^{r}\Sigma_{tot}^{>,<}G^{a}, \tag{24}$$

where Σ_{tot} is the total electron self-energy given by the sum of the tunneling contributions Σ_α and a term Σ_{int} due to many-body interactions on the nanostructure:

$$\Sigma^{>,<,r,a} = \sum_\alpha \Sigma_\alpha^{>,<,r,a} + \Sigma_{int}^{>,<,r,a}. \tag{25}$$

Within NEGF method, equations for fermions and bosons are similar. Indeed, the phonon energy current $J_{ph,\alpha}$ related to the lead α has a structure similar to eq. (23) for electrons.

In the regime of linear response, charge and energy currents allow to determine not only the electron transport quantities, such as the conductance G, the thermopower S, and the electron thermal conductance K^{el}, but also the phonon thermal conductance K^{ph}. Hence, the total thermal conductance is $K = K^{el} + K^{ph}$, and the thermoelectric figure of merit becomes $ZT = GS^2T/K$.

4·2. *Electron-vibration interactions.* – In this subsection, we analyze the effects of the electron-vibration interaction on the thermoelectric properties starting from spinless Anderson-Holstein model for molecular junctions [3, 11]. In particular, we consider a single electronic level of energy ϵ coupled to leads with a damping rate Γ, and a single vibrational mode of low frequency ω_0 coupled to leads with damping rate γ. For nano-devices with massive molecules, the relevant vibrational degrees of freedom are characterized by low energies, therefore a non-equilibrium adiabatic approach based on the NEGF method has been proposed to study the transport properties [39-44]. This approach is reliable for $\omega_0 \ll \Gamma$, therefore it is semiclassical. However, it is valid for arbitrary strengths of electron-vibration coupling E_P. The adiabatic approach has been recently employed to study the effects of electron-vibration interaction on the thermoelectric coefficients of junctions with massive molecules, such as fullerene [45-47].

In fig. 6, we report the thermoelectric figure of merit ZT obtained within the adiabatic approach as a function of the level energy ϵ for different values of the electron-vibration coupling E_P at room temperature $T = 1.25$ (in units of $\hbar\Gamma/k_B$, with $\hbar\Gamma$ of the order of 20 meV [45]). Two values of γ are considered: 0.15Γ (upper panel of fig. 6) and 0.4Γ (lower panel of fig. 6). These are somewhat extremal values for γ with varying the type and coupling of leads [45]. As shown in fig. 6, the electron-vibration interaction induces a shift (proportional to the coupling energy E_P) of the resonance at higher values of ϵ. With increasing E_P, the peak values of the charge conductance G get reduced, and the minimal and maximal values of the thermopower S are lowered in absolute value. Therefore, the figure of merit ZT gets globally decreased. For the intermediate coupling $E_P = 1$, the reduction of the peak in comparison with the value at $E_P = 0$ is about twenty-five per cent. For molecules like fullerene, the electron-vibration interaction is estimated to be in the weak to intermediate coupling regime ($E_P < 1$). In any case, the electron-vibration interaction is quite effective in decreasing the thermoelectric performance. Moreover, from the comparison between upper and lower panel of fig. 6, we point out the an increase of the lead phonon-vibration rate γ gives rise to an enhancement of the phonon transport which drastically reduces the figure of merit ZT.

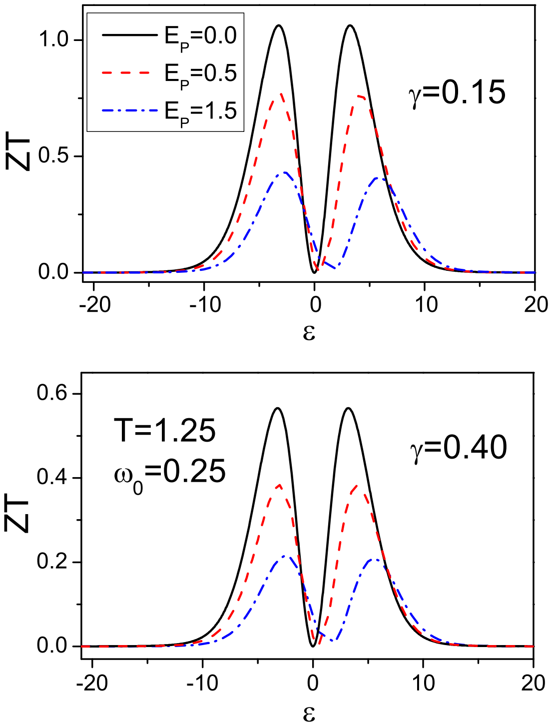

Fig. 6. – Thermoelectric figure of merit ZT at vibrational damping rate $\gamma = 0.15$ (in units of Γ, upper panel) and $\gamma = 0.4$ (in units of Γ, lower panel) as a function of level energy ϵ (in units of $\hbar\Gamma$) for different values of the electron-vibration coupling E_P (in units of $\hbar\Gamma$). In the plots, $T = 1.25$ (in units of $\hbar\Gamma/k_B$) and $\omega_0 = 0.25$ (in units of Γ). Reprinted with permission from [45].

Finally, we focus on the non-equilibrium Coulomb blockade regime, studying the single-level Anderson-Holstein-Hubbard model within the adiabatic approach for $\mu_L = 0$, $T_L = T + \Delta T$, and $\mu_R = \Delta V$, $T_R = T$ (with T close to room temperature) [46]. In fig. 7, we analyze the maximal efficiency $\eta_{\max}$ as a function of the temperature difference ΔT for different values of lead phonon-molecule coupling: $\gamma = 0$ (black solid line with circles) and $\gamma = 0.15\Gamma$ (red solid line with squares). The situation analyzed in the figure corresponds to the case where γ is not large and the electron-vibration coupling is in the weak to intermediate regime. Therefore, the maximal efficiency is not drastically reduced in comparison with the ideal Carnot efficiency η_C defined in eq. (2) and reported in fig. 7 as a dashed line. Indeed, for large ΔT, $\eta_{\max}$ for $\gamma = 0$ is about half of the Carnot limit. Moreover, the quantity $\eta_{\max}$ for $\gamma = 0.15\Gamma$ is slightly smaller than the maximal efficiency for $\gamma = 0$. In the inset of fig. 7, we show the ratio R between the maximal efficiency $\eta_{\max}$ and the Carnot efficiency η_C for different values of γ pointing out their different behaviors. Summarizing, in the case of nano-junctions with weak phonon-molecule and weak to intermediate electron-vibration coupling, the maximal efficiency gets decreased but it is characterized by a behavior similar to that of ideal performance standards.

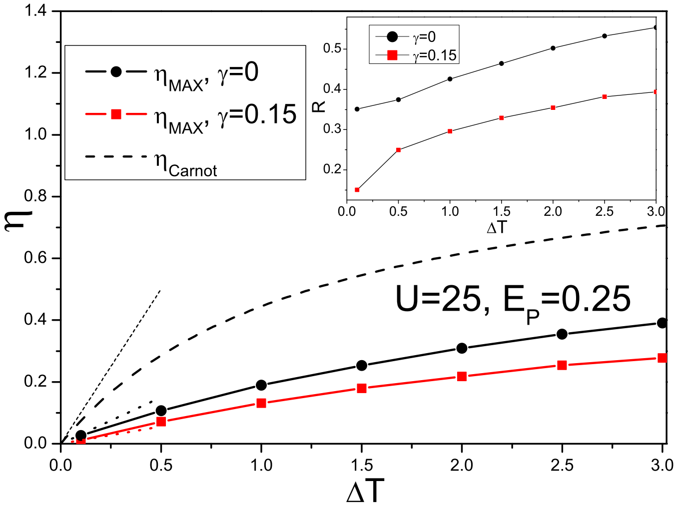

Fig. 7. – Maximal efficiency $\eta_{\max}$ as a function of the temperature difference ΔT (in units of $\hbar\Gamma/k_B$) for $\gamma = 0$ (black solid line with circles), and $\gamma = 0.15$ (red solid line with squares, in units of Γ). In the plot, $U = 25\hbar\Gamma$, $T = 1.25\hbar\Gamma/k_B$ (close to room temperature), $E_P = 0.25\hbar\Gamma$ and $\omega_0 = 0.25\Gamma$. The dashed line reports the Carnot efficiency η_C. The dotted line refers to the slopes in the regime of small ΔT. In the inset, the ratio R between $\eta_{\max}$ and η_C for $\gamma = 0$ (solid line with black circles), and $\gamma = 0.15\Gamma$ (solid line with red squares). Reprinted with permission from [46].

5. – Conclusions and perspectives

In this paper we have analyzed several important theoretical approaches used for the analysis of thermoelectric phenomena at the nanoscale: Landauer-Büttiker method for quantum coherent transport, kinetic equations for the incoherent Coulomb blockade regime, NEGF for treating electron-vibration couplings in molecular junctions. For each of these methods, we have analyzed advantages and drawbacks, fixing in particular their regime of validity. In the coherent regime, we have discussed energy filtering effects relevant to improve the thermoelectric performances of nano-devices. In the Coulomb blockade regime, we have pointed out that electron-electron correlations are able to enhance the thermoelectric figure of merit of Coulomb islands. On the other hand, we have stressed that both phonon transport and electron-vibration coupling tend to induce a decrease of thermoelectric conversion in molecular junctions.

In this paper, we have mainly discussed semi-empirical Hamiltonian models for electronic and vibrational degrees of freedom, thus the analysis of *ab initio* theories has been neglected [11]. Moreover, we have focused on the most simple electron-vibration interactions, those Holstein-type with local couplings. In order to improve the description of the transport properties of molecular junctions, it would be interesting to analyze the role of non-local electron-vibration interactions [48]. Finally, all the approaches discussed in this paper can be generalized to study the effects induced by time perturbations on the thermoelectric properties in the case without [49,50] and with [51,52] many-body interactions.

* * *

GB acknowledges the financial support of the INFN through the project "QUANTUM".

REFERENCES

[1] Datta S., *Lessons from Nanoelectronics: A New Perspective on Transport* (World Scientific Publishing Company, Singapore) 2012.

[2] Benenti G., Casati G., Saito K. and Whitney R. S., *Phys. Rep.*, **694** (2017) 1.

[3] Perroni C. A., Ninno D. and Cataudella V., *J. Phys.: Condens. Matter*, **28** (2016) 373001.

[4] Nolas G. S., Sharp J. and Goldsmid J., *Thermoelectrics: Basic Principles and New Materials Developments* (Springer-Verlag, Berlin, Heidelberg) 2001.

[5] Heremans J. P., Dresselhaus M. S., Bell L. E. and Morelli D. T., *Nat. Nanotechnol.*, **8** (2013) 471.

[6] Sothmann B., Sanchez R. and Jordan A. N., *Nanotechnology*, **26** (2015) 032001.

[7] Venkatasubramanian R., Siivola E., Colpitts T. and O'Quinn B., *Nature*, **413** (2001) 597.

[8] Harman T. C., Taylor P. J., Walsh M. P. and LaForge B. E., *Science*, **297** (2002) 2229.

[9] Hochbaum A. I., Chen R., Delgado R. D., Liang W., Garnett E. C., Najarian M., Majumdar A. and Yang P., *Nature*, **451** (2008) 163.

[10] Aradhya S. V. and Venkataraman L., *Nat. Nanotechnol.*, **8** (2013) 399.

[11] Cuevas J. C. and Scheer E., *Molecular Electronics: An Introduction to Theory and Experiment* (World Scientific Publishing Company, Singapore) 2010.

[12] Datta S., *Electronic Transport in Mesoscopic Systems* (Cambridge University Press, Cambridge) 1995.

[13] Imry Y., *Introduction to Mesoscopic Physics* (Oxford University Press, Oxford) 1997.

[14] Mahan G. D. and Sofo J. O., *Proc. Natl. Acad. Sci. U.S.A.*, **93** (1996) 7436.

[15] Humphrey T. E., Newbury R., Taylor R. P. and Linke H., *Phys. Rev. Lett.*, **89** (2002) 116801.

[16] Humphrey T. E. and Linke H., *Phys. Rev. Lett.*, **94** (2005) 096601.

[17] Whitney R. S., *Phys. Rev. Lett.*, **112** (2014) 130601.

[18] Whitney R. S., *Phys. Rev. B*, **91** (2015) 115425.

[19] Bekenstein J. D., *Phys. Rev. Lett.*, **46** (1981) 623.

[20] Bekenstein J. D., *Phys. Rev. D*, **30** (1984) 1669.

[21] Pendry J. B., *J. Phys. A.: Math. Gen.*, **16** (1983) 2161.

[22] Whitney R. S., *Entropy*, **18** (2016) 208.

[23] Luo R., Benenti G., Casati G. and Wang J., *Phys. Rev. Lett.*, **121** (2018) 080602.

[24] Saito K., Benenti G. and Casati G., *Chem. Phys.*, **375** (2010) 508.

[25] Benenti G., Casati G. and Wang J., *Phys. Rev. Lett.*, **110** (2013) 070604.

[26] Benenti G., Casati G. and Mejía-Monasterio C., *New J. Phys.*, **16** (2014) 015014.

[27] Chen S., Wang J., Casati G. and Benenti G., *Phys. Rev. E*, **92** (2015) 032139.

[28] Erdman P. A., Mazza F., Bosisio R., Benenti G., Fazio R. and Taddei F., *Phys. Rev. B*, **95** (2017) 245432.

[29] Beenakker C. W. J., *Phys. Rev. B*, **44** (1991) 1646.

[30] Beenakker C. W. J. and Staring A. A. M., *Phys. Rev. B*, **46** (1992) 9667.

[31] Zianni X., *Phys. Rev. B*, **75** (2007) 045344.

[32] Zianni X., *Phys. Rev. B*, **78** (2008) 165327.
[33] Zianni X., *Phys. Rev. B*, **82** (2010) 165302.
[34] Koch J. and von Oppen F., *Phys. Rev. Lett.*, **94** (2005) 206804.
[35] Koch J., von Oppen, Oreg Y. and Sela E., *Phys. Rev. B*, **70** (2004) 195107.
[36] Leijnse M., Wegewijs M. R. and Flensberg K., *Phys. Rev. B*, **82** (2010) 045412.
[37] Nazarov Y. V. and Blanter Y. M., *Quantum Transport: Introduction to Nanoscience* (Cambridge University Press, Cambridge) 2009.
[38] Haug H. and Jauho A. P., *Quantum Kinetics in Transport and Optics of Semiconductors* (Springer, Berlin) 2008.
[39] Nocera A., Perroni C. A., Marigliano Ramaglia V. and Cataudella V., *Phys. Rev. B*, **83** (2011) 115420.
[40] Nocera A., Perroni C. A., Marigliano Ramaglia V. and Cataudella V., *Phys. Rev. B*, **86** (2012) 035420.
[41] Nocera A., Perroni C. A., Marigliano Ramaglia V., Cantele G. and Cataudella V., *Phys. Rev. B*, **87** (2013) 155435.
[42] Perroni C. A., Nocera A. and Cataudella V., *EPL*, **103** (2013) 58001.
[43] Perroni C. A., Romeo F., Nocera A., Marigliano Ramaglia V., Citro R. and Cataudella V., *J. Phys.: Condens. Matter*, **26** (2014) 365301.
[44] Biggio M., Cavaliere F., Storace M. and Sassetti M., *Ann. Phys.*, **526** (2014) 541.
[45] Perroni C. A., Ninno D. and Cataudella V., *Phys. Rev. B*, **90** (2014) 125421.
[46] Perroni C. A., Ninno D. and Cataudella V., *New J. Phys.*, **17** (2015) 083050.
[47] Nocera A., Perroni C. A., Marigliano Ramaglia V. and Cataudella V., *Beilstein J. Nanotechnol.*, **7** (2016) 439.
[48] Perroni C. A., Piegari E., Capone M. and Cataudella V., *Phys. Rev. B*, **69** (2004) 174301.
[49] Crepieux A., Simkovic F., Cambon B. and Michelini F., *Phys. Rev. B*, **83** (2011) 153417.
[50] Ludovico M. F., Battista F., von Oppen F. and Arrachea L., *Phys. Rev. B*, **93** (2015) 075136.
[51] Zhou H., Thingna J., Hänggi P., Wang J.-S. and Li B., *Sci. Rep.*, **5** (2015) 14870.
[52] Bagheri Tagani M. and Rahimpour Soleimani H., *Physica E*, **48** (2013) 36.

Proceedings of the International School of Physics "Enrico Fermi"
Course 207 "Advances in Thermoelectricity: Foundational Issues, Materials and Nanotechnology",
edited by D. Narducci, G. J. Snyder and C. Fanciulli
(IOS, Amsterdam; SIF, Bologna) 2021
DOI 10.3254/ENFI210009

Electronic transport simulations in complex band structure thermoelectric materials

NEOPHYTOS NEOPHYTOU

University of Warwick - Warwick, UK

Summary. — Thermoelectric materials convert heat through temperature gradients into electricity, and vice versa provide cooling capabilities once a potential difference is applied across them. The realization of complex band structure materials and their alloys, as well as nanostructured materials, have revived the field of thermoelectric from decades of moderate activity, as they allow possibilities to largely improved performance. Theory and simulation of electro-thermal transport properties of materials have also been rapidly advancing. A variety of simulation software and techniques has been developed, or are in the process of being developed to improve the accuracy of these calculations. The most common simulations for the thermoelectric properties of complex materials employ *ab initio* techniques (DFT) for the dispersion of materials, which are then used within the Boltzmann Transport Equation (BTE) formalism to extract the thermoelectric coefficients. In the majority of studies, the solutions to the BTE assume the constant relaxation time approximation, despite the fact that we know that the scattering mechanisms are not only energy, but momentum, and band dependent. This is due to the vast computational costs in treating energy-dependent scattering mechanisms properly. This paper introduces the BTE formalism, and explains the numerical implementation of the energy-dependent relaxation time approximation.

1. – The Boltzmann transport equation for electronic transport under linear response

The Boltzmann Transport Equation (BTE) is the most common theoretical formalism employed in the studies of thermoelectric materials. The BTE is essentially an equation for the distribution function of particles in position and velocity/momentum spaces. The particles obey Newton's laws of motion, and particle positions and velocities are all

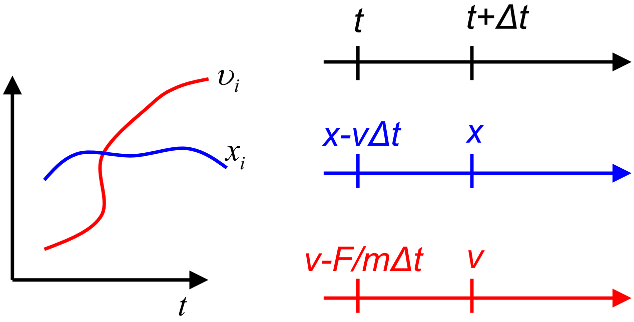

Fig. 1. – The motion of particles in position and velocity spaces.

accounted for. In typical thermoelectric studies, the electronic structure of a material is computed using *ab initio* Density Functional Theory (DFT) calculations, usually on a sparse grid, then interpolated using appropriate methods, and then employed within the BTE to obtain the thermoelectric coefficients, most commonly in the relaxation time approximation [1, 2].

Pictorially, the motion of particles can be described in a 6-dimensional space, with three coordinates describing the position, and the other three the velocity of particles, as depicted in fig. 1. The collective viewpoint is that one can form the distribution function $f(x, \boldsymbol{\upsilon}, t)$, which is a function that describes the positions and momenta/velocities of all particles *i.e.* how many electrons at time t, are located at position x_i, and have velocity $\boldsymbol{\upsilon}_i$. Once this function is known, then the current can be computed by multiplying the unit charge of each electron by its velocity and summing them up as (here assuming 1D for brevity):

$$J = \frac{1}{L}\sum_{\upsilon_x}(-q)\upsilon_x f\left(\upsilon_x\right). \tag{1}$$

The distribution function in general changes in time due to the application of a driving force, F, for example the application of a potential difference, or a temperature difference. This is done by adding the distance travelled to the old position of the particles (electrons) of effective mass m, and by adding the velocity change to the old velocity of the particles, as

$$f\left(x, \upsilon, t + \Delta t\right) = f\left(x - \upsilon\Delta t, \upsilon - \frac{F}{m}\Delta t, t\right). \tag{2}$$

For small time steps, using Taylor series expansion, and the mathematical chain rule, we can write the distribution function as

$$\begin{aligned} f(x,\upsilon,t+\Delta t) &= f(x,\upsilon,t)+\frac{\partial f}{\partial t}\Delta t \\ &= f(x,\upsilon,t)+\left(\frac{\partial f}{\partial x}\frac{\partial x}{\partial t}+\frac{\partial f}{\partial \upsilon}\frac{\partial \upsilon}{\partial t}\right)\Delta t \\ &= f(x,\upsilon,t)+\left(\frac{\partial f}{\partial x}(-\upsilon)+\frac{\partial f}{\partial \upsilon}\left(-\frac{F}{m}\right)\right)\Delta t. \end{aligned} \tag{3}$$

By bringing everything to the left-hand side, we reach to the so-called collisionless BTE:

$$\frac{\partial f}{\partial t}+\upsilon\nabla_r f+\frac{F}{m}\nabla_\upsilon f=0. \tag{4}$$

The second and third terms of the equation above refer to diffusion and drift processes, respectively. However, carriers interact with the environment and undergo scattering. Thus, the BTE needs to be modified to include the so-called "scattering operator", usually denoted as S_{op}:

$$\frac{\partial f}{\partial t}+\upsilon\nabla_r f-qE_{\mathrm{field}}\nabla_p f=\left.\frac{\partial f}{\partial t}\right|_{\mathrm{collisions}}=S_{\mathrm{op}}f=-\frac{f-f_0}{\tau_s}, \tag{5}$$

where the derivative of the velocity is replaced with the derivative of the momentum, which removes the particle mass from the equation, and the force on the particles is replaced with the electric field $-qE_{\mathrm{field}}$ (the relevant force on electrons). Using the carrier's momentum is a commonly used notation in the literature. The term $\frac{\partial f}{\partial t}|_{\mathrm{collisions}}=-\frac{f-f_0}{\tau_s}$ is the simple approximation that we commonly make for the scattering operator, namely, indicating that the rate at which the distribution function relaxes back to its equilibrium state depends on how far off equilibrium is positioned, and on a characteristic time constant, the so-called scattering relaxation time, and thus, the method is referred to as the *relaxation time approximation* (RTA).

Assuming a steady state such that $\frac{\partial f}{\partial t}=0$, and assuming a long uniform system such that no carrier variations exist, then $\nabla_r n=0$ (meaning that we ignore any diffusion processes), the BTE is simplified to:

$$f\simeq f_0+q\tau_s E_{\mathrm{field}}\nabla_p f. \tag{6}$$

This essentially says that the new distribution which describes the system after an electric field being applied, is the same as the old distribution f_0, plus an additional term that depends on the derivative of the distribution with respect to momentum. In the case of small fields, this is called "linear response", and the formalism is called "linearized Boltzmann transport". Using the Taylor series expansion backwards, we get

$$f(p_x)=f_0(p_x+q\tau_s E_{\mathrm{field}}) \tag{7}$$

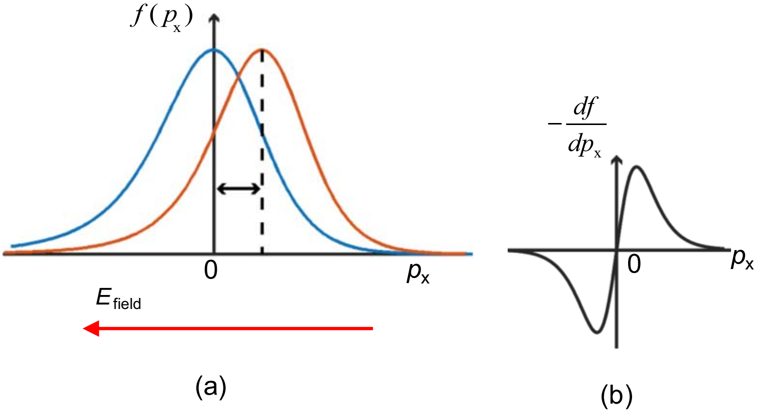

Fig. 2. – (a) The equilibrium distribution function (blue line) and the "displaced" distribution function after the application of an electric field (orange line). (b) The (negative) derivative of the distribution function with respect to the momentum, indicating a surplus of carriers with positive momenta, and a deficit of carriers with negative momenta.

which indicates, as earlier, that the new distribution function (of momenta in the system), is the old one, with its argument being shifted by a (small) momentum term. That term depends on the electric field and the relaxation time.

Pictorially, this is described in fig. 2. A typical distribution function is a Maxwellian distribution. Under equilibrium conditions, the distribution of momenta is symmetric (blue line in fig. 2(a)). The application of an electric field "displays" the distribution as indicated by the orange line, indicating a difference in the numbers of carriers with positive *vs.* negative momenta, which leads to an current flow imbalance. Mathematically, since the symmetric distribution does not provide any current, a simple rearrangement of eq. (6) to

$$f - f_0 \equiv f_{\text{A}} \simeq q\tau_s E_{\text{field}} \nabla_p f \tag{8}$$

shows the so-called asymmetric part of the distribution function, *i.e.* the deviation from symmetric conditions.

Its shape is as shown in fig. 2(b), which indicates depletion of carriers with negative momenta (or velocities), and an excess of carries with positive momenta (or velocities) —note the minus sign appearing due to the fact that the distribution is displaced in the opposite direction of the applied E_{field}. Thus, it is the asymmetric part of the distribution function which contributes to current, and the symmetric part does not, as in the latter case the two opposite fluxes counterbalance each other. Mathematically, the net flux $\Im$ can be expressed as the summation of the symmetric f_{S} and asymmetric distributions

f_{A} as

$$
\begin{aligned}
\Im &= \frac{1}{L}\sum_k \upsilon_x f = \frac{1}{L}\sum_k \upsilon_x \left(f_{\mathrm{S}} + f_{\mathrm{A}}\right)\\
&= \frac{1}{L}\sum_k \upsilon_x f_{\mathrm{S}} + \frac{1}{L}\sum_k \upsilon_x f_{\mathrm{A}}\\
&= 0 + \frac{1}{L}\sum_k \upsilon_x f_{\mathrm{A}}\\
&\Rightarrow \Im = \frac{1}{L}\sum_k \upsilon_x f_{\mathrm{A}}.
\end{aligned}
\tag{9}
$$

Thus, the net flux ends up being the summation of the asymmetric part of the distribution, weighted by the velocities of the particles. The normalization constant $1/L$ appears in the summation over k-states in 1D.

Substituting eq. (8) for the asymmetric part of the distribution function into eq. (9) for the flux, we obtain

$$
\Im = \frac{1}{L}\sum_k \upsilon_x q\tau_s E_{\text{field}} \frac{\partial f}{\partial p_x}\,. \tag{10}
$$

By using the chain rule for the derivative we can write

$$
\Im = \frac{1}{L}\sum_k \upsilon_x q\tau_s E_{\text{field}} \frac{\partial f}{\partial E}\frac{\partial E}{\partial p_x} \tag{11}
$$

and by recognizing that the kinetic energy of particles can be written as

$$
E = \frac{1}{2}m\upsilon_x^2 \Rightarrow \frac{\partial E}{\partial p_x} = \frac{\partial(\frac{1}{2}m\upsilon_x^2)}{\partial(m\upsilon_x)} = \upsilon_x \tag{12}
$$

the flux can be written as

$$
\Im = \frac{1}{L}\sum_k q\tau_s \upsilon_x^2 E_{\text{field}} \frac{\partial f}{\partial E}\,. \tag{13}
$$

To obtain the current density it is sufficient to multiply the flux with the electronic charge $-q$, such as:

$$
J = (-q)\Im = q^2 E_{\text{field}} \frac{1}{L}\sum_k \tau_s \upsilon_x^2 \left(-\frac{\partial f}{\partial E}\right). \tag{14}
$$

Since the summation over all k-space states is equivalent to an integral over the density-of-states in energy, we reach

$$J = q^2 E_{\text{field}} \int_E \tau_s \upsilon_x^2 g \left(-\frac{\partial f}{\partial E}\right) \mathrm{d}E. \tag{15}$$

The conductivity, which is defined as $\sigma = J/E_{\text{field}}$, can be extracted as

$$\sigma = q^2 \int_E \tau_s \upsilon_x^2 g \left(-\frac{\partial f}{\partial E}\right) \mathrm{d}E. \tag{16}$$

The distribution function f, under low-field transport, can be assumed to be the equilibrium distribution of carriers, following Boltzmann statistics, or Fermi-Dirac statistics. Thermoelectric materials are highly doped and the Fermi level is usually around the band edge, thus the Fermi-Dirac distribution needs to be employed. Under linear response, only a portion of the charge density is participating to transport, namely only the carriers having energies around the Fermi level (picked up by its derivative as shown in fig. 2), quantitatively defined by the $k_B T$-dependent broadening.

The quantity

$$\Xi(E) = \tau_s(E)\upsilon_x^2(E)g(E) \tag{17}$$

which appears under the integral of eq. (16) for the conductivity is the so-called "transport distribution function" (TDF), or the "transport function" [3]. Although under this simplified 1D derivation the TDF is a function of ν_x^2, it should be understood that in 3D it is a tensor quantity, effectively having $\nu_i \nu_j$ components, where i and j being x-, y-, and z- coordinates. This quantity turns out to be crucial in understanding the electronic and thermoelectric transport in advanced materials. All quantities that define it, the scattering (momentum) relaxation times, the band structure velocities, and the density of states, are all energy, momentum, and band dependent in the case of complex band structure materials. Under the simplified assumption of isotropic acoustic phonon scattering, the scattering rate becomes proportional to the density of states, thus relaxation times are inversely proportional to the density of states. The scattering times and density of states then cancel out, and the transport distribution function becomes proportional to the band structure velocity squared, with linear energy dependence, *i.e.* $\Xi(E) \propto \frac{E}{m_{\mathrm{C}}^*}$ [4].

To extract the thermopower (or Seebeck coefficient), we need to extract the conductivity in the case where a temperature gradient applied across the material constitutes the driving force for the current. The application of a potential voltage ΔV across the material results in a split between the electrochemical potentials of the contacts which is translated as the derivative of the Fermi distribution with energy in BTE, $\mathrm{d}f/\mathrm{d}E$. In a similar manner, when the driving force is the temperature difference of the Fermi distributions of the two contacts, the corresponding conductivity follows a one-to-one correspondence with eq. (16) as [5]

$$\sigma_S = q^2 \int_E \tau_s \upsilon_x^2 g \left(-\frac{\partial f}{\partial T}\right) \mathrm{d}E. \tag{18}$$

Since

$$\left(-\frac{\partial f}{\partial T}\right) = \left(-\frac{\partial f}{\partial E}\right) \frac{(E - E_\mathrm{F})}{qT}\,, \tag{19}$$

we reach

$$\sigma_S = \frac{q}{T} \int_E \Xi(E)\,(E - E_\mathrm{F}) \left(-\frac{\partial f}{\partial E}\right) \mathrm{d}E. \tag{20}$$

In the case where the driving force is a voltage difference the conductivity is determined by states around E_F, both above and below. In the applied temperature difference case, however, the flow of current above E_F has a different sign compared to the flow of carriers below the Fermi level. The corresponding conductivity is determined by the difference of the fluxes above and below E_F, essentially by the energy asymmetry in transport around the Fermi level. This description finds several different manifestations in the literature, encountered in the derivative of the density of states (DOS) around the E_F, the slope of the DOS, the asymmetry in carrier scattering and mean free paths around E_F, etc. In general terms through, though, it is the asymmetry of the transport distribution function that determines the difference in the fluxes.

2. – Thermoelectric coefficients

To determine the efficiency of the thermoelectric material, and the ZT figure of merit, we turn to the circuit analysis as discussed in ref. [5]. The total current density under the application of all driving forces is the superposition of the different components, as

$$I = G\Delta V + G_S \Delta T, \tag{21}$$

where the capital G here refers to total conductance due to the application of a potential difference, and G_S is the total conductance due to the application of a temperature difference. In experimental setups, the conductivity due to the application of thermal gradient is extracted by measuring the open circuit voltage V_OC. In that case, the open circuit current is by definition zero and we reach

$$G_S = -\frac{GV_\mathrm{OC}}{\Delta T} \Rightarrow -\frac{G_S}{G} = \frac{V_\mathrm{OC}}{\Delta T} \equiv S, \tag{22}$$

where V_OC is called the Seebeck voltage, and S the Seebeck coefficient defined as

$$S = -\frac{G_S}{G} = -\frac{I_{(\Delta T \neq 0)}}{\Delta T} \frac{\Delta V}{I_{(\Delta V \neq 0)}} = -\frac{I_{(\Delta T \neq 0)} \Delta V}{I_{(\Delta V \neq 0)} \Delta T}\,, \tag{23}$$

which is just the ratio of the two conductances: the one driven by temperature difference over the one driven by voltage difference. The maximum power that can be extracted from the thermoelectric generator is determined by a simple circuit analysis as well. For maximum power extraction, the requirement is that the load resistance is equal to the resistance of the thermoelectric material, as $R_{\mathrm{L}} = R_{\mathrm{TE}} = 1/G$. In this case, the power delivered to the load (considering that the voltage is split equally in the internal and load resistances) is:

$$P_{\max\text{-Load}} = \left(\frac{V_{\mathrm{OC}}}{2}\right)^2 \Big/ R_{\mathrm{L}} = (S\Delta T)^2 \frac{G}{4} = S^2 G \frac{(T_1 - T_2)^2}{4}\,. \tag{24}$$

To derive the efficiency of the thermoelectric engine, we also need to consider the power supplied from the application of the temperature gradient in the form of the hear current, J_{Q}. We simply assume a heat conductance G_{K} for the material such that

$$I_{\mathrm{Q}} = G_{\mathrm{K}} \Delta T. \tag{25}$$

The efficiency of the thermoelectric material is the ratio of the maximum possible power that can be extracted from the material (in the form of electrical power), over the power supplied (in the form of heat driven by the temperature gradient) as

$$\frac{P_{\max}}{P_{\mathrm{supplied}}} = \frac{S^2 \sigma (T_1 - T_2)^2 / 4}{\sigma_{\mathrm{K}} (T_1 - T_2)} = \frac{S^2 \sigma T}{\sigma_{\mathrm{K}}} \frac{(T_1 - T_2)}{4T} = ZT \frac{(T_1 - T_2)}{4T}\,. \tag{26}$$

Above it is set $T = \frac{T_1 + T_2}{2}$. We can replace the "conductances" with "conductivities", as the difference between the two is just a geometrical factor that gets cancelled from both the numerator and denominator. The dimensionless thermoelectric figure of merit ZT is then defined as

$$ZT = \frac{S^2 G T}{G_{\mathrm{K}}} \equiv \frac{S^2 \sigma T}{\kappa}\,. \tag{27}$$

The denominator of ZT is the thermal conductivity of the material, adding up heat contributions from phonon transport (the term referred to as the lattice thermal conductivity, κ_{l}), as well as the heat carried by electrons (the electronic part of the thermal conductivity, κ_{e}), such that ZT is commonly written as

$$ZT = \frac{S^2 \sigma T}{\kappa_{\mathrm{l}} + \kappa_{\mathrm{e}}}\,. \tag{28}$$

In summary, within the electronic BTE, we can define the moments of the transport distribution function as

$$R^{(\alpha)} = q_0^2 \int_{E_0}^{\infty} \mathrm{d}E \left(-\frac{\partial f_0}{\partial E}\right) \Xi(E) \left(\frac{E - E_{\mathrm{F}}}{k_B T}\right)^{\alpha} \tag{29}$$

and from that all relevant transport coefficients as

$$\sigma = R^{(0)}, \tag{30a}$$

$$S = \frac{k_B}{q_0}\frac{R^{(1)}}{R^{(0)}}, \tag{30b}$$

$$\kappa_{\mathrm{e}} = \frac{k_B^2 T}{q_0^2}\left[R^{(2)} - \frac{[R^{(1)}]^2}{R^{(0)}}\right]. \tag{30c}$$

In the case of bipolar transport in small bandgap materials, in which case both majority and minority carriers are excited and participate in transport, an additional thermal conductivity component arises, the bipolar thermal conductivity κ_{bi}, which makes the total electronic part of the thermal conductivity a summation of three quantities, $\kappa_{\mathrm{tot}} = \kappa_{\mathrm{e}} + \kappa_{\mathrm{h}} + \kappa_{\mathrm{bi}}$. It is given by

$$\kappa_{\mathrm{bi}} = \frac{\sigma_{\mathrm{e}}\sigma_{\mathrm{h}}}{\sigma_{\mathrm{e}} + \sigma_{\mathrm{h}}}(S_{\mathrm{e}} - S_{\mathrm{h}})^2 T. \tag{30d}$$

3. – Carrier scattering

The parameters needed to extract the thermoelectric coefficients are, thus, the density of states, band structure velocities, and scattering times. The first two are extracted through DFT calculations. A number of software packages are available [6-9]. The momentum relaxation times are much more less frequently "properly" extracted. This is because of the huge complexity in extracting energy-dependent values for arbitrary band structures. Recently, more sophisticated calculations using the Electron-Phonon Wannier (EPW) simulator package [10], allow the extraction of the electron-phonon scattering rates from first principles. However, these simulations are computationally extremely expensive requiring dense electron and phonon dispersions, and only treat electron-phonon scattering. At the densities in which the power factor peaks, ionized impurity scattering is the dominant scattering mechanism [11-13]. Thus, in most TE studies in the literature, when it comes to complex band structure materials it is common to employ a constant relaxation time, usually of value $\tau_{\mathrm{S}} = 10^{-14}$ s [2].

A middle ground is to extract energy-dependent scattering rates using some parameters, such as deformation potentials, the dominant phonon energies, and dielectric constants. In general, the use of energy-dependent scattering methods has been the norm in the semiconductor electronic transport community for years [14, 15].

In the event of scattering, a carrier located at an initial state with a given energy, momentum and band (E, k, n), scatters after the interaction with a perturbation U, to a final state (E', k', m) as pictured in fig. 3 below. The carrier in the initial state has velocity v_i, given by the slope of the band at that k-point (blue line). After scattering, its velocity can change. Back-scattering events, but also forward-scattering events are possible, and what is important is to account for the velocity change, as this is what causes randomization of motion.

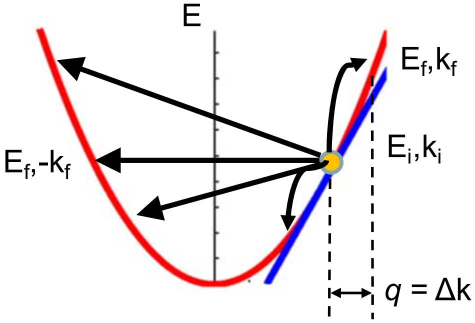

Fig. 3. – A schematic of the scattering processes that a carrier in an initial state (E_i, k_i) in a parabolic band undergoes under elastic (energy invariant) and inelastic (energy changing) scattering processes. Isotropic scattering processes do not depend on the momentum exchange Δk, but anisotropic processes do. The largest the Δk is, the weaker the scattering process is in the case of anisotropic mechanisms. The velocity is determined by the slope of the band (blue line), and the change in the velocity is what determines the randomization of carriers.

The scattering description begins with the formulation of the quantum mechanical scattering matrix element, following Fermi's Golden Rule, which employs the wave functions of the initial and final states together with the perturbing potential as [11,14]

$$H_{k',k}^{m,n} = \frac{1}{\Omega}\int_R \psi_m(\vec{r})^* U_S(\vec{r})\psi_n(\vec{r})\mathrm{d}r. \tag{31}$$

From the matrix element we define the transition rate as the square of the matrix element for all states that obey energy conservation according to the scattering process considered, as

$$S_{n,m}(k,k') = \frac{2\pi}{\hbar}\left|H_{k',k}^{m,n}\right|^2 \delta\left(E_m(k') - E_n(k) - \Delta E\right). \tag{32}$$

For example, electron-acoustic phonon scattering and ionized impurity scattering are considered as elastic, whereas optical phonon scattering events are inelastic. The momentum relaxation scattering rate includes an additional term that accounts for the difference in the momentum of the initial and final states as (here we can replace the momentum with velocities, as it is a more straightforward quantity to define from the band structures):

$$\frac{1}{\tau_n(k_x)} = \sum_{m,k'_x} S_{n,m}(k,k')\left(1 - \frac{\upsilon_m(k'_x)}{\upsilon_n(k_x)}\right). \tag{33}$$

The main scattering mechanisms we consider in the case of thermoelectric materials are phonon scattering (acoustic and optical including polar optical), ionized impurity scattering, alloy scattering, and boundary scattering. In all cases, scattering is proportional to the density of final states that the carriers can scatter into. The scattering rate for acoustic phonon scattering is given by

$$\frac{1}{\tau_{\mathrm{ADP}}(E)} = \frac{\pi D_{\mathrm{A}}^2 k_B T}{\hbar \rho v_s^2} g(E) \tag{34}$$

where D_{A} is the deformation potential (representing the scattering strength), ρ is the mass density of the material, and ν_s is the sound velocity.

The scattering rate for optical phonon scattering is given by

$$\frac{1}{\tau_{\mathrm{ODP}}(E)} = \frac{\pi D_{\mathrm{O}}^2}{2\rho\omega_{\mathrm{ph}}} \left(N_\omega + \frac{1}{2} \mp \frac{1}{2}\right) g\left(E \pm \hbar\omega_{\mathrm{ph}}\right), \tag{35}$$

where D_{O} is the optical deformation potential, ω_{ph} is the optical phonon frequency, and N_ω is the Bose-Einstein distribution function. For ionized impurity scattering, the most common model used is the Brooks-Herring model, under which the scattering rate is given by

$$\begin{gathered} \tau_{\mathrm{IIS}}(E) = \frac{16\sqrt{2m^*}\pi\kappa_s^2\varepsilon_0^2}{N_I q^4} \left[\ln\left(1+\gamma^2\right) - \frac{\gamma^2}{(1+\gamma^2)}\right] E^{3/2}, \\ \gamma^2 = \frac{8m_{\mathrm{DOS}}(E-E_0)L_{\mathrm{D}}^2}{\hbar^2}, \quad L_{\mathrm{D}} = \sqrt{\frac{\kappa_s\varepsilon_0}{q}\frac{\partial E_{\mathrm{F}}}{\partial n}} \approx \sqrt{\frac{\kappa_s\varepsilon_0 k_B T}{q^2 n}\frac{\Im_{1/2}(\tilde{\eta}_F)}{\Im_{-1/2}(\tilde{\eta}_F)}}, \end{gathered} \tag{36}$$

where L_{D} is the screening length, which depends on the dielectric constant, κ_s, and the density n —specifically its derivative with the Fermi level E_{F}. For simple bands, equivalently one can use the second expression, which includes the Fermi Dirac distributions, but for generic bands, the more accurate expression is the first one, which takes directly the variation of the charge with the Fermi level. The discrepancies between the two methods are minimal. N_I is the impurity density (the doping density), and n is the carrier density, which can differ from N_I. The ionized impurity scattering rates are elastic and anisotropic, since a scattering event does not change the carrier's energy, but the momentum with the scattering rate depending on the length of the momentum (wavevector) exchange vector $\Delta k = k - k'$. The scattering rate becomes weaker at higher energies when the exchange momentum vector is large (*i.e.* it favours narrow angles), and depends linearly on the number of impurities. At very high impurity densities, the ionized impurities are strongly screened by the electron cloud, and the scattering rate converges to an isotropic relation, proportional to the density of states as in the case of electron-phonon scattering as

$$\frac{1}{\tau_{\mathrm{IIS}}(E)} = \frac{\pi N_I}{\hbar} \left(\frac{q L_{\mathrm{D}}}{\kappa_s \varepsilon_0}\right)^2 g(E). \tag{37}$$

Another important scattering mechanism for TE materials is alloy scattering, since large families of materials are indeed alloys. Alloy scattering is due to the random variation of the crystal potential that the carriers encounter as they travel through the lattice. The scattering rate (as derived for crystals with zincblende structure) is given by [14,16,17]:

$$\frac{1}{\tau_{\text{alloy}}} = \frac{3\pi^3}{16\hbar} x(1-x)\Omega \left(V_{\text{A}} - V_{\text{B}}\right)^2 g(E), \tag{38}$$

where V_{A} and V_{B} are the potential of the lattice that each element introduces, Ω is the volume of the primitive cell and $g(E)$ is the density of states of the alloy, as obtained by interpolating the density of states of the constituent compounds.

Finally, in the case of nanostructured thermoelectric materials, boundary scattering is one of the dominant mechanisms. Boundary scattering is in general a complex mechanism, and cannot be easily treated accurately. Depending on the nature of boundaries, whether they are specular or randomizing, depending if they are localized (as in the case of nanoinclusions) or elongated (as grain boundaries and superlattices), depending if they introduce large or small potential barriers, the scattering rate is different, and thus, it becomes very difficult to model it accurately. An effective way to model the rate of this scattering event is to define it as the velocity of electrons divided by an effective distance at which the carriers undergo scattering. Simply, a mean free path for scattering is the effective distance between defects (d_{eff}). A constant C can be usually included to describe the strength of the scattering event and match experimental data as

$$\frac{1}{\tau_{\text{defect/boundary}}} = C\left(\frac{\upsilon(E)}{d_{\text{eff}}}\right). \tag{39}$$

In the case of grain boundaries or interfaces between dissimilar materials, in which case potential barriers of average height V_{B} are formed for carriers, it is common to impose thermionic emission above the barriers as

$$\sigma(E) = 0, \quad \text{for } E \leqq V_{\text{B}}, \tag{40a}$$

$$\sigma(E) = \sigma_0(E) T_r(E), \quad \text{for } E > V_{\text{B}}. \tag{40b}$$

In this case, transport over the barrier provides energy filtering, which improves the Seebeck coefficient, at the expense of the conductivity. The transmission, T_r, used, is usually a step function, which takes zero values below V_{B}, and unity above V_{B}. However, this can be quite generic, and the transmission can be a function that includes tunnelling, or quantum reflections, or the mismatch between the states of the constituent materials, etc. In particular, although a step function transmission is the easier to be used, it does not account for well/barrier momentum state mismatch/conservation, and typically overestimates the conductivity over the barrier.

Finally, the strength of all scattering mechanisms is combined to an overall strength using Matthiessen's rule, under which the total scattering time is then given by [18]

$$\frac{1}{\tau_{\text{tot}}} = \frac{1}{\tau_{\text{ADP}}} + \frac{1}{\tau_{\text{ODP}}} + \frac{1}{\tau_{\text{IIS}}} + \frac{1}{\tau_{\text{alloy}}} + \frac{1}{\tau_{\text{B}}} + \dots . \tag{41}$$

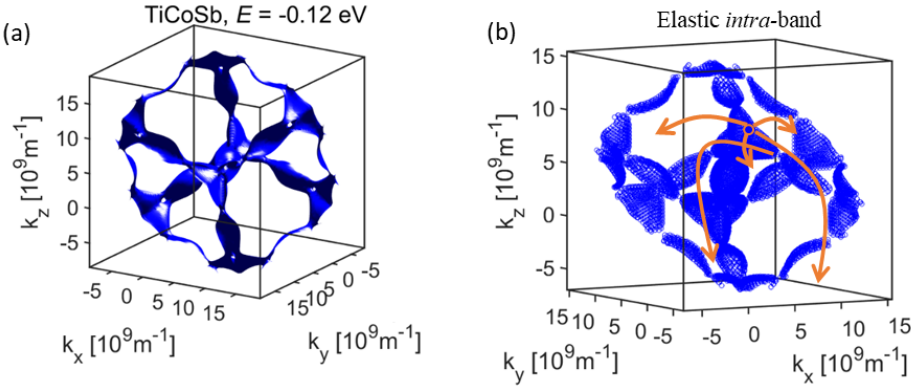

Fig. 4. – (a) Constant energy surface for the valence band of the half-Heusler TiCoSb at energy $E = -0.12\,\mathrm{eV}$ into the valence band. (b) The energy surface k-states with the arrows indicate the transition processes for different elastic intra-band scattering events [13].

In the equation above, it is understood that the rate is computed at each energy E, and for each k-state.

4. – Numerical extraction of relaxation times in arbitrary band structures

Typical electronic structure codes such as DFT and tight-binding, compute the $E(k)$ on a regular k-discretized grid in the three Cartesian coordinates. The density of states and velocities can easily be extracted using the band structures. If the scattering times for each k-state were also known, then a simple numerical summation over the Brillouin zone will have sufficed in obtaining the transport properties. The equations that describe the scattering rates, however, are functions of the density of states resolved in energy. The availability of the state attributes in a regular k-grid, rather than a regular E-grid that is required for the $\tau(E)$, imposes a significant computational task in these calculations, as the uniform k-grid resolved $E(k)$ needs to be converted into a regular E-grid [19]. In essence, the iso-energy surfaces (in 3D) or lines (in 2D), that form the electronic structure, and from there the density of states at all energies, need to be evaluated. In a fully numerical calculation we need to group all states according to their energy and do so for each band (or valley) as well. In general, the k-states will have numerically different energies, thus, in order to form the iso-energy surfaces from groups of k-space points, interpolation schemes need to be used. Once the iso-energy surfaces are formed, then the area of the surface, together with the perpendicular band structure velocities, allows for the extraction of the DOS(E) to be used for the extraction of $\tau(E)$. An example of the iso-energy surface for the valence band of TiCoSb half-Heusler at $E = -0.12\,\mathrm{eV}$ is shown in fig. 4. The iso-energy surface has a large number of valleys, which are beneficial for TEs. It also has elongated features which indicate large anisotropy in the effective mass, another beneficial property for TE materials, pointing out to potential optimization routes for high power factors.

The 3D energy surfaces can be in general built by using the tetrahedron approach [20] by means of a local Delaunay Triangulation (DT), where the reciprocal unit cell is sampled by a regular mesh of 3D elements. All mesh elements are scanned numerically to check if the 3D constant energy surface passes through them in a geometrical fashion. All the relevant elements are then triangulated, forming tedrahendra, whose vertices will be "cut" by the energy surface. The $E(k)$ is then interpolated linearly between these points to obtain the estimated k-point at the energy of interest. The surface area of the triangles formed, dA_k, is computed using geometrical considerations —that area, together with the perpendicular velocity vector will determine the density of states associated with that element of the iso-energy surface as $g_{k,n,E} = \frac{dA_{k,n,E}}{\hbar|\overrightarrow{v_{k,n,E}}|}$.

A simpler and computationally faster approach is suggested in ref. [13]. In this case, a search through all k-points' energies and their nearest neighbors is performed, to identify if the iso-energy of interest passes through them. Then a linear interpolation is performed along the edges connecting the nearest neighbors. A collection of k-points that belong to the iso-energy of interest is then formed (see fig. 4(b)). The difference from the Delaunay triangulation method is that the energy surface itself is not formally constructed. Because of that, a surface element area dA_k needs to be assigned for each point in a different way. To do that, for every relevant k-point, the nearest neighbours are explored in a radius of length $\sqrt{2}dk$, where dk is the discretization of the k-space mesh. Then, the average distance between the given point and its detected neighbours, $\langle \Delta k \rangle$, is calculated. The surface element associated to the k-point is approximated by a circle of radius half the average distance to the neighbouring points, *i.e.* $dA_k = \pi(\frac{\langle \Delta k \rangle}{2})^2$. The approximation provides very good agreement in evaluating the DOS from simple parabolic band cases, to complex band structure materials such as half-Heuslers [12, 13].

Finally, going back to the TDF of eq. (17), we now account the contribution to transport from all individual states as

$$\Xi(E) = \frac{2}{(2\pi)^3} \frac{1}{V_c} \sum_{k,n}^{BZ} v_{k,n,E}^2 \tau_{k,n,E} \delta(E_k - E) = \frac{2}{(2\pi)^3} \sum_{k,n}^{\mathfrak{L}_E^n} v_{k,n,E}^2 \tau_{k,n,E} g_{k,n,E}. \tag{42}$$

Each scattering relaxation time above is defined by the summation of all transition rates of an initial state (E, k, n) to all available final scattering states (E', k', m) for each scattering mechanism, evaluated on the relevant iso-energy surface. For acoustic phonons this is

$$\frac{1}{\tau_{\mathrm{ADP}}(E)} = \frac{\pi D_{\mathrm{A}}^2 k_B T}{\hbar \rho v_s^2} \sum_{m,k'} g_{k'}(E) \left(1 - \frac{v_m(k_x')}{v_n(k_x)}\right). \tag{43}$$

For optical phonons

$$\frac{1}{\tau_{\mathrm{ph}}^{\mathrm{ODP}}(E)} = \frac{\pi}{\hbar} \frac{(N_\omega + \frac{1}{2} \mp \frac{1}{2})}{\rho \hbar \omega_{\mathrm{ph}}} \sum_{m,k'} g_{k'}\left(E \pm \hbar \omega_{\mathrm{ph}}\right) \left(1 - \frac{v_m(k_x')}{v_n(k_x)}\right). \tag{44}$$

For polar optical phonons
(45)
$$\frac{1}{\tau_{\mathrm{POP}}(E)}=\frac{\pi q^2\omega_{\mathrm{ph}}}{\varepsilon_0}\left(\frac{1}{\kappa_\infty}-\frac{1}{\kappa_s}\right)\left(N_\omega+\frac{1}{2}\mp\frac{1}{2}\right)\sum_{m,k'}\frac{g_{k'}(E\pm\hbar\omega_{\mathrm{ph}})}{|k-k'|^2}\left(1-\frac{v_m(k'_x)}{v_n(k_x)}\right).$$

For ionized impurity scattering

$$\frac{1}{\tau_{\mathrm{IIS}}(E)}=\frac{2\pi}{\hbar}\frac{Z^2q^4N_{\mathrm{imp}}}{\kappa_s^2\varepsilon_0^2}\sum_{k'_x}\frac{g_{k'}(E\pm\hbar\omega_{\mathrm{ph}})}{(|k-k'|^2+\frac{1}{L_{\mathrm{D}}^2})^2}\left(1-\frac{v_m(k'_x)}{v_n(k_x)}\right). \tag{46}$$

These equations sum up all different states for every iso-energy surface and for all relevant scattering mechanisms. They are combined to extract the overall scattering rate and then the contribution of all states to the TDF that is needed to extract the conductivity and the TE coefficients. A pictorial example of elastic transitions is shown in fig. 4(b). The different arrows indicate examples of various scattering events that take place in the same iso-surface.

5. – Conclusions

The Boltzmann Transport formalism that is commonly employed in the extraction of thermoelectric coefficients is introduced, and how the thermoelectric coefficients and figure of merit are extracted from simple circuit theory considerations is explained. The different scattering mechanisms and their contribution to the overall relaxation scattering times used in the BTE formalism are introduced. Finally, the paper describes a numerical scheme that allows the description of the relaxation times as function of energy for arbitrary band structures, as is the case for complex thermoelectric materials. Such energy-dependent scattering rates provide different trends for the thermoelectric coefficients compared to constant relaxation time considerations, and could lead to better predictions and optimization routes in material identification and design.

* * *

This work has received funding from the Marie Skłodowska-Curie Actions under the Grant agreement ID: 788465 (GENESIS - Generic semiclassical transport simulator for new generation thermoelectric materials) and from the European Research Council (ERC) under the European Union's Horizon 2020 Research and Innovation Programme (Grant Agreement No. 678763).

REFERENCES

[1] Madsen G. K. and Singh D. J., "BoltzTraP. A code for calculating band-structure dependent quantities", *Comput. Phys. Commun.*, **175** (2006) 67.
[2] Pizzi G., Volja D., Kozinsky B., Fornari M. and Marzari N., BoltzWann: "A code for the evaluation of thermoelectric and electronic transport properties with a maximally-localized Wannier functions basis", *Comput. Phys. Commun.*, **185** (2014) 422.

[3] Mahan G. D. and Sofo J. O., “The best thermoelectric”, *Proc. Natl. Acad. Sci. U.S.A.*, **93** (1996) 7436.

[4] Neophytou N. and Kosina H., “Atomistic simulations of low-field mobility in Si nanowires: Influence of confinement and orientation”, *Phys. Rev. B*, **84** (2011) 085313.

[5] Datta S., *Lessons from Nanoelectronics: A New Perspective on Transport*, Vol. **1** (World Scientific) 2012.

[6] Kresse G. and Hafner J., *Phys. Rev. B*, **47** (1993) 558.

[7] Kresse G. and Hafner J., *Phys. Rev. B*, **49** (1994) 14251.

[8] Clark S. J., Segall M. D., Pickard C. J., Hasnip P. J., Probert M. J., Refson K. and Payne M. C., *Z. Kristallogr.*, **220** (2005) 567.

[9] Giannozzi P., Baroni S., Bonini N., Calandra M., Car R., Cavazzoni C., Ceresoli D., Chiarotti G. L., Cococcioni M., Dabo I., Dal Corso A., Fabris S., Fratesi G., de Gironcoli S., Gebauer R., Gerstmann U., Gougoussis C., Kokalj A., Lazzeri M., Martin-Samos L., Marzari N., Mauri F., Mazzarello R., Paolini S., Pasquarello A., Paulatto L., Sbraccia C., Scandolo S., Sclauzero G., Seitsonen A. P., Smogunov A., Umari P. and Wentzcovitch R. M., *J. Phys.: Condens. Matter*, **21** (2009) 395502.

[10] Poncé S., Margine E. R., Verdi C. and Giustino F., “EPW: Electron-phonon coupling, transport and superconducting properties using maximally localized Wannier functions”, *Comput. Phys. Commun.*, **209** (2016) 116.

[11] Neophytou N. and Kosina H., “Effects of confinement and orientation on the thermoelectric power factor of silicon nanowires”, *Phys. Rev. B*, **83** (2011) 245305.

[12] Kumarasinghe C. and Neophytou N., “Band alignment and scattering considerations for enhancing the thermoelectric power factor of complex materials: The case of Co-based half-Heusler alloys”, *Phys. Rev. B*, **99** (2019) 195202.

[13] Graziosi Patrizio, Kumarasinghe Chathurangi and Neophytou Neophytos, “Impact of the scattering physics on the power factor of complex thermoelectric materials”, *J. Appl. Phys.*, **126** (2019) 055105.

[14] Lundstrom M., *Fundamentals of Carrier Transport* (Cambridge University Press) 2000.

[15] Nag B. R., *Electron Transport in Compound Semiconductors, Springer Series in Solid-State Sciences, SSSOL*, Vol. **11** (Springer) 1980.

[16] Rode D. L. and Fedders P. A., “Electron scattering in semiconductor alloys”, *J. Appl. Phys.*, **54** (1983) 6425.

[17] Fischetti M. V., “Monte Carlo simulation of transport in technologically significant semiconductors of the diamond and zinc-blende structures, I. Homogeneous transport”, *IEEE Trans. Electron Dev.*, **38** (1991) 634.

[18] Matthiessen A. and Vogt C., “On the influence of temperature on the electric conducting-power of alloys”, *Philos. Trans. R. Soc. London*, **154** (1864) 167.

[19] Neophytou N., Karamitaheri H. and Kosina H., “Atomistic calculations of the electronic, thermal, and thermoelectric properties of ultra-thin Si layers”, *J. Comput. Electron.*, **12** (2013) 611.

[20] Martin R. M. and Martin R. M., *Electronic Structure: Basic Theory and Practical Methods* (Cambridge University Press) 2004.

Proceedings of the International School of Physics "Enrico Fermi"
Course 207 "Advances in Thermoelectricity: Foundational Issues, Materials and Nanotechnology",
edited by D. Narducci, G. J. Snyder and C. Fanciulli
(IOS, Amsterdam; SIF, Bologna) 2021
DOI 10.3254/ENFI210010

Heat conversion in solar thermoelectric harvesters

B. Lorenzi

Department of Materials Science, University of Milano Bicocca
via R. Cozzi 55, 20125 Milano, Italy

Department of Mechanical Engineering, Massachusetts Institute of Technology
MA 02139, USA

Summary. — Solar thermoelectric generators (STEGs) are two steps energy harvesting systems that convert solar power into electricity. Even if the first generation of this kind of systems was developed in the first half of the twentieth century the interest around this technology has been intermittent. Only in recent years the progress of the thermoelectric material efficiency stimulated a renewed interest on STEGs as a viable alternative to harness solar energy. In this paper the basic aspects of STEG technology, along with the analysis of its efficiency, and the state of the art of this field are discussed.

1. – An introduction to STEGs

It is everyone day life experience that Sun's light can heat up materials. It is therefore natural, knowing the way how thermoelectric devices work, to imagine the possibility to use them to convert solar power into electricity. In this terms a solar thermoelectric generator (STEG) is a two-step energy converter. Firstly it converts Sun's light into heat, and then heat into electricity. Both steps have their own conversion efficiency. It

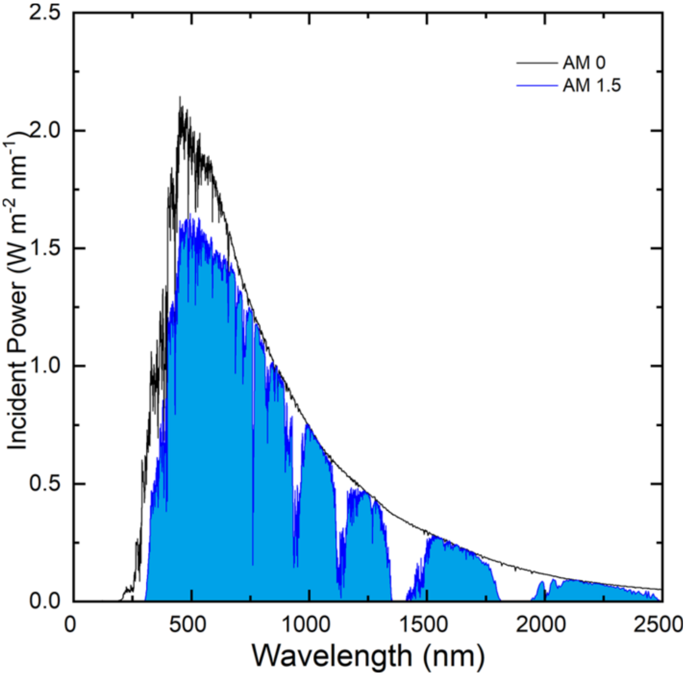

Fig. 1. – Solar spectrum above the atmosphere (indicated with the acronym AM 0), and at the sea level (indicated with the acronym AM 1.5).

is clear that, for thermodynamic reasons, these efficiencies have to be lower than one. But let us firstly assume, for the sake of simplicity, that the efficiency of the first step (the conversion of Sun's radiation into heat) is equal to one. Even in this case it easy to understand that Sun's power is too small to heat up common thermoelectric generators to temperature high enough to result into interesting conversion efficiencies.

This is understandable taking a look to the solar spectrum reported in fig. 1. From this picture, it can be seen how the spectrum above the Earth's atmosphere (the so-called AM 0 spectrum, where AM stand for air mass, and 0 means no absorption from the atmosphere) ranges between 200 to 4000 nm wavelength, and that it can be approximated by a black body at $\sim 6000\,\mathrm{K}$. In this case the incident power density (the integral over wavelength of the spectral power density) is around $1300\,\mathrm{W/m^2}$. This value reduces to $\sim 1000\,\mathrm{W/m^2}$ at the sea level, because of the various absorptions coming from the different components of the atmosphere (in this case the spectrum is called AM 1.5). If we then take the incoming power density and the typical thermal resistance of commercial thermoelectric generators (TEG), we can determine the difference of temperature across the thermoelectric generator using Fourier's law

$$\Delta T = \Phi R_{\mathrm{teg}}, \tag{1}$$

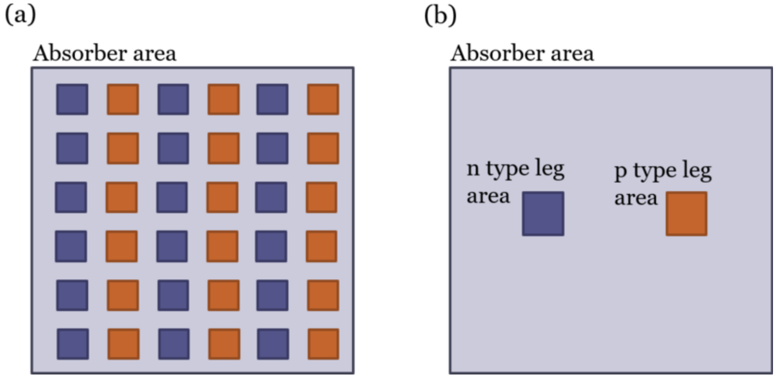

Fig. 2. – Schematic top view of common TEGs (a) and thermally concentrated TEGs (b). In the second case the ratio of the absorbent area and the active thermoelectric area (the so-called thermal concentration) is much higher.

where ΔT is the difference of temperature across the TEG sides, Φ is the incoming power density, and R_{teg} the TEG thermal resistance. Inputting $1000\,\text{W/m}^2$ as the incident power density and 0.001–$0.005\,\text{m}^2\,\text{K/W}$ as the typical TEG thermal resistance we obtain a ΔT ranging between 1 and 5 K. With such a small ΔT, the resulting thermoelectric efficiency is only 0.05–0.3%. It is clear that these efficiency values are too small to arouse any interest for practical applications of STEGs.

In order to increase the ΔT and thus the STEG efficiency, one can act on the system configuration. In particular, from eq. (1) it is clear that the two possible solutions are 1) increase the value of the incoming power density Φ, and 2) increase the TEG thermal resistance R_{teg}. In the first case it is possible to implement optical concentration, by means of lens or mirrors. In the second case it is possible to use thermal concentration increasing the ratio between the absorbent area, and the active thermoelectric area, given by the sum of all the thermoelectric leg areas (fig. 2). In both cases a concentration ratio of ten, means a tenfold increase of the ΔT, and a consequent increase of the STEG efficiency. It is also possible to use both strategies together. In that case a concentration ratio of ten for both concentration options means a 100fold increase of the ΔT. Taking the above example, this would mean a ΔT of 100–500 K, and a STEG efficiency ranging between 5 and 14%. In this perspectives STEGs are much more appealing.

This it is valid of course only because we are considering unitary efficiency in the conversion of the input power into heat. It is also clear that while increasing the ΔT, the working temperature of the device hot side increases. This will result into an increase of heat exchange between the device and the environment. As we will see into details in the next section, this heat exchange is essentially the most important source of losses in the energy balance. In fact the TEG generates electrical power only proportionally to the heat flowing through it.

This is a fundamental concept, and deserves to be highlighted. The heat not flowing through the TEG, and therefore exchanged with the environment, is an energy loss and

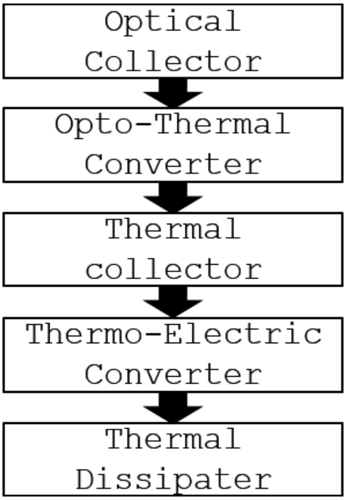

Fig. 3. – Scheme of the main components of a STEG system.

it will decrease the device efficiency.

As well known, heat exchange can be conductive, convective and radiative, and the heat transfer between the hot surface at temperature T_h, and the cold surface at temperature T_c is governed by the following equations:

$$q_\mathrm{cond} = \kappa \frac{T_\mathrm{h} - T_\mathrm{c}}{L_\mathrm{cond}}\,, \tag{2a}$$

$$q_\mathrm{conv} = h \frac{T_\mathrm{h} - T_\mathrm{c}}{L_\mathrm{conv}}\,, \tag{2b}$$

$$q_\mathrm{rad} = \varepsilon\sigma\left(T_\mathrm{h}^4 - T_\mathrm{c}^4\right), \tag{2c}$$

where κ, and L_cond are, respectively, the thermal conductivity and the length of the conductive medium, h and L_conv, respectively, the heat transfer coefficient and the length of the convective medium, ε and σ, respectively, the hot surface emittance, and the Stefan-Boltzmann constant. As we will see in the next section, in order to reduce heat losses, STEGs are normally placed in vacuum tubes, so that the radiative contribution dominates heat exchanges.

We are now ready to analyse into details the various STEG components and how to calculate the efficiency of the whole system.

2. – The STEG efficiency

In general terms STEGs are typically made of five main elements (as shown in fig. 3): an optical collector, which collects the photons coming from the Sun; an opto-thermal convert, which converts the photons into heat; a thermal collector, which drives the heat towards the converter; a thermo-electric convert, which converts heat into electricity; and a thermal dissipation system, which ejects the exceeding heat out from the system. As will be shown later, the overall STEG conversion efficiency is the product of all the component efficiencies in collecting, converting, and dissipating energy. The technological solutions, and the designs implemented for these components define the various possible approaches.

The optical collector type defines a first classification of the approaches reported in the literature for STEGs, which can be optically concentrated or not. Optical concentration collector can be based on cylindrical lenses, fresnel lenses, dish mirrors, and compound parabolic concentrators. Non-concentrated solution are instead limited to evacuated and non-evacuated flat plane collectors, or evacuated tubes. The kind of optical collector sets the amount of power hitting the opto-thermal converter, and thus contributes to set the difference of temperature on the TEG.

Let us define the input power as

$$P_{\mathrm{in}} = C\Phi A_{\mathrm{opt}}, \tag{3}$$

where C is the optical concentration, and A_{opt} the optical collector aperture area. The efficiency of the optical collector in transmitting the input power to the opto-thermal converter can be defined as

$$\eta_{\mathrm{opt}} = \frac{P_{\mathrm{in}}\tau_{\mathrm{opt}}}{P_{\mathrm{in}}} = \tau_{\mathrm{opt}} \tag{4}$$

with τ_{opt} the optical collector transmittance or reflectivity depending if it is a lens or a mirror. Since τ_{opt} is expected to be high (0.9 or more) a good approximation is to consider that the optical collector does not absorb power, and thus does not heat up. Therefore one can normally consider η_{opt} to be temperature independent.

The efficiency of the opto-thermal converter, on which the optical power is hitting can be found instead considering the opto-thermal absorbance along with the heat lost towards the environment. For the sake of simplicity let us assume that the system works within an evacuated environment, as in the major part of the works in the literature. In this case the opto-thermal converter efficiency can be written as

$$\begin{aligned}\eta_{\mathrm{otconv}} &= \frac{P_{\mathrm{in}}\tau_{\mathrm{opt}}\alpha_{\mathrm{otconv}} - [\epsilon_{\mathrm{otconv}}\sigma A_{\mathrm{abs}}(T_{\mathrm{h}}^4 - T_{\mathrm{a}}^4)]}{P_{\mathrm{in}}\tau_{\mathrm{opt}}} = \\ &\alpha_{\mathrm{otconv}} - \frac{\epsilon_{\mathrm{otconv}}\sigma A_{\mathrm{abs}}(T_{\mathrm{h}}^4 - T_{\mathrm{a}}^4)}{P_{\mathrm{in}}\tau_{\mathrm{opt}}},\end{aligned} \tag{5}$$

where α_{otconv}, and $\epsilon_{\mathrm{otconv}}$ are the opto-thermal convert absorbance and emittance. Since the opto-thermal converter is normally directly deposited on the thermal collector top surface radiative losses are considered to occur only at the opto-thermal converter top surface. It should be stressed that differently from the case of η_{opt}, η_{otconv} is strongly dependent on temperature.

Now analysing the thermal collector operation, we can assume that heat can be lost by radiation from the part of the top surface which is not covered by the opto-termal converter, and from the bottom. Summing these contributions the thermal collector efficiency can be written as

$$\eta_{\text{thcol}} = 1 - \frac{\epsilon_{\text{thcol}'}\sigma A_{\text{thcol}}[(T^4_{\text{thcol}} - T^4_{\text{a}}) + (T^4_{\text{thcol}} - T^4_{\text{c}})]}{\eta_{\text{otconv}}}\,, \tag{6}$$

where A_{thcol}, and T_{thcol} are, respectively, the area, and the temperature of the thermal collector. In the second therm of the square brackets we suppose that, as in most of the STEGs, the bottom of the thermal collector acts also as the TEG hot plate, and is then faced to the TEG cold side. Thus the therm $\epsilon_{\text{thcol}'}$ is the resultant emittance of the TEG parallel surfaces, one at temperature T_{thcol} with emittance ϵ_{thcol}, and the second with temperature T_{c} and emittance ϵ_{c} calculated as [1]

$$\epsilon_{\text{thcol}'} = \frac{1}{\frac{1}{\epsilon_{\text{thcol}}} + \frac{1}{\epsilon_{\text{c}}} - 1}\,. \tag{7}$$

If the opto-thermal converter and the thermal collector have the same area eqs. (5) and (6) can be usefully joined as suggested by Chen [2] defining an opto-thermal efficiency η_{ot} which is the system efficiency in converting the optical solar power into heat flowing through the TEG. In this case the opto-thermal efficiency can be written as

$$\eta_{\text{ot}} = \alpha_{\text{otconv}} - \frac{\sigma A_{\text{abs}}\epsilon_{\text{abs}}(T^4_{\text{h}} - T^4_{\text{a}})}{P_{\text{in}}\tau_{\text{opt}}} \tag{8}$$

with

$$\epsilon_{\text{abs}} = \epsilon_{\text{otconv}} + \epsilon_{\text{thcol}'} \tag{9}$$

and where we also neglect the small thermal resistance between the opto-thermal converter and the thermal collector. Therefore we assume that $T_{\text{thcol}} = T_{\text{h}}$. It is useful to note that η_{ot} is basically

$$\eta_{\text{ot}} = \alpha_{\text{otconv}} - \frac{Q_{\text{loss}}}{P_{\text{in}}\tau_{\text{opt}}}\,, \tag{10}$$

where in this case we consider only radiative losses to contribute to Q_{loss}. In this perspective it is fundamental the implementation of a opto-thermal converter, normally called Solar Selective Absorber (SSA) with good properties. The research of materials and systems with high optical absorption, small emittance, and stability at high temperatures, its a active scientific field, and literature is plenty of studies on SSAs [3].

Finally, regarding the thermal dissipater, it can be either based on the natural or forced circulation of air, or of a liquid. In both cases its efficiency has to be evaluated

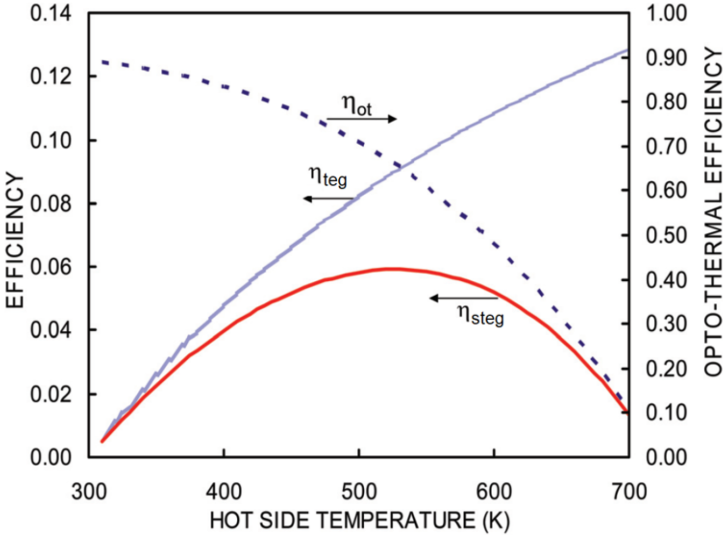

Fig. 4. – $\eta_{\rm ot}$ and $\eta_{\rm teg}$, and the resultant $\eta_{\rm steg}$ as a function of the TEG hot side temperature $T_{\rm h}$. Reproduced with permission from [2].

taking into account the electrical power needed to circulate the cooling fluid ($P_{\rm diss}$). In these therms is possible to define

$$\eta_{\rm diss} = 1 - \frac{P_{\rm diss}}{P^{\rm out}_{\rm steg}}\,, \tag{11}$$

where $P^{\rm out}_{\rm steg}$ is the STEG electrical output power. It is clear that for the case of natural circulation $\eta_{\rm diss}$ is equal to one, while for forced circulation a dimensioning of the heat dissipater geometry has to be done. A useful example of this is reported by Yazawa and Shakouri who take into account a heat dissipater made of parallel circular tubes [4] dimensioned following a heat impendance matching condition between the heat leaving the TEG cold side and that carried away from the dissipater [5]. The authors showed that even if power needed for heat dissipation varies depending on the system dimensions and the working temperature, $P_{\rm diss}$ is expected to not impact significantly on the STEG output power for systems with optical concentration smaller than 200.

Finally, as already mentioned, the overall STEG efficiency is

$$\eta_{\rm steg} = \eta_{\rm opt}\eta_{\rm ot}\eta_{\rm teg}\eta_{\rm diss}. \tag{12}$$

Apart from $\eta_{\rm diss}$ which, as mentioned, has to be evaluated case by case, and from $\eta_{\rm opt}$ which is independent from temperature, the main factor influencing $\eta_{\rm steg}$ is the product $\eta_{\rm ot}\eta_{\rm teg}$. Actually, $\eta_{\rm ot}$ and $\eta_{\rm teg}$ are both strongly temperature dependent, but with opposite trends as represented in fig. 4. This leads to the conclusion that there is an optimal operation temperature $T_{\rm h}$ maximizing the STEG efficiency depending on the system

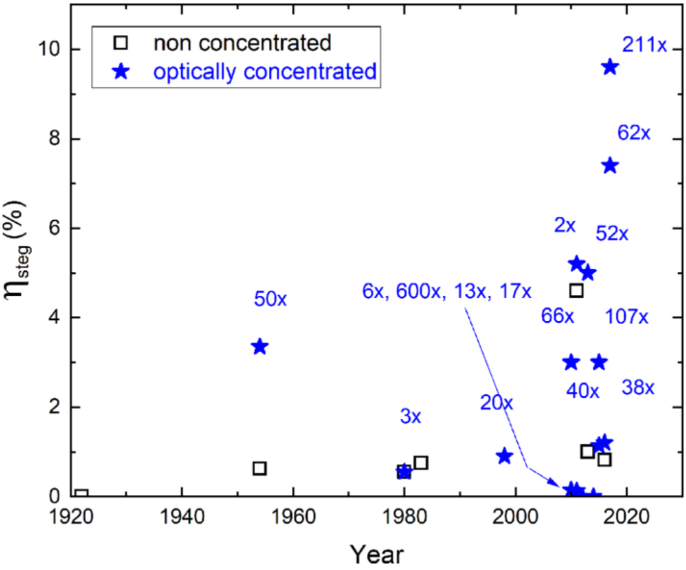

Fig. 5. – Historical view of STEGs efficiencies for the main experimental work appeared in the literature. Blue stars and black squares represent, respectively, optical concentrated and non-concentrated systems. The concentration ratio is reported next to stars.

characteristics. The dimensioning of thermoelectric generator has to be done in order to make the system work near this optimal temperature.

In the following section we will take a look to the history of STEG technology development.

3. – State of the art

Analysing the history of STEG development, the first attempt to harnessing power from the Sun by a STEG system was reported in 1922 by Coblentz [6]. His system, which was made of copper-constantan thermocouples soldered to a black painted copper foil exhibited a very poor efficiency of less than 0.01%. A major progress was then achieved by Telkes in 1954 [7], which demonstrated an efficiency of 0.63%, and 3.35% respectively at 1× and 50× optical concentration. At that time this efficiency was extremely competitive with other solar harvesting technology [8]. The main reason of the efficiency enhancement was the development of more efficient thermoelectric elements made of BiSb/ZnSb alloys [9]. Starting from Telkes's seminal work along the following twenty years the efforts on developing effective STEGs systems were mainly focused on space applications [10-14] with no significant improvements for terrestrial utilization. The interest for this latter application were renewed starting from the eighties and it has been rather intermittent without significant progresses until the last five-six years during which the main improvements were achieved (fig. 5). This recent escalation it is mainly due to the progress of the thermoelectric material figure of merit (ZT) happened in the last decade [15] which made the achievement of effective thermoelectric conversion efficiency possible, stimulating increasing attention around the possibility of using TEGs as viable solar harvesters. In the next paper of this volume we will analyse the main solutions reported in the literature for all the STEG main components.

* * *

The author acknowledge the support by the European Union's Horizon 2020 research and innovation programme under the Marie Skłodowska-Curie grant agreement No. 745304.

REFERENCES

[1] SIEGEL R., HOWELL J. R. and MENGUC M. P., *Thermal Radiation Heat Transfer*, 5th edition (Taylor & Francis, New York) 2002.
[2] CHEN G., *J. Appl. Phys.*, **109** (2011) 104908.
[3] KENNEDY C. E., Technical Report, National Renewable Energy Laboratory Research (2002).
[4] YAZAWA K. and SHAKOURI A., "System optimiztion of hot water concentrated solar", in *2010 3rd International Conference on Thermal Issues in Emerging Technologies Theory and Applications, Cairo, 2010* (IEEE) 2010, pp. 283–290, `https://doi.org/10.1109/THETA.2010.5766410`.
[5] YAZAWA K., SOLBREKKEN G. L. and BAR-COHEN A., "Thermofluid Design of Energy Efficient and Compact Heat Sinks", in *Proceedings of 2003 International Electronic Packaging Technical Conference and Exhibition*, Vol. **2** (ASME) 2003, pp. 509–516.
[6] COBLENTZ W. W., *Sci. Am.*, **127** (1922) 324.
[7] TELKES M., *J. Appl. Phys.*, **25** (1954) 765.
[8] CHAPIN D. M., FULLER C. S. and PEARSON G. L., *J. Appl. Phys.*, **25** (1954) 676.
[9] TELKES M., *J. Appl. Phys.*, **181** (1947) 1116.
[10] GLASSBURN G. W., *IEEE Trans. Aerospace*, **1** (1963) 1396.
[11] FUSCHILLO N., GIBSON R., EGGLESTON F. K. and EPSTEIN J., *IEEE Trans. Aerospace*, **AS-3** (1965) 652.
[12] EGGLESTON F. K. and FUSCHILLO N., *IEEE Trans. Aerospace*, **AS-3** (1965) 674.
[13] FUSCHILLO N., GIBSON R., EGGLESTON F. and EPSTEIN J., *Adv. Energy Convers.*, **6** (1966) 103.
[14] SWERDLING M. and RAAG V., *J. Energy*, **3** (1979) 291.
[15] HEREMANS J. P., DRESSELHAUS M. S., BELL L. E. and MORELLI D. T., *Nat. Nanotechnol.*, **8** (2013) 471.

This page intentionally left blank

Proceedings of the International School of Physics "Enrico Fermi"
Course 207 "Advances in Thermoelectricity: Foundational Issues, Materials and Nanotechnology",
edited by D. Narducci, G. J. Snyder and C. Fanciulli
(IOS, Amsterdam; SIF, Bologna) 2021
DOI 10.3254/ENFI210011

Heat conversion in hybrid solar thermoelectric harvesters

B. Lorenzi

Department of Materials Science, University of Milano Bicocca
via R. Cozzi 55, 20125 Milano, Italy

Department of Mechanical Engineering, Massachusetts Institute of Technology
MA 02139, USA

Summary. — Hybrid thermoelectric-photovoltaic (HTEPV) generators can be seen as an evolution of STEGs. In their structure the opto-thermal converter is constituted by a solar cells. The intention is to implement thermoelectric materials to recover the high fraction of heat losses occurring in solar cell, adding an extra output power to the system. HTEPV have been already shown to be able to enhance the efficiency of solar cells, even if researchers are still trying to make this approach good enough to become reality. In this paper we will analyse the layout and the achievable efficiency of this hybrid devices, highlighting the challenges and the strong points of this approach.

1. – An introduction to HTEPVs

Analysing the structure and the achievable efficiencies of solar thermoelectric generators (STEGs), one can conclude that with actual material development, STEGs are still unlike to be competitive with photovoltaic (PV) devices. Actually the highest STEGs efficiency practically demonstrated in laboratory is around 10% [1], while a commercial

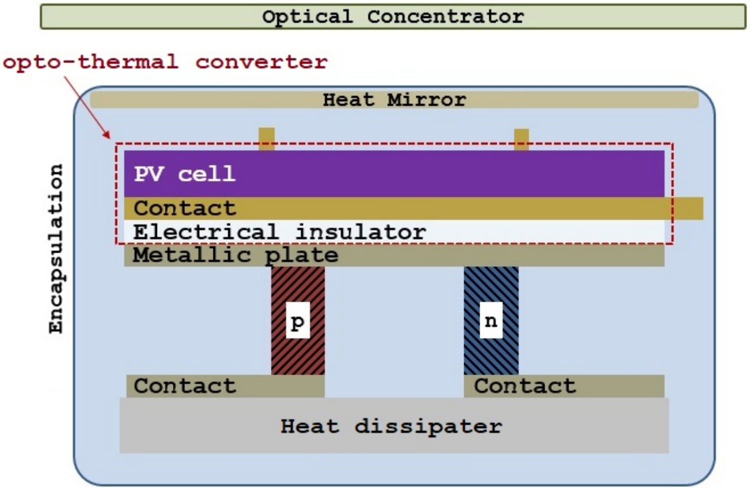

Fig. 1. – Scheme of a generic thermally coupled HTEPV.

silicon solar cell can easily reach values of 13–15%, even without the need of optical concentration and an evacuated environment. For this reason in recent years most of the attention on solar thermoelectric harvesting, shifted onto the possibility to implement thermoelectric generators (TEGs) in combination with solar cells. The reason for this interest is easily explained.

It is evident that nowadays commercial solar cells (the so-called first generation of PV) has still efficiencies much smaller than the thermodynamic limit of 93%. For example silicon solar cells, which represent the 90% of the PV market only recently reached 25% of efficiency, which approaches the technological limit for this kind of devices. Even the most performing solar cells up to date, the so-called multi-junction solar cells, which are normally used only for space applications, show a maximum efficiency of $\sim 40\%$. This means that more than 50% of the incoming solar power is lost.

The interesting evidence is that solar cells lose their efficiency mostly as heat. This is the reason why a solar panel heats up during operation. Recent studies showed that depending on the location, the weather conditions, and the kind of mounting, the working temperature of solar cells can reach 50–60 °C [2], meaning 30–40 degrees higher than the ambient temperature.

The two ingredients needed for the generation of an electrical power with a TEG are actually a heat flow and a difference of temperature (ΔT). Thus in these terms the hybridization of solar cells with thermoelectrics seems favourable.

The easiest hybrid thermoelectric-photovoltaic generator (HTEPV) has the same scheme of a STEG with the difference that in the HTEPV case the opto-thermal converter is the solar cell itself. In this case, as shown in fig. 1, the TEG is directly attached to the bottom of the solar cell, so that the TEG hot side is at the same temperature of the solar cell. For this reason, this configuration is normally called, thermally coupled.

Another approach is the so-called spectrum splitting (or optically coupled) approach in which a beam splitter is implemented in order to split the solar spectrum and direct only the infra-red (IR) part of the spectrum towards the TEG. We will see in details, why this second approach is less convenient than the thermally coupled one.

In the next section we will analyse in details the origin of heat losses occurring in solar cell, to understand their nature and amount.

2. – Thermal losses in PV

In order to understand thermal losses in solar cells it is necessary to understand how the PV effect works. To do that we need to introduce the process of light absorption in semiconductors.

In few words, photons are absorbed in semiconductors when they can exchange energy with electrical carriers within the material. In semiconductors the electrons of the external shells are shared between atoms to form the material crystalline lattice. In this state electrons are bound. When a photon interact with the lattice it can give its energy to a bound electron and promotes it to an excited state. This happens only if the photon energy is higher than the energy difference between the bound and the excited states. This energetic difference is called energy gap (E_g), and every semiconductor has it own value. For example silicon has 1.12 eV of energy gap. Therefore only photons with energy higher than 1.12 eV are absorbed in silicon. In solar cells therefore the absorbed photons transfer their energy to electrons that are promoted to an exited level and are then collected by an internal electric field to contribute to the solar cell output current. The internal electric field is built by the different characteristics (the work function) of the materials implemented in the device. That is the reason why, in order to make working solar cells, material junctions (able to built up internal electric field) are implemented. These few lines on the PV effect are far from being exhaustive, but the reader can refer to numerous handbooks and reviews on this matter [3].

As discussed in the previous paper on STEGs, the solar spectrum can be approximated by a black body at 6000 K, with wavelength ranging between 250 and 4000 nm. This means an energy range of 0.4–4.0 eV. It follows that for the case of silicon all the photons from 0.4 to 1.12 eV are not absorbed, and cannot contribute to set-up the device output current. This represents the first source of loss in solar cells, as pictured in fig. 2.

Also part of the energy carried by photons with an energy higher than the energy gap is lost. Actually, when a photon with energy higher than E_g transfers its energy to a carrier, promotes it to a meta-state with energy higher than the allowed excited electron state. Within times in the order of picoseconds the carrier "*thermalize*" to the allowed exited state, loosing part of the energy transferred by the absorbed photon. This represents the second kind of loss, normally called thermalization loss, as pictured in fig. 2.

The two losses reported above constitute the major part of the losses occurring in solar cells. However, there are other sources of losses due to the thermodynamic equilibrium between the device, and the Sun. This equilibrium shows itself explicitly by the fact that

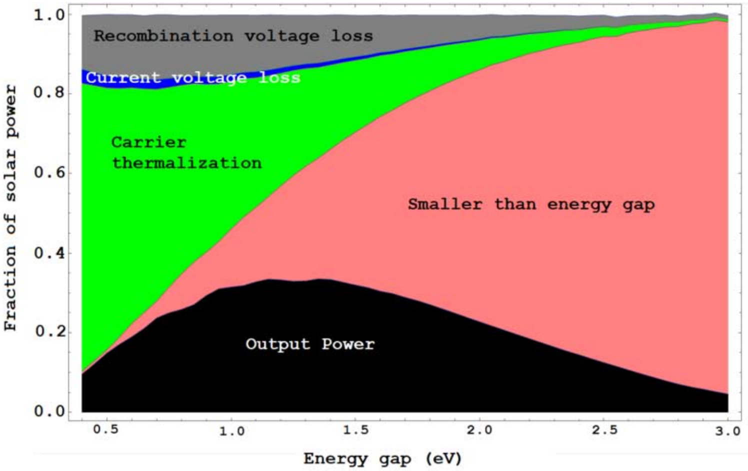

Fig. 2. – Fraction of different kind of losses occurring in solar cells *vs.* the E_g of the absorbing material.

exited electrons can "*recombine*" back to their bound state, loosing the energy and emitting a photon with the same energy of the absorbed photon. This recombination process is the opposite of absorption and leads to current and voltage losses as shown in fig. 2.

Taking a look to fig. 2 it can be seen that for different absorbing materials (namely different values of E_g) the contribution of the described losses changes. It follows that the efficiency of solar cells has a theoretical maximum of $\sim 32\%$ for $E_\mathrm{g} \sim 1.3\,\mathrm{eV}$. It should be pointed out that this theoretical limit decreases for real devices where defects present in the crystal lattice, unwanted absorption and reflections, and other kind of technological limitations, increase carriers recombination and energy losses.

As mentioned above, most of the losses just described are heat losses. Recently, thermal losses in solar cells have been the object of different studies [4-6], with the aim to identify their origin, amount, and spectral distribution. It was shown by these studies that in general, apart from optical reflections, all the remaining losses are in the form of heat. This means that more than 90% of the losses in PV generates heat.

Moreover, it was shown that heat losses are equally distributed over the whole range of energies of the solar spectrum, and not only on the IR part. This is shown in fig. 3 where the distribution of the heat losses occurring in three different kind of solar cells (silicon, copper indium/gallium di-selenide (CIGS), and triple-junction solar cells (TJ)) is reported, compared with the solar spectrum. In fig. 3 a dashed line it is also reported. This line was drawn at the wavelength normally implemented in the spectrum splitting based HTEPV devices. In this case the part of the solar spectrum to the left of the line (higher energies) is directed towards the solar cells, while the other part, is directed towards the TEG. This means that all the heat losses on the left, amounting to the 70–80% of the total amount, cannot be recovered by the TEG, and then are lost. This is the reason why, by definition spectrum splitting approaches for HTEPV applications are weak, and thermal coupling should be preferred.

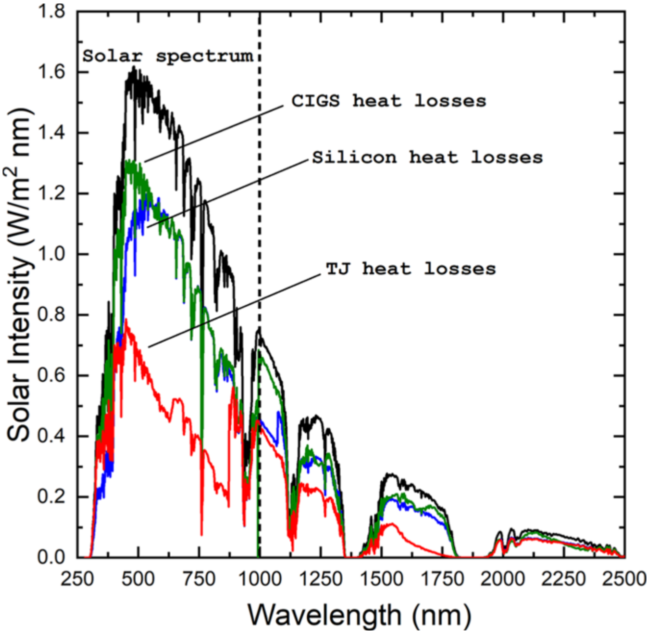

Fig. 3. – Wavelength distribution of heat losses occurring in three kind of solar cells compared with the solar spectrum. Reproduced with permission from [6].

Now that we have learned more on the PV effect and PV losses we can take a close look to the achievable efficiencies of HTEPV systems.

3. – Efficiency of HTEPVs

The calculation of a HTEPV system efficiency is easily derived from the pure STEG case. In the previous paper on STEGs we saw that their efficiency can be calculated by the product of the efficiencies of the various systems elements as follows:

$$\eta_{\mathrm{steg}} = \eta_{\mathrm{opt}} \eta_{\mathrm{ot}} \eta_{\mathrm{teg}} \eta_{\mathrm{diss}}, \tag{1}$$

where η_{opt}, η_{ot}, η_{teg}, and η_{diss} are the efficiencies of, respectively, the optical collector, the opto-thermal converter, the thermoelectric converter, and the dissipation system. We also saw that the STEG efficiency is mainly given by the product η_{ot} η_{teg}, since η_{opt}, and η_{diss}, are essentially given by the system layout and are not influenced by the working temperature. Therefore, let us simply ignore η_{opt}, and η_{diss} from now on.

In this perspective the HTEPV efficiency can be simply calculated as follows:

$$\eta_{\mathrm{htepv}} = \eta_{\mathrm{ot}} \eta_{\mathrm{teg}} + \eta_{\mathrm{pv}} \tag{2}$$

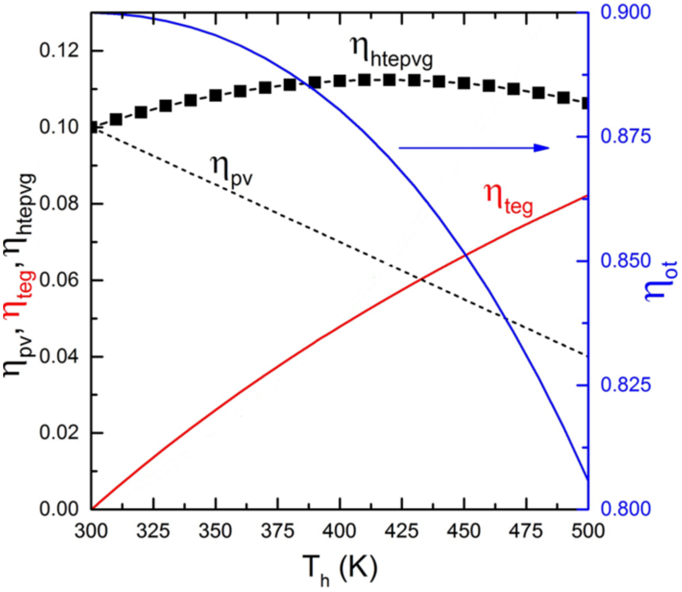

Fig. 4. – Variation of the various components of η_{htepv} *vs.* temperature.

with

$$\eta_{\mathrm{pv}} = \eta^0_{\mathrm{pv}} \left[1 + \beta_{\mathrm{th}} \left(T_{\mathrm{pv}} - T_{\mathrm{a}}\right)\right], \tag{3}$$

where η^0_{pv} is the PV efficiency at room temperature T_{a}, β_{th} the negative solar cell temperature coefficient, and T_{pv} the actual solar cell temperature. It is in fact well known that for most solar cells the efficiency is a decreasing linear function *vs.* temperature. The coefficient β_{th} is the slope of the linear decrease of the solar cell efficiency normalized on η^0_{pv}.

We should also point out that eq. (2) is valid only in the case in which the solar cell and the TEG are electrically separated. In this case the two systems will have their own electrical load to be powered by their electrical output. In the case of electrically hybridized systems the situation is much more complicated and it is outside to the scopes of this essay. The reader should refer to this paper for further details on this matter [7]. In fig. 4 the contribution of the various components of η_{htepv} is reported *vs.* temperature for typical values.

The interesting fact around the temperature sensitivity of solar cells, is that β_{th} depends on the energy gap of the absorbing material. Actually the temperature sensitivity of solar cells is determined by the fact that increasing the temperature, carrier recombination also increases. For this reason in wide band gap materials, where carrier recombination is lower than in small energy gap materials, also temperature sensitivity is smaller. This trend is shown in fig. 5 where the dependence of β_{th} on the material E_{g} is reported.

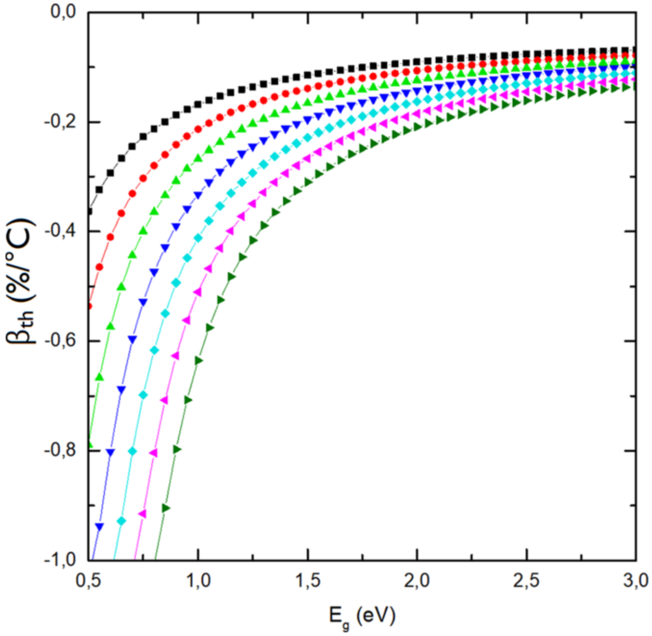

Fig. 5. – β_{th} *vs.* E_{g}. The different lines refer to different material qualities. Better quality implies lower β_{th}, and thus smaller temperature sensitivity.

The other two factors influencing β_{th} are the material quality, and the optical concentration. Regarding the material quality, namely the presence of defects in the crystal lattice, it can modify β_{th} by influencing the recombination process. More defects imply more recombination centres and consequently higher temperature sensitivities. Regarding the optical concentration instead, higher concentrations mean a higher photo-generation of carries without changing the recombination ratio. This imply that recombination will have a smaller impact, resulting into a smaller temperature sensitivity of the solar cell.

Therefore, relating to eq. (2) where a smaller PV temperature sensitivity leads to higher HTEPV efficiencies, the best case will happen hybridizing a high-quality wide gap solar cell operating under optical concentration.

This is shown in fig. 6 where the efficiency gain due to the thermoelectric hybridization is reported as a simultaneous function of the PV temperature (T_H in the graphs) and the energy gap of the PV material. The efficiency gain is normally defined as the difference between the efficiency of the HTEPV system and the efficiency of the solar cell at room temperature.

Figure 6(a) refers to the case of no optical concentration. As can be seen, in this case efficiency gain is smaller than zero for E_{g} smaller than $\sim 1.6\,\text{eV}$. This imply that for solar cells with absorbing material E_{g} smaller than this value, thermoelectric hybridization is detrimental. This evidence leads to the conclusion that for solar cells based on silicon and CIGS thermoelectric hybridization does not work. For other kind of solar cells like

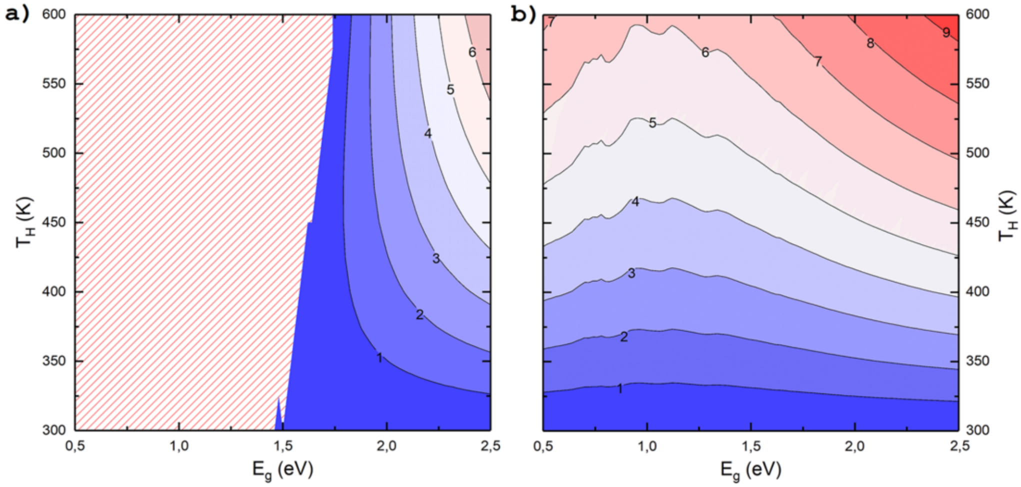

Fig. 6. – Efficiency gains of HTEPV systems compared with the sole PV efficiency at room temperature for two extreme cases. (a) HTEPV implementing perfect materials without optical concentration. (b) HTEPV implementing perfect materials at maximum optical concentration ratio of 46200.

those based on amorphous silicon (a-Si), gallium indium phosphide (GaInP), copper zinc tin sulphide (CZTS), the hybridization can be beneficial.

Figure 6(b) refers instead to the case of optical concentration. In this case the maximum concentration ratio achievable on Earth is considered (namely 46200 X) in order to define the upper theoretical limit. As can be seen, in this case positive value of the gain are found for any given E_{g}. Also silicon and other small gap materials can be beneficially hybridized with thermoelectrics.

It should be pointed out that fig. 6 reports intentionally the upper limits for the two cases of concentrated and not-concentrated HTEPV systems implementing perfect materials (without defects). Real cases of defective materials at concentration ratio practically achievable with nowadays technologies will result in efficiencies gains falling between the two extreme cases reported in fig. 6. A more realistic and detailed analysis of the theoretical efficiency of HTEPV is reported in [8].

The last important point to be considered is the emittance of solar cells. In the previous paper on STEGs we have seen how for evacuated systems heat losses are in the form of radiative heat from the top and the back of the opt-thermal converter. In this case the equation for the opto-thermal efficiency becomes

$$\eta_{\mathrm{ot}} = \alpha_{\mathrm{abs}} - \frac{\sigma A_{\mathrm{abs}} \epsilon_{\mathrm{abs}} (T_{\mathrm{h}}^4 - T_{\mathrm{a}}^4)}{P_{\mathrm{in}} \tau_{\mathrm{opt}}} \tag{4}$$

with α_{otconv}, A_{abs}, ϵ_{abs} respectively, the absorptance, the area, and the emittance of the opto-thermal converter, T_{h} and T_{a} the temperatures of the opto-thermal converter and the ambient, P_{in} and τ_{opt} the input power coming from the Sun, and the optical transmittance of the optical collector. Therefore it is fundamental the choice of a opto-thermal converter (often call solar selective absorber) with high absorptance and low emittance. A good opto-thermal converter should exhibit absorptance of ~ 0.95 and emittance of ~ 0.01.

For HTEPV systems the situation is exactly the same, with the difference that the emittance of solar cells is in general high, ranging between 0.6 and 0.9. Since it is not possible to change the emittance of PV materials without changing their other properties, researchers have found a different way to reduce radiative losses. The solution comes from the so-called heat mirrors (HMs), namely materials able to transmit the full solar spectrum, and with high reflectance in the IR. HMs are normally designed to be deposited on the glass of the evacuated pipe, where the HTEPV system is encapsulated. Their high reflectance in the IR guarantees that radiative heat losses are reflected back to the HTEPV system in a sort of greenhouse effect. The implementation of HMs can considerably enhance the thermoelectric hybridization gains, especially in the case of HTEPV systems working at high temperature and with high emittance solar cells. Further details on this matter can be found in [8].

* * *

The author acknowledges the support by the European Union's Horizon 2020 research and innovation programme under the Marie Skłodowska-Curie grant agreement No. 745304.

REFERENCES

[1] Kraemer D., Jie Q., McEnaney K., Cao F., Liu W., Weinstein L. A., Loomis J., Ren Z. and Chen G., *Nat. Energy*, **1** (2016) 16153.

[2] Nordmann T. and Clavadetscher L., in *Proceedings of the 3rd World Conference on Photovoltaic Energy Conversion, 2003*, Vol. **3** (IEEE) 2003, p. 2243.

[3] Gray J. L., "The physics of the solar cell", in *Handbook of Photovoltaic Science and Engineering*, edited by Antonio Luque López and Steven Hegedus (John Wiley and Sons Ltd) 2003, pp. 106–107.

[4] Dupré O., Vaillon R. and Green M. A., *Sol. Energy Mater. Sol. Cells*, **140** (2015) 92.

[5] Dupré O., Vaillon R. and Green M. A., *Sol. Energy*, **140** (2016) 73.

[6] Lorenzi B., Acciarri M. and Narducci D., *J. Mater. Eng. Perform.*, **27** (2018) 6291.

[7] Lorenzi B., Acciarri M. and Narducci D., *Designs*, **2** (2018) 32.

[8] Lorenzi B. and Chen G., *J. Appl. Phys.*, **124** (2018) 024501.

This page intentionally left blank

Proceedings of the International School of Physics "Enrico Fermi"
Course 207 "Advances in Thermoelectricity: Foundational Issues, Materials and Nanotechnology",
edited by D. Narducci, G. J. Snyder and C. Fanciulli
(IOS, Amsterdam; SIF, Bologna) 2021
DOI 10.3254/ENFI210012

Thermal spin transport and spin in thermoelectrics(*)

Joseph P. Heremans

Department of Mechanical and Aerospace Engineering
Department of Material Science and Engineering and Department of Physics
The Ohio State University, Columbus, OH 43210, USA

Summary. — This paper reviews the principles that govern the combined transport of spin, heat, and charge, both from a macroscopic point of view (the Onsager relations) and microscopically (transport by spin-polarized electrons and magnons). The extensive thermodynamic quantity associated with spin transport is the magnetization; its Onsager-conjugate force is in general the derivative of the free energy with respect to the magnetization. The spin-angular momentum is uniquely associated with the magnetization, so that the words "spin" and "magnetization" are used interchangeably. Spins are carried in one of the following two ways: 1) by spin-polarized free electrons in magnetic metals and doped semiconductors, or 2) by spin waves (magnons) that reside on localized electrons on unfilled d- or f-shells of transition metal or rare-earth elements. The paper covers both cases in separate sections. In both cases, it is possible to define a spin chemical potential whose gradient is the more practical conjugate force to spin transport. The paper further describes the anomalous Hall, spin Hall, and inverse spin Hall effects in magnetic

---

(*) This paper summarizes the notes for two lectures on thermal spin transport given at the *International School of Physics "Enrico Fermi"*, Varenna, in July 2019. The first lecture was on the equilibrium thermodynamics of magnetism and the second on thermally driven spin transport. A third lecture in the series was given by the author on thermal transport in topological materials. The notes for that are being written as a review article for *Rep. Prog. Phys.*

and non-magnetic solids with strong spin-orbit coupling because these effects are used to generate and measure spin fluxes. Spin transport across interfaces is described next, and includes spin pumping and spin transfer torque. The final section then puts all these concepts together to describe the spin-Seebeck, spin-Peltier, and magnon-drag effects, which exist in ferromagnetic, antiferromagnetic, and even paramagnetic solids. Magnon-drag, in particular, is a high-temperature effect that boosts the thermopower of metals by an order of magnitude and that of semiconductors by a factor of 2 or 3 above the electronic diffusion thermopower. This is the only example where a spin-driven effect is larger than a charge-driven effect. Magnon drag leads a simple binary paramagnetic semiconductor, MnTe, to have $zT \geq 1$ without any optimization. This shows how adding spin as an additional design parameter in thermoelectrics research is a new and promising approach toward the quest for high-zT materials.

1. – Introduction

Thermal spin transport concerns the mixed transport of heat and spin, or, more precisely, magnetic moment, just as thermoelectric transport is concerned with the mixed transport properties of heat and electrical charge. Thermoelectric research has struggled for long to overcome the counterindicated nature of the classical transport properties, namely the electrical resistivity, the thermoelectric power, and the thermal conductivity, that constitute the zT, the thermoelectric figure of merit that covers thermoelectric conversion efficiency. Adding spin to the number of controllable variables adds a new design parameter that inevitably must lead to a better optimum zT. Explaining how is the purpose of this paper. The field of thermal spin transport, or *spin caloritronics*, is actually quite old, manifesting mainly by magnon drag identified in ferromagnetic (FM) transition metals like Fe [1] and antiferromagnetic (AFM) semiconductors like MnTe [2] half a century ago. However, the discovery of the spin-Seebeck effect (SSE) on Permalloy in 2008 [3] has started a resurgence of the field. Here, we attempt to give a self-contained didactic review, and refer the reader to the numerous review articles [4, 5] enumerating more exhaustively the effects involved and the details of the theories in spin-caloritronics.

The flow of any well-defined thermodynamic quantity based on a physical, observable effect, along with its conjugate force, obeys Onsager reciprocity. The Onsager relations describe the effect on a flux of an extensive thermodynamic quantity, here charge C, heat Q, and magnetic moment M or spin, of thermodynamic forces, which themselves are gradients of potentials (intensive thermodynamic variables). Table I gives an overview of the quantities involved. The flux of charge is the current density $\vec{j}_C$, and so on with spin and heat. The direct thermodynamic force that generates charge flow is $\vec{F} = e\vec{E}$, where e is the charge of the electron ($e = 1.6 \times 10^{-19}\,\mathrm{C}$), the electric field $\vec{E} = -\nabla\mu/e$ being itself the gradient of the electrochemical potential μ. In heat transport, the heat is the extensive quantity, and its flux $\vec{j}_Q$ is driven by its conjugate force, the

TABLE I. – *Thermodynamic quantities for combined charge, spin and heat transport.*

Extensive	Name	Charge	Spin, moment	Heat	Particle
	Symbol	C	$\hbar\vec{S}$, $\vec{\mu} = -g\mu_B\vec{S}$	Q	$\#$
	Units	Coulomb	$\hbar$, μ_B	Joules	
Flow	Name	Current	Spin current	Heat current	Particle current
	Symbol	I	I_S	I_Q	$I_\#$
	Units	Ampere	$\hbar$/s, μ_B/s	Watt	1/s
Flux	Name	Current density	Spin flux	Heat flux	Particle flux
	Symbol	$\vec{j}_C$	$\vec{j}_S$	$\vec{j}_Q$	$\vec{j}_\#$
	Units	A m^{-2}	$\hbar$ s^{-1} m^{-2}, μ_B s^{-1} m^{-2}	W m^{-2}	m^{-2}
Potential	Name	Electrochemical potential	Spin chemical potential	Temperature	Chemical potential
	Symbol	μ	μ_S	T	μ
	Units	eV	eV	K	eV
Conjugate force	Name	Electric field	Spin potential gradient	Temperature gradient	
	Symbol	$\vec{E} = -\nabla\mu/e$	$\nabla\mu_S$	∇T	$\nabla\mu$
	Units	V/m	eV/m	K/m	eV/m

temperature gradient ∇T. Relations between fluxes and thermodynamic forces are the Onsager relations, and, in most cases, are assumed to be linear.

Spin transport formally is treated the same way as charge and heat transport, and the Onsager relations will be extended here to include it. The most important thermodynamic quantity is the magnetization itself, the quantity whose transport is considered in this paper. The notation used for magnetization or magnetic moment (magnetization per unit volume) is as follows: $\vec{M}$ is the total magnetization of the sample, $\vec{m}$ is the moment per unit volume, and $\vec{\mu}$ is the moment per atom. The most convenient unit used to express the moment is the Bohr magneton $\mu_B = e\hbar/2m = 5.788\ 10^{-5}$ eV/tesla, where m is the free electron mass. The spin-angular momentum on each atom is $\hbar\vec{S}$. The magnetic moment of each atom is then

$$\vec{\mu} = -g\mu_B\vec{S}, \tag{1}$$

where g is the Landé factor, typically 2. The same equation also relates the time derivatives of moment and spin-angular momentum, and, thus, also the spin flux $\vec{j}_S$ and the flux of magnetization. Therefore, we use the words spin flux and magnetization flux interchangeably.

There are three distinct ways to carry a flux of magnetization or spin across a sample:

1) In metals and semiconductors, the free electrons that carry charge and heat in the sample come in either spin-up or spin-down flavor. In non-magnetic material, which we label a *normal metal* (NM), the densities of both are equal. In spin-polarized materials, *e.g.*, FM metals, there are more electrons with their spins oriented parallel to the net magnetization. When this is the case, charge transport is accompanied by spin transport. The thermoelectric effect in mixed charge and heat transport are also accompanied by what is known as *spin-dependent Seebeck and Peltier effects*. This will be treated in sect. **2**.

2) Spin waves exist in FM solids, both FM metals and FM insulators, and in AFMs. They are precessions of the magnetization that resides on the unfilled d and f levels of the core electrons. Magnon propagation carries both heat and spin fluxes, but no charge flux. This will be treated in sect. **3**. However, magnons can interact with free electrons and transfer their momentum to them, giving rise to an advective transport process called *magnon drag* (MD), that greatly boosts the thermopower of the materials affected and increases their thermoelectric figure of merit zT [6-8]. Furthermore, magnons can spin-polarize conduction electrons in a NM across an interface between an FM and the NM, by a process called *spin pumping* described in sect. **4**. When this happens, this FM/NM heterojunction can develop the *spin-Seebeck effect* (SSE) [3, 9]. The two mixed effects, MD and SSE, will be described in sect. **6**.

3) For completion, we add that spin also can be transported by the motion of magnetic domains in a sample, although this will not be described any further.

A few more particularities to spin transport need to be mentioned.

The first difference between spin and heat or charge transport results from the fact that while heat and charge are scalars, magnetization and spin-angular momentum are vectors: they point in the direction $\vec{\sigma}$ (a unitary vector) of the spin polarization (so $\vec{S}\|\vec{\mu}_m\|\vec{\sigma}$). In practice, $\vec{\sigma}$ either is imposed by an external applied magnetic field, or is aligned with the magnetization of a FM sample. In general, $\vec{\sigma}$ is different from the propagation direction of the spin flux $\vec{j}_S$, which is thus formally a tensor. For simplicity, we keep using a vector notation for $\vec{j}_S$, with the arrow denoting its propagation direction.

Second, quantifying spin transport requires developing a technique to measure spin fluxes, a "spin-ammeter" so to speak. The usual method is to evaporate a Pt film on top of a FM sample, and rely on the *inverse spin-Hall effect* (ISHE). We will describe this in detail in sect. **5**.

Third, unlike charge, spin is not conserved; it decays naturally over the scale of nanometers to microns in the solids in which it resides. This is not a problem for the Onsager relations, but it requires the introduction of one additional concept: the spin lifetime τ_S and the accompanying spin diffusion length $L_S = \sqrt{D\tau_S}$: they are related by the usual diffusion relation with diffusion constant D. The diffusion constant itself depends on whether the spin resides on spin-polarized electrons or in magnons (see sects. **3** and **4**).

Fourth, the conjugate force for spin transport in the Onsager relations is in principle the Landau-Lifshitz effective field $\vec{H}_{eff}$ [10]. The $(\vec{M}, \vec{H}_{eff})$ pair enters Onsager symmetry on par with other thermoelectric quantities. As all thermodynamic potentials, $\vec{H}_{eff}$ is the derivative of the free energy with respect to the magnetization, a formal definition that does not identify the microscopic nature of $\vec{H}_{eff}$. It has contributions from the applied, anisotropy, and exchange magnetic fields. The applied field $\vec{B} = \mu_0 \vec{H}_{ext}$ generates a force $\vec{F} = \nabla(\vec{M} \cdot \vec{B})$ that drives $\vec{j}_S$; anisotropy and exchange fields (explained in sect. **3**) follow the same treatment. To this we add the concept of *spin chemical potential* μ_S for the spin systems studied here. The magnetic force is then its gradient, $-\nabla\mu_S$. The exact nature of μ_S will be discussed in detail in the subsequent sections because it is defined differently for spin-polarized electrons, which are fermions, and magnons, which are bosons.

2. – Spin-polarized electrons

The densities of spin-up and spin-down electrons in metals and semiconductors are labeled $n_\uparrow$ and $n_\downarrow$, respectively. In non-magnetic metals and semiconductors, and in the absence of spin injection, $n_\uparrow = n_\downarrow$. Spin polarization can occur in metals and semiconductors by an external magnetic field, by the net magnetic moment that develops in magnetically aligned materials, FMs and ferrimagnets, or by direct spin-injection of carriers of one spin polarization. When the spin relaxation is weak, *i.e.*, in the limit for τ_S, $L_S \to \infty$, one can approximate FM metals by a two-fluid model: spin-up and spin-down electrons, which use spin-up and spin-down densities $n_\uparrow \neq n_\downarrow$ as well-defined thermodynamic quantities (and which could be conserved approximately) that enter Onsager reciprocity relations. Transport of charge current then is accompanied by a spin current.

In the two-fluid model, named after Stoner [11], fig. 1, the spin-up and spin-down electron bands are distinct. The electrochemical potential level at equilibrium is the same for all bands, so that the chemical potentials $\mu_\uparrow$ and $\mu_\downarrow$ for spin-up and spin down electrons, measured *vis-à-vis* their band edges, are distinct. In the presence of a gradient in these potentials, generated, *e.g.*, by an electric field, the Onsager relations relate the charge current densities in the two fluids via their partial conductivities $\sigma_\uparrow$ and $\sigma_\downarrow$:

$$\begin{bmatrix} j_\uparrow \\ j_\downarrow \end{bmatrix} = \begin{bmatrix} \sigma_\uparrow & 0 \\ 0 & \sigma_\downarrow \end{bmatrix} \begin{bmatrix} -\nabla\mu_\uparrow \\ -\nabla\mu_\downarrow \end{bmatrix}. \tag{2}$$

We define the charge current j_C and the spin current j_S by:

$$\begin{aligned} j_C &\equiv j_\uparrow + j_\downarrow, \\ j_S &\equiv \frac{\hbar}{e}\left(j_\uparrow - j_\downarrow\right) \end{aligned} \tag{3}$$

and define the average chemical potential as μ and the spin chemical potential as μ_S:

$$\begin{aligned} \mu &= \frac{1}{2}\left(\mu_\uparrow + \mu_\downarrow\right), \\ \mu_S &= \left(\mu_\uparrow - \mu_\downarrow\right), \end{aligned} \tag{4}$$

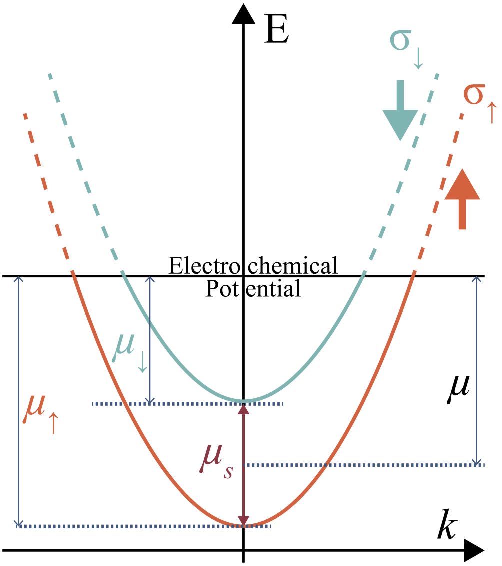

Fig. 1. – The two-fluid model for conduction by spin-polarized electrons.

and the electrical conductivity σ and the spin conductivity σ_S as

$$
\begin{aligned}
\sigma &= \sigma_\uparrow + \sigma_\downarrow, \\
\sigma_S &= \sigma_\uparrow - \sigma_\downarrow.
\end{aligned}
\tag{5}
$$

Substituting (3)–(5) into (2) gives a new Onsager relation (6) that now describes the charge current and the spin current:

$$
\begin{bmatrix} j_C \\ j_S\, e/\hbar \end{bmatrix} = \begin{bmatrix} \sigma & \sigma_S \\ \sigma_S & \sigma \end{bmatrix} \begin{bmatrix} -\nabla\mu \\ \dfrac{-1}{2}\nabla\mu_S \end{bmatrix}. \tag{6}
$$

The gradient in spin chemical potential can have several physical origins. As explained in the introduction, the rigorous conjugate force for spin transport is the Landau-Lifshitz effective field H_{eff}. An applied external magnetic field, or the magnetization in the sample, contribute to H_{eff}. Thus, a gradient in either external field or in magnetization exerts a magnetic force, $\vec{F} = \nabla(\vec{M}\cdot\vec{H})$ on the carriers [12]. Another mechanism to generate a $\nabla\mu_S$ is to inject spin-polarized carriers into the metal dynamically: examples of how this can be done are given in sect. **5**.

The effect of spin-flipping electron interactions that limit τ_S, when not so intense as to invalidate the two-fluid model completely, are taken into account by using the drift-diffusion equation [13]. Equation (2) then becomes:

$$
j_{S\uparrow} = \sigma_\uparrow \nabla\mu_\uparrow - D\nabla n_\uparrow; \qquad j_{S\downarrow} = \sigma_\downarrow \nabla\mu_\downarrow - D\nabla n_\downarrow, \tag{7}
$$

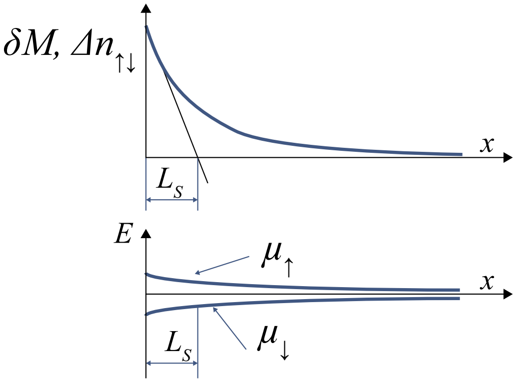

Fig. 2. – Electron spin diffusion length L_S in the two-fluid model.

where $D = \mu_m k_B T/e$ is the electron diffusion constant and μ_m is the charge carrier mobility, and the presence of gradients in $n_\uparrow$ and $n_\downarrow$ is related to the spin-flip transitions that govern both.

Consider a one-dimensional picture (fig. 2) where an accumulation of spins is injected into a metal at the left side ($x = 0$), with an initial $n_\uparrow(x = 0) - n_\downarrow(x = 0) = \Delta n_{\uparrow\downarrow,0}$ accumulation. Over a distance x into the metal, spin-flip transitions between the two populations, with a spin lifetime τ_S will reduce the amount of spin imbalance $\Delta n_{\uparrow\downarrow}(x) = n_\uparrow - n_\downarrow$; thus, the net magnetization $\delta|\vec{M}| = \mu_B \Delta n_{\uparrow\downarrow}$ also will be reduced. This is determined by the diffusion equation

$$\Delta n_{\uparrow\downarrow} = \Delta n_{\uparrow\downarrow 0} \exp(-x/L_S) \tag{8}$$

as shown in fig. 2. Here, the diffusion length is $L_S = \sqrt{D\tau_S}$. Since Fermi-Dirac statistics directly relate the partial charge carrier concentrations to the chemical potentials

$$n_{\uparrow or \downarrow} = \int_0^\infty \frac{\mathfrak{D}(E)\mathrm{d}E}{1 + \exp\left(\frac{E-\mu_{\uparrow or\downarrow}}{k_B T}\right)}\,, \tag{9}$$

where $\mathfrak{D}(E)$ is the electronic density of states (DOS), $\Delta n_{\uparrow\downarrow}(x) = n_\uparrow - n_\downarrow$ is equivalently represented by a change in $\mu_\uparrow(x)$ and $\mu_\downarrow(x)$, and thus $\mu_S(x)$ as shown in fig. 2.

Adding a temperature gradient to the problem results in a mixed charge-spin-heat Onsager relation:

$$\mathbf{j} = \begin{bmatrix} j_C \\ j_Q \\ j_S\, e/\hbar \end{bmatrix} = \begin{bmatrix} \sigma & L_{ET} & \sigma_S \\ L_{TE} & \kappa & L_{TM} \\ \sigma_S & L_{MT} & \sigma \end{bmatrix} \begin{bmatrix} -\nabla\mu \\ -\nabla T \\ \frac{-1}{2}\nabla\mu_S \end{bmatrix} \tag{10}$$

with a production of irreversible entropy (spin propagation is dissipative):

$$\dot{S} = \mathbf{j} \cdot \mathbf{F}/T. \tag{11}$$

Here, we recognize the classical thermoelectric conductivity L_{ET}, which gives rise to the thermopower $\alpha = L_{ET}/\sigma$, but it should be pointed out that this thermopower is driven by spin-polarized carriers; thus, it is a spin-dependent Seebeck coefficient, reviewed by Boona *et al.* [4] and Vandaele *et al.* [7]. The spin-dependent Peltier conductivity L_{TE} is accompanied by a thermally driven spin flux via the non-zero coefficient L_{MT}. The van Wees group have seen the spin-dependent Seebeck [14] and Peltier [15] coefficients experimentally, as have many others [16,17]. In the two-fluid model, the partial thermopowers for spin-up and spin-down electrons, $\alpha_\uparrow = L_{ET\uparrow}/\sigma_\uparrow$ and $\alpha_\downarrow = L_{ET\downarrow}/\sigma_\downarrow$ are given by the Mott formula. The total thermopower is given by the conductivity-weighted average of the partial thermopowers, as is customary for all multi-carrier systems:

$$\alpha = \frac{\alpha_\uparrow \sigma_\uparrow + \alpha_\downarrow \sigma_\downarrow}{\sigma_\uparrow + \sigma_\downarrow}\,. \tag{12}$$

For the purpose of thermoelectric performance, only the total thermopower matters. The two-fluid model has also been used to interpret the Nernst effect in metallic FMs [6].

3. – Magnons

3·1. *Ferromagnets.* – Consider a FM insulator at 0 K in which all moments reside on the core electrons on unfilled *d*- or *f*-shells of the atoms in the solid. This is the ground state of the system, represented in fig. 3(A). The interatomic distance is a, and the spins are coupled to each other by the magnetic *exchange energy* J. The p-th atom interacts with its neighbors of index $p-1$ and $p+1$. The ground state energy of the system is

$$U = -2J \sum_{p=1}^{N} \vec{S}_p \cdot \vec{S}_{p+1}. \tag{13}$$

At finite temperature, the individual spins do not start flipping arbitrarily through the system, as this would cost too much energy. Instead, all spins share the decrease of magnetization by developing a precession motion, as shown in fig. 3(B). The precession motion becomes a wave, called a *magnon*, much like phonons are waves of atomic displacements. The projection of each moment along the direction of magnetization at 0 K, the saturation magnetization $\vec{M}_S(T)$ of the sample at finite temperature T, is decreased: $\vec{M}_S(T) < \vec{M}_S(T=0)$. The dynamic magnetization $\vec{m}(\vec{r},T)$ (see fig. 4) is the quantity that will form the wave. To carry the analogy between magnons and phonons further, $|\vec{m}(\vec{r},T)|$ (or the apex cone angle) is, for magnons, the quantity equivalent to the amplitude of the atomic motion for phonons. The phase angle of $\vec{m}(\vec{r},T)$ is equivalent to the phase of the atomic motion in phonon propagation.

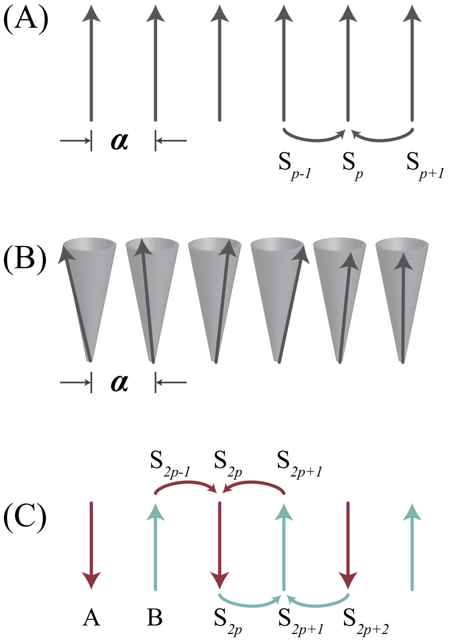

Fig. 3. – (A) Magnetic moments in a ferromagnet of lattice constant a at zero K. Neighboring spins of index $p-1$, p and $p+1$ couple. (B) At finite temperature, spin waves develop. (C) Antiferromagnets have two sublattices A and B; two sets of couplings are possible.

The equation of motion of magnons is different from that of phonons (the ball-and-spring model): the individual moment $\vec{\mu}_p(t)$ of the p-th atom is shown in fig. 4. From interactions with its neighbors (fig. 3) via exchange energy J, the effective magnetic induction felt by the p-th atom is:

$$\vec{B}_p = -\left(\frac{2J}{g\mu_B}\right)\left(\vec{S}_{p-1} + \vec{S}_{p+1}\right). \tag{14}$$

This exchange field will generate magnons called *exchange-coupled magnons*. The time dependence of the moment in the presence of $\vec{B}_p$ is then [18]

$$\frac{\hbar}{g\mu_B}\,\frac{\mathrm{d}\vec{\mu}_p(t)}{\mathrm{d}t} = -\vec{\mu}_p(t) \times \vec{B}_p(t), \tag{15}$$

where the right side of the equation is the torque that drives the precession. Equivalently, one can write

$$\frac{\mathrm{d}\vec{S}_p}{\mathrm{d}t} = \left(-\frac{g\mu_B}{\hbar}\right)\left\{\vec{S}_p(t) \times \vec{B}_p(t)\right\} = \left(\frac{2J}{\hbar}\right)\left\{\vec{S}_p \times \vec{S}_{p-1} + \vec{S}_p \times \vec{S}_{p+1}\right\}. \tag{16}$$

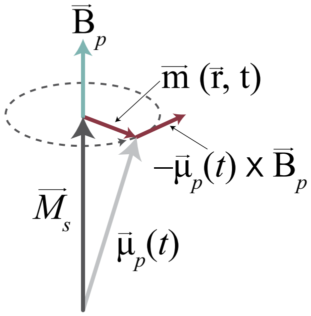

Fig. 4. – Equation of motion for magnons.

The solution to eq. (16) in Cartesian coordinates (z being the direction of $\vec{M}_S$) is $S_p^x = u \exp(ipka - \omega t)$; $S_p^y = v \exp(ipka - \omega t)$. The dynamic part of the magnetization, $\vec{m}(\vec{r}, t)$ (see fig. 4), with the same periodic boundary conditions as apply to phonon physics, is a propagating wave with a wavevector in k-space and an angular frequency ω:

$$\vec{m}(\vec{r}, t) = m_0 \exp\left\{ i \left(\vec{k} \cdot \vec{r} - \omega t \right) \right\}. \tag{17}$$

The difference between the equations of motion for phonons and magnons in ferromagnets results in a difference between their dispersion relations. Considering only one dimension, the dispersion relation for FM magnons is

$$\hbar\omega = 4JS(1 - \cos ka), \tag{18}$$

which resembles that of electrons in a tight-binding model. At low frequency, eq. (18) gives a Taylor expansion that is parabolic in k, $\hbar\omega \cong (2JSa^2)k^2$, which more generally is written as $\hbar\omega \cong Da^2k^2$, where D is the magnon stiffness. Here, the magnon stiffness is derived for these exchange-coupled magnons. This quadratic dispersion now looks like that of electrons near the band edge. If we add an external magnetic field B_{ext}, it adds a Zeeman energy $g\mu_B B_{ext}$ to the magnon dispersion, which, being independent of k, looks like a band gap in the magnon dispersion.

Finally, to all this we add the presence of magnetic anisotropy, the tendency of the atomic moments to orient along a specific direction in the sample due either to a geometrical effect or to the anisotropy of the crystal structure. Magnetic anisotropy is quantified by the anisotropy energy, *i.e.*, the energy gain this alignment gives to the magnetic system. This energy also can be expressed in terms of an anisotropy field B_a by writing it as a Zeeman energy $g\mu_B B_a$. In turn, B_a then can be added to the external field B_{ext} to form an "effective" field B_{eff}. The final magnon dispersion for FMs is then

$$\hbar\omega = g\mu_B B_{eff} + Da^2k^2. \tag{19}$$

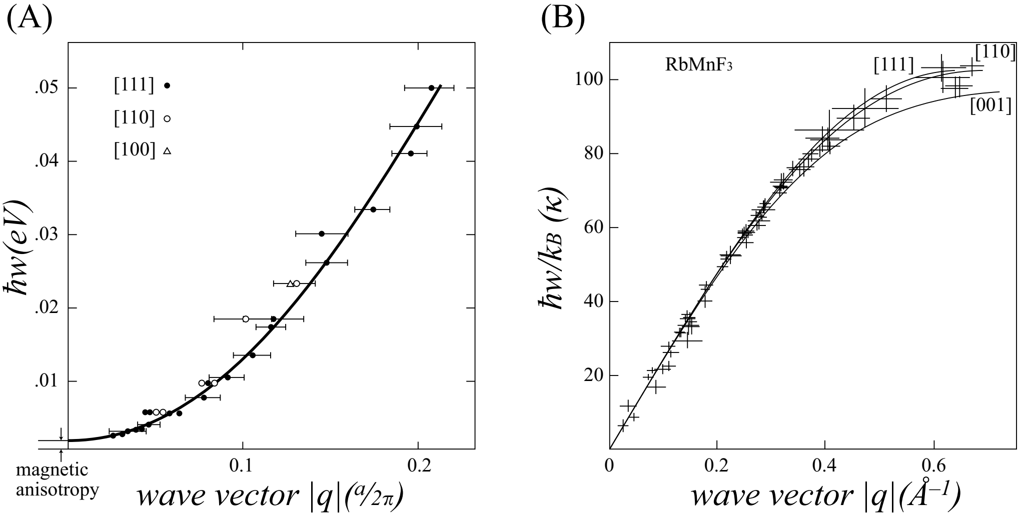

Fig. 5. – (A) FM exchange-coupled magnon dispersion in cobalt; (B) AFM exchange-coupled magnon dispersion. Redrawn and adapted from ref. [19] (A) and ref. [20] (B).

Experimentally, since neutrons are sensitive to spin, inelastic neutron scattering can be used to map out magnon dispersions as well as phonon dispersions, and the results confirm the calculated dispersion relations quite well, see fig. 5(A) [19]. The gap at $k = 0$ can be detected by optical techniques, which involve no exchange in k-vector. *Ferromagnetic resonance* (FMR) is the classical technique for this that uses microwaves (the gap is typically a few GHz). The microwave absorption shows a maximum when $\omega = g\mu_B(B_a + B_{ext})/\hbar$. The absorption peak can be followed or tuned by applying an external magnetic field B_{ext}.

In addition to exchange-coupled magnons, there are *dipole-coupled magnons*, coupled by dipole interactions, which are mostly at the surface and at very low energy. Their dispersion is not necessarily quadratic, and their group velocities are very small and can even be negative ("backward-propagating magnons"). The dipole-coupled magnons are seen by inelastic light scattering techniques such as *Brillouin light scattering*, which involve infinitesimally small k-vectors. Because of their low velocity, dipole-coupled magnons contribute little to transport and will not be considered here further.

3˙2. *Antiferromagnets.* – AFMs support magnons as well, but their dispersion is quite different from that of FM magnons. There are many types of AFM ordering in various solids. The simplest consists of the one-dimensional magnetic sublattices A and B, shown in fig. 3 as green and red sublattices. The 3D version of this would be a cubic AFM ordering where each site's spin is the opposite of each of its nearest neighbors ($RbMnF_3$, $LiNiF_3$): this gives a very small magnetic anisotropy. Many other types of AFM ordering exist, such as sheets of FM-ordered planes stacked in an AFM fashion (*e.g.*, MnTe along

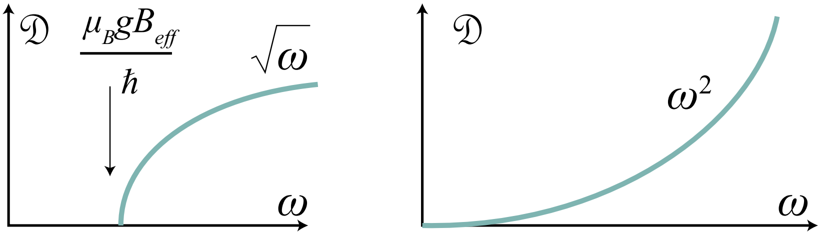

Fig. 6. – Magnon DOS: (A) in a FM; (B) in an AFM.

the $\langle 001 \rangle$ direction), or triangular or helical lattices (*e.g.*, one of the phases in many heavy elemental rare-earth metals) [18].

In this paper, we only consider the very simple case of fig. 3, with sublattices A (red) and B (green). There are now two coupled equations of motion like eq. (16), one per sublattice. Assuming that the moments are equal but opposite ($\vec{S}_A = -\vec{S}_B = \vec{S}$), the effective fields for atom index $2p$ of sublattice A and for atom of index $2p+1$ of sublattice B are

$$\vec{B}^A_{2p} = -\left(\frac{2J}{g\mu_B}\right)\left(\vec{S}_{2p-1} + \vec{S}_{2p+1}\right); \qquad \vec{B}^B_{2p+1} = -\left(\frac{2J}{g\mu_B}\right)\left(-\vec{S}_{2p} - \vec{S}_{2p+2}\right). \tag{20}$$

Equations (15)–(17) are now replaced a system of two equations for indices $2p$ and $2p+1$:

$$\begin{aligned} S^x_{2p} &= u_A \exp[i(2pka - \omega t)]; \qquad & S^y_{2p} &= v_A \exp[i(2pka - \omega t)], \\ S^x_{2p+1} &= u_B \exp[i((2p+1)ka - \omega t)]; \qquad & S^y_{2p+1} &= v_B \exp[i(2(2p+1)ka - \omega t)]. \end{aligned} \tag{21}$$

This system has roots only if $\omega^2 = (-4JS/\hbar)^2(1 - \cos^2(ka))$ and the dispersion relation becomes [18]:

$$\hbar\omega = \hbar\omega_{\max} \left|\sin(ka)\right|. \tag{22}$$

Interestingly, while the magnon dispersion in a FM solid looks like the dispersion of electrons, magnon dispersion in an AFM looks like the dispersion of phonons. The Taylor expansion at low energy is linear

$$\hbar\omega = \hbar\omega_{\max} ka. \tag{23}$$

As for FM magnons, magnetic anisotropy adds a Zeeman term, which looks like an energy gap. The magnon dispersion relation measured by neutron scattering on $RbMnF_3$, which has negligible anisotropy, is shown in fig. 5(B) [20] and follows eq. (22) perfectly.

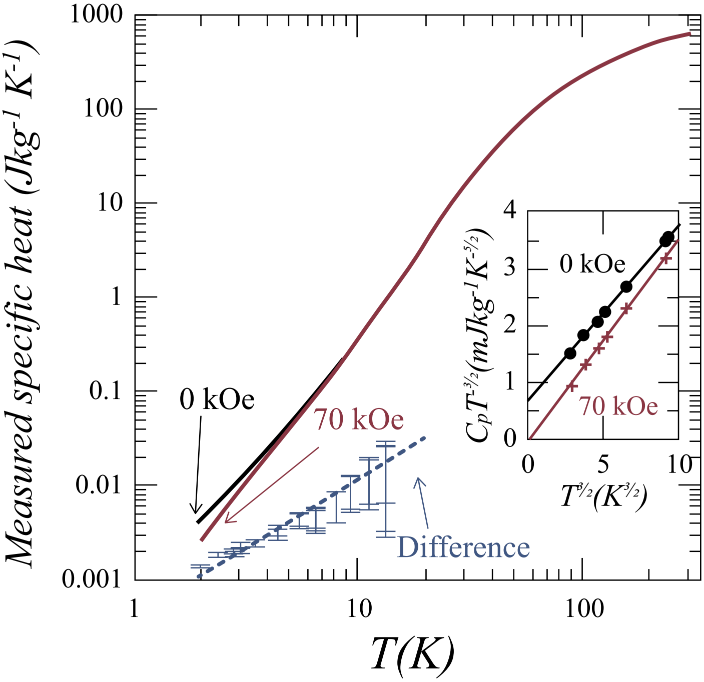

Fig. 7. – Specific heat in yttrium iron garnet (YIG), an insulating ferrimagnetic garnet. Applying an external magnetic field isolates the phonon contribution. The magnon contribution can then be obtained from the difference between measurements at zero field and at 70 kOe [21].

3˙3. *Equilibrium thermodynamic properties of magnons.* – The DOS $\mathfrak{D}(E)$ of FM and AFM magnons is calculated from the dispersion relations as for all other quasiparticles, and is shown in fig. 6. Given the similarity between FM magnons and electrons, it is not surprising that their DOS follows a $\sqrt{E}$ or $\sqrt{\omega}$ law, with an offset that is the gap eq. (19). In particular, this gap can be changed by applying an external magnetic field. Likewise, given the similarity of the AFM magnon dispersion to that of phonons, the AFM DOS follows a E^2 or ω^2 law.

Like phonons and electrons, magnons carry heat and entropy, in an amount k_B per particle. Thus, there is a magnon specific heat C_m, calculated like with all other quasiparticles as the temperature derivative of the internal energy U of the system. U is obtained by integrating the energy per quasiparticle over the ensemble of particles, itself obtained by using the appropriate DOS and statistical distribution function.

For FM magnons, this results in a $C_m \propto T^{1.5}$ law at low temperature (see fig. 7 [21]). The existence of a field-dependent gap in the dispersion offers a way to separate C_m from the other contributions to the specific heat C, in particular the phonon contribution C_p: C_m can be frozen out by applying a high magnetic field [21]. At zero field, $C = C_p + C_m$, in yttrium iron garnet (YIG), an electrically insulating ferrimagnet that has a net magnetic

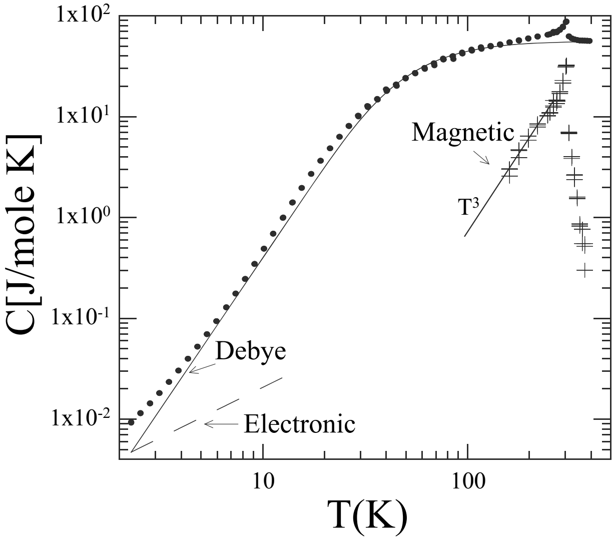

Fig. 8. – Specific heat of the AFM MnTe. The magnon contribution is isolated near the ordering temperature $T_N = 305\,\mathrm{K}$ [8].

moment and thus behaves like a FM. As the applied field is increased, the magnon DOS shifts to a higher energy, and no magnons contribute to C_m at low T. As a result, at the highest field, only the phonon specific heat is measured. Therefore, by taking the difference between C ($B_{ext} = 0$ Oe) and C ($B_{ext} = 7$ kOe), one can isolate C_m.

The specific heat of AFM magnons at temperatures far below the ordering or Néel temperature (T_N) is congruent to that of phonons because the energy dependence of the dispersion relation and the DOS are congruent for both quasiparticles, and their statistical distribution functions are the same. At $T \ll T_N$, C_m follows a Debye-like law with $\hbar\omega_{\max}/k_B$ as a magnon cutoff temperature. At low temperature, $C_m \propto T^3$ and it is practically impossible to separate C_m experimentally from the phonon contribution. The specific heat of the AFM MnTe is shown in fig. 8 [8]. An electronic contribution is observed in this heavily doped sample, but the magnon contribution cannot be resolved from the phonon contribution at low temperature. However, above 150 K and especially near the ordering temperature ($T_N = 305\,\mathrm{K}$), an additional heat capacity appears over the behavior expected from phonons. Given that the Debye temperature for MnTe (217 K) is much lower than T_N, C_p has nearly reached its Dulong-Petit value at T_N. Thus, values for C_p can be obtained with reasonable accuracy from a Debye model fit (the full line in fig. 8). Subtracting this from the data (the electronic contribution is negligible above 100 K) gives values for C_m in the 150–350 K range: they follow a T^3 law, as predicted, except very near and above T_N. It is not surprising that an excess heat should appear near T_N because the behavior of magnetic lattices near their melting points is governed by the physics of critical phenomena, and not magnon physics.

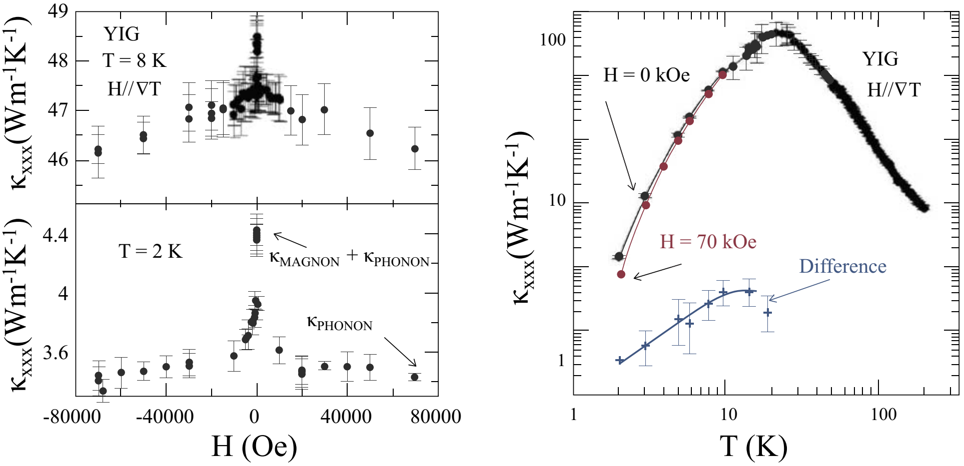

Fig. 9. – Magnon thermal conductivity of YIG, an electrically insulating FM, in an applied external magnetic field [21].

3˙4. *Magnon thermal transport.* – The approach used for the specific heat applies to the magnon thermal conductivity κ_m as well, and one can use the kinetic formula

$$\kappa_m = \frac{1}{3} C_m v_m \ell_m \tag{24}$$

for each magnon mode and frequency. In FMs, where one can freeze out the contribution of C_m by applying a magnetic field that opens a Zeeman-energy gap in the dispersion, the same technique can be applied to freeze out κ_m. This was done for YIG by Boona *et al.* [21], and the results are shown in fig. 9. The magnetic-field dependence of the total thermal conductivity $\kappa = \kappa_p + \kappa_m(B_{ext})$ is given as a function of T and the applied magnetic field. Here κ_p is the phonon thermal conductivity. The freeze-out of κ_m is visible in its field dependence, which shows a saturation at low temperature. Assuming that this saturation value is κ_p, and neglecting phonon scattering on magnons (see fig. 10), the value for $\kappa_m(T)$ can then be obtained by taking the difference as $\kappa_m = \kappa(0\,\mathrm{T}) - \kappa(7\,\mathrm{T})$, as shown.

Magnons can scatter phonons as well as carry heat; when this is their dominant effect, they lower κ_p often to the extent that their contribution results in reducing κ as opposed to enhancing it. An example is shown in fig. 10 [22], where the thermal conductivity of non-magnetic CaF_2 and AFM MnF_2, which have the same crystal and phonon structure, are compared. Below T_N, MnF_2 has a much lower conductivity, hinting at magnon scattering of phonons. This is more pronounced when non-magnetic ZnF_2 is compared to the AFM CoF_2; ZnF_2 and CoF_2 also share the same crystal and phonon structure. In CoF_2 scattering of phonons by the magnons at T_N is particularly intense, reminiscent of the very large, excess magnetic specific heat near T_N and already shown in fig. 8.

Since all propagating excitations contribute to κ, its measurement can provide infor-

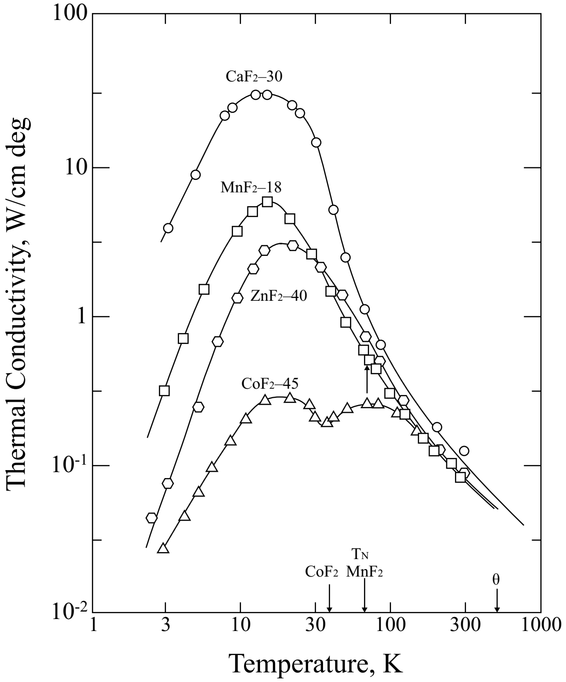

Fig. 10. – Magnon scattering of phonons. From ref. [22].

mation about transport in insulating FMs and AFMs that is not accessible experimentally otherwise. In such materials, entropy and spin are the only two extensive quantities whose flux can be measured. This paper considers only the most elemental versions of spin waves, but magnon physics is very rich. Magnons can develop esoteric topological properties and, in principle, develop topologically protected transport. One particularly interesting form of magnetization propagation are spinons in quantum spin liquids (QSLs), collective modes that appear in frustrated magnets and are not bosons, but fermions. Gapless fermionic spinons are expected to have $\kappa \propto T^1$ [23], as opposed to the T^3 for κ_p; this temperature dependence is considered the fingerprint of fermionic particles.

3˙5. *Thermal Hall effect.* – If one breaks time-reversal symmetry on such topological magnon systems, typically by adding a magnetic field, topologically non-trivial spin structures can generate a thermal Hall effect κ_{xy}. The measurement of κ_{xy} [24, 25] can provide definitive evidence for chiral topological phases that host a gapped bulk, together with gapless chiral-edge spin excitations [26, 27], *e.g.*, in chiral spin liquids and fractional quantum Hall effects [28, 29]. When edge states dominate spin transport, the conduction of heat becomes more pronounced along the edge that allows conduction from hot to cold than along the other, giving rise to a transverse temperature gradient and thus, a thermal Hall effect. This signature feature has been observed in α-RuCl$_3$ [25]. Hirschberger *et al.* report a thermal Hall effect in a frustrated quantum magnet [30] and

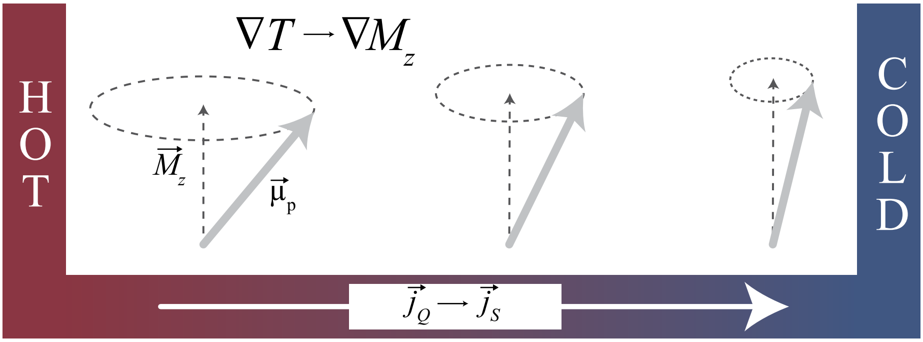

Fig. 11. – Magnon spin current and magnon heat current.

Kagome magnet [31]. Measurements of κ_{xy} are particularly difficult because the copper used in most measurement instrumentation, and in heat spreaders and heat sinks, has an electronic thermal Hall effect (the Righi-Leduc effect) that impose spurious transverse gradients on the samples: instruments have to be redesigned with care with this in mind.

3˙6. *Thermally driven magnon spin currents.* – In the simplest possible picture, the number flux of magnons, $j_\#$ is related directly to the magnon heat flux, as each magnon carries $k_B T$ of heat and the spin flux j_S or flux of magnetization j_m, as illustrated in fig. 11:

$$\begin{aligned} j_Q &= -\kappa_m \nabla T, \\ j_Q &= k_B T \cdot j_\#, \\ j_S &= \hbar \cdot j_\#, \\ j_m &= g\mu_B \cdot j_\#. \end{aligned} \tag{25}$$

As magnons move from hot to cold, the local saturation magnetization $\vec{M}_S$ (the projection of the atomic moment onto the vertical axis) increases, which amounts to a transport of magnetization from hot to cold. This is expressed by eq. (25).

3˙7. *Spin chemical potential for magnons.* – The theoretical concept of the existence of a spin chemical potential for magnons has been proposed recently. It is long accepted that magnons at thermal equilibrium obey Bose statistics with no chemical potential. However, two recent experiments [32, 33] have demonstrated that in the presence of a spin current injected by a source external to the sample, a magnon gas can be described as being in quasi-thermodynamic equilibrium with Bose statistics and both a temperature and a spin chemical potential μ_S. The external source of spin current can be FMR pumping or the ISHE in an adjacent layer (see sect. **5**˙3). By analogy with the electronic μ_S eq. (4), the magnon μ_S is useful to characterize how the spins residing on magnons diffuse. If an external source pumps an excess of Δn_S spins into the magnon

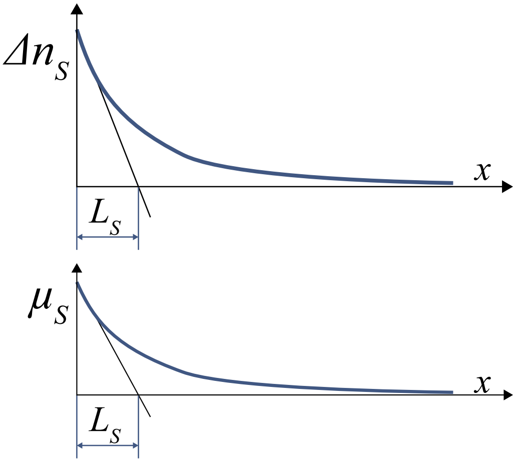

Fig. 12. – Spin chemical potential for magnons.

system at the surface of a sample (or the edge of a 1D sample of fig. 12), the excess can be described at each point in the sample by

$$\Delta n_S(x) = \int_0^\infty \frac{\mathfrak{D}(E)\mathrm{d}E}{1 - \exp\left(\frac{E-\mu_S(x)}{k_B T}\right)}. \tag{26}$$

The decay of the excess spins is governed by a characteristic diffusion length $L_S = \sqrt{D\tau_S}$ where D is the thermal diffusion constant of magnons and τ_S is the spin lifetime limited by spin-flip transitions. For magnonic systems, electron-magnon interactions typically are the main source of spin-flip transitions, so the metallic FMs have much shorter spin lifetimes and diffusion lengths than FM insulators, where L_S can reach tens of micrometers. Further, in FM insulators $L_S \gg \ell_m$, the mean free path in eq. (24), which correspond to interactions that change the moment of the magnon. Thus, in FM insulators, it is only very rarely that a magnon scattering event flips its spin. The concept of spin chemical potential is quite useful in developing magnon transport theories in ferromagnetic insulators [34]. The concept of magnon chemical potential recently has been extended to apply to the sublattices of AFM insulators [35].

3˙8. *Magnonic thermopower*. – Gradients in the spin chemical potential can be treated as conjugate forces for spin transport in Onsager relations. By analogy with the thermoelectric Onsager relations, mixed linear thermo-spin Onsager relations [7] connect magnonic spin and heat currents:

$$\begin{pmatrix} j_S \\ j_{Q,m} \end{pmatrix} = \begin{pmatrix} \sigma_S & \zeta \\ \pi_m & \kappa_m \end{pmatrix} \begin{pmatrix} -\nabla\mu_S \\ -\nabla T \end{pmatrix}, \tag{27}$$

where κ_m is the magnon thermal conductivity described above. The spin conductivity σ_s describes the strength of the spin flux driven by a gradient $\nabla\mu_S$ in the spin chemical potential. New is ζ, the *thermomagnonic conductivity*, the equivalent for magnons of the coefficient L_{ET}, the thermoelectric conductivity, used for free electrons. New also is the ratio $\alpha_m \equiv -\zeta/\sigma_S$, the *magnonic thermopower* defined by taking eq. (27) under spin-open-circuit conditions (setting $j_S = 0$), where we allow for spin accumulation to occur

$$\alpha_m \equiv -\frac{\nabla\mu_S}{\nabla T} = -\frac{\zeta}{\sigma_S}\,. \tag{28}$$

Both α_m and ζ have Onsager reciprocals, the magnonic Peltier coefficient and the magnon Peltier conductivity π_m; these contains essentially the same physics as ζ.

To obtain a microscopic expression for the magnonic thermopower, one can treat the magnon gas as an ideal gas of free particles with internal energy density $U(T,\mu_S)$. In the presence of a thermal gradient ∇T, an inhomogeneous distribution of magnons arises through the system, which can be expressed in terms of a non-vanishing spin chemical-potential gradient $\nabla\mu_S$. Denoting C_m the volumetric specific heat, the total gradient in the internal energy is now

$$\nabla U = C_m\nabla T + n_m\nabla\mu_S. \tag{29}$$

This exerts a force $\vec{F}$ that drives the magnon flow. The force is the magnon pressure P, in an ideal gas $P = 2/3U$, on a unit surface. Newton's second law, applied to a volume δV of the magnon gas, gives

$$n_m M\delta V\frac{\mathrm{d}\vec{v}_m}{\mathrm{d}t} = \delta\vec{F}, \tag{30}$$

where M is the magnon mass and $\vec{v}_m$ its drift velocity. Combining eqs. (29) and (30), and then dividing by δV gives

$$\frac{\mathrm{d}\vec{v}_m}{\mathrm{d}t} = -\frac{2}{3n_mM}\frac{\partial U}{\partial T}\nabla T - \frac{2}{3n_mM}\frac{\partial U}{\partial\mu}\nabla\mu_S = -\frac{2}{3n_mM}C_m\nabla T - \frac{2}{3M}\nabla\mu_S. \tag{31}$$

The condition $j_s = 0$ means that $\frac{\mathrm{d}\vec{v}_m}{\mathrm{d}t} = 0$. Equation (31) now gives the magnonic thermopower as

$$\alpha_m = \frac{C_m}{n_m}\,. \tag{32}$$

It is important to note that the magnonic thermopower is the specific heat per spin carrier, to the first order just equal to the Boltzmann constant k_B. Thus, the magnonic thermopower does not decrease as the density of magnons increases, unlike the electronic thermopower. The decrease of the electronic thermopower with electron concentration, expressed by the Mott formula [36], is a consequence of the Pauli exclusion principle that limits the number of degrees of freedom of electrons, and thus their entropy. The Mott formula itself follows directly [36] from the Fermi-Dirac statistical distribution function and the Pauli exclusion principle. Magnons are bosons, and therefore are not subject to the same limitations in number of degrees of freedom.

4. – Spin-Hall and anomalous Hall effects

One of the most useful tools in spin transport technology is the ability to generate and detect spin currents by means of the spin Hall effect (SHE) and the inverse spin Hall effect (ISHE). Both spin-orbit coupling (SOC) in all materials and the presence of permanent magnetic moments in FMs give rise to these effects. In FMs, the SHE is also closely related to the anomalous Hall effect (AHE), which was discovered by Hall himself [37]. A schematic representation of the definitions of AHE, SHE and ISHE in FM's, and of SHE and ISHE in NMs with strong SOCs, is given in fig. 13. Excellent reviews exist on this topic [38]. The equivalent thermal effect, the Spin Nernst (SNE), Anomalous Nernst (ANE), and planar Nernst (PNE) effects are reviewed in Boona *et al.* [4].

4˙1. *AHE, SHE, and ISHE in ferromagnetic metals.* – Phenomenologically, in FM conductors, the Hall resistivity, measured in the geometry fig. 13(A), takes the form $\rho_{xy} = R_H H_z + \rho'_{xy}$, where ρ_{xy} is the measured Hall resistivity, R_H is the ordinary Hall coefficient, H_z is the applied field and ρ'_{xy} is the anomalous contribution. The term ρ'_{xy} generally is defined as $\rho'_{xy} = 4\pi R_{AH} M$, where R_{AH} is the anomalous Hall coefficient and M is the magnetization. A common misunderstanding is to regard the AHE as being simply the ordinary Hall coefficient corrected for the real magnetization in the sample; quite to the contrary, $R_{AH} \neq R_H$ and both can even have the opposite signs.

Various mechanisms may produce R_{AH} in FMs, although even after over a century of research, the situation is not always clear because many of these mechanisms are extrinsic and depend on the defect chemistry in the FM. Generally, R_{AH} depends on the material type, temperature, and strength of the applied field [39-41]. The approaches are inspired by the two-fluid model eq. (2), to which is added the concept of differential scattering of the spin-up and spin-down electrons. In the first mechanism, *skew scattering* [42,43], the differential scattering cross-section of the charge carriers that interact with localized impurity states is asymmetric with respect to the carrier spin state. In the second, *side-jump*, mechanism [44], the wave functions of the free electrons are distorted locally during impurity scattering events, as a result of spin-orbit interactions. This causes a spin-dependent offset in the final trajectories of the scattered electrons. Third, the *anomalous velocity* due to the presence of a Berry phase has been invoked as a source of AHE [45-48].

The AHE gives rise to several other transverse effects in FM conductors. First is the ANE, which is related to the energy dependence of the AHE by the Mott relation, which holds for metals for transverse thermoelectric coefficients as it does for direct ones:

$$\alpha_{xy} = \frac{\pi^2}{3}\frac{k_B}{e}\frac{k_B T}{\rho_{xy}}\frac{\mathrm{d}\rho_{xy}(E)}{\mathrm{d}E}\,. \tag{33}$$

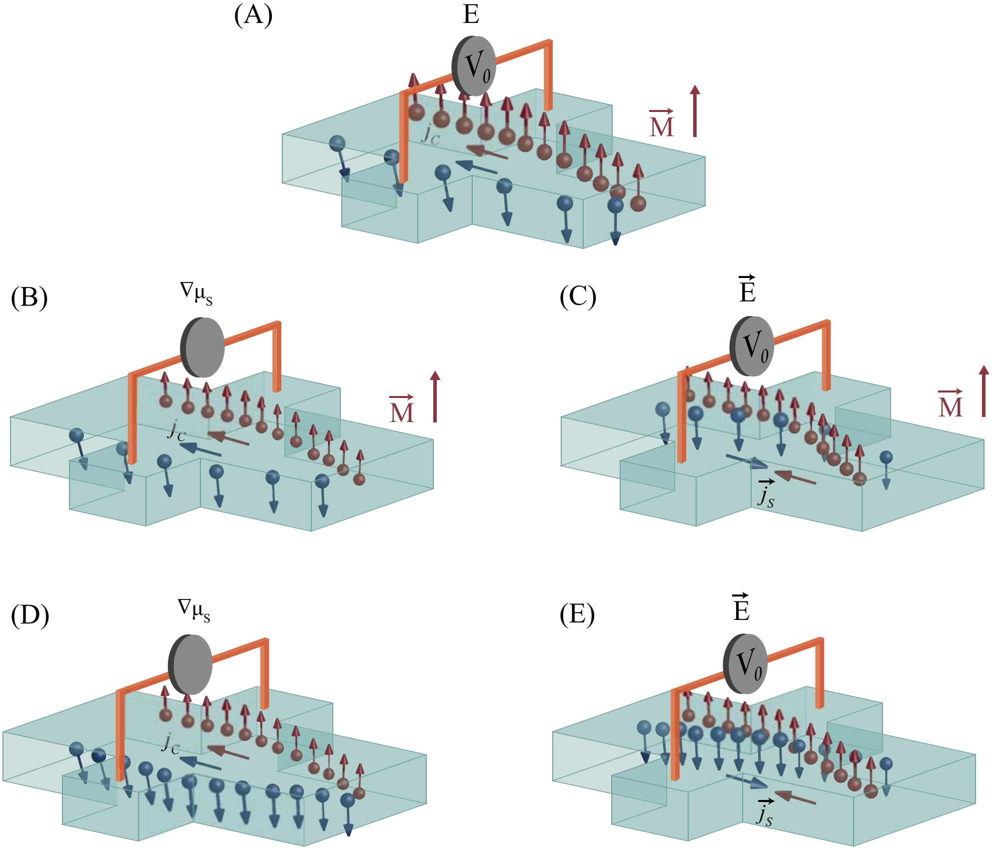

Fig. 13. – Spin-Hall (SHE), Inverse Spin-Hall (ISHE) and Anomalous Hall (AHE) effects. The directions of the spin polarization, of the spin or charge current propagation, and of the electric field or gradient in spin chemical potential are orthonormal to each other. (A) AHE in FM with magnetization $\vec{M}$: a charge current $\vec{j}_C$ gives a Hall field $\vec{E}$. (B) SHE in FM with magnetization $\vec{M}$: a charge current $\vec{j}_C$ gives a spin polarization $\nabla\mu_S$. (C) ISHE in FM with magnetization $\vec{M}$: a spin current $\vec{j}_S$ gives a Hall field $\vec{E}$. (D) SHE in NM with strong SOC: a charge current $\vec{j}_C$ gives a spin polarization $\nabla\mu_S$. (E) ISHE in NM with SOC: spin current $\vec{j}_S$ gives Hall field $\vec{E}$. Expanded from ref. [38].

The second comes from the direct relation between AHE and SHE, illustrated in fig. 13. Again, based on the transformation of variables in eq. (3), the SHE is related to the AHE simply by the fact that the SHE considers the spin accumulation, whereas the AHE considers the charge accumulation that accompany the same effect. The SHE trans-resistance ($-\nabla\mu_S/|\vec{j}_C|$) is then proportional to the AHE trans-resistance ($|\vec{E}|/|\vec{j}_C|$), multiplied by the appropriate constants. The ISHE in FM metals is represented in fig. 13(C). It is the Onsager reciprocal of the SHE: if instead of injecting a charge current and measuring a spin accumulation (the SHE), one injects a spin current, then one must observe a charge accumulation, the ISHE.

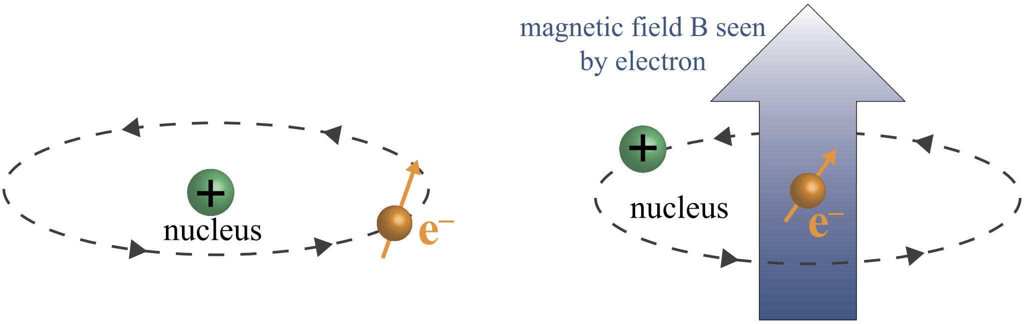

Fig. 14. – Interaction between the electron spin and the orbital magnetic field around the nucleus of an isolated atom.

4·2. *Spin-orbit coupling.* – SHE and ISHE do not require a spin imbalance to pre-exist in a conductor at thermodynamic equilibrium, and also can be induced by transport in non-magnetic conductors (NMs) with an equal number of spin-up and spin-down carriers, see fig. 13(D) and (E). It is, in principle, ubiquitous in electrically conducting solids, but really observed only in those where spin-orbit coupling (SOC) is important. The SHE mechanism in NMs is understood much better than the AHE mechanisms in FMs because SOC is intrinsic and not very sensitive to the defect chemistry of the samples. SOC also can be predicted with reasonable accuracy from the band structure or calculated by Density Functional Theory (DFT). The original theoretical idea was published in 1971 [49], but a clean experimental observation of this SHE had to wait for third of a century [50].

SOCs rely on the interactions between orbital magnetic moments and electron spins. Consider first an electron interacting with a single atom in fig. 14. The electron spin interacts with the moment $\vec{L} = \vec{r} \times m\vec{v}$ that arises from the orbital motion of the core electrons around the nucleus (fig. 14). Here, $\vec{r}$ is the radius of the orbit and $\vec{v}$ the electron orbital velocity. The motion gives rise to an orbital magnetic field $\vec{B}_{HO} \propto \vec{L}$, which in turn increases the energy of the electron by a Zeeman term $\propto g\mu_B\vec{\sigma}\cdot\vec{B}_{HO}$. This additional energy means that a term must be added to the Hamiltonian of that electron, $H_{SOC} = \lambda\vec{\sigma}\cdot\vec{L}$, where λ is the proportionality constant and $\vec{\sigma}$ the unitary vector along the direction of spin polarization.

The band structure of solids reflects the equations of motion of electrons as influenced by interactions between electrons and the collective presence of all atoms in the solid (fig. 15). These interactions first take the form of Coulombic interactions between the electron charge and the periodic potential wells $V(r)$ that represent the charged atomic nuclei in the solid, screened by the charges on the core electrons (fig. 15 top). The Hamiltonian then has a kinetic energy term and a potential term: $H = \hbar^2k^2/2m + V(r)$. The second contribution comes from the electromagnetic interaction of the spin $\vec{\sigma}$ of the electron with the orbital magnetic fields of the nuclei in the solid (fig. 15, middle). The Hamiltonian now has a first term $V(r)$ and a spin-orbit term $H_{SOC} = \lambda\vec{\sigma}\cdot\vec{k}$, which is an odd function of the crystal momentum $\vec{k}$, instead of the moment $\vec{L}$, as is the case for

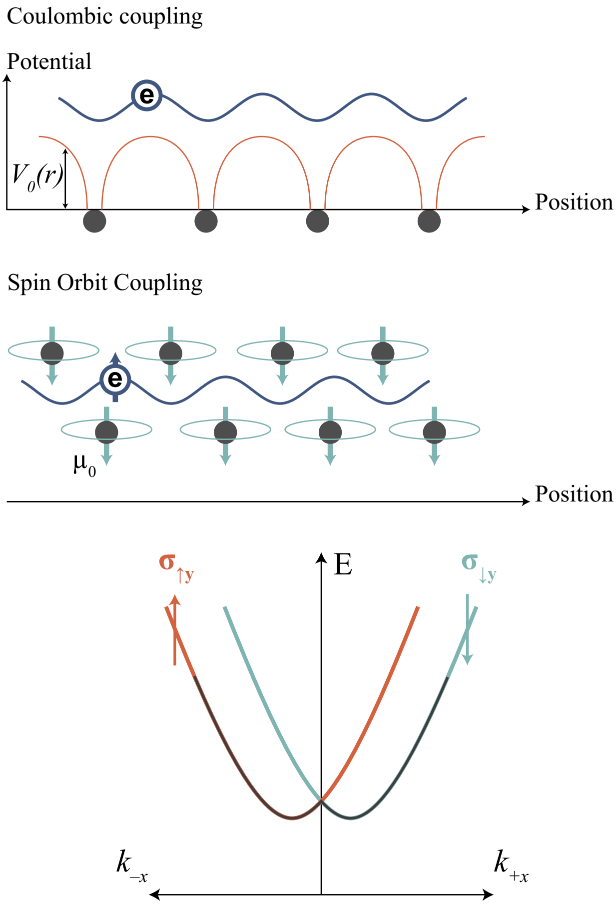

Fig. 15. – The effect of SOCs on the band structure.

an electron moving around a single atom, fig. 14. As a result, the bands split along k into a spin-down band that has a lower energy in the $+k$ direction, and a spin-up band that has a lower energy in the $-k$ direction (fig. 15, bottom). For completion, note that SOC gives rise to many variations of this band structure, as they depend on crystal-field splitting and must obey symmetry relations. However, in all variations the bands split in k-space depending on the sign of $\vec{\sigma}$ (in the image in fig. 15, the k vector points along x and $\vec{\sigma}$ is polarized along y).

The split bands, in turn, give rise to the SHE and ISHE, as shown in fig. 16 [51], via $\vec{\sigma}$-dependent scattering of the electrons. An external magnetic field along y defines $\vec{\sigma}$. Applying an electric field $\vec{E}$ along x results in a shift of the bands by a drift velocity parallel to k_x, and limited by electron back-scattering from $+k_x$ to $-k_x$ as in the Boltzmann transport equation. This back-scattering (dark blue line in fig. 16, left) is accompanied by a decrease in $\sigma_\downarrow$ electrons and an increase in $\sigma_\uparrow$ electrons, a net spin

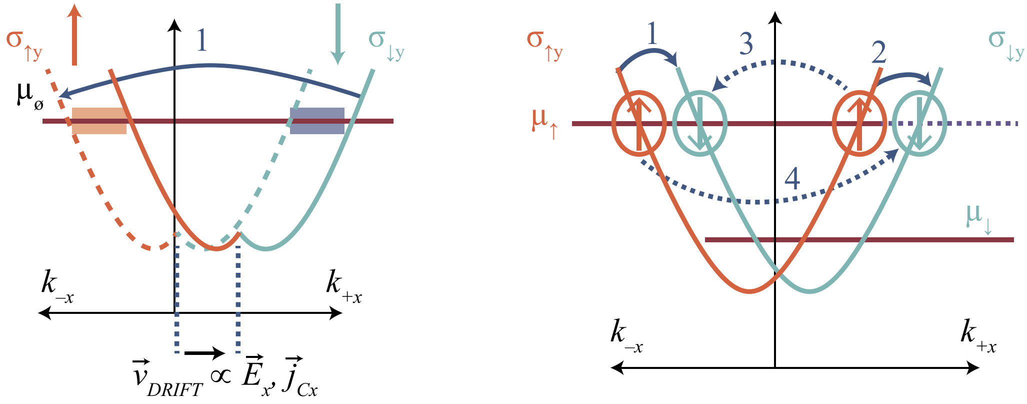

Fig. 16. – The origin of the intrinsic SOC SHE (left) and ISHE (right) [51].

polarization. Thus, it gives rise to a transverse spin flux j_{Sz} that creates a transverse spin accumulation along the third direction z. Because of the analogy with the AHE, this new effect also took the Hall name to become the SHE.

The intrinsic SHE was observed in GaAs by Kato *et al.* [50], who used the optical Kerr effect to detect spin polarization in GaAs (see fig. 17, where the axes were relabeled *vis-à-vis* the original publication in order to correspond to fig. 16). In this experiment, polarized light is incident onto a sample. Its reflection on spin-polarized electrons creates a small rotation in the polarization of the reflected light, the Kerr rotation, which is detected and used as a measure of spin polarization. The figure clearly shows that when current is applied in the x-direction of the sample and a polarizing field sets $\vec{\sigma}$ along y, a spin polarization appears along z. Since no spin current is allowed outside the sample, the spin polarization accumulates at the sample edges. The spin chemical potential $\mu_S = \mu_\uparrow - \mu_\downarrow$ (eq. (4)) is congruent with the curve A_0 in fig. 17. If the same measurement had been taken with a closed spin circuit, *e.g.*, if the sides of the sample had been coated with a spin-absorbing material, a spin flux $j_{S,z}$ would have appeared. The ratio between this spin current and the charge current that drives it gives the spin-Hall angle θ_{SH}:

$$\tan(\theta_{SH}) \equiv \frac{j_{S,z}}{j_{C,x}}\,. \tag{34}$$

More details about measurement in spin-open-circuit and closed circuit are given in Boona *et al.* [4]. A table giving θ_{SH} and L_S for a large variety of solids is given by Hoffmann [52]. As a general rule, strong SOCs result in a high value for $|\theta_{SH}|$, but also in a short spin lifetime and diffusion length.

The Onsager reciprocal of the SHE is the ISHE. Here, injecting electrons spin-polarized along the y-direction into a sample, by injecting a spin flux j_S along the z direction, results in the appearance of an electric field (fig. 13(E)). The effect is the open-

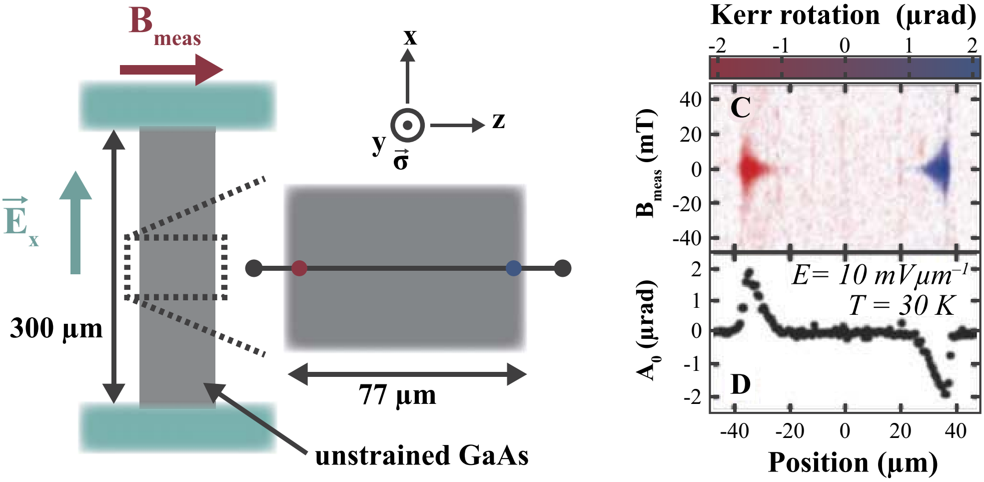

Fig. 17. – Direct observation of the SHE in GaAs. Adapted from ref. [50].

circuit equivalent of the spin-galvanic effect, where instead of a transverse field, a transverse charge current j_C appears. The physics underlying the intrinsic spin-galvanic effect, and by extension ISHE, is illustrated in fig. 16. The injected $\vec{j}_S$ results in an unbalance between the densities of spin-up and spin-down electrons, say so that $\mu_S = \mu_\uparrow - \mu_\downarrow > 0$. Considering now the number of possible spin-flip events from the spin-up majority carrier to the spin-down minority carrier bands (labeled 1–4 in fig. 16), one notices that transitions 1, 2, and 4 all tend to impel momentum in the direction $+k_x$, with only transition 3 impelling momentum along $-k_x$. Thus, a net charge current $\vec{j}_C$ will appear in the sample in the direction of $+k_x$. Again, the ratio between spin and charge current is given by the same θ_{SH} as the SHE, eq. (34). In open circuit conditions, $\vec{j}_C$ will create a charge accumulation, and, thus, an electric field $\vec{E}$, the ISHE field, which is normal to both the spin-polarization direction and the direction of the injected spin flux.

The ISHE has been measured experimentally first, as far as this author is aware, by Valenzuela and Tinkham [53] and the Saitoh group [54]. It has become the most direct, all-electrical spin flux measurement, functioning essentially like a spin-ammeter. Conversely, the SHE has become an all-electrical method to inject spin currents into a material, acting in practice like a spin-current source. Both designs require depositing a thin film of a metal with strong SOC on top of a material in which one wishes to inject or measure spin currents. Thus the transmission of spin currents across interfaces has to be discussed first; it is the object of sect. **5**.

There also are thermoelectric (Nernst) effects associated with the intrinsic SHE and ISHE via the Mott formula, eq. (33). A direct equivalent of the Kato experiment, fig. 16, where a heat flux replaces the current flux, thus, predicted to give a spin-Nernst effect (SNE), has been attempted by several groups, but has not been successful to date. However, the SNE has been measured successfully indirectly [55, 56]. A review of spin-based Nernst effects is given by Boona *et al.* [4].

5. – Spin transport across interfaces

Interfacial magnetism is a field of study in its own right [57]. Only a few aspects that pertain to thermal spin transport, as will be described in sect. **6**, are reviewed in this paper. Spin currents can cross metal/metal interfaces just as electrical currents do. On top of that, thermally driven spin currents actually can cross interfaces between electrically insulating FMs (and sometimes even AFMs) and metals: the spin current resides in magnons on the FM side, and is converted, by conservation of spin-angular momentum, from a magnon current into a spin-polarized electron current in the metal. These two effects are treated separately.

5˙1. *Electronic spin transport across metal FM/NM interfaces.* – In a seminal paper, Johnson and Silsbee [58] (JS) measure and explain the generation of a spin current in a NM via the application of a voltage across the junction of a single-domain FM metal and the NM. While they were not the first to study the problem of spin-current decay in the NM (see review [59]), their results inspired significant development in the field of spin-current injection. JS use the two-fluid model (fig. 1) for the spin-polarized band structure of the FM. At thermodynamic equilibrium, the electrochemical potentials of the spin-up and spin-down bands in FM and NM are all aligned (fig. 18 [59], top). When a current is passed through the FM metal to the NM under the effect of an applied potential (fig. 18, bottom), more electrons from the $\mu_\uparrow$ band are injected into the NM than from the $\mu_\downarrow$ band if the DOS of the former is larger at the chemical potential (see, fig. 18). The formalism of eqs. (2)–(6), applied to bulk conductivities $\sigma_\uparrow$ and $\sigma_\downarrow$, can be applied to interfacial electrical trans-conductances $G_\uparrow$ and $G_\downarrow$, of the spin-up and spin-down electrons. At the interface, eq. (5) becomes

$$\begin{aligned} G &= G_\uparrow + G_\downarrow, \\ G_{\uparrow\downarrow} &= G_\uparrow - G_\downarrow. \end{aligned} \tag{35}$$

Here, G is the electrical trans-conductance, whereas $G_{\uparrow\downarrow}$ is the *spin mixing conductance.* Thus, the spin polarization of the current in the FM is transferred into the adjacent NM: JS show that the corresponding magnetization flux j_M associated with the spin current is

$$j_M = j_C \frac{\mu_B}{e} \eta, \tag{36}$$

where $\eta = \frac{G_\uparrow - G_\downarrow}{G_\uparrow + G_\downarrow} = \frac{G_{\uparrow\downarrow}}{G}$ is a dimensionless constant.

Once the spin flux has penetrated into the NM, it decays by spin-flip interactions following the description in fig. 2 and eqs. (8), (9). The length scale for this decay is L_S, which is on the order of a few nanometers in platinum and gold, but can several microns in copper and aluminum [60]. Note that, as a general rule, the materials with the strongest SOC and largest θ_{SH} also have the shortest values of L_S: strong SOCs promote spin-flip transitions. Such materials also act as spin-sinks: depositing a

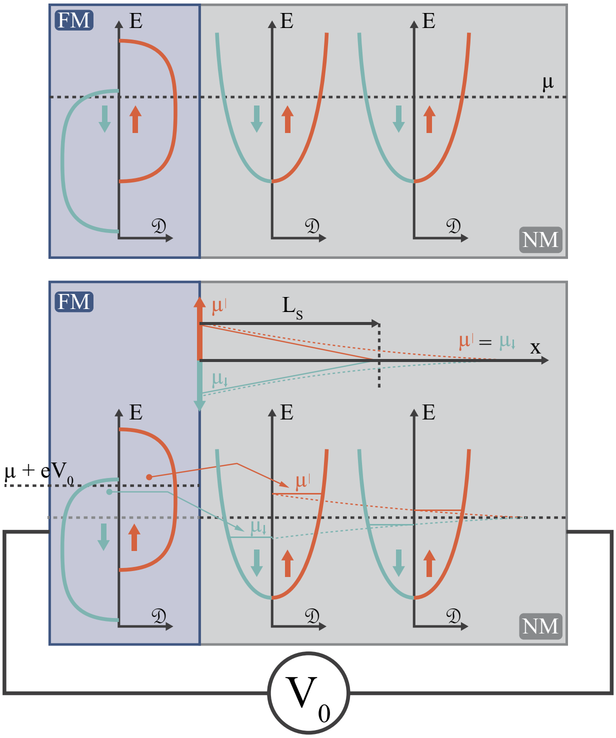

Fig. 18. – Spin transfer torque between FM and normal metals. Adapted with permission from ref. [59], from the Royal Society of Chemistry.

film of a high-SOC metal, like Pt, decreases the spin accumulation in the magnetic or non-magnetic material under it.

The inverse problem from fig. 18, the NM/FM interface, is also described by JS. If the NM layer thickness is below L_S, so that there is still electron spin polarization throughout the NM, the transmission of current across the NM/FM will re-transfer this polarization to the FM, affecting its magnetization.

5˙2. *Spin pumping and spin transfer torque*. – Consider now the case, fig. 19 [61], where the spin in the FM layer resides not in conduction electrons, but in magnons. This case applies to interfaces between NMs and both metallic and insulating FMs. The FM layer has a magnetization $\vec{\mu}$ that precesses, as shown in fig. 19. This moving magnetization causes a spin-polarization of the electrons in the adjacent NM layer, in effect "pumping" a spin flux j_S across the interface from the FM to the NM. The spin-polarization of the electrons in the NM arises from the conservation of spin-angular momentum across that interface. The effect can be estimated by calculating the reflection and transmission coefficients of the magnetization flux at the interfaces, in a fashion that is analogous to scattering theory valid for electron transmission across interfaces (eq. (35)). In this

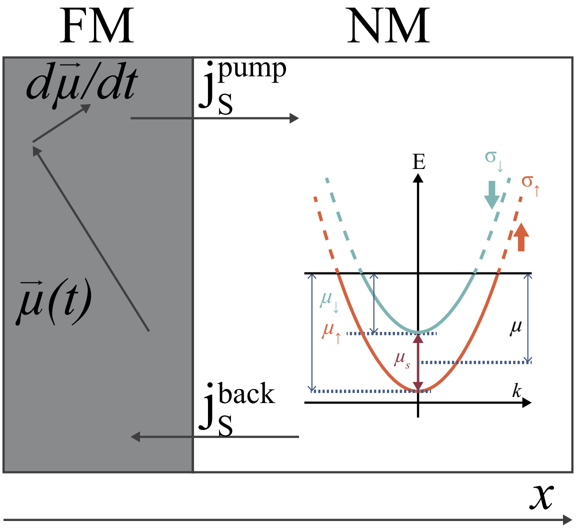

Fig. 19. – Spin transfer torque and spin pumping between magnons in an FM and electrons in a NM layers. This applies to both metallic and non-metallic FMs. Adapted with permission from ref. [61], copyrighted by the American Physical Society.

situation, the scattering is similar to *s*-*d* scattering in FMs, where by "*s*-electrons," we mean the conduction electrons in the NM, and by "*d*-electrons," we mean the core electrons in the unfilled *d*-shells in the FM on which the magnetization resides.

Once again, the Onsager reciprocal of spin pumping exists, known as *spin transfer torque* (STT) [62]. Consider the case where the FM in fig. 19 is an electrical insulator, so that only magnons can support a spin flux in it. A spin polarization in the NM, induced either by passing a charge current through a FM metal or by inducing an ISHE in a metal with high SOCs, will transfer spin torque to the FM, and induce a spin flux j_S carried by magnons, the STT.

5·3. *Designing spin current sources and measurements.* – Combining spin pumping with ISHE makes it possible to design all-electrical spin flux detectors. Conversely, combining SHE with STT makes it possible to design all-electrical spin-flux sources. Any detector or source design must keep the directions of the spin polarization (typically via an applied magnetic field or spontaneous magnetic moment), the spin current or flux, and the electric field or current orthonormal to each other.

All-electrical spin detectors can be designed to measure a spin flux moving from an insulating material into an adjacent NM film with strong SOC. For example, suppose a 7 nm ($< L_S$) thick Pt or W NM-film with large θ_{SH} is deposited on a sample. The spin-flux propagation direction must be normal to the plane of the film. Both the spin polarization (*i.e.*, the applied magnetic field) and the ISHE voltage to be measured must be in the plane of the NM-film, but normal to each other. The spin flux will cross the sample/Pt-film or sample/W-film interface (see sect. **5**) and spin-polarize electrons in the Pt or W. This in turn will generate an ISHE field that is measured. Pt and W have opposite signs of θ_{SH}. This sign change can be used to test that any measured voltage indeed arises from a spin flux and ISHE: the polarity of the voltage signals should change sign when the film is changed from Pt to W. The film thickness has to be maintained at or below L_S; otherwise, the fraction of the film thickness that is above L_S acts as an electrical short to the ISHE (see decay in fig. 18).

This approach does not apply when the spin flux to be measured originates from a metallic FM with a higher electrical conductivity than Pt or W, because that metal will short-circuit the ISHE voltage. However, the approach can work if the spin source has a lower electrical conductivity than the detector, *e.g.*, when it is a semiconductor with spin-polarized electrons. In principle, also, since spin currents can traverse AFM electrical insulators with long L_S [63], presumably in the form of AFM magnons, it is possible to grow a thin, electrically insulating, but spin-transmitting layer between a FM and NM, and still detect an ISHE field in the NM [63].

A source that can inject a spin flux into an electrically insulating material is obtained as the Onsager reciprocal of the structure above. Again, a Pt or W NM-film is evaporated onto the material in which a spin flux is to be injected, but now one passes an electrical current through the NM film. In the presence of a magnetic field perpendicular to the current, this causes the injection of a spin current j_S normal to the thickness of the strip via the SHE. Thus, the same structure can serve the purpose of a spin current source. Finally, to inject a spin current into an electrically conducting material, one can inject a charge current normal to the interface between a NM and an FM, as in fig. 18.

6. – The spin-Seebeck effect

Both the spin-Seebeck (SSE) and magnon-drag (MD) effects are advective transport processes involving two separate fluids; here, either magnons and electrons, or electrons in two separate solids, one with spin-polarized electrons and the other a NM with ISHE. The similarity between SSE and MD was first pointed out by Lucassen and Duine [64].

The longitudinal geometry for measuring the SSE is shown in fig. 20. It is very similar to the geometry one would use to measure the Nernst effect on a bulk sample; therefore, it is only applicable to FM insulators as any free electron in the FM would give rise to a Nernst voltage that would contaminate the SSE signal. The most studied FM insulator is YIG (actually a ferrimagnet in which the Fe atoms on octahedral sites have a magnetic alignment opposite to that of the Fe atoms on the tetrahedral sites, but with a net moment nonetheless). The spin current in the FM is supported by magnons. A temperature gradient is applied to the FM insulator along the z direction in fig. 20. Because heaters, heat sinks, and thermometers connect only with the phonon bath, the heat then is transferred from the phonons to the magnon system by phonon-magnon scattering. The characteristic length for this process [65] is of the order of 200 nm in YIG. Once the heat flux is in the magnon system, $\vec{j}_Q$ generates a spin flux $\vec{j}_S$ by eq. (25)

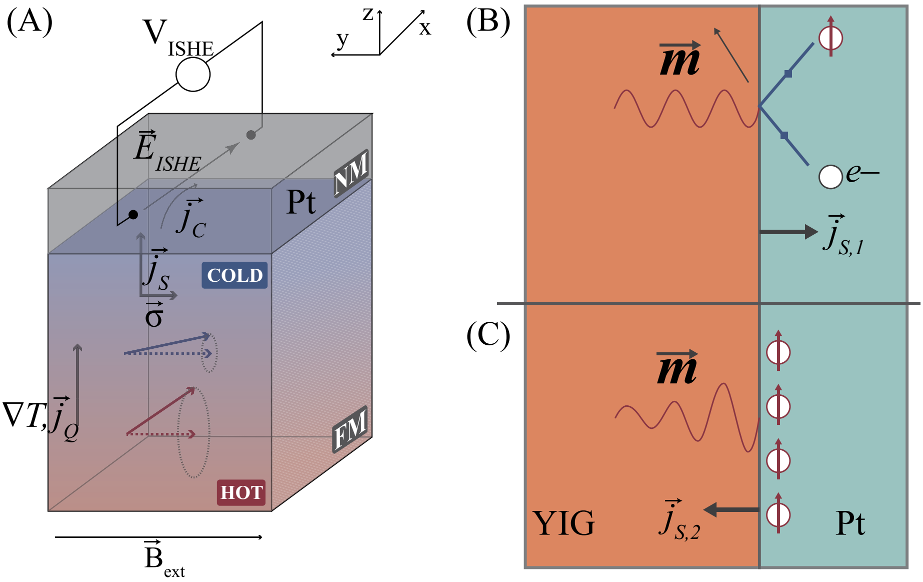

Fig. 20. – Spin Seebeck (A) and (B) and Spin-Peltier (C) effects.

(fig. 20). An external magnetic field sets the spin polarization $\vec{\sigma}//\vec{H}$ along the y direction (fig. 20). A NM (Pt) layer thinner than L_S (typically 5 to 10 nm thick for Pt) is applied to the FM insulator. Spin pumping (sect. **5**˙2) spin-polarizes the electrons in the Pt, giving rise to an ISHE field long the x direction that is picked up as a voltage, as shown. The total structure transforms a temperature difference into a voltage, the SSE.

The SSE was measured first [3] on a Pt-metallic FM (Permalloy) bilayer in a different geometry, which was labelled the transverse SSE [4]. It then was measured in a FM semiconductor GaMnAs [9] and an insulating FM [66]. The largest effect was measured on Landau levels of a non-magnetic semiconductor (InSb) [67]. At a field sufficiently high to confine all electrons on the last Landau level, these electrons are fully spin-polarized, and the SSE reaches 8 mV/K, a value that exceeds all thermoelectric effects on the bulk of the InSb by an order of magnitude. The transverse geometry allows for the use of FM conductors, but its results are easily contaminated by the effect of heat losses and the method requires a rigorously adiabatic mount. Because this is not widely available in laboratories that specialize in magnetic measurements, the transverse geometry is now abandoned in favor of the geometry in fig. 20 developed in 2010 [66]. Non-local measurements of spin transport in insulating FMs, driven by either electrical injection (sect. **5**˙3) or SSE, were performed [68-71]. Cornelissen's PhD [72] provides an excellent review. Optically induced, non-local thermal spin transport has been reported [73], and again, a drift-diffusion model (eq. (7)) explains the data quantitatively [74]. SSE measurements also were used to measure the transmission of magnons though AFM layers deposited on FMs [63]. Both AFMs and paramagnetic solids provide a SSE signal, when the spin-polarization is provided by an appropriate external magnetic field [75, 76]. The zT of SSE measurements can be calculated, but is impractical ($\sim 10^{-3}$).

The Onsager reciprocal of the SSE, the spin-Peltier effect (SPE), also was reported [77] (fig. 20(C)). Passing a current through the Pt cools or heats the magnons in the FM. The reciprocity between SSE and SPE [78] is the product of three separate reciprocity relations, as illustrated by comparing fig. 20(B) and (C): a) between SHE and ISHE (sect. **4**˙2), b) between spin pumping and STT (sect. **5**˙2), and c) in the spin/heat flux Onsager relations eq. (27). Where the ISHE generates the voltage in the SSE measurements, the SHE generates spin polarization in the Pt at the Pt/FM interface in the SPE measurements. Where in SSE, magnons in the FM spin-polarize electrons in the Pt by spin pumping, in SPE the spin accumulation in the Pt transfers spin-angular momentum into the FM magnon system by STT. Finally, where the temperature gradient drives the spin flux in the magnon system during SSE, the magnonic Peltier coefficient eq. (27) drives a temperature gradient in the SPE experiment.

7. – Magnon drag

Whereas the SSE generally is a very small effect ($< 1\,\mu$V/K) at room temperature and has almost no potential applications in thermoelectric technology, the same does not hold for MD. The MD thermopower is often an order of magnitude higher than the regular diffusion thermopower in metals, and also dominates it in magnetic semiconductors. It is the only example where a spin-based effect is much larger than a charge-based effect. MD is also quite useful in the quest for high zT materials [79]. Figure 21 illustrates the similarities and differences between SSE (top) and MD (bottom) effects. The spin-flux generation mechanism is common to both: a temperature gradient, initially imposed on the phonon system, is transferred to the magnons system, where the magnon heat current also generates a spin current. The first difference is that in the SSE, the FM must be electrically insulating, whereas in MD, it must be an electrical conductor. The second difference is one of material quantity: in the SSE, the spin current goes though an interface; therefore, the structure must have a thin Pt (or other metal with strong SOC) film, whereas the MD effect is a bulk effect using the conduction electrons of the FM material itself. Whereas in SSE, the FM spin current transfers spin-angular momentum through an interface in the spin-pumping mechanism, in MD, the spin current transfers linear momentum to the electrons, thereby increasing the longitudinal electric field by a quantity $\vec{E}_{MD}$. The underlying physics is common: both spin pumping and linear-momentum transfer are caused by *s*-*d* scattering, which is very intense. *s*-*d* scattering it is the reason why the mobility in FM and paramagnetic conductors is much lower than in non-magnetic conductors. It is also quite independent of temperature, and persists to very high temperatures. The MD thermopower is then the ratio between the two collinear gradients:

$$\alpha_{md} \equiv \frac{\vec{E}_{MD}}{\nabla T}\,. \tag{37}$$

Spin Seebeck Effect

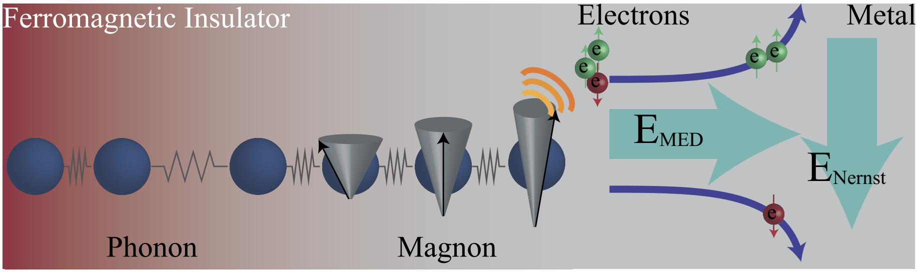

Magnon-Drag Effect

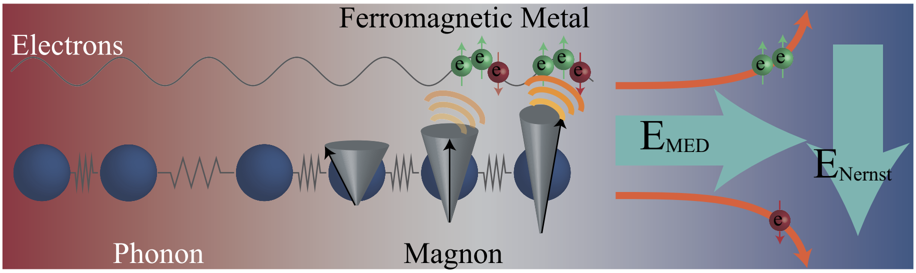

Fig. 21. – Spin Seebeck *vs.* magnon-drag effects.

For completion, we mention that, in principle, magnons also can transfer spin-angular momentum to conduction electrons and add to the spin polarization of the free electrons in the FM, thereby adding to the electric field $\vec{E}_{Nernst}$ due to the AHE and the ISHE; this possibility, however, has not been evinced experimentally to date.

Historically, MD was suspected to be the source of the very large thermopower of iron [1] and the AFM MnTe [2]. Early theories for MD were inspired by those from phonon drag, but required excruciating calculations of scattering times, which in practice are never really accurate. Based on the modern concepts of spin transport outlined above, two practical MD theories have emerged recently [6]. One is the hydrodynamic theory based on a magnon-electron two-fluid model. The other is a spin-dynamic theory that allows for subtler predictions, but is more difficult to implement in real materials. For metals, the hydrodynamic theory is predictive and allows for the design of high-thermopower alloys [8].

7·1. *The hydrodynamic theory of magnon drag.* – This theory considers the magnetic conductor as comprising [80] an electron and a magnon fluid. The electrons have a momentum density $\vec{p}_e = n_e m \vec{v}_e$ in terms of their number density n_e, mass m, and drift velocity $\vec{v}_e$. The magnons have momentum density $\vec{p}_m = n_m M \vec{v}_m$ expressed as a function of mass $M = \frac{\hbar^2}{2D}$ (D is the magnetic exchange stiffness, eq. (19)), velocity $\vec{v}_m$, and density n_m. The equations of motion for the two coupled fluids, assuming quadratic dispersions and thus Galilean invariance, are

$$\frac{\mathrm{d}\vec{v}_e}{\mathrm{d}t} = \frac{e}{m}\left(\vec{E} - \alpha_d \vec{\nabla} T\right) - \frac{\vec{v}_e}{\tau_e} - \frac{\vec{v}_e - \vec{v}_m}{\tau_{me}}\,, \tag{38}$$

$$\frac{\mathrm{d}\vec{v}_m}{\mathrm{d}t} = -\frac{\alpha_m}{M}\vec{\nabla} T - \frac{\vec{v}_m}{\tau_m} - \frac{\vec{v}_m - \vec{v}_e}{\tau_{em}}\,,$$

where $\vec{E}$ is the electric field and τ_e and τ_m are transport scattering mean free times for the electrons and magnons, respectively. The ordinary electronic diffusion thermopower in a metal is α_d given by

$$\alpha_d = \left(\pi^2/3\right)(k_B/e)(k_B T/\mu)\,. \tag{39}$$

The magnonic thermopower α_m is derived in (28)–(32). The time scales τ_{me} (the scattering time of electrons on magnons) and τ_{em} (the scattering time of magnons on electrons) parametrize the magnon-electron collision rate. Per the conservation of linear momentum, $\frac{n_e m}{\tau_{me}} = \frac{n_m M}{\tau_{em}}$.

Under steady-state conditions and for zero electric current ($v_e = 0$), the above equations are solved to determine the electric field required to counteract the thermal gradient. The total electron thermopower, including both the diffusive and magnon-drag contributions, becomes

$$\alpha \equiv \frac{|\vec{E}|}{|\vec{\nabla} T|} = \alpha_d + \frac{2}{3}\frac{C_m}{n_e e}\frac{1}{1+\frac{\tau_{em}}{\tau_m}} \tag{40}$$

and the magnon-drag contribution, isolated, is [6]

$$\alpha_{md} = \frac{2}{3}\frac{C_m}{n_e e}\frac{1}{1+\frac{\tau_{em}}{\tau_m}}\,. \tag{41}$$

In the hydrodynamic theory, the frictional forces between magnon and electrons push the electrons, alongside the magnons, toward the cold side of the sample, giving a thermopower that has the sign of the effective mass of the main charge carrier times the charge of the electron, *i.e.*, $\alpha_{md} < 0$ when $m > 0$.

The factor $(1+\tau_{em}/\tau_m)^{-1}$ in eq. (41) contains the ratio between τ_{em}, the magnon scattering time for collisions with electrons, and τ_m, the total magnon scattering time, which includes collisions with all scatterers, electrons, defects, phonons, or other magnons. The scattering ratio $\tau_{em}^{-1}/\tau_m^{-1}$ represents the efficiency with which magnons transfer their momentum to electrons. The scattering ratio is different depending whether the solid with MD is a metal, where it is about unity, or a semiconductor, where it can be of order 10^{-2}. It also varies with temperature.

We consider the total magnon scattering frequency τ_m^{-1} first. Its temperature dependence is different below and above a threshold temperature T^*. At higher temperature ($T > T^*$), magnon scattering is likely to be taken over by Gilbert damping [81] in semiconductors, where there are less than 10^{-3} free electrons per atom. It is then parametrized by the dimensionless constant γ as $\tau_m^{-1} \propto \gamma T$. The crossover takes place at $T^* \sim \frac{T_c}{s^{2/3}}(\gamma l)^2$. Here, s is the saturation spin density, about 1 per atom, so that $s \sim a^{-3}$. Using $\gamma \sim 10^{-2}$, $a \sim 1\,\mathrm{nm}$ and scattering length $\ell_m \sim 1\,\mu\mathrm{m}$, we obtain a range of $T^* \sim (10^{-1}$ to $10^{-3})T_c$ (for iron, $T^* \sim 100\,\mathrm{K}$). At lower temperature ($T < T^*$) and in semiconductors, we assume an energy-independent disorder-dominated magnon mean-free path ℓ_m, and then we expect that τ_m scales with temperature as $\tau_m^{-1} \propto \sqrt{T}$ because the FM-magnon DOS scales as $\mathfrak{D} \propto \sqrt{\hbar\omega}$. In metals, conductors with about one free electron per atom, magnon scattering is dominated by electrons $\tau_m^{-1} \sim \tau_{em}^{-1}$ at low temperature.

The electron-magnon scattering frequency τ_{em}^{-1} is expected to scale with temperature as $\tau_{em}^{-1} \propto T^2$. This results from the combination of momentum and energy conservation constraints for electron-magnon scattering, which give a factor of $\sqrt{T}$, and the reduced phase space for occupied magnon states, which gives a factor of $T^{3/2}$.

In all cases, the factor $(1 + \tau_{em}/\tau_m)^{-1}$ should tend to unity with temperature as temperature approaches zero. In semiconductors, in the Gilbert-damping dominated limit, the attenuation of the MD thermopower is expected to have a linear dependence on T. Conversely, in the regime where τ_m is dominated by magnon-phonon scattering, τ_m^{-1} vanishes faster than τ_{em}^{-1} due to the rapidly shrinking phase space, and the factor $(1 + \tau_{em}/\tau_m)^{-1}$ approaches unity. In metals, the factor $(1 + \tau_{em}/\tau_m)^{-1}$ also tends to unity (it becomes 1/2) as $\tau_m^{-1} \sim \tau_{em}^{-1}$. Thus, except for the case of semiconductors at high temperature, α_{md} should follow the T^1 to $T^{1.5}$ law of C_m in FMs, or T^3 in AFMs.

7·2. *Magnon drag due to internal spin pumping.* – The spin-dynamic MD theory considers the motion of the electrons over a magnetically textured landscape, where the texture comes from the presence of magnons. The electron spins then track this texture in a way similar to the calculations of spin-orbit interactions in fig. 15, but because this texture is magnon-induced and dynamic, it gives the electrons a dynamic magnetization. The MD thermopower is calculated from the electric current pumped by the magnetization associated with a magnon heat flux $\vec{j}_Q$ as calculated by Lucassen *et al.* [64]:

$$\vec{j}_C = \sigma \left(\vec{E} + \beta p \frac{\hbar}{2e} \frac{\vec{j}_Q}{sD} \right). \tag{42}$$

Here, β is a dimensionless coefficient (typically around $0:1$ to $0:001$) quantifying the lack of spin conservation in the interaction between spin current and magnetization dynamics, and p is the spin polarization of the electric current (typically of order 1). D

is the stiffness, eq. (19). The thermopower is then

$$\alpha'_{md} = \beta p \frac{\hbar}{2e} \frac{\kappa_m}{sD} \,. \tag{43}$$

Equation (41) is rooted in purely nonrelativistic Galilean momentum transfer between magnons and electrons, while eq. (43) is based on spin-orbit interactions, an effect based on the relativistic Hamiltonian $H_{SOC} = \lambda\vec{\sigma}\cdot\vec{k}$. Remarkably, the estimates in eqs. (41) and (43) coincide if we set the scattering factor in (41) to unity and set $s/n_e = 1$ and $\beta p = 1$, a reasonable assumption for iron, cobalt, or nickel [6]. In particular, the sign of α_{md} and α'_{md} is the same.

The internal spin-pumping theory requires fewer assumptions than the hydrodynamic theory. In particular, if $\beta < 1$, expressing a lack of spin conservation in magnon transport, the transport becomes non-hydrodynamic in nature. There also are transport regimes in which the hydrodynamic and spin-pumping MD thermopowers give very different predictions, in particular about the sign of the MD thermopower. For example, eq. (43) considers only the frictional forces between electrons and magnons as contributing to the advective transport process. A subsequent theory paper [82] includes the effect on the thermopower of the magnon dissipation mechanisms. This adds a second force to magnon-on-electron interactions related to the solid angle subtended by the magnon precession that pushes the magnons towards the hot side. Including this force, the MD thermopower of eq. (43) becomes [82]

$$\alpha'_{md} = (\beta - 3\alpha_G)\, p \frac{\hbar}{2e} \frac{\kappa_m}{sD} \,. \tag{44}$$

The sign of α'_{md} now can change when the effect of magnon decay (expressed by the Gilbert damping term α_G) dominates over the frictional forces (the β term). The ratio β/α_G equals [83] the ratio s_t/s_i between the total amount of spin-angular momentum s_t present in the system and the amount s_i residing on delocalized electrons. This is proportional to the ratio of the net spin-polarization residing on conduction electrons and the total spin polarization, including the fraction that resides on the unfilled d- or f-levels.

7˙3. *Magnon drag in metals.* – Equations (41) and (43) calculate the thermopower of the elemental metals Fe, Co and Ni very well and without having to use any adjustable parameter [6]: fig. 22 shows the thermopower of Fe, which is positive. The dashed line is the MD contribution (eq. (41)) calculated from the known magnon dispersion and calculated specific heat, as well as the known charge carrier concentration, and setting the factor $(1+\tau_{em}/\tau_m)^{-1}$ to unity, as justified above. Adding the diffusion term (eq. (40)) gives the full line, which reproduces the data up to T^*. Figure 22 also gives the zT of the metals that are known to have the highest zT. Except for the case of Cu-Ni alloys, the high zT of all these metals and alloys are attributable to MD because, via the Mott

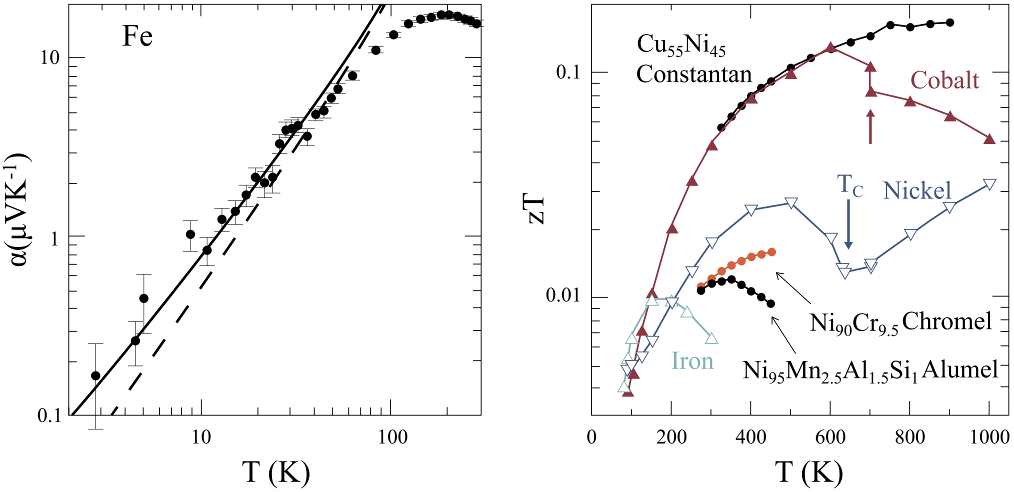

Fig. 22. – Magnon drag in metals. Left: calculated magnon-drag thermopower of iron (dashed line); calculated total electron thermopower with diffusion term (full line) and measured thermopower (data points) [6]. Right: some of the highest thermoelectric figures of merit achieved in metals [7]. The magnon-drag contribution to the thermopower of iron, cobalt and nickel makes these three elements and some of their alloys the metals with the highest zT. The arrows indicate phase transitions.

formula, the thermopower of metals is of the order of $\alpha_d \sim (k_B/e)(k_BT/\mu) \sim 1\,\mu\text{V/K}$ so that for metals without MD, $zT \sim \alpha_d^2/L_0 \sim 10^{-5}$ to 10^{-4}.

Recently, the theory also has been proven to be predictive [84]. DFT is very good at predicting electron DOS and charge-carrier density, and magnon dispersions can be calculated. Therefore, it is possible to design metal alloys to have specific values of α_{md}, as long as $\tau_m^{-1} \sim \tau_{em}^{-1}$, *i.e.*, when magnon scattering by free electrons dominates. Thus, the α_{md} of bcc Fe-Co alloys was predicted and verified experimentally [84].

While the zT of metals, shown in fig. 22, is limited still to $zT \leq 0.16$, the power factor of metals is much higher than that of thermoelectric semiconductors, with thermopowers reaching $60\,\mu\text{V/K}$ [7]. In fact, the power factor of cobalt reaches $160\,\mu\text{W/cm}\,\text{K}^2$ between 300 and 400 K. There is one class of applications where the combination of a high power factor and a high thermal conductivity is very advantageous: cooling devices that operate above ambient temperature, such as electronic devices and batteries [85]. In refrigeration applications, heat backflow from the ambient temperature to the device that must be cooled is an additional parasitic load. However, in cooling applications, heat that flows spontaneously between a load that operates above ambient to ambient is beneficial to the operation of the device. Therefore, classical Bi_2Te_3-based Peltier coolers are not as good at cooling devices such as CPUs as a Peltier cooler made from thermoelectric metals would be. A metal Peltier cooler already provides good cooling performance passively, and adding an active Peltier heat flux to that enhances the effect manifold [85]. MD-metals, such as elemental cobalt, are suited ideally for such application.

Note that the Mott relation [36] does not apply to the MD thermopower. This is because the Mott relation follows from the electron statistical distribution function at thermodynamic equilibrium, whereas drag effects, like all advective transport effects, bring the electron population out of equilibrium. Finally, it is noteworthy that MD, unlike phonon drag, is a high-temperature effect. In phonon drag, phonon momentum is dissipated easily into interactions with other phonons and defects before it is transferred to electrons. This is because electron-phonon coupling is relatively weak, while phonons are subjected strongly to defect and Umklapp scattering at temperatures as low as 1/10-th of their Debye temperature. This limits the operating temperature of phonon drag to typically below 77 K, since most materials have a Debye temperature between 100 and 300 K. In contrast, the magnon-electron interactions that drive the MD thermopower are mediated by *s*-*d* scattering, which is dominant in magnetic metals. As an illustration of the relative strength of phonon-electron and magnon-electron interactions, we point out that the electron mobility in magnetic materials is typically an order of magnitude smaller than in similar non-magnetic materials. That is because the mobility in magnetic materials is limited by *s*-*d* scattering, whereas in NMs, phonons are the dominant electron scatterers. As a result, MD remains dominant to the ordering temperature, typically above 1000 K for most FM metals, although the range of applicability of eq. (41) is limited to T^*, about one tenth of the ordering temperature. The more sophisticated eq. (44) must be used above T^*. As will be shown next, MD boosts the thermopower of magnetic systems even above the ordering temperature.

7˙4. *Magnon drag and paramagnon drag in semiconductors.* – Good thermoelectrics are degenerately doped semiconductors with typically 10^{-3} to 10^{-4} free charge carriers per atom. MD applies to that situation as well, and the factor $1/n_e$ in eq. (41) should result in a high α_{md}, if it were not for two unfortunate facts. First, many mechanisms other than free electrons scatter magnons in semiconductors so that $\tau_m < \tau_{em}$. Besides decreasing α_{md} and thus zT, this also means that eq. (41) loses its predictive quality because scattering times are notoriously difficult to calculate. Second, there are no FM semiconductors known with ordering temperatures $T_C > 80\,\mathrm{K}$. There are AFM semiconductors with T_N above room temperature, but we know of none where $T_N \sim 1000\,\mathrm{K}$. Thus, the discovery of *paramagnon drag* (PMD) was critical [8].

Figure 23 shows the thermopower of Li-doped MnTe samples. MnTe, a hexagonal crystal, is an AFM with magnetic sublattice orientations that are FM in the hexagonal planes, but AFM-like between planes. The ordering temperature is $T_N = 305\,\mathrm{K}$. At $T < T_N$, the thermopower follows a functional $\alpha(T) = \alpha_1 T + \alpha_2 T^3$ where $\alpha_1 T$ is the diffusion thermopower and $\alpha_2 T^3$ can be fitted to eq. (41), which is also valid for AFMs, with a single parameter $\tau_{em}/\tau_m \sim 100$ for all temperatures and charge carrier concentrations.

What is surprising is that the thermopower in the paramagnetic (PM) regime at $T > T_N$ does not decrease back to the $\alpha_1 T^1$ law valid for the diffusion thermopower, which should extrapolate to zero in the limit for $T \to 0$ [8]. Instead, at $T > T_N$, the

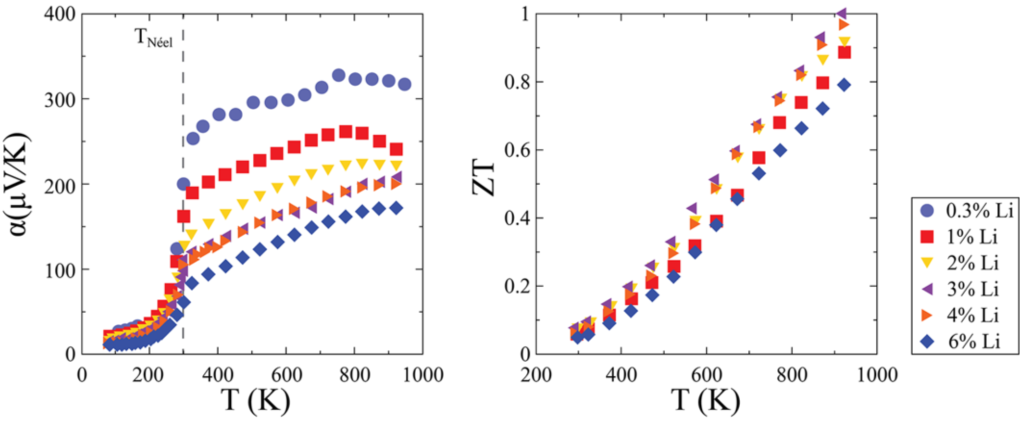

Fig. 23. – Magnon drag in semiconducting AFM MnTe doped with Li [8]. Left: thermopower below the Neel temperature ($T_N = 305\,\mathrm{K}$) follows a mostly T^3 law but maintains a very high value at $T > T_N$, due to paramagnon drag. Right: this allows for a very high zT to be reached in these simple binary semiconductors in their paramagnetic regime.

thermopower follows a law $\alpha(T) = \alpha_1 T + \alpha_{PMD}$ where α_{PMD} is T-independent, but increases with decreasing n_e. Inelastic neutron scattering data [8] show the existence of the magnon dispersion below T_N, as expected (see fig. 5(B)). Above T_N, this spin structure in PM-MnTe does not disappear, as would be expected if the spin orientations became completely random. Instead, a broad spin structure remains in the paramagnetic material at the energy where the magnon band was in the antiferromagnetic material. Furthermore, the width of the structure, while larger in the PM phase than in the AFM phase, remains quite independent of temperature from T_N to 450 K, the highest temperature of the experiment. From its width, the authors derive that the spin structure in the PM regime has a temperature-independent spin-spin correlation length $\xi \sim 2.3 \pm 0.2\,\mathrm{nm}$, and a spin lifetime of $\tau_{L,PM} \sim 27 \pm 1\,\mathrm{fs}$. This spin structure is known as a *paramagnon*. Because ξ is much larger than the electron de Broglie wavelength, $1/k_F \sim 0.6\,\mathrm{nm}$, and because the spin lifetime is much longer than the electron scattering time calculated from mobility $\tau_e \sim 3 \pm 2\,\mathrm{fs}$, the authors suggest that, to the electrons, this paramagnon looks like a fully developed magnon that can give an MD thermopower α_{PMD}. Surprisingly, the only T-dependence of α comes from α_d, while α_{PMD} appears to not be temperature dependent at least to $T = 3\ T_N$, except in the lowest-doped sample.

Paramagnons typically consist of a set of a few AFM-coupled spins, (*e.g.*, in a 1D picture ↑↓↑), extending spatially over ξ. The paramagnon-neutron scattering signature has no T-dependence at all to 450 K (no data are available above that). A simple physical picture for this lack of temperature dependence is based on the fact that to destroy the spin-spin correlation in a short-range ↑↓↑-spin structure requires flipping a single spin 180°. This is because, unlike the case of long-range magnons, there simply are not an unlimited number of aligned spins available over which to spread the decrease of magnetization like in ordered solids (see fig. 3). The energy it takes to flip the middle spin in such a structure from ↑↓↑ to ↑↑↑ is much higher than the exchange coupling energy J that binds the long-range collective spin waves at $T < T_N$, because to flip a single spin, one must count the interactions of that spin with all its nearest (or next-nearest) neighbors. Because each Mn in MnTe has 4 nearest neighbors, flipping a single spin 180° requires about 4 times more energy, and thus ξ is not expected to decrease before the temperatures reaches 3 to 4 T_N.

The excess thermopower ascribed to PMD makes it possible to reach $zT > 1$ in this simple binary semiconductor without any additional optimization of grain size or nanostructuring to reduce thermal conductivity. Note that PMD is a higher-temperature effect yet than MD. It also extends the number of semiconductors that are candidate high-zT materials. In the past, adding magnetic ions to a semiconductor was recognized to be detrimental to the charge carrier mobility, because magnetic s-d scattering is extremely effective and reduces mobility. The new knowledge that this very same interaction can result in the appearance of PMD, which can quite possibly boost the thermopower to such as extent that it more than compensates the loss of mobility in zT, opens a completely new approach to optimizing thermoelectrics. Indeed, the large number of known PM semiconductors constitute a hitherto unexplored class of materials that should be investigated to find other high-zT semiconductors. Finally, in principle, it should be easier to reduce the lattice thermal conductivity in materials with PMD, because the electronic mobility in those materials is already limited by s-d scattering to a low number. Alloying or nanostructuring to lower the lattice thermal conductivity will thus have a smaller relative detrimental effect on the electron mobility than it has in non-magnetic systems.

8. – Conclusion

This paper is an attempt to give a didactic introduction to the field of spin caloritronics, which studies mixed spin, heat, and charge transport under the combined effects of a magnetic field gradient, an electrical field, and a temperature gradient. The classical field of thermoelectrics (mixed heat/charge transport) thus is broadened by the number of possible combinations of effects, *i.e.*, a factor $3!/2! = 3$. The paper also reviews a few of basics of magnetism, *e.g.*, magnons, as well as of the tools used to measure and generate spin fluxes, *e.g.*, the SHE and ISHE effects. These tools are as critical to the field of spin transport as voltmeters, current sources, thermometers, and heat sinks are to thermoelectrics. Perhaps this introduction and review will make it possible for the community to develop new ideas and find new materials for solid-state thermal-to-electrical energy conversion. The paper refers to many review articles that, in turn, can guide the reader through the research literature.

* * *

The author acknowledges support of the OSU Center for Emerging Materials, an NSF MRSEC, under grant number DMR-2011876.

REFERENCES

[1] BLATT F. J., FLOOD D. J., ROWE V., SCHROEDER P. A. and COX J. E., *Phys. Rev. Lett.*, **18** (1967) 395.

[2] WASSCHER J. D. and HAAS C., *Phys. Lett.*, **8** (1964) 302.

[3] UCHIDA K., TAKAHASHI S., HARII K., IEDA J., KOSHIBAE W., ANDO K., MAEKAWA S. and SAITOH E., *Nature*, **455** (2008) 778.

[4] BOONA S. R., MYERS R. C. and HEREMANS J. P., *Energy Environ. Sci.*, **7** (2014) 885.

[5] BAUER G. E. W., SAITOH E. and VAN WEES B. J., *Nat. Mater.*, **11** (2012) 391.

[6] WATZMAN S. J., DUINE R. A., TSERKOVNYAK Y., BOONA S. R., JIN H., PRAKASH A., ZHENG Y. and HEREMANS J. P., *Phys. Rev. B*, **94** (2016) 144407.

[7] VANDAELE K., WATZMAN S. J., FLEBUS B., PRAKASH A., ZHENG Y., BOONA S. R. and HEREMANS J. P., *Mater. Today Phys.*, **1** (2017) 39.

[8] ZHENG Y., LU T., POLASH MD. M. H., RASOULIANBOROUJENI M., LIU N., MANLEY M. E., DENG Y., SUN P. J., CHEN X. L., HERMANN R. P., VASHAEE D., HEREMANS J. P. and ZHAO H., *Sci. Adv.*, **5 eaat** (2019) 9461.

[9] JAWORSKI C. M., YANG J., MACK S., AWSCHALOM D. D., HEREMANS J. P. and MYERS R. C., *Nat. Mater.*, **9** (2010) 898.

[10] TSERKOVNYAK Y. and WONG C. H., *Phys. Rev. B*, **79** (2009) 014402.

[11] STONER E. C., *Proc. R. Soc. London, Ser. A*, **169** (1939) 339.

[12] BAUER G. E. W., BRETZEL S., BRATAAS A. and TSERKOVNYAK Y., *Phys. Rev. B*, **81** (2010) 024427.

[13] TORREY H. C., *Phys. Rev.*, **104** (1956) 563.

[14] DEJENE F. K., FLIPSE J. and VAN WEES B. J., *Phys. Rev. B*, **86** (2012) 024436.

[15] FLIPSE J., BAKKER F. L., SLACHTER A., DEJENE F. K. and VAN WEES B. J., *Nat. Nanotechnol.*, **7** (2012) 166.

[16] EREKHINSKY M., CASANOVA M. F., IVAN K., SCHULLER I. and SHARONI A., *Appl. Phys. Lett.*, **100** (2012) 212401.

[17] CHOI G.-M., MOON C.-H., MIN B.-C., LEE K.-J. and CAHILL D. G., *Nat. Phys.*, **11** (2015) 576.

[18] KITTEL C., *Introduction to Solid State Physics*, 4th edition (John Wiley and Sons, New York) 1971.

[19] SINCLAIR R. N. and BROCKHOUSE B. N., *Phys. Rev.*, **120** (1960) 1638.

[20] WINDSOR C. G. and STEVENSON R. H. W., *Proc. Phys. Soc.*, **8** (1966) 501.

[21] BOONA S. R. and HEREMANS J. P., *Phys. Rev. B*, **91** (2015) 226401.

[22] SLACK G. A., *Phys. Rev.*, **122** (1961) 1662.

[23] KANODA K. and KATO R., *Annu. Rev. Condens. Matter Phys.*, **2** (2011) 167.

[24] KITAEV A., *Ann. Phys.*, **321** (2006) 2.

[25] KASAHARA Y., OHNISHI T., MIZUKAMI Y., TANAKA O., MA S., SUGII K., KURITA N., TANAKA H., NASU J., MOTOME Y., SHIBAUCHI T. and MATSUDA Y., *Nature*, **559** (2018) 227.

[26] KATSURA H., NAGAOSA N. and LEE P. A., *Phys. Rev. Lett.*, **104** (2010) 066403.

[27] WEN X. G., *Phys. Rev. B*, **43** (1991) 11025.

[28] KANE C. and FISHER M. P. A., *Phys. Rev. B*, **55** (1997) 15832.

[29] READ N. and GREEN D., *Phys. Rev. B*, **61** (2000) 10267.

[30] HIRSCHBERGER M., CHISNELL R., LEE Y. S. and ONG N. P., *Phys. Rev. Lett.*, **115** (2015) 106603.

[31] HIRSCHBERGER M., KRIZAN J. W., CAVA R. J. and ONG N. P., *Science*, **348** (2015) 106.

[32] DU C., VAN DER SAR T., ZHOU T. X., UPADHYAYA P., CASOLA F., ZHANG H., ONBASLI M. C., ROSS C. A., WALSWORTH R. L., TSERKOVNYAK Y. and YACOBY A., *Science*, **357** (2017) 195.

[33] DEMIDOV V. E., URAZHDIN S., DIVINSKIY B., BESSONOV V. D., RINKEVICH A. B., USTINOV V. V. and DEMOKRITOV S. O., *Nat. Commun.*, **8** (2017) 1579.

[34] CORNELISSEN L. J., PETERS K. J. H., BAUER G. E. W., DUINE R. A. and VAN WEES B. J., *Phys. Rev. B*, **94** (2016) 014412.

[35] FLEBUS B., *Phys. Rev. B*, **100** (2019) 064410.

[36] CUTLER M. and MOTT N. F., *Phys. Rev.*, **181** (1969) 1336.

[37] HALL E. H., *Philos. Mag. Ser. 5*, **12** (1881) 157.

[38] SINOVA J., VALENZUELA S. O, WUNDERLICH J., BACK C. H., and JUNGWIRTH T, *Rev. Mod. Phys.*, **87** (2015) 1213.

[39] NAGAOSA N., *J. Phys. Soc. Jpn.*, **75** (2006) 042001.

[40] ONODA S., SUGIMOTO N. and NAGAOSA N., *Phys. Rev. B*, **77** (2008) 165103.

[41] HANKIEWICZ E. M. and VIGNALE G., *Phys. Rev. Lett.*, **100** (2008) 026602.

[42] SMIT J., *Physica*, **24** (1958) 39.

[43] CHENG J. L. and WU M. W., *J. Phys.: Condens. Matter*, **20** (2008) 085209.

[44] BERGER L., *Phys. Rev. B*, **2** (1970) 4559.

[45] JUNGWIRTH T., NIU Q. and MACDONALD A. H., *Phys. Rev. Lett.*, **88** (2002) 20.

[46] NAGAOSA N., SINOVA J., ONODA S., MACDONALD A. H. and ONG N. P., *Rev. Mod. Phys.*, **82** (2010) 1539.

[47] YE J., KIM Y.-B., MILLIS A. J., SHRAIMAN B. I., MAJUMDAR P. and TEŠANOVIĆ Z., *Phys. Rev. Lett.*, **83** (1999) 3737.

[48] TAGUCHI Y., OOHARA Y., YOSHIZAWA H., NAGAOSA N. and TOKURA Y., *Science*, **291** (2001) 2573.

[49] DYAKONOV M. I. and PEREL V. I., *Sov. Phys. JETP Lett.*, **13** (1971) 467.

[50] KATO Y., MYERS R. C., GOSSARD A. C. and AWSCHALOM D. D., *Science*, **306** (2004) 1910.

[51] GANICHEV S. D., IVCHENKO E. L., BEL'KOV V. V., TARASENKO S. A., SOLLINGER M., WEISS D., WEGSCHEIDER W. and PRETTL W., *Nature*, **417** (2002) 153.

[52] HOFFMAN A., *IEEE Trans. Magn.*, **49** (2013) 5172.

[53] VALENZUELA S. O. and TINKHAM M., *Nature*, **442** (2006) 176.

[54] SAITOH E., UEDA M., MIYAJIMA H. and TATARA G., *Appl. Phys. Lett.*, **88** (2006) 182509.

[55] MEYER S., CHEN Y.-T., WIMMER S., ALTHAMMER M., WIMMER T., SCHLITZ R., GEPRÄGS S., HUEBL H., KÖDDERITZSCH D., EBERT H., BAUER G. E. W., GROSS R. and GOENNENWEIN S. T. B., *Nat. Mater.*, **16** (2017) 977.

[56] Sheng P., Sakuraba Y., Lau Y.-C., Takahashi S., Mitani S. and Hayashi M., *Sci. Adv.*, **3** (2017) 977.

[57] Hellman F., Hoffman A., Tserkovnyak Y., Beach G., Fullerton E., Leighton C., MacDonald A., Ralph D., Arena D., Durr H., Fischer P., Grollier J., Heremans J., Jungwirth T., Kimel A., Koopmans B., Krivorotov I., May S., Petford-Long A., Rondinelli J., Samarth N., Schuller I., Slavin A., Stiles M., Tchernyshyov O., Thiaville A. and Zink B., *Rev. Mod. Phys.*, **89** (2017) 025006.

[58] Johnson M. and Silsbee R. H., *Phys. Rev. B*, **37** (1988) 10.

[59] Boona S. R., Myers R. C. and Heremans J. P., “Spin Caloritronics”, *Energy Environ. Sci.*, **7** (2014) 885.

[60] Jedema F. J., Nijboer M. S., Filip A. T. and van Wees B. J., *Phys. Rev. B*, **67** (2003) 085319.

[61] Tserkovnyak Y., Brataas A. and Bauer G. E. W., *Phys. Rev. B*, **66** (2002) 224403.

[62] Slonczewski J. C., *J. Magn. & Magn. Mater.*, **159** (1996) L1.

[63] Prakash A., Brangham J., Yang F. and Heremans J. P., *Phys. Rev. B*, **94** (2016) 014427.

[64] Lucassen M. E., Wong C. H., Duine R. A. and Tserkovnyak Y., *Appl. Phys. Lett.*, **99** (2011) 265506.

[65] Prakash A., Flebus B., Brangham J., Yang F., Tserkovnyak Y. and Heremans J. P., *Phys. Rev. B*, **97** (2018) 020408(R).

[66] Uchida K., Xiao J., Adachi H., Ohe J., Takahashi S., Ieda J., Ota T., Kajiwara Y., Umezawa H., Kawai H., Bauer G. E. W., Maekawa S. and Saitoh E., *Nat. Mater.*, **9** (2010) 894.

[67] Jaworski C. M., Myers R. C., Johnston-Halperin E. and Heremans J. P., *Nature*, **487** (2012) 210.

[68] Shan J., Cornelissen L. J., Liu J., Ben Youssef J., Liang L. and van Wees B. J., *Phys. Rev. B*, **96** (2017) 184427.

[69] Cornelissen L. J., Shan J. and van Wees B. J., *Phys. Rev. B*, **94** (2016) 180402R.

[70] Cornelissen L. J., Oyanagi K., Kikkawa T., Qiu Z., Kuschel T., Bauer G. E. W., van Wees B. J. and Saitoh E., *Phys. Rev. B*, **96** (2017) 104441.

[71] Cornelissen L. J., Liu J., Duine R. A. and van Wees B. J., *Phys. Rev. Lett.*, **120** (2018) 097702.

[72] Cornelissen L. J., *Magnon spin transport in magnetic insulators*, PhD Dissertation, Rijksuniversiteit Groningen (2018) `https://www.rug.nl/research/portal/files/59286993/Complete_thesis.pdf`.

[73] Giles B. L., Yang Z., Jamison J. S., Gomez-Perez J. M., Vélez S., Hueso L. E., Casanova F. and Myers R. C., *Phys. Rev. B*, **96** (2017) 180412(R).

[74] Jamison J. S., Yang Z., Giles B. L., Brangham J. T., Wu G., Hammel P. C., Yang F. and Myers R. C., *Phys. Rev. B*, **100** (2019) 134402.

[75] Wu S. M., Zhang W., Amit K. C., Borisov P., Pearson J. E., Jiang J. S., Lederman D., Hoffmann A. and Bhattacharya A., *Phys. Rev. Lett.*, **116** (2016) 097204.

[76] Wu S. M., Pearson J. E. and Bhattacharay A., *Phys. Rev. Lett.*, **114** (2015) 186602.

[77] Flipse J., Dejene F. K., Wagenaar D., Bauer G. E. W., Ben Youssef J. and van Wees B. J., *Phys. Rev. Lett.*, **113** (2014) 027601.

[78] Sola A., Basso V., Kuepferling M., Dubs C. and Pasquale M., *Proceedings*, **26** (2019) 15.

[79] Boona S. R., Watzman S. J. and Heremans J. P., *APL Mater.*, **4** (2016) 104502.

[80] Grannemann G. N. and Berger L., *Phys. Rev. B*, **13** (1976) 2072.
[81] Gilbert T. L., *IEEE Trans. Magn.*, **40** (2004) 3443.
[82] Flebus B., Duine R. A. and Tserkovnyak Y., *EPL*, **115** (2016) 57004.
[83] Tserkovnyak Y., Brataas A. and Bauer G. E. W., *J. Magn. & Magn. Mater.*, **320** (2008) 1282.
[84] Zheng Y., Weiss E. J., Antolin N., Windl W. and Heremans J. P., *J. Appl. Phys.*, **126** (2019) 125107.
[85] Adams M. J., Verosky M., Zebarjadi M. and Heremans J. P., *Phys. Rev. Appl.*, **11** (2019) 054008.

This page intentionally left blank

International School of Physics “Enrico Fermi”
Villa Monastero, Varenna
Course 207
15 – 20 July 2019

Advances in Thermoelectricity: Foundational Issues, Materials and Nanotechnology

Directors

DARIO NARDUCCI
Dipartimento di Scienza dei Materiali
Università di Milano Bicocca
Via R. Cozzi 55
20125 Milano
Italy
dario.narducci@unimib.it

G. JEFFREY SNYDER
Northwestern University
McCormick School of Engineering
Technological Institute
2145 Sheridan Rd.
Evanston, IL 60208
USA
gjeffsnyder@gmail.com
jeff.snyder@northwestern.edu

Scientific Secretary

CARLO FANCIULLI
CNR-ICMATE
Via Previati 1/E
23900 Lecco
Italy
carlo.fanciulli@cnr.it

Lecturers

GIULIANO BENENTI
Dipartimento di Scienza e Alta Tecnologia
Università dell’Insubria
Via Valleggio 11
22100 Como
Italy
Giuliano.Benenti@uninsubria.it

YURI GRIN
Max-Planck-Institut für Chemische Physik
fester Stoffe
Nöthnitzer Str. 40
D-01187 Dresden
Germany
grin@cpfs.mpg.de

JOSEPH HEREMANS
Ohio State University
Department of Mechanical
& Aerospace Engineering
201 W 19th Ave W494 Scott Lab
Columbus, OH 43210
USA
heremans.1@osu.edu
ripley.25@osu.edu

Kunihito Koumoto
Nagoya Industrial Science
Research Institute
1-13 Yotsuya-dori, Chikusa-ku
Nagoya, 464-0819
Japan
`koumoto@apchem.nagoya-u.ac.jp`

Bruno Lorenzi
Dipartimento di Scienza dei Materiali
Università di Milano Bicocca
Via R. Cozzi 55
20125 Milano
Italy
`bruno.lorenzi@unimib.it`
`blorenzi@mit.edu`

Marisol Martin-Gonzalez
MM-Instituto de Microelectrónica
de Madrid
Calle de Isaac Newton, 8
28760 Tres Cantos
Madrid
Spain
`marisol@imm.cnm.csic.es`

Neophytos Neophytou
University of Warwick
School of Engineering
Coventry CV4 7AL
UK
`N.Neophytou@warwick.ac.uk`
`nneoph@gmail.com`

Riccardo Rurali
ICMAB
Campus de la UAB
Bellaterra
Spain
`rrurali@icmab.es`

Henning Sirringhaus
University of Cambridge
Microelectronics Research Centre
Cavendish Laboratory
JJ Thomson Avenue
Cambridge CB3 0HE
UK
`hs220@cam.ac.uk`

Students

Mohamed Atwa	Okinawa Institute of Science & Technology, Japan
Francesco Aversano	Università di Torino, Italy
Trevor Bailey	University of Michigan, USA
Julia Camut	German Aerospace Center, Koln, Germany
Antonio Cappai	Università di Cagliari, Italy
Dhritiman Chakraborty	University of Warwick, Coventry, UK
Kamil Ciesielski	Institute of Low Temperature and Structure Research Wroclaw, Poland
Chiara Cignarella	Università di Roma “La Sapienza”, Italy
Filipe Correia	University of Minho, Guimaraes, Portugal
Laura De Sousa Oliveira	University of Warwick, Coventry, UK
Dennis Groeneveld	IMTEK, Freiburg, Germany
Ramya Gurunathan	Northwestern University, Evanston, USA
Hikaru Horii	Tokyo University of Science, Japan
Eleonora Isotta	Università di Trento, Italy
Felix Kaiser	Max Planck Institute for Chemical Physics of Solids, Dresden, Germany
Nikola Kanas	Norwegian University of Science and Technology, Trondheim, Norway
Shoya Kawano	Kyushu Institute of Technology, Fukuoka, Japan
Haruno Kunioka	Tokyo University of Science, Japan
Caterina La Terra	Politecnico di Milano, Italy
Giovanna Latronico	Shibaura Institute of Technology, Saitama, Japan
Ketan Lohani	Università di Trento, Italy
Stefano Magagna	Università di Milano Bicocca, Italy

PANAGIOTIS MANGELIS	Università di Pisa, Italy
ARTURO KLAUS MARQUEZ GUAMAN	Università di Milano Bicocca, Italy
MATTEO MASTELLONE	CNR-ISM, Roma, Italy
GEORGIOS MESARITIS	University of Cyprus, Larnaca, Cyprus
BUSRA METE	Koc University, Istanbul, Turkey
KUNAL MITRA	German Aerospace Center, Koln, Germany
DUARTE MOCO	Universidade Lisboa, Portugal
MICHELE PIGLIAPOCHI	Universitat Autonoma de Barcelona, Spain
CANDIDA PIPITONE	Università di Palermo, Italy
JOANA RIBEIRO	University of Minho, Guimaraes, Portugal
RODRIGO RUBIO GOVEA	Helmholtz-Zentrum fur Materialen und Energie, Berlin, Germany
FERNAN SAIZ	Universitat Autonoma de Barcelona, Spain
OLIVER SCHMUCK	Swiss Federal Labs for Materials Science and Research, Zurich, Switzerland
PENGPENG SHANG	INFN - Laboratori Nazionali di Frascati, Italy
BHUVANESH SRINIVASAN	National Institute for Materials Science, Tsukuba, Japan
DIONISIUS H. L. TJHE	Cavendish Laboratory, Cambridge, UK
VANIRA TRIFILETTI	Queen Mary University of London, UK
ANASTASIIA TUKMAKOVA	ITMO University, Saint Petersburg, Russia
FEDERICA URSI	Università di Palermo, Italy
MARIJN VAN DE PUTTE	University of Twente, Enschede, The Netherlands
RUBEN BUENO VILLORO	Max Planck Institute for Iron Research, Dusseldorf, Germany
MUJDE YAHYAOGLU	Koc University, Istanbul, Turkey
LU ZHANG	Cavendish Laboratory, Cambridge, UK

Observers

YARON AMOUYAL	Technion-Israel Institute of Technology, Haifa, Israel
ALBERTO CASTELLERO	Università di Torino, Italy
RAIMONDO CECCHINI	CNR-IMM, Agrate Brianza, Italy
JAYWAN CHUNG	Korea Electrotechnology Research Institute, Changwon, Korea
SHRIKANT SAINI	Kyushu Institute of Technology, Fukuoka, Japan
FEDERICA VIGNATI	Politecnico di Milano, Italy

This page intentionally left blank

Finito di stampare
nel mese di maggio 2021

This page intentionally left blank

This page intentionally left blank